



Toland, Karl W. (2020) *Aspects of fused silica fibres for use in gravitational waves research*. PhD thesis.

<http://theses.gla.ac.uk/81461/>

Copyright and moral rights for this work are retained by the author

A copy can be downloaded for personal non-commercial research or study, without prior permission or charge

This work cannot be reproduced or quoted extensively from without first obtaining permission in writing from the author

The content must not be changed in any way or sold commercially in any format or medium without the formal permission of the author

When referring to this work, full bibliographic details including the author, title, awarding institution and date of the thesis must be given

Enlighten: Theses

<https://theses.gla.ac.uk/>  
[research-enlighten@glasgow.ac.uk](mailto:research-enlighten@glasgow.ac.uk)

# **Aspects of fused silica fibres for use in gravitational waves research**

Karl W. Toland, B.Sc(Hons), M.Sc

Submitted in fulfilment of the requirements for the  
Degree of Doctor of Philosophy

First Supervisor: Prof. Giles Hammond  
Second Supervisor: Prof. Sheila Rowan

Institute for Gravitational Research  
School of Physics and Astronomy  
College of Science and Engineering  
University of Glasgow



University  
of Glasgow

June 2020

# Abstract

A pivotal aspect in increasing the sensitivity of the Advanced LIGO (aLIGO) detectors to enable for the detection of gravitational waves was the installation of the monolithic fused silica suspensions in the detectors. 40 kg fused silica test masses were installed and suspended by four 400  $\mu\text{m}$  fused silica fibres to lower the thermal noise of the detector compared to initial LIGO. Along with various other instrument upgrades to increase the sensitivity of the aLIGO detectors, it allowed the LIGO-Virgo Collaboration to directly observe gravitational waves from coalescing binary black hole and binary neutron star systems. There is always a desire to make these detectors even more sensitive by changing parameters of the instrument, and in the case of this thesis, parameters associated with the monolithic suspensions.

This thesis presents various areas of research related to the use of fused silica fibres for gravitational wave research. Firstly, a procedure was documented to standardise the alignment process of the aLIGO fibre pulling machine. Previously, this alignment process was subjective to the user as there were no documented set of instructions, which increased the probability of manufacturing defects to be introduced into the fibre production. This procedure also highlighted common issues that were related to the misalignment of the pulling machine and how these misalignments could be corrected.

One of the manufacturing defects that could be introduced into the fibres were angular misalignments in the thermoelastic nulling region. This became a prominent issue during the commissioning break between O2 and O3 where there were several instances of suspension fibres failing where these misalignments were observed. Though it was not concluded that these were the cause of the failures, an investigation was carried out to determine how great of an effect these angular misalignments have on the ultimate strength of the fibres. This investigation confirmed that these angular misalignments could be introduced into the fibre due to beam distribution misalignment around the stock material during the pulling process. These angular misalignments however did not show any adverse effect on the ultimate strength of the fibre.

The opportunity to work at LHO arose for a four-month period on a long term attachment (LTA). During this LTA, an investigation into the stress fatigue of fused silica fibres was carried out in the fibre production lab at LHO looking at a stress range between 3-5 GPa. The results of these investigations were then compared to an investigation by Proctor in the 1960s to see if there were any differences observed. It was found that data from both LHO and Glasgow did not

align with the data that Proctor had obtained in his investigation, but did align with each other, showing that investigations carried out at LHO or Glasgow can be considered to be consistent with each other. Due to the data not aligning with Proctor's results, a follow-on investigation looking at fibres with comparable diameters were investigated.

To do this, a dedicated fibre profiler had to be developed first that was designed specifically to profile fibres within this diameter range. This included being able to profile fibres that were under  $10\ \mu\text{m}$  in diameter. The thin fibre strength tester was also upgraded to add a magnetic encoder to measure the distance travelled by the motorised stage.

An investigation into the stress fatigue of sub- $40\ \mu\text{m}$  diameter fibres was then carried out to compare results with the previous investigation with aLIGO fibres. It was found that fibres that were above  $10\ \mu\text{m}$  in diameter showed strong performances similar to that of Proctor, regardless of the initial stock material being polished, double polished, or no polish. Fibres under  $10\ \mu\text{m}$  however did not show this strong performance and were weaker performing. Polishing the initial stock material did show an increase in suspension time, however these were still weaker than the  $>10\ \mu\text{m}$  diameter fibres. To see if this behaviour was consistent with other fibre characteristics, an investigation into the Young's modulus of the ultra-thin fibres was investigated.

A previous investigation into the Young's modulus of ultra-thin fibres was carried out by the author, however there were several factors in the equipment used at the time that lead to large uncertainties being associated with the Young's modulus values obtained. With the new upgraded strength tester and dedicated fibre profiler, this investigation was revisited to see if results obtained were consistent or different to that previously found. The uncertainties associated with the Young's modulus were successfully decreased from 16%, down to 7%. For fibres that had a minimum diameter greater than  $10\ \mu\text{m}$ , the Young's modulus value tended to agree with the accepted value of 72 GPa. The average value of three batches that were tested with diameters greater than  $10\ \mu\text{m}$  were found to be  $(72.3 \pm 2.3)$  GPa,  $(71.8 \pm 1.8)$  GPa and  $(75.9 \pm 3.0)$  GPa. This gives a weighted average of  $(72.7 \pm 1.3)$  GPa. For the batch that had fibres under  $10\ \mu\text{m}$  in diameter, the average Young's modulus value was  $(63.3 \pm 2.7)$  GPa and a weighted average of  $(62.8 \pm 1.9)$  GPa. Non-destructive tests on these fibres showed an average value of  $(62.9 \pm 2.8)$ . This is consistent with the stress fatigue tests where fibres under  $10\ \mu\text{m}$  showed different characteristics.

# Contents

<b>Abstract</b>	<b>i</b>
<b>Acknowledgements</b>	<b>xxii</b>
<b>Declaration</b>	<b>xxiii</b>
<b>Preface</b>	<b>xxiv</b>
<b>1 Gravitational Waves</b>	<b>1</b>
1.1 Introduction to gravitational waves . . . . .	1
1.2 Gravitational wave sources . . . . .	3
1.2.1 Compact Binary Coalescence (CBC) . . . . .	4
1.2.2 Supernovae . . . . .	5
1.2.3 Continuous Waves (CW) . . . . .	6
1.2.4 Stochastic background . . . . .	7
1.3 Instruments to detect gravitational waves . . . . .	7
1.3.1 Resonant bar detectors . . . . .	8
1.3.2 Laser Interferometry . . . . .	8
1.3.3 Ground-based laser interferometers . . . . .	11
1.3.4 Space-based laser interferometers . . . . .	16
1.4 Detection of gravitational waves . . . . .	17
1.5 Overview of the aLIGO four-stage quasi-monolithic suspension system . . . . .	20
1.6 Noise sources . . . . .	23
1.6.1 Quantum noise . . . . .	24
1.6.2 Gravity gradient noise . . . . .	26
1.6.3 Seismic noise . . . . .	26
1.6.4 Thermal noise . . . . .	29
1.7 Thesis outline . . . . .	33
<b>2 Alignment of the aLIGO fibre pulling machine.</b>	<b>34</b>
2.1 Introduction . . . . .	34

2.2	Pulling machine layout . . . . .	35
2.3	Pulling machine mechanical alignment . . . . .	41
2.3.1	Bench, tower and baseplate . . . . .	41
2.3.2	Conical mirrors . . . . .	44
2.3.3	Top and bottom basic clamps . . . . .	47
2.3.4	Top and bottom fuse end clamps . . . . .	52
2.4	Laser beam alignment . . . . .	55
2.4.1	Red alignment beam . . . . .	59
2.4.2	Optical bench mirror mounts . . . . .	60
2.4.3	Beam position within the pulling machine . . . . .	64
2.4.4	Lens system . . . . .	67
2.5	Conclusion . . . . .	69
<b>3</b>	<b>Angular defects of fused silica fibres used in aLIGO monolithic suspensions</b>	<b>70</b>
3.1	Introduction . . . . .	70
3.2	Fibre production . . . . .	71
3.2.1	Fibre production . . . . .	71
3.3	Fibre bonding . . . . .	73
3.3.1	Cardboard-copper bonding . . . . .	75
3.3.2	Cardboard sandwich . . . . .	76
3.4	Strength tester . . . . .	80
3.5	High speed camera . . . . .	82
3.6	Beam misalignment . . . . .	83
3.7	Results and analysis . . . . .	86
3.7.1	Fibre profiles . . . . .	86
3.7.2	Python 3 fibre analysis script . . . . .	88
3.7.3	Fibre angle calculations . . . . .	91
3.7.4	Strength tests and breaking locations . . . . .	96
3.8	Discussion . . . . .	104
3.8.1	Fibre failures due to cardboard sandwich failure . . . . .	104
3.8.2	Breaking location . . . . .	106
3.8.3	Effect angles have on ultimate strength of fibre . . . . .	111
3.9	Future research . . . . .	112
3.10	Conclusion . . . . .	114
<b>4</b>	<b>Stress fatigue in fused silica suspension fibres</b>	<b>116</b>
4.1	Introduction . . . . .	117
4.1.1	Motivation . . . . .	118
4.2	Experimental method and set-up . . . . .	119

4.2.1	Fibre production and characterisation . . . . .	119
4.2.2	Method . . . . .	128
4.3	Analysis . . . . .	132
4.3.1	Results . . . . .	132
4.3.2	Uncertainties . . . . .	133
4.3.3	Discussion . . . . .	133
4.4	Improvements . . . . .	138
4.5	Conclusion . . . . .	139
<b>5</b>	<b>Development of a dedicated diameter characterisation profiler and strength tester for <math>\leq 50 \mu\text{m}</math> diameter fibres</b>	<b>141</b>
5.1	Motivation . . . . .	141
5.2	Dedicated ultra-thin fibre profiler . . . . .	144
5.2.1	Improved optical set-up . . . . .	148
5.2.2	Hardware and design . . . . .	153
5.2.3	LabVIEW . . . . .	159
5.2.4	Varying magnifications and repeated profiles . . . . .	164
5.2.5	Uncertainties . . . . .	174
5.2.6	Future improvements . . . . .	178
5.3	Upgrades to ultra-thin fibre strength tester . . . . .	180
5.3.1	Installation of upgrades . . . . .	181
5.3.2	Uncertainties . . . . .	186
5.4	Conclusion . . . . .	186
<b>6</b>	<b>Stress fatigue in 10-40 <math>\mu\text{m}</math> diameter fibres</b>	<b>188</b>
6.1	Motivation . . . . .	188
6.2	Production and characterisation of ultra-thin fused silica fibres . . . . .	188
6.2.1	ultra-thin fibre pulling machine hardware overview . . . . .	188
6.2.2	Velocity profiles and fibre production . . . . .	191
6.3	Experimental set-up . . . . .	196
6.4	Results . . . . .	205
6.4.1	First stage pull down . . . . .	205
6.4.2	10 $\mu\text{m}$ velocity profile fibre batch . . . . .	206
6.4.3	20 $\mu\text{m}$ velocity profile fibre batch . . . . .	210
6.5	Discussion . . . . .	213
6.6	Conclusion . . . . .	216
<b>7</b>	<b>Measuring Young's modulus of sub-20 <math>\mu\text{m}</math> fibres</b>	<b>218</b>
7.1	Motivation . . . . .	218

7.2	Experimental set-up . . . . .	219
7.3	Fibre production . . . . .	221
7.4	Results . . . . .	223
7.5	Discussion . . . . .	225
7.5.1	Young's modulus values and uncertainty calculations . . . . .	225
7.5.2	Comparison to other investigations . . . . .	228
7.6	Conclusion . . . . .	230
<b>8</b>	<b>Conclusion</b>	<b>231</b>
<b>A</b>	<b>Fused silica fibre angle python script</b>	<b>234</b>
<b>B</b>	<b>Ultra-thin fibre profiler LabVIEW block diagram</b>	<b>235</b>

# List of Tables

3.1	The high speed camera settings used in this investigation. . . . .	83
3.2	Values for profiler settings used during this investigation. . . . .	88
3.3	aLIGO fibre profiler settings that were used for profiling fibres in this investigation.	88
3.4	The quantity of fibres obtained with various stock-to-TNR angles. Note these were all top fibre end measurements as that was where the maximum angles occur.	95
3.5	The quantity of fibres obtained with various TNR-to-thin angles. . . . .	96
3.6	The quantity of fibres obtained with various net angles. . . . .	96
4.1	Range of fibre diameters obtained with the four pulling profiles . . . . .	133
4.2	Predicted in-air hang time values of four gravitational wave detector stress scenarios. . . . .	134
5.1	The goals that were aimed to be achieved through the development and upgrades of the ultra-thin fibre characterisation apparatus in this chapter. . . . .	144
5.2	The number of pixels occupied by the feeler gauge’s shadow and the resulting size of the image. Data from final report [154]. . . . .	152
5.3	Minimum diameter of the fibre for all five profiles. . . . .	173
5.4	Micrometre per pixel values for a range of magnification values. These magnifications would give the step-like artefacts with intervals of the corresponding $\mu\text{m}$ per pixel values. . . . .	175
5.5	Distance travelled by motorised stage during repeated up and down movements.	178
5.6	Distance of motorised stage moving up from calipers and magnetic encoder. Data taken from Erin Momany’s final report [165]. . . . .	184
5.7	Distance of motorised stage moving down from calipers and magnetic encoder. Data taken from Erin Momany’s final report [165]. . . . .	184
6.1	The first stage velocity pulling profile for the $10\ \mu\text{m}$ diameter fibres. . . . .	193
6.2	The second stage velocity pulling profile for the $10\ \mu\text{m}$ diameter fibres. . . . .	193
6.3	The first stage velocity pulling profile for the $20\ \mu\text{m}$ diameter fibres. . . . .	194
6.4	The second stage velocity pulling profile for the $20\ \mu\text{m}$ diameter fibres. . . . .	194

7.1	The first stage velocity pulling profile for both velocity profiles used in this investigation. This first stage is used with a corresponding feed velocity of $0.8 \text{ mm s}^{-1}$ . . . . .	222
7.2	The second stage velocity pulling profile used to produce fibres for batches 1-3. This second stage is used with a corresponding feed velocity of $0.05 \text{ mm s}^{-1}$ , $0.7 \text{ mm s}^{-1}$ and $1 \text{ mm s}^{-1}$ for batches 1, 2 and 3, respectively. . . . .	222
7.3	The second stage velocity pulling profile used to produce batch 4 fibres. This second stage is used with a corresponding feed velocity of $0.5 \text{ mm s}^{-1}$ . . . . .	222
7.4	The range of minimum diameter values that were obtained for all 4 batches of fibres that were produced. . . . .	223
7.5	The range of breaking stress values for the 4 batches of tested fibres. . . . .	224
7.6	The range of Young's modulus values for the 4 batches of tested fibres. Note that 1A includes the average value without fibre 12 with a Young's modulus of $48.0 \text{ GPa}$ , and 1B shows the average value with fibre 12. . . . .	227

# List of Figures

1.1	Simulated representation of the Sun and the Earth to show the difference in curvature that the two bodies create [2]. . . . .	2
1.2	Diagram showing a ring of free particles for the two types of polarisation, + and ×, of gravitational waves, where the length value refers to the length of the arrows between two particles. . . . .	3
1.3	The gravitational strain, $\sqrt{Hz}$ , and corresponding frequency of several types of sources [3]. . . . .	4
1.4	A simulation of a supernova explosion, showing the asymmetric aspect of the explosion that would produce gravitational waves [8]. . . . .	5
1.5	The orbital decay of PSR B1913+16 compared to the general relativistic prediction of the orbital decay [12]. . . . .	6
1.6	A schematic of a Michelson interferometer. . . . .	9
1.7	The effect of a + polarised gravitational wave passing through normal to a Michelson interferometer illustrating how the arm lengths change by a distance $dL$ . . . . .	10
1.8	Schematic of a Michelson interferometer with Fabry-Perot cavities installed in the arms. . . . .	13
1.9	Schematic of a Michelson interferometer with delay line cavities installed in the arms. . . . .	14
1.10	Schematic of a Michelson interferometer with a power recycling mirror (PRM) installed in between the laser and the beam splitter. . . . .	14
1.11	Schematic of a dual recycled Michelson interferometer with Fabry-Perot cavities, where the signal recycling mirror (SRM) is installed between the output photodiode and the beam splitter. . . . .	15
1.12	An artists impression of The Einstein telescope showing the layout of the interferometer arms underground [37]. . . . .	16
1.13	Waveforms and simulated images of BBH coalescences observed in O1 and O2 [50]. The shape of the waveform can be seen to change depending on the mass of the black holes involved, where the smaller BBHs inspiral over a longer timescale than heavier ones. . . . .	17

1.14	A comparison of the length of selected BBH coalescences compared to the BNS coalescence, GW170817 [54]. . . . .	18
1.15	Sky localisation of the BNS gravitational wave signal from the aLIGO (green) and a combination of the aLIGO and Virgo detectors (dark green), the Fermi GRB signal (dark blue), and the resulting optical discovery from the Swope 1 m telescope 10.9 hours after the initial signal. For reference, the same area of sky is shown 20 days prior to the signal arriving from the DLT40 collaboration to show the difference [52]. . . . .	19
1.16	An optical (left) and near infra-red (right) view of the optical counterpart to GW170817 (labelled SSS17a). Photo credit: 1M2H/UC Santa Cruz and Carnegie Observatories/Ryan Foley. . . . .	19
1.17	The layout of the four-stage suspension system for the main chain (front suspension) and the reaction chain (rear suspension) [59]. Within the top and upper intermediate mass are cantilever blades similar to that on the top stage. . . . .	21
1.18	Comparison between the initial LIGO suspension and the aLIGO suspension systems. . . . .	22
1.19	The aLIGO noise budget showing the various noise sources that limit and affect the interferometer [68]. . . . .	23
1.20	The current differential arm length (DARM) signal of the two aLIGO interferometers (LHO and LLO), Virgo and GEO600 during O3 [69]. . . . .	24
1.21	Illustration of the fluctuation experienced with radiation pressure noise on a test mass (left) and photon shot noise on the output photodiode (right) [70]. . . . .	24
1.22	The effect a propagating surface wave has on a suspended test mass. . . . .	26
1.23	Seismic noise spectrum obtained for LLO under various scenarios [78]. . . . .	27
1.24	An incoming earthquake being picked up by the seismometers at LHO [69]. . . . .	27
1.25	An example of the noise human activity has on seismometers at LHO [69]. . . . .	28
1.26	The horizontal and vertical modes of an aLIGO suspension. It can be seen that the bulk of the noise occurs at the resonant frequency as a sharp spike [57]. . . . .	32
2.1	A: The monolithic fused silica suspension at LHO that had fibres installed during one of the two fibre pulling visits by the author. B: The coated front face of the fused silica test mass. . . . .	35
2.2	Solidworks rendering of the fibre pulling machine [94]. A: The full pulling machine assembly, and B: exploded view of the pulling machine to clarify labeled components. . . . .	36
2.3	The current state of the fibre pulling machine at the University of Glasgow as of writing this thesis. . . . .	37

2.4	Illustration of the beam path for the pulling machine at Glasgow with a side-view cross section of the optical path within the optical system of the pulling machine. . . . .	38
2.5	The beam path and optical set up on the pulling machine at LHO. Note there is no periscope in the beam path compared to the Glasgow pulling machine in figure 2.4. . . . .	39
2.6	Rod of fused silica undergoing laser polishing. The difference between the unpolished and polished stock material can be clearly seen in the insert in the bottom right where the unpolished region is visibly more opaque than the clear polished region. . . . .	40
2.7	Arm connector for the tower. . . . .	42
2.8	Offset of the baseplate to the tower baseplate. A: Offset of left side. B: Offset of right side. . . . .	43
2.9	Installation of the reference plate to align baseplate to the tower baseplate. A: Reference plate prior to installation. B: Reference plate after installation. . . . .	44
2.10	The back plate that connects the feed mirror holder to the feed mirror stage on the tower. The finger in the image is pointing to one of the screws that attach the plate to the tower that should be checked for tightness. Inset shows SolidWorks rendering with attachment plate highlighted in green. . . . .	45
2.11	Disassembled (A) and assembled (B) conical mirror plastic alignment tool. . . . .	46
2.12	Installation of the conical mirror plastic alignment tool (A) and an installed alignment tool highlighted in the red box (B). . . . .	46
2.13	The groove on the plastic alignment tool to align the feed mirror. A: underside of feed mirror. B: Topside of feed mirror. . . . .	47
2.14	Horizontal offset of a piece of fused silica stock. . . . .	47
2.15	A: A basic clamp. B: Top basic clamp attached to its holder. . . . .	48
2.16	The centre post that holds the bottom clamp holder at Glasgow (A) and LHO (B). . . . .	48
2.17	Aluminium alignment plate, D1800247, used to align the clamps to the centre of the feed mirror. . . . .	49
2.18	Zoomed view of the 3mm groove on the alignment plate. . . . .	50
2.19	Aluminium alignment plate to check fused silica stock is in position. . . . .	50
2.20	Alternate angle of aluminium alignment plate to check fused silica stock is in position. . . . .	51
2.21	The top and bottom clamps brought close to contact with each other to align the clamp holders. . . . .	51
2.22	Fused silica stock with fuse end attachments. . . . .	52
2.23	Fuse end attachment showing the two flat faces and two curved sides. . . . .	52

2.24	A: A fuse end clamp. B: A fused silica stock rod with a fuse end sitting in the top fuse end clamp in the fibre pulling machine. . . . .	53
2.25	Top row: ideal scenario of a fuse end sitting in a fuse end clamp. Middle row: Top down view of a well aligned fuse end sitting within a fuse end clamp with an angle induced by a flat tip screw with the resulting stock shape after heating. Bottom row: Well aligned fuse end with a pointed tip screw used instead of a flat tip screw. . . . .	54
2.26	Top row: ideal scenario of a fuse end sitting in a fuse end clamp. Bottom row: Top down view of a fuse end sitting within the fuse end clamp at an angle with the resulting stock shape after heating. . . . .	54
2.27	SolidWorks rendering and an image of the optical setup within the fibre pulling machine. . . . .	56
2.28	Rotating 45° mirror at the centre of the bottom conical mirror. Inset shows location in the SolidWorks rendering, highlighted in green. . . . .	56
2.29	Cross section of beam path for an aligned pulling machine to the fused silica stock.	57
2.30	Distribution of beam around fused silica stock for an aligned pulling machine. . . . .	57
2.31	Cross section of beam path for a mechanical misalignment of the feed mirror. . . . .	58
2.32	Distribution of the beam around fused silica stock for a feed mirror mechanical misalignment. . . . .	58
2.33	A Thorlabs VRX6S temperature-sensitive target card that can be used for laser alignment [106]. Bottom right target highlighted for clarity. . . . .	59
2.34	Periscope system currently installed on the Glasgow fibre pulling machine. . . . .	61
2.35	Cross section of beam path with the laser coming into the pulling machine optical system at an angle. . . . .	62
2.36	Distribution of beam distribution around the fused silica stock with an angular misalignment. . . . .	62
2.37	A: The path of the laser beam across the 2D surface of the fused silica stock. B: The beam path of the laser on the rotating 45° mirror with an angular misalignment.	63
2.38	10 frames from a slow motion video plotting out the path of the beam around the fused silica stock. The red + that is shown in the bottom right inset of each frame is the position of the beam along the path that it travels. This path is the same shape as shown in figure 2.37. . . . .	63
2.39	Cross section of the beam path coming in high on the fixed 45° mirror. . . . .	65
2.40	A Thorlabs LMR1AP target cover that can be modified to sit on top of the rotating 45° mirror [109]. . . . .	65
2.41	Plastic alignment tool for laser alignment check. . . . .	66
2.42	A: Well aligned laser distribution around the stock during polishing and pulling, respectively. B: Misalignment of the same situation. . . . .	67

2.43	Shirt target attached onto the lens cage to check alignment. . . . .	68
2.44	Example of a lens cage with both a fixed length post and a post within a post holder. . . . .	69
3.1	A photograph of a fibre that was installed into ETMx at LHO that shows a visible angle in the fibre. The labeled angles were calculated from pixel analysis of the photo [114]. . . . .	71
3.2	Graph of fibre pulling profile used to produce the fibres in this investigation. . .	72
3.3	The fibre storage fridge used to store the fibres when not in use at Glasgow. . .	73
3.4	A schematic of the bonding procedure. Cardboard and copper were first bonded together (A), before two halves were bonded together with fused silica stock in between and left to cure (B) and the final product for testing (C). . . . .	74
3.5	Cardboard and copper rectangles used to create the cardboard holders . . . . .	75
3.6	The method to remove the cardboard-copper sheets when epoxy overflows onto the bosch struts. . . . .	76
3.7	Illustration of the bonding process to produce the cardboard sandwiches. Photo inset A: Cardboard-copper halves attached to the metal plates with blu-tack. Photo inset B: Araldite 2 part epoxy applied to each cardboard half. Photo inset C: Fused silica stock placed into the epoxy. Note that the plate with the screws was used for this stage. The pinky finger was used to secure the stock in position to minimise movement within the epoxy during handling. The ruler attached to the plate was used at a reference for the length of stock within the cardboard. Photo inset D: Second plate attached by passing screws through the holes and attached with wing nuts. These were tightened as far as possible. . . . .	78
3.8	A: The metal bonding plates sitting on the Bosch strut. B: The cardboard sandwich bonding rail set up. Note that there was no shield or anything protecting the fibres from the surrounding lab environment. . . . .	79
3.9	A fully bonded fibre ready for strength testing. Note that the fibre in this figure was not used for testing and was placed on a table for illustration purposes. . .	80
3.10	The experimental set-up of the fused silica fibre within the aLIGO fibre strength tester. Photo inset: Self tightening clamp with cardboard sandwich within. . . .	81
3.11	A: The enclosure around the strength tester to contain the aftermath of the destructive testing. The halogen lights were used to provide enough light to the fibre to be seen in the high speed camera. B: The high speed camera used for this investigation with the digital camera placed on top that will be utilised later in this chapter. . . . .	83

3.12	A: A view of the molten fused silica through welding goggles to show the difference in intensity that was viewed. B: Screenshot of the beam distribution of an aligned beam around the fused silica stock during initial heating. C: Aligned beam around the fused silica stock during the start of the pull. . . . .	84
3.13	Screenshot of the misaligned beam distribution around the fused silica stock. A: Misaligned beam around the fused silica stock during initial heating. B: Misaligned beam around the fused silica stock during the start of the pull. . . .	85
3.14	The aLIGO fibre profiler at Glasgow used to profile the fibres used in this investigation. . . . .	87
3.15	A fibre profile of the top end (TE) scan of fibre 58 with corresponding labels to indicate the different regions of the fibre. . . . .	89
3.16	The bottom end (BE) scan profile for cameras 1 and 2 of a selected fibre. Note the bottom two graphs contains the data used to calculate the angles within the bottom end of the fibre. The highlighted region indicating the section within the cardboard sandwich was determined through the use of a ruler attached to the aluminium plates during the bonding process. The cardboard sandwiches were attached after the profiling process was completed. . . . .	90
3.17	The top end (TE) scan profile for cameras 1 and 2 of a selected fibre. . . . .	91
3.18	An example of the 6 different sliced sections of the profiler data, with the full fibre profile of this region in black. . . . .	92
3.19	Illustration showing how the angle between two lines could be calculated using the $\tan(A \pm B)$ identity. . . . .	94
3.20	Annotated angle profile of fibre 20 that was tested in this investigation. . . . .	94
3.21	Photograph of fibre 20 in figure 3.20 showing the coordinates of the edge lines used to calculate the angle in the fibre end for comparison to the angles obtained from the Python script. . . . .	95
3.22	Three consecutive frames from the high speed camera footage of a fibre breaking. Note the image colour has been inverted to make it easier to observe the fibre. Top: Frame prior to the fibre breaking. Middle: Frame fibre breaks. Two artefacts of interest in this frame were the explosion for the TNR, which could be misinterpreted as the breaking region, and the actual breaking region highlighted in the red box. The break in the fibre in this region could clearly be seen. Bottom: Frame after fibre break. Remaining fibre from the left side of the break travels towards the bottom neck. Fibre on the right side of the break has disintegrated. . . . .	97
3.23	An example of a wide spread break location from the high speed camera footage. Note that this was the first frame where the fibre appears to break. . . . .	98

3.24	An example of a narrow spread break location from the high speed camera footage. Top zoom frame colour not inverted due to lack of clarity in image when inverted. . . . .	99
3.25	Zoomed in image from a high speed frame of the top stock reference point that was used to determine the distance of the fibre break. . . . .	100
3.26	A stretched fibre profile lined up with the breaking frame of the high speed footage.	101
3.27	Location of the minimum diameter region on the fibre and the spread of the breaking region from the high speed footage. From this image, the number of fibres that have a minimum diameter within the breaking region could be observed.	102
3.28	A stretched fibre profile lined up with the breaking frame of the high speed footage. In this example, the breaking region was not near the minimum diameter location. . . . .	103
3.29	Screenshot of a fused silica fibre where the top stock was pulled out of the cardboard sandwich holder. It could be seen from this image that the thin section of the fibre was still intact as the top stock was falling to the ground. . . . .	104
3.30	A: An example of a cardboard sandwich that was likely to have the fused silica pulled out of it during testing. This was determined from the lack of epoxy around the stock at the edge of the cardboard sandwich. B: An example of a cardboard sandwich with a sufficient amount of epoxy to keep the stock in place.	105
3.31	A: An overlay of two frames from the start of the strength test procedure (black border frame) and just before the fibre fails (pink border frame) observe if there was any slippage of the cardboard sandwich in the clamps. It could be seen from this image that there was no obvious visual movement of the stock between the two images. B: Pink border frame moved laterally over the black frame image to observe if there was any vertical movement of the stock. C: Zoomed in view of B. . . . .	106
3.32	The stress in the fibre in the location where the fibre broke and at the minimum diameter region for all the fibres tested in this investigation. . . . .	107
3.33	Fibre profile that shows the breaking region sitting in a location where there was a dip in diameter. This fibre was of particular interest as the difference in profiler diameter data between the minimum diameter of the fibre and the minimum diameter of the breaking region was 0.6 $\mu\text{m}$ . Therefore the stress in both of these locations would be extremely close. This was the only fibre that had this scenario. . . . .	108
3.34	Fibre profile that shows the breaking region sitting in a location where there was no visual artefact in the breaking region. . . . .	109
3.35	The maximum angle (left Y-axis) in both the stock-TNR and TNR-thin, and the breaking stress (right Y-axis) of the fibres that were tested in this investigation .	111

3.36	An offset of the stock material relative to the horn on the ear attached to the test mass [114]. . . . .	113
4.1	An arial photograph of LIGO Hanford Observatory while descending for landing at the Tri-Cities Airport. . . . .	117
4.2	The fibre pulling machine at the LIGO Hanford Observatory with a rod of fused silica installed and being heated to the point where it was molten. . . . .	120
4.3	SolidWorks rendering of a fused silica stock with attached fuse ends [134]. . .	121
4.4	Assembly of a fused silica rods with fuse ends attached curing on a hotplate at 80°C. . . . .	121
4.5	The pulling voltage profile used to produce the fibres that were investigated within this chapter. . . . .	123
4.6	Feed stage voltage profile used to produce the fibres that were investigated within this chapter. Note that the data points at 0.9V is there for all 3 profiles, therefore only voltage profile 3 is shown due to the overlay of points. . . . .	124
4.7	A fibre cartridge which allows transportation of the fibre around the lab. The blocks and struts allow for easy physical handling without touching any fused silica. . . . .	125
4.8	The aLIGO fused silica fibre profiler at LHO. . . . .	126
4.9	A full fibre profile of a fused silica fibre that was pulled with pulling voltage profile 1. This plot consists of all the data that was obtained from the three files that were saved during the profiling process as previously described. . . . .	127
4.10	The thin section of the fused silica fibre in figure 4.9. . . . .	127
4.11	The bottom neck of the fused silica fibre in figure 4.9. Here, the bump artefact that was described could be seen. For aLIGO suspension fibres, a variation of $800 \pm 80 \mu\text{m}$ was allowed in this region. . . . .	128
4.12	The top neck of the fused silica fibre in figure 4.9. Note that the neck in this fibre does not satisfy the 10% error allowed for the neck regions for suspension fibres. However, this error was not critical for this investigation and was therefore not an issue that needed to be addressed. . . . .	128
4.13	Schematic of the experimental set up to suspend a mass from a fused silica fibre. Inset: The proof tester enclosure with a fibre undergoing a proof test. . . . .	130
4.14	The timer switch that was used to record the total hang time of the mass. . . . .	131
4.15	Total hang time of the suspended masses plotted against breaking stress values for the fibres that were tested in LHO (blue dots). The $\times$ data points were the data points from Proctor's in-air research for comparison [131]. . . . .	132

4.16	Predicted in-air lifetime of fused silica fibres at relevant detector stress values. Note that the highlighted points for GEO600, MIT and LHO were all experimental results. Out of the three square indicators, only the LHO fibre lab suspension has been dismantled to allow equipment use for suspension welding practice. GEO600 and MIT are still hanging. . . . .	134
4.17	The comparison of results discussed in this chapter with data from Lee [92] and Proctor [131]. . . . .	137
5.1	Screenshot of the image of an ultra-thin fibre being profiled on the aLIGO fibre profiler. . . . .	142
5.2	Highlighted issues with the previous set-up of the ultra-thin fibre strength tester. . . . .	143
5.3	Current iteration of the ultra-thin fibre profiler. . . . .	145
5.4	Diagram of the ultra-thin fibre profiler. . . . .	146
5.5	Image A: One end of the ultra-thin fibre cartridge, B: SolidWorks rendering of a full fibre cartridge. Labels: 1 - Cartridge chuck, 2 - cartridge nut, 3 - fused silica fibre, 4 -Cartridge strut. . . . .	147
5.6	Top left: Cartridge block holder sitting on the 360° rotation stage. Bottom left: Fibre cartridge sitting within slot of block holder. Right: Full fibre cartridge. . . . .	147
5.7	An ultra-thin fibre cartridge within the aLIGO profiler . . . . .	149
5.8	Left: current installed lens tubes on the aLIGO fibre profiler [149]. Right: Various lengths of lens tubes and the pinhole cover that could be installed to increase magnification. . . . .	150
5.9	The current lens and camera set-up of the ultra-thin fibre profiler. . . . .	151
5.10	Experimental set-up of early tests of the new optical set-up for ultra-thin fibre profiler (LED out of shot). Original image taken from final report [154] with labels added. . . . .	152
5.11	Screenshot of a 75 $\mu\text{m}$ wire under a magnification of $\times 16$ . Original image from final report [154]. . . . .	153
5.12	Circuit schematic for the motor controller board. . . . .	154
5.13	A schematic of a H-bridge concept to control the profiler motor. S# dictates the switch and its associated number. . . . .	154
5.14	A: Limit switches fixed to the top of the profiler tower. B: Limit switches fixed to the bottom of the profiler tower. C: Wiring of software and hardware limit switches. . . . .	156
5.15	Example of the pattern on the magnetic encoder strip showing the high-low pattern the encoder passes over. . . . .	157
5.16	The circuit schematic for the encoder read-in board, initially designed for the aLIGO profiler [159]. . . . .	158
5.17	Front panel of the LabVIEW program for the ultra-thin fibre profiler. . . . .	161

5.18	Input boxes to determine interval between points during the thin section of the fibre and the length of measurements for the top and bottom necks. . . . .	162
5.19	Calibration boxes to calibrate the profiler. . . . .	162
5.20	Screenshot of a 500 $\mu\text{m}$ slip gauge being profiled for calibration at a magnification of approximately $\times 12$ . . . . .	163
5.21	Illustration of the experimental set-up of the depth of field tests. . . . .	165
5.22	Two screenshots of a 25 $\mu\text{m}$ wire under $\times 20$ magnification. The left image was the wire in focus and the right image was the wire out of focus. The difference in camera position between these two images was approximately 10-15 $\mu\text{m}$ . . .	166
5.23	The 25 $\mu\text{m}$ wire imaged with various magnifications. . . . .	166
5.24	Diameter values obtained for magnifications $\times 6$ , $\times 8$ and $\times 10$ during the depth of field tests. The horizontal lines at diameter values 26.25 $\mu\text{m}$ and 23.75 $\mu\text{m}$ indicate the wire tolerance. . . . .	167
5.25	Diameter values obtained for magnifications $\times 12$ , $\times 16$ , $\times 20$ , $\times 24$ and $\times 28$ during the depth of field tests. The horizontal lines at diameter values 26.25 $\mu\text{m}$ and 23.75 $\mu\text{m}$ indicate the wire tolerance. . . . .	167
5.26	A full profile of a $25 \pm 1.25 \mu\text{m}$ wire at a magnification of $\times 24$ . The distance between each scan point was 0.1 mm and the distance in the middle region between data points was 2 mm. . . . .	169
5.27	The zoomed in view of the bottom scan of the $25 \pm 1.25 \mu\text{m}$ wire. Note that all data points in this region sit within the wire tolerance. . . . .	169
5.28	The zoomed in view of the bottom scan of the $25 \pm 1.25 \mu\text{m}$ wire. Note that all data points in this region sit within the wire tolerance. . . . .	170
5.29	Fused silica fibre imaged at various magnifications. The diameter values at each magnification are shown in figures 5.30 and 5.31. . . . .	171
5.30	Fibre diameter values obtained for $\times 6$ , $\times 8$ , $\times 10$ and $\times 12$ magnifications during depth of field tests. . . . .	171
5.31	Fibre diameter values obtained for $\times 16$ , $\times 20$ , $\times 24$ and $\times 28$ magnifications during depth of field tests. . . . .	172
5.32	Five separate profiles of one fused silica fibre. A stepping artefact could be seen in the profiles, similar to that seen in figures 5.27 and 5.28. . . . .	173
5.33	A schematic illustrating the possible cause of the stepping artefact that appears in figure 5.32. . . . .	175
5.34	The set-up of the SIOS for the motorised stage position measurements investigation. . . . .	177
5.35	SolidWorks CAD rendering of the ultra-thin fibre strength tester prior to upgrades [164]. . . . .	181
5.36	Left: The original drive rods. Right: The newly installed lengthened drive rods. . . . .	182

5.37	The MSK5000-0373 magnetic encoder installed onto the side of the motorised stage. . . . .	183
5.38	The updated custom LabVIEW program for the ultra-thin fibre strength tester [165]. . . . .	185
6.1	SolidWorks rendering of the ultra-thin fibre pulling machine that was used to produce the fibres that were investigated in this chapter. Labels: 1 - Cartridge chuck. 2 - Feed mirror. 3 - First conical mirror. 4 - Pulling stage. 5 - Fused silica stock. 6 - Feed mirror motorised stage. 7 - Axicon [99]. . . . .	189
6.2	The ultra-thin fibre pulling machine in its current set-up as of writing this thesis.	190
6.3	Left: The axicon that was used to spread the CO <sub>2</sub> beam out to the first conical mirror. Right: Cross section of the beam path of the CO <sub>2</sub> mirror after reflecting off the axicon. [99]. . . . .	191
6.4	The extraction process of a fibre cartridge from the pulling machine. . . . .	195
6.5	Fibre storage that was used for the fibres investigated in this chapter. The bottom tray was filled with desiccant to reduce the humidity within. . . . .	196
6.6	The experimental set-up that was used to carry out the stress fatigue investigation in this chapter. The two switches that were connected to the Raspberry Pi were connected together in parallel so that the timer recording was triggered when either switch was pressed. . . . .	197
6.7	The closed enclosure used in this investigation. Photo inset: Shaved screw used to adjust the height of the universal joint within the enclosure. . . . .	198
6.8	An open view of the enclosure showing the internal layout, and indicating how one half of the enclosure comes apart from the other half. . . . .	199
6.9	The inside of the enclosure that was used to enclose the fibres in this investigation. Note that the black paint allowed for the fibre to be easily seen as the reflective metal background cause difficulty. . . . .	200
6.10	Top: The mass installation jig used to remove the bottom chuck and to install the mass to the bottom stock of the fibre. Back (bottom left) and side (bottom right) view of the mass installation jig showing the XYZ adjustments that were available. The position of the holder for both stages could be set prior to installation and moved along the strut they were attached to. . . . .	201
6.11	Top left: Tweezers moved into position and tightened to secure the bottom stock as the chuck was removed from the stock. Top right: Mass installed by inserting stock into hole in mass. Stock secured in place by inserting and tightening grub screws on opposite sides. Bottom left: Tweezers loosened and retracted once mass was secured to the stock. Bottom right: Mass platform lowered until mass was suspended. The platform could then be retracted. . . . .	202

6.12	The two types of masses that were used during this investigation. Additional modifications were made to change the mass. . . . .	204
6.13	Profile of the first stage pulldown for the 10 $\mu\text{m}$ velocity profile. The first stage pulldown for the 20 $\mu\text{m}$ was the same, except that the final length was longer. . . . .	205
6.14	The first stage pull down from which the final fibre was pulled, held in a fibre cartridge. . . . .	206
6.15	A fibre profile of a fibre that was produced with the 10 $\mu\text{m}$ velocity profile. Note that only the thin middle section was shown due to the high magnification that was used. . . . .	206
6.16	All minimum diameter values from the non-polished and polished fibres that were produced with the 10 $\mu\text{m}$ velocity profile. Blank spaces in fibre numbers were fibres that were not successfully suspended. . . . .	207
6.17	A fuse end mass suspended on a fused silica fibre. The front of the enclosure was then attached to ensure the fibre was protected from the surrounding environment.	209
6.18	The failure time of the fibres that were produced using the 10 $\mu\text{m}$ velocity profile under a range of stresses. . . . .	210
6.19	A fibre profile of a fibre that was produced with the 20 $\mu\text{m}$ velocity profile. Note that only the thin middle section was shown due to the high magnification that was used. . . . .	211
6.20	All minimum diameter values from the non-polished and polished fibres that were produced with the 20 $\mu\text{m}$ velocity profile. Blank spaces in fibre numbers were fibres that were not successfully suspended. . . . .	211
6.21	The experimental set-up for the fibres that were tested in this subsection. Note that the chuck masses were used in this set-up. This was also carried out prior to spray painting the enclosures black, making it difficult to see the fibre in this set-up. . . . .	212
6.22	The failure time of the fibres that were produced using the 20 $\mu\text{m}$ velocity profile under a range of stresses. . . . .	213
6.23	All stress fatigue data obtained from chapters 4 and 6 compared to the data obtained by Proctor [131]. Shown here were the values obtained from the investigation carried out at LHO, and the fibres that were produced using the 10 $\mu\text{m}$ and 20 $\mu\text{m}$ velocity profiles (VP) under various polish/non-polish conditions. . . . .	216
7.1	The experimental set-up used in this Young's modulus investigation with key components of the strength tester labelled. . . . .	220
7.2	Selected profiles from batch 1 [99]. Note that "fibre 2" does not appear on this graph as it is part of batch 2. . . . .	223

7.3	Graph of the load applied to the fused silica fibre against the extension of the fibre for fibre 17. This fibre was chosen to show the clear slack removal period that could occur prior to the fibre going under stress. Inset: Zoom in view of the slack removal period. . . . .	224
7.4	Young's modulus values obtained for all fibres from batches 1-4 [99]. . . . .	225
7.5	Zoomed in view of the sudden dip artefact that appeared in fibre 12 of batch 1 that was being treated as an outlier. . . . .	227
7.6	Non-destructive Young's modulus results from a fibre that was pulled under the same conditions as batch 1. . . . .	228
7.7	Data from all four fibre batches that were tested in this investigation compared to the data that was previously obtained during the MSc investigation [93]. . . . .	229

# Acknowledgements

I would like to firstly thank my supervisors Giles and Sheila for all their support throughout this PhD (as well as my MSc). Their guidance and input allowed me to not only travel the World to present my research at conferences, but to also spend a significant amount of time working at LIGO Hanford contributing directly to the experimental and fabrication side of the LIGO collaboration.

I would also like to thank Alan for all his guidance in the research carried out in this thesis, Russell for all the help with drawing up parts to get manufactured, Stevie and Colin for manufacturing those parts and giving me advice when I was in the workshop, and Angus for getting me trained up with LIGO suspension procedures. On the LHO side of things, I would like to thank Betsy and Travis for being so welcoming on my arrival to Hanford and providing lots of guidance during all my trips to LHO. Also thanks to everyone who was at Hanford for making all 3 of my trips such an amazing experience.

I would also like to thank everyone in the IGR for making it an amazing group to work in. Thanks to morning coffee breaks, the lunch breaks, the afternoon coffee breaks, in-office breaks and the-walk-around-the-building-before-going-home breaks for being a thing. Also would like to say thanks to Russell, MPL, Liam and Stevie for the fitbaw chats. I have no idea what I would do if I did not have anyone to talk to about Celtic winning 9 league titles in a row, which included winning a treble treble, an invincible treble and 11 domestic trophies in a row. I would also like to thank everyone I grannied at table football. You know who you all are (special mention to Chris since he liked being reminded of the time he was grannied).

To The Piledriver... No words needed.

Outside of the Kelvin building, I would like to thank all my family and friends for their support. Thank you to my grandparents for not only taking an interest in my work, but for all their help when I phone when something breaks in the house or with the car and I'm stumped with how to fix it.

Finally, my biggest thanks goes to my Mum and Dad, and my fiancée, Mairéad. I cannot put into words how much I have appreciated all the support you all have given me throughout this journey and I hope I have made you all proud.

# Declaration

The material presented in this thesis is the result of my own work, except where explicit reference is made to the contribution of others, in the Institute for Gravitational Research within the School of Physics and Astronomy at the University of Glasgow. It has not been submitted for any other degree at the University of Glasgow, or at any other institution.

# Preface

This thesis is a document of work carried out by the author for the degree of Doctor of Philosophy with the Institute for Gravitational Research within the School of Physics and Astronomy at the University of Glasgow.

Chapter 1 contains an introduction into the field of gravitational waves, including discussion on instruments used for gravitational wave detections, noise sources and detections made so far.

Chapter 2 contains a documented procedure to align the fibre pulling machine. Steps discussed in the alignment procedure were developed in collaboration with Dr Alan Cumming.

Chapter 3 is a discussion on the cause of angular defects that occur during the fibre pulling procedure and the subsequent effect these defects have on the ultimate strength of the fibre.

Chapter 4 contains work that was carried out during a long term attachment to LIGO Hanford investigating stress fatigue of fused silica fibres.

Chapter 5 contains a discussion on the development of a dedicated thin fibre profiler and upgrades made to the thin fibre strength tester. This work was carried out alongside two IREU summer students, Leah Perri and Erin Momany. Leah Perri assisted with the early development of the fibre profiler, and Erin Momany assisted with the upgrades that were carried out to the thin fibre strength tester.

Chapter 6 describes further stress fatigue work, but with ultra thin fibres instead of aLIGO fibres.

Chapter 7 is a follow up investigation on previous work carried out by the author investigating the Young's modulus of ultra-thin fibres using the newly developed profiler and strength tester.

Appendix A is the python script developed by the author to calculate the angular defects in fibres.

Appendix B is the LabVIEW program that was modified to work for the newly developed ultra-thin fibre profiler. This program is a modified version of the aLIGO fibre profiler LabVIEW program that was originally developed by Dr Alan Cumming.

Throughout all the above investigations, various components related to the experimental set up that were not manufactured by the author were drawn and designed with the assistance of Mr Russell Jones, and manufactured by Mr Stephen Craig and Mr Colin Craig.

Work carried out in this thesis was presented at the following conferences:

- LIGO Virgo Collaboration meeting
  - Glasgow 2016
  - Geneva 2017
  - Wisconsin 2019
- Gravitational Wave Advance Detector Workshop
  - Elba 2019
- Third year post-graduate conference 2018
- LIGO Fellowship seminar 2017

# Chapter 1

## Gravitational Waves

### 1.1 Introduction to gravitational waves

Over a hundred years ago, Albert Einstein came up with a theory, known as Einstein's Theory of General Relativity [1]. In this theory, Einstein explained how an object in the universe can affect the curvature of spacetime and the resulting impact it has on the motion of bodies around it. This curvature can be described as the gravitational influence of the object. This means that any body passing the path of an object would be influenced by the curvature created in spacetime. The degree of curvature produced from the object depends on the density of the object. This can be demonstrated with a rubber sheet with a square grid marked out on it to represent two-dimensional spacetime. If a heavy sphere is placed into the middle to represent a dense body in space, the sphere creates a curvature in the rubber sheet as it sinks down. An example of two different bodies curving spacetime is shown in figure 1.1 [2].

Einstein's theory of General Relativity predicted that massive accelerating objects in the universe would cause ripples in spacetime where energy is transported away from the source at the speed of light in the form of gravitational radiation, called gravitational waves. In the same way that an accelerated electric charge generates electromagnetic waves in the electromagnetic field, an accelerated mass in space can generate gravitational waves as long as this acceleration is asymmetrical [3]. The result of this asymmetric acceleration is the creation of gravitational waves that are quadrupole in nature.

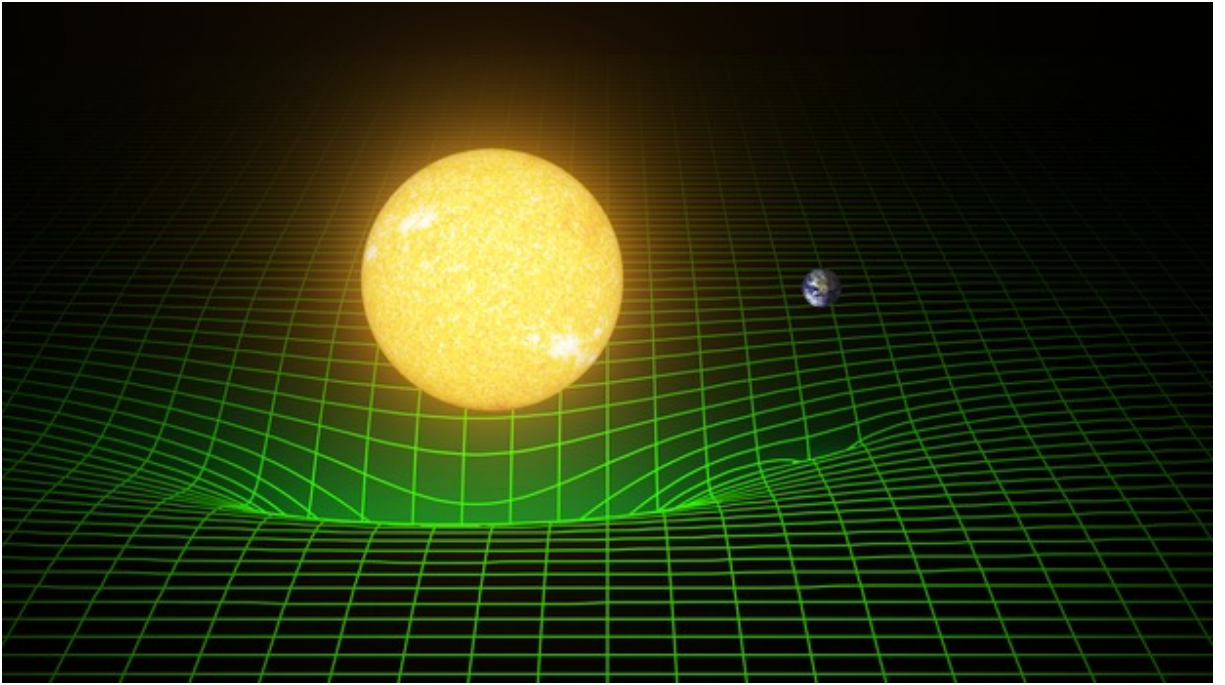


**Figure 1.1:** Simulated representation of the Sun and the Earth to show the difference in curvature that the two bodies create [2].

The quadrupole nature of gravitational waves is due to the conservation of two features:

- Conservation of mass which forbids the existence of gravitational monopoles as the mass does not change with time.
- Conservation of momentum which forbids the existence of gravitational dipoles as the momentum does not change with time.

The quadrupole nature of gravitational waves results in the stretching and squeezing of space-time as the waves propagate from the source at the speed of light, in an orthogonal direction to the direction the wave is moving in. Gravitational waves come in two distinct polarisations:  $+$  and  $\times$ . This is illustrated in figure 1.2. In this example for the  $+$  polarisation, the length change between particles 1 and 3 increases by a distance,  $dL$ , giving a total distance of  $L + dL$ . However, for an orthogonal pair of particles, particles 2 and 4, the length decreases to a distance of  $L - dL$ . The ring of particles then returns to its original position before changing in length again by  $dL$ , but with the opposite sign as before. The strain amplitude,  $h$ , of the gravitational wave is a dimensionless variable and indicates the strength of the gravitational wave signal that would be observed:

$$h = \frac{2dL}{L} \quad (1.1)$$

where  $L$  is the distance between the two free particles and  $dL$  is the change in distance.

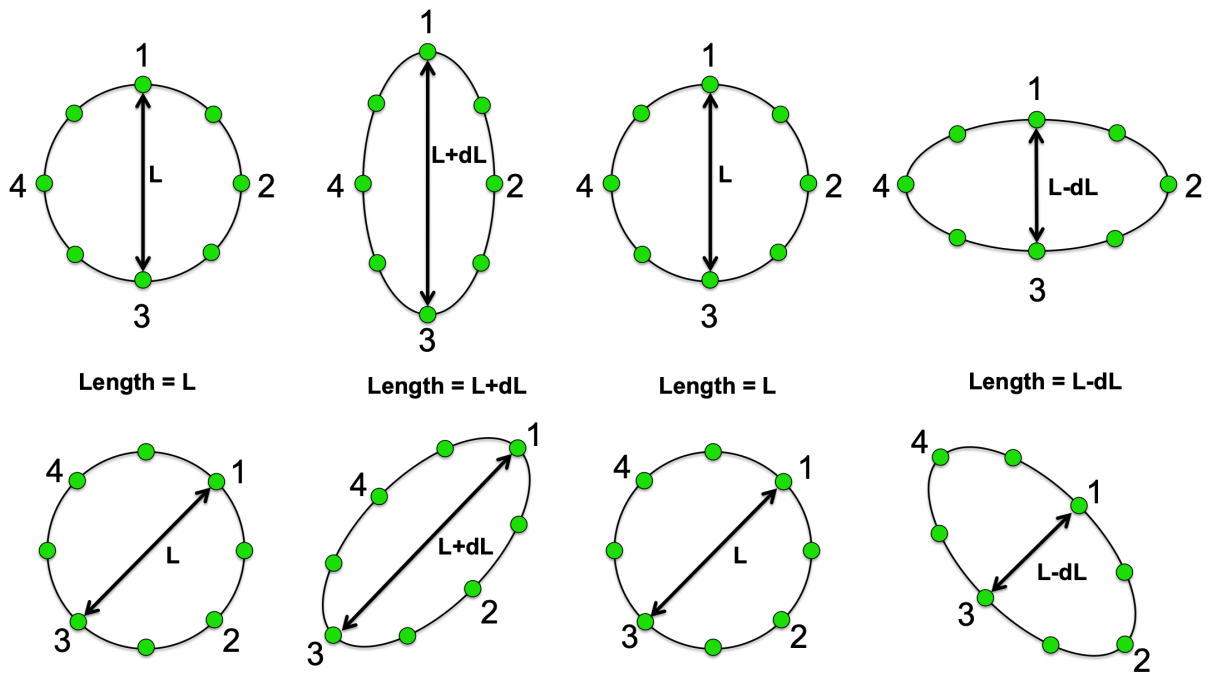


**Figure 1.2:** Diagram showing a ring of free particles for the two types of polarisation, + and  $\times$ , of gravitational waves, where the length value refers to the length of the arrows between two particles.

## 1.2 Gravitational wave sources

Out of the four fundamental forces that appear in nature (weak, strong, electromagnetism and gravity), gravity is by far the weakest in strength. This results in the quadrupole amplitude of gravitational waves to be extremely small, thus making them incredibly difficult to detect. For example, to generate a gravitational wave in a laboratory environment with two  $10^3$  kg spherical masses on a rod of length 2 m rotating at a frequency of 1000 Hz, the amplitude of the gravitational wave signal observed would be of the order  $10^{-38}$  [4]. For comparison, a current generation gravitational wave detector such as the advance Laser Interferometer Gravitational-wave Observatory (aLIGO) [5] [6] in its current form is sensitive to  $10^{-23} / \sqrt{Hz}$  for detecting gravitational wave signals from black holes and neutron stars in the universe. Laboratory generated gravitational waves are therefore not an option to study and must rely on gravitational waves from sources in the universe. Figure 1.3 shows the frequency range for several types of sources.

For gravitational waves to be produced from these sources, there has to be an asymmetrical aspect to the acceleration of the object. The following subsections will describe several types of sources that show this behaviour.

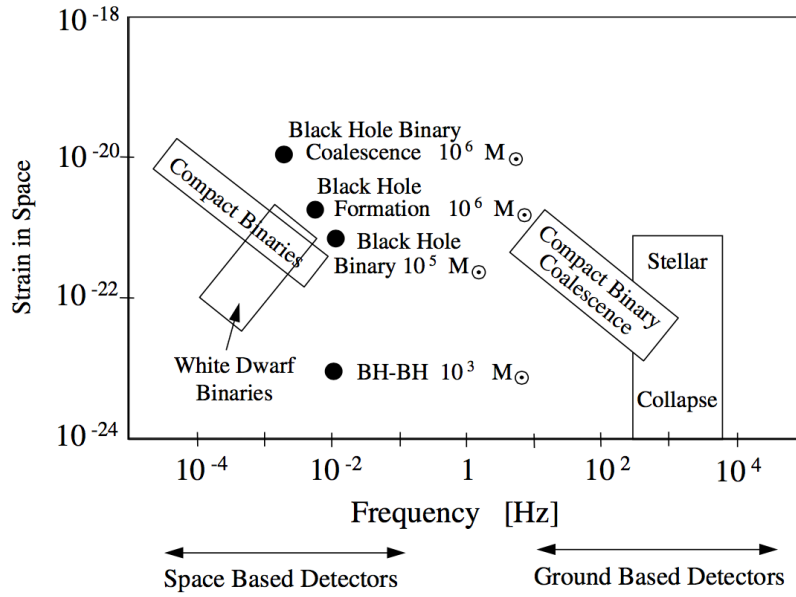


**Figure 1.3:** The gravitational strain,  $\sqrt{Hz}$ , and corresponding frequency of several types of sources [3].

### 1.2.1 Compact Binary Coalescence (CBC)

CBCs come in three different pairings:

- Binary neutron star (BNS)
- Black hole / neutron star (BHNS)
- Binary black hole (BBH)

CBCs orbit around a common centre of mass as they are gradually pulled closer to each other through gravity. This results in the system radiating energy in the form of gravitational radiation. The loss of energy in the system decreases the distance between each body in the system.

The amplitude of a gravitational wave signal from a BNS can be calculated by [7]:

$$h \approx 1 \times 10^{-23} \left( \frac{100 \text{Mpc}}{r} \right) \left( \frac{M_B}{1.0 M_\odot} \right)^{\frac{5}{3}} \left( \frac{f}{100 \text{Hz}} \right)^{\frac{2}{3}} \quad (1.2)$$

where  $r$  is the distance to the source,  $f$  is the frequency of the gravitational wave signal and  $M_B$  is the chirp mass that is equal to:

$$M_B = \frac{(M_1 M_2)^{\frac{3}{5}}}{(M_1 + M_2)^{\frac{1}{5}}} \quad (1.3)$$

where  $M_1$  and  $M_2$  are the masses of the stars.

The nature of the signal that would be observed for a CBC would be a sinusoidal signal that would increase in amplitude over time, reaching a maximum when the two objects merge

together. After the point of maximum amplitude, the signal amplitude decreases extremely sharply, oscillating down to zero as no more gravitational waves would be produced. This is called the ring down. The length and amplitude of the signal that is observed is determined by the density of the objects involved. A BNS coalescence for example will have a longer observable signal before merging compared to a BBH coalescence due to the BNS having a lot less mass and therefore taking longer to coalesce than a BBH coalescence. Examples of this will be shown later in section 1.4.

## 1.2.2 Supernovae

One of the potential final stages of a star's life is to explode in what is called a supernova. When a star burns fuel, the outwards pressure generated counteracts the gravitational pull of the star's core such that they are in equilibrium. Supernovae occur when a massive star has burned all of its fuel and starts producing iron. As fusing iron takes more energy than you get out from fusing two iron atoms, the gravitational pull of the core takes over the outwards force that was generated by the burning of fuel. All the gas around the star suddenly collapses causing the star to explode. A simulation of a supernova explosion is shown in figure 1.4 [8]. Should the collapse and explosion of the star be perfectly symmetric, no gravitational waves would be produced. However, if the collapse and explosion of the star was asymmetric in any way, gravitational waves with the following amplitude would be obtained [9]:

$$h \approx 6 \times 10^{-21} \left( \frac{E}{10^{-7} M_{\odot}} \right)^{\frac{1}{2}} \left( \frac{1ms}{T} \right)^{\frac{1}{2}} \left( \frac{1kHz}{f} \right) \left( \frac{10kpc}{r} \right) \quad (1.4)$$

where  $E$  is the total energy radiated,  $M_{\odot}$  is a solar mass,  $T$  is the time to collapse, and  $r$  is the distance to the source. For the example in equation 1.4 for a supernova in the Milky Way, the signal would be large enough to detect with current gravitational wave detectors, however the event rate for a supernova in this region is extremely low, meaning at this time signals from these sources can only be modelled and not compared to real data [9].

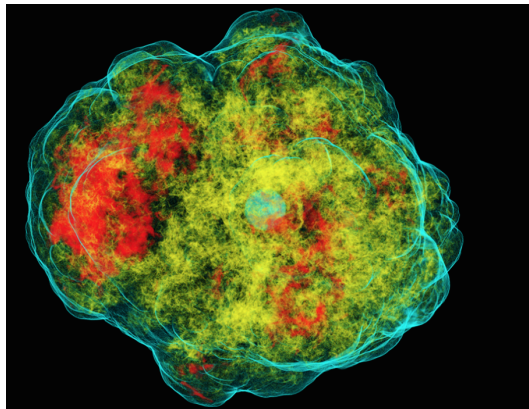


**Figure 1.4:** A simulation of a supernova explosion, showing the asymmetric aspect of the explosion that would produce gravitational waves [8].

### 1.2.3 Continuous Waves (CW)

Continuous wave (CW) sources have so far remained elusive to the current generation of online detectors. CW sources, as the name suggests, supply a continuous emission of gravitational waves that can be observed by gravitational wave detectors over a much greater period of time than the signals obtained from CBCs. An example of a CW source would be pulsars. The first indirect observation of this behaviour was achieved with a BNS in 1975 by R. A. Hulse and J. H. Taylor [10] [11]. They observed a pulsar, PSR B1913+16, that consisted of two neutron stars gradually coalescing over time. They were able to plot out the orbital decay of the system over time showing that as the orbital distance between the bodies decreased, the system must be radiating the energy away, shown in figure 1.5.

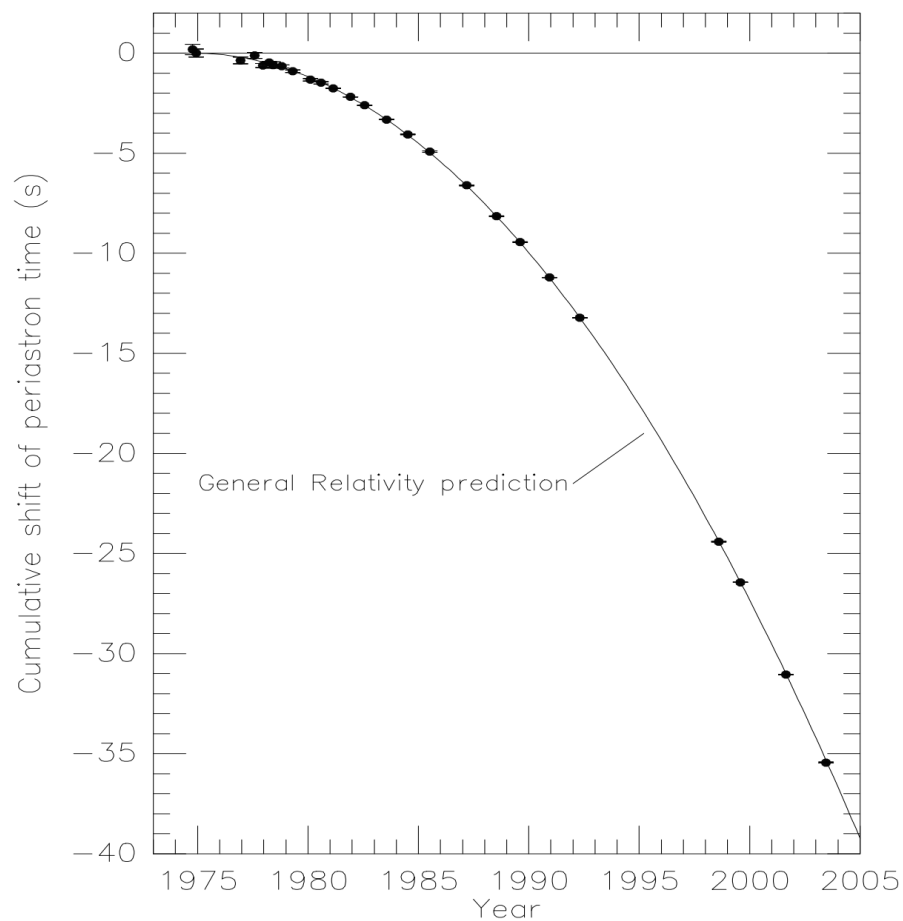


**Figure 1.5:** The orbital decay of PSR B1913+16 compared to the general relativistic prediction of the orbital decay [12].

For single pulsars, the emission of gravitational waves relies on an asymmetrical acceleration component to emit radiation. Pulsars that are not perfect spheres, but instead have a small hill-like structure on the surface, will not rotate on its axis perfectly. This bump would cause the pulsar to wobble as it rotates, emitting gravitational waves. These signals are however extremely

difficult to obtain due to the signal being buried in the noise of the interferometers and require several months to years of analysed data. The amplitude spectral density of a CW source can be calculated by [13]:

$$h \approx 6 \times 10^{-25} \left( \frac{f_{rot}}{500\text{Hz}} \right)^2 \left( \frac{1\text{kpc}}{r} \right) \left( \frac{\varepsilon}{10^{-6}} \right) \quad (1.5)$$

where  $f_{rot}$  is the rotational frequency of the pulsar,  $r$  is the distance to the source and  $\varepsilon$  is the ellipticity of the pulsar.

Theoretically, it would be possible to deduce a CW signal with one detector. As the Earth rotates, the orientation of a gravitational wave detector will change relative to the source [14]. This means that the sensitivity of the detector changes with the rotation of the Earth. As CW searches analyse months to years worth of data looking for signals, the change in the amplitude of a CW could be deduced with the change of detector sensitivity. The data from a network of gravitational wave detectors can be combined to limit this sensitivity change. Comparing equations 1.2 and 1.4 to equation 1.5, it can be seen that the CW sources will produce the smallest signal. As of the end of the second operating run of aLIGO (O2), no CW signal has yet been obtained.

### 1.2.4 Stochastic background

Another potential source of gravitational waves is what is known as the stochastic background [15] [16]. Similar to the Cosmic Microwave Background in the electromagnetic spectrum, the stochastic background of gravitational waves should theoretically be detectable. This background would be isotropic in nature and range over an extremely broadband frequency. It would not be possible to distinguish this background from one detector as the signal from this source would be buried within the noise of the interferometers. It is therefore necessary to have a large network of gravitational wave detectors to distinguish correlated signals between them [4]. From the first observing run of the aLIGO detectors, the upper limit for the stochastic gravitational wave background energy density,  $\omega_{GW}$ , was found to be  $< 1.7 \times 10^{-7}$  [15].

## 1.3 Instruments to detect gravitational waves

Attempts to detect gravitational waves have focused on the use of two types of instruments:

- Resonant bars
- Michelson interferometers

### 1.3.1 Resonant bar detectors

Joseph Weber was one of the main endorsers for the use of resonant bars in the early era of attempting to detect gravitational waves. He proposed to have two separate aluminium cylinders, referred to as bars, located at two locations separated by a large distance [17] [18]. These cylinders were located in Maryland and Chicago in the United States of America (USA). The theory was that, should a gravitational wave pass by, both aluminium bars would resonate within a narrow frequency band. This resonance would be picked up by piezoelectric crystals attached to the detector to convert the resonance to an electrical signal. The reason two bars were needed was to allow for the ability to distinguish a signal from local noise sources. As a bar could resonate through local noise factors to give what would appear to be a gravitational wave signal, it would be possible to deduce that this was a local noise source if no signal appeared at the second bar detector. If only one bar were present, then it would be impossible to distinguish any signal to be a gravitational wave or local noise.

It was claimed by Weber in 1969 that a gravitational wave had been detected through his experimental set up [19]. He claimed to observe a total of 17 gravitational wave events over an 81 day time period. With the high frequency of events detected, multiple replica detectors were made worldwide to try and observe the same signals Weber was detecting through his bar detectors. Unfortunately, these replica detectors failed to detect any signals similar to what Weber had detected, publishing results disproving his claims of detecting gravitational waves [20]. Attention was then turned towards the development of gravitational wave detectors through the technique of interferometry.

### 1.3.2 Laser Interferometry

Following the unsuccessful attempts to detect gravitational waves through the use of resonant bar detectors, a second technique utilising a Michelson interferometer was investigated that showed the capabilities of detecting gravitational waves. The concept of a Michelson interferometer, shown in figure 1.6, is that a laser beam passes through a beam splitter down two perpendicular arms towards a mirror at the end of each arm. The mirror reflects the two beams back down the arms to the beam splitter where the two beams interfere with each other. The resulting output, picked up on the photodiode, is what is known as an interference pattern which consists of bright and dark fringes. The nature of the fringe is determined by the phase of the two beams when they interfere with each other. Should two peaks interfere, the resulting output is a bright fringe, known as constructive interference. Should two troughs interfere, the resulting output is a dark fringe, known as destructive interference.

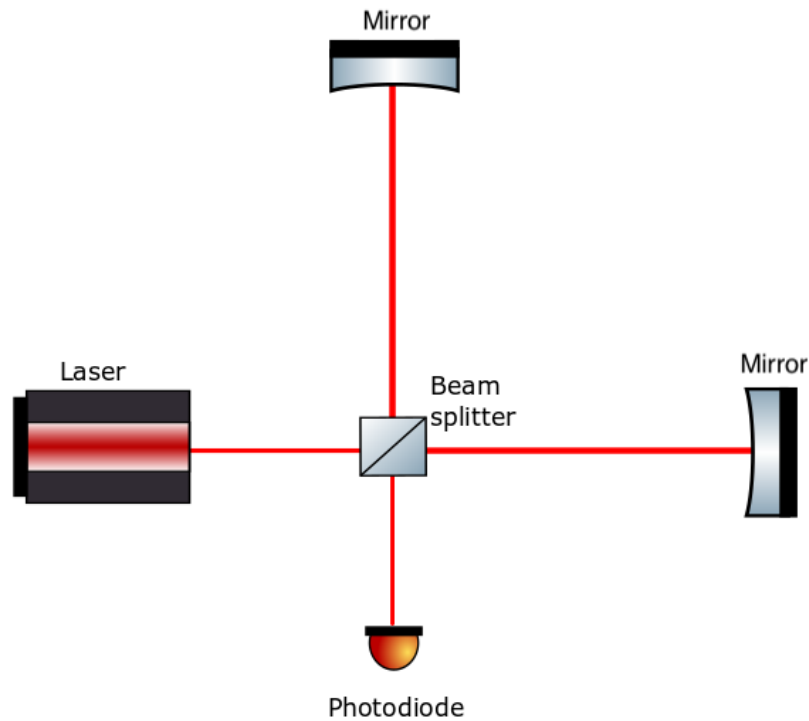


**Figure 1.6:** A schematic of a Michelson interferometer.

As mentioned previously, when a gravitational wave passes through a ring of free particles, it stretches the ring in one direction, and squeezes it in the perpendicular direction. When a gravitational wave passes through an interferometer, this same principle applies where one arm, of length  $L$ , would be stretched by a distance  $dL$ , and the perpendicular arm is shortened by a distance  $dL$ . This is illustrated in figure 1.7 to show the example of a  $+$  polarisation gravitational wave passing through the interferometer. As the arm length changes, the amount of time the laser beam is inside the arm changes. This differential in time is what causes the interference pattern at the photodiode to change.

To utilise the technique of interferometry to detect the faint signal of a gravitational wave, long interferometer arms are needed to have a sensitivity large enough. Optimal sensitivity can be achieved in an interferometer when the time it takes for the beam to recombine back at the beam splitter is half the period of a gravitational wave. This is because this is the moment the mirror displacement will be at its maximum. The optimal length,  $L_{opt}$ , of an interferometer arm can be calculated via:

$$L_{opt} = \frac{\lambda}{4} = \frac{vt}{2} \quad (1.6)$$

where  $v$  is the speed of light and  $t$  is the time the beam is in the arm of the interferometer. For a gravitational wave with a frequency of 100 Hz,  $t = 0.5 \times 10^{-2} s$  giving a value  $L = 750000$  m. The possibility of building an interferometer with an arm length of 750 km is not practically and financially feasible. Therefore other techniques must be implemented to increase the sensitivity of the interferometer.

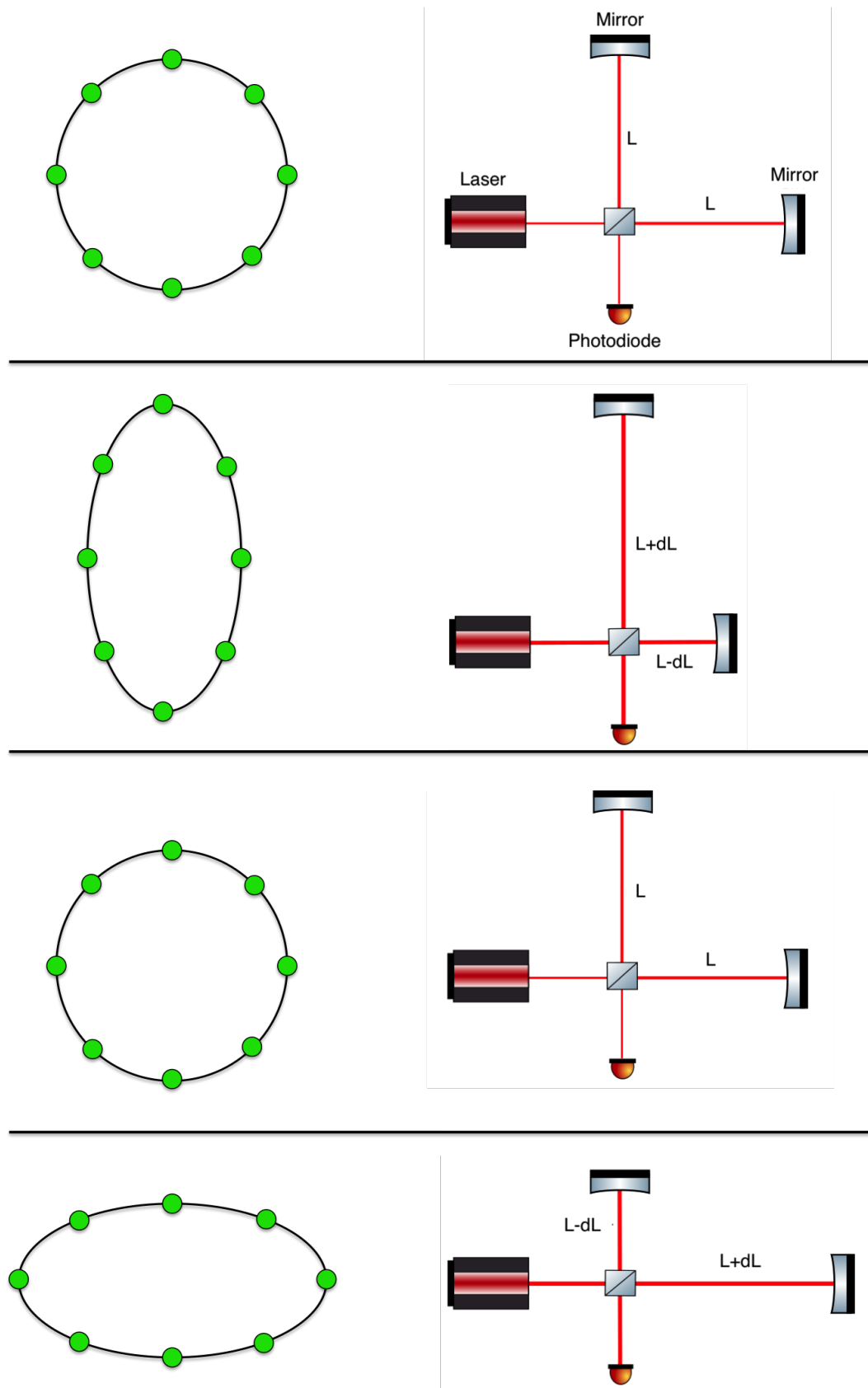


**Figure 1.7:** The effect of a + polarised gravitational wave passing through normal to a Michelson interferometer illustrating how the arm lengths change by a distance  $dL$ .

### 1.3.3 Ground-based laser interferometers

There are currently four ground based interferometers that are operational and observing as of writing this thesis. These are:

- The advanced Laser Interferometer Gravitational-wave Observatory: aLIGO [21] [5] [6]
  - One located in Hanford, WA, USA - LIGO Hanford Observatory: LHO
  - Second located in Livingston, LA, USA - LIGO Livingston Observatory: LLO
  - Arm length of 4 km
  - 40 kg fused silica test mass, 400  $\mu\text{m}$  suspension fibre diameter
  - Operates at room temperature
- Advanced Virgo [22] [23] [24]
  - Located in Pisa, Italy
  - Arm length of 3 km
  - 40 kg fused silica test mass, 400  $\mu\text{m}$  suspension fibre diameter
  - Operates at room temperature
- GEO 600 [25] [26] [27]
  - Located in Ruthe, Germany
  - Arm length of 600 m
  - 5.6 kg fused silica test mass, 270  $\mu\text{m}$  suspension fibre diameter
  - Operates at room temperature

There are also currently two ground based interferometers currently being built:

- Kamioka Gravitational Wave Detector: KAGRA [28] [29]
  - Located within Mount Ikenoyama, Japan
  - Due to join aLIGO and Virgo during the third observing run (O3) in 2020
  - Arm length of 3 km
  - 22.8 kg silicon test mass, 1.6 mm suspension fibre diameter
  - Operates at cryogenic temperature of 22 K
- LIGO India
  - Under development in Maharashtra, India. Based on the same design as the two aLIGO detectors in the USA

- Completion due in 2024
- Similar design to the aLIGO detectors in the USA

None of the above mentioned interferometers have arm lengths close to the previous example of having 700 km arm lengths. The two aLIGO detectors have 4 km long arms, Virgo has 3 km and GEO600 has 0.6 km. Although GEO600 is classed as an online and observing gravitational wave detector, it is not anywhere near sensitive enough as the aLIGO and Virgo detectors. For this reason, a lot of updated detector technology with the goal of making gravitational wave detectors more sensitive is implemented at GEO600 and tested thoroughly before installation at aLIGO and Virgo.

There are several techniques and upgrades that have been installed in the past decade at the aLIGO and Virgo observatories that improve the sensitivity of the detectors to make up for the fact that, for example, a 700 km arm length is not a possibility. Though the arms will not physically be this length, they can effectively be increased through the use of Fabry-Perot cavities and delay lines [3] [30]. An example of a Fabry-Perot cavity in the arms of the interferometer is shown in figure 1.8. To create a cavity in the arm of the interferometer, additional mirrors, referred to as test masses (TM), are needed compared to the simple Michelson interferometer. When the beam passes through the beam splitter, it passes through the back of the input test mass (ITM) and travels down the arm until it reflects off the end test mass (ETM). At the face of the ITM are several layers of highly reflective coating material that allows for an extremely small amount of transmission through the test mass, while reflecting the rest, of the order of one in 3-million photons being absorbed by the test mass. The coating on the ETM however reflects all the light back into the arm. For the cavity to work, the test masses must be held in position to build up a resonance between the two test masses where the length of the cavity is an integral number of the wavelength of the laser. This allows for energy build up within the cavity and increases the amount of time the beam travels within the arm, effectively increasing the arm length. For aLIGO, the effective arm length is approximately 1800 km [6].

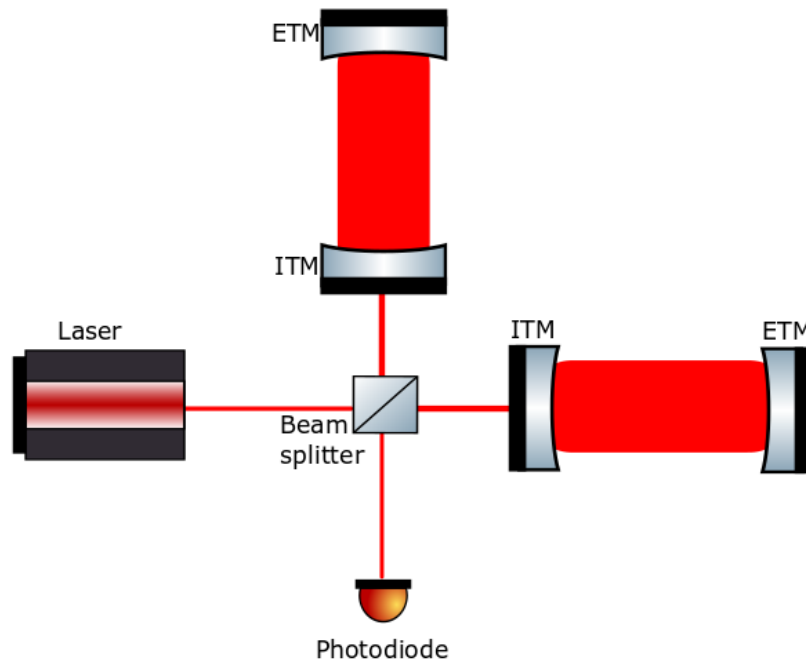


**Figure 1.8:** Schematic of a Michelson interferometer with Fabry-Perot cavities installed in the arms.

A similar technique to Fabry-Perot cavities is the use of delay lines [31] [32], shown in figure 1.9. The main difference with this technique is that the beam is not reflected over itself, but follows one singular traced path reflecting back and forth between the ITM and ETM to increase the effective arm length inside the cavity. This technique however would require larger mirrors to get an effective arm length similar to that found with Fabry-Perot cavities, which in turn would be a larger cost factor in terms of fabrication. Also due to the wider area needed to reflect the beams, this results in a greater amount of scattered light appearing in the arms, which can be a limiting noise source [33].

Additional mirrors can be placed along the beam path of the interferometer to increase the sensitivity of the detector. The input laser for the aLIGO detectors is approximately 125 W [6], but this can be increased through the addition of a mirror between the laser and the beam splitter. This is called power recycling, and is shown in figure 1.10.

The configuration of the interferometer is such that when the arms are locked and resonating, the output at the photodiode is next to a dark fringe. This means that the majority of the light is therefore reflected back to the beam splitter. By adding a mirror in between the laser and the beam splitter, referred to as the power recycling mirror (PRM), this light can be recycled back into the interferometer arms. The PRM also creates a smaller interferometer with the ITMs and when resonant, will increase the laser power by what is known as the power recycling gain. For aLIGO, this gain is approximately 42 which results in 5.2 kW of laser power at the beamsplitter before entering the Fabry-Perot arm cavities. This results in approximately 750 kW of power in the arm cavities [6].

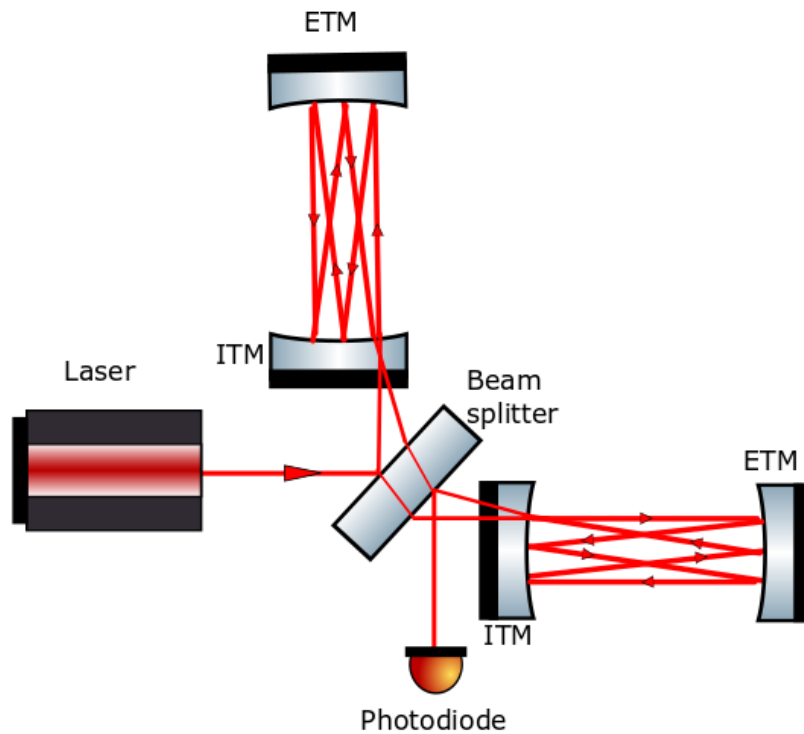


**Figure 1.9:** Schematic of a Michelson interferometer with delay line cavities installed in the arms.

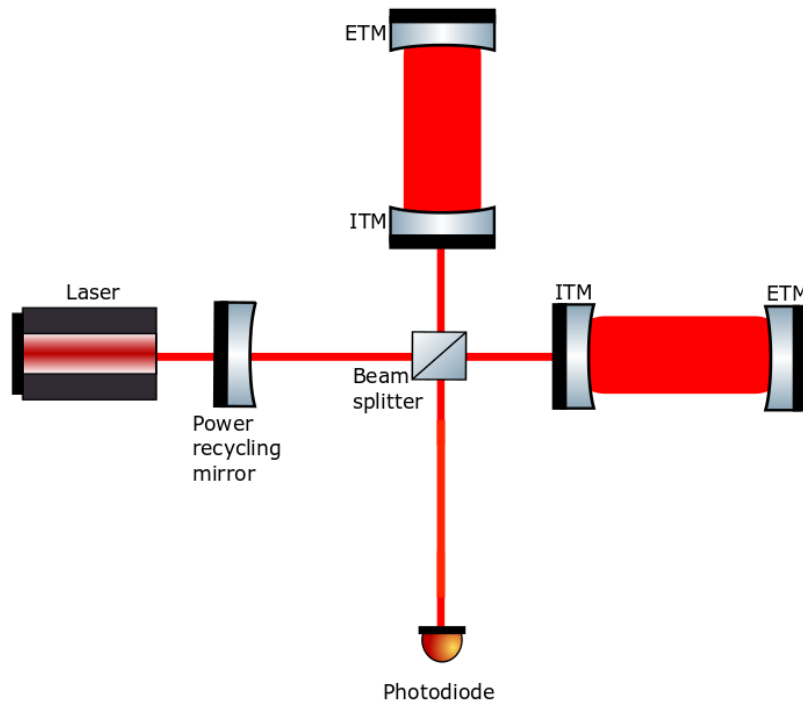


**Figure 1.10:** Schematic of a Michelson interferometer with a power recycling mirror (PRM) installed in between the laser and the beam splitter.

Again, the same technique with power recycling can be applied to the signal before the output photodiode. Signal recycling [34] [35] can be achieved by placing a mirror, known as the

signal recycling mirror (SRM), in between the beam splitter and the output photodiode as shown in figure 1.11. The addition of a SRM allows for a greater frequency response to an incoming gravitational wave signal by enhancing the signal at a specific frequency, or by broadening the bandwidth and reflecting the sidebands back into the arm cavities. Broadening the bandwidth will result in the detector being less sensitive at particular frequencies, but allows for a wider range of signals to be observed. Narrowing the bandwidth would result in the detector being more sensitive at a particular frequency, which would aid searches in CW searches, but sacrifices sensitivity to signals outside this band.

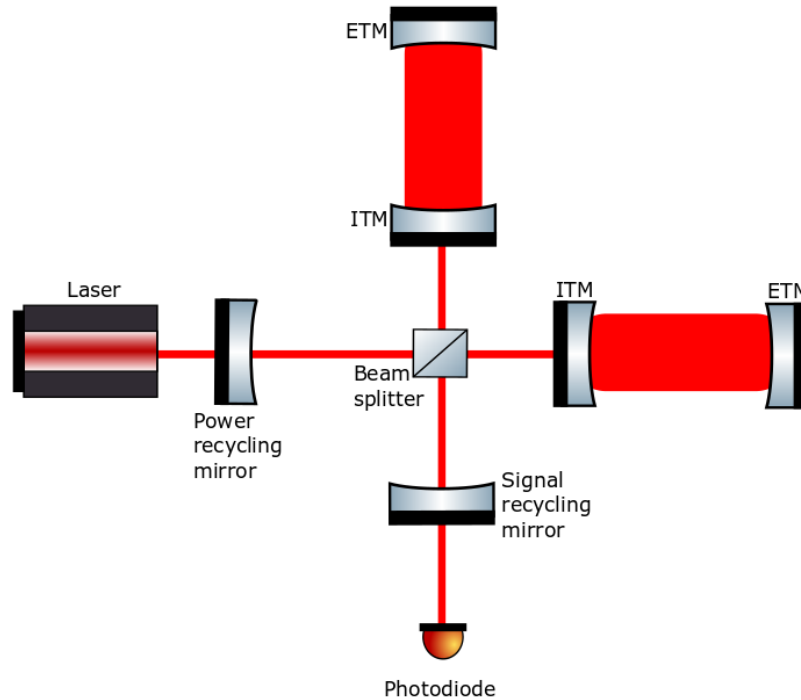


**Figure 1.11:** Schematic of a dual recycled Michelson interferometer with Fabry-Perot cavities, where the signal recycling mirror (SRM) is installed between the output photodiode and the beam splitter.

Plans for the next generation of ground-based gravitational wave detectors are already under way. In particular, there has been significant planning for the Einstein Telescope to be built in Europe which is designed to be between 100-200 m underground and an order of magnitude more sensitive than the aLIGO detectors [36] [37]. This underground detector will consist of a triangular configuration layout which houses 6 interferometers in total with an arm length of 10 km, shown in figure 1.12. Having a triangular formation means that the detector will be sensitive to gravitational waves coming in from all directions, unlike the current detectors that are optimally sensitive to signals coming in aligned with the interferometer. Three of the interferometers will be built to perform at room temperature and therefore focus on high-frequency signals, whereas the other three are designed to operate at a cryogenic temperature, focusing on

low-frequency signals. In addition to this, the sizes of the test masses will increase from 40 kg to approximately 200 kg for the room temperature interferometers. For the cryogenic test masses, silicon will be used instead of silica due to its better thermal properties at cryogenic temperatures [38]. The Einstein Telescope is not scheduled to be in operation until at least the second half of the decade of 2020 [37].

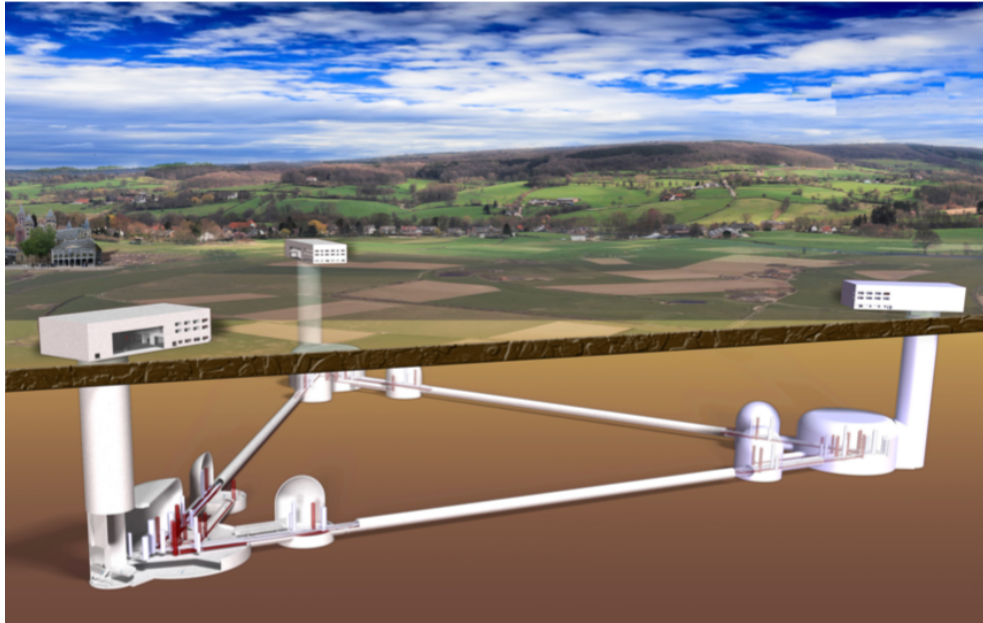


**Figure 1.12:** An artists impression of The Einstein telescope showing the layout of the interferometer arms underground [37].

### 1.3.4 Space-based laser interferometers

The next generation of gravitational wave detectors aims to have a space-based detector to accompany the ground-based detectors, in particular, the Laser Interferometer Space Antenna (LISA) [39] [40]. LISA will consist of 3 satellites in an equilateral triangle formation following the Earth's orbit by approximately  $20^\circ$ , with each satellite spaced 2.5 million km apart. This will give the detector a bandwidth of 0.1 mHz to 100 mHz to detect signals from super massive black holes. In 2015, LISA Pathfinder (LPF) was launched to test various components and systems, such as an optical metrology, that would be essential to the LISA project. LPF was launched with two gold-platinum test masses on board with the goal of observing the motion of the test masses under just the influence of gravity. As well as this, systems such as an optical metrology system, drag-free control system and micro-Newton thruster systems were tested for performance. Results showed that the test masses performed by a factor of 5 better than required, indicating that the masses were essentially motionless with respect to each other demonstrating that the technology required for LISA was achievable at this early stage [41]. LISA is currently scheduled to launch by 2034.

## 1.4 Detection of gravitational waves

On the 14<sup>th</sup> of September 2015, the two aLIGO detectors detected a signal that originated from the coalescence of a binary black hole (BBH) system, GW150914 [42]. Two black holes of 36 and 29 solar masses merged to form a black hole of 62 solar masses. This meant that 3 solar masses worth of energy was radiated away in the form of gravitational waves. This was not only the first direct observation of a binary black hole system, but also the first confirmed detection of gravitational waves. A total of 11 confirmed detections have been published from the first and second observation runs (O1 and O2) with data from aLIGO and Virgo. These include 10 binary black hole coalescences [42] [43] [44] [45] [46] [47] [48] and 1 binary neutron star (BNS) coalescence [49]. The waveforms from the 10 black hole coalescences are shown in figure 1.13 [47].

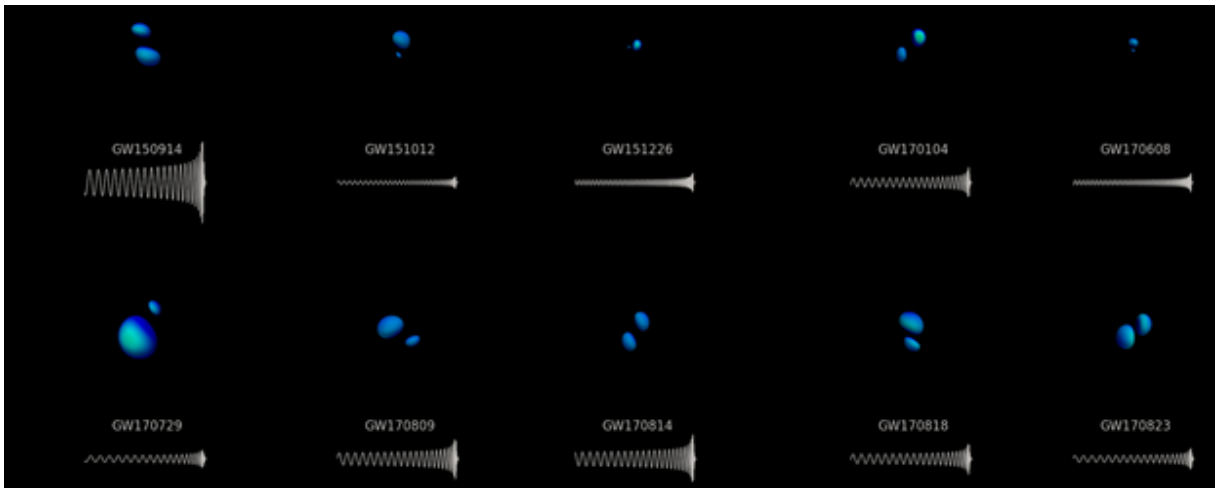


**Figure 1.13:** Waveforms and simulated images of BBH coalescences observed in O1 and O2 [50]. The shape of the waveform can be seen to change depending on the mass of the black holes involved, where the smaller BBHs inspiral over a longer timescale than heavier ones.

The first BNS detection, GW170817 [49] [51], was significant for several reasons. The gravitational wave signal obtained was approximately 100 seconds, which is 2 orders of magnitude longer than the signals produced from black holes. An example of how this waveform compared to selected BBH coalescences is shown in figure 1.14. This signal also occurred at the same time as a gamma ray burst (GRB) was observed. The Fermi Gamma-ray Burst Monitor had independently observed a GRB signal where the delay between the aLIGO detectors gravitational wave signal and Fermi was approximately 1.7 seconds [52]. When two neutron stars merged together, an optical counterpart could be detected by telescopes stationed around the world and in space. This is unlike the case for BBH coalescences which do not emit an optical counterpart. A world-wide array of telescopes and satellites then began a search in the sky from the aLIGO and Virgo data to observe any visible remnants of an optical counterpart. Within 11 hours of the gravitational wave and GRB signal being detected, an optical counterpart was observed by the

1 metre, 2 hemisphere team using the Swope 1 m telescope, shown in figure 1.15. In total, over 70 ground and space based observatories were able to confirm the signal. All of this confirmed that BNS mergers are progenitors of short GRBs [53].

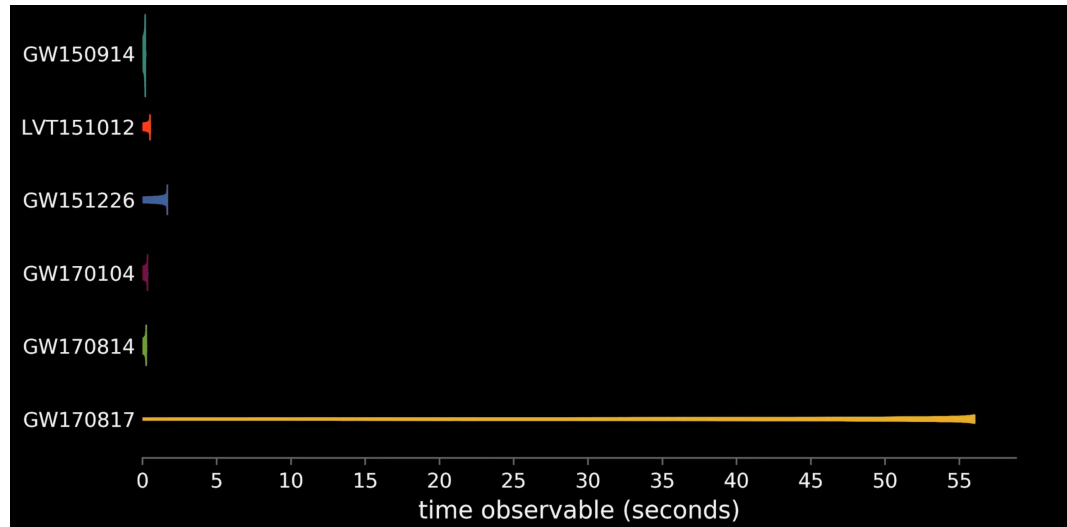


**Figure 1.14:** A comparison of the length of selected BBH coalescences compared to the BNS coalescence, GW170817 [54].

The optical counterpart was determined to be a kilonova, which forms some of the most exotic material in the universe such as gold and platinum. This confirmed a source of the production of elements in the universe heavier than iron. The optical counterpart was observable for weeks after the initial signal over the whole optical spectrum, as shown in figure 1.16. This is the first instance of multi-messenger astronomy where both gravitational and electromagnetic radiation were observed for the same astronomical event [52]. Analysis of the arrival time between the photons from the GRB and the gravitational wave allowed for a constraint to be applied to the fractional difference between the speed of gravitational waves and the speed of light to between  $10^{-15}$  and  $10^{-16}$  [53].

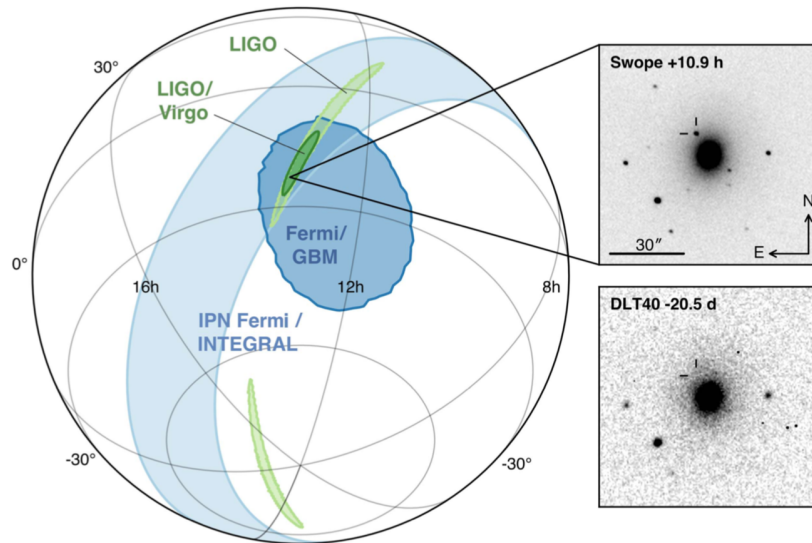


**Figure 1.15:** Sky localisation of the BNS gravitational wave signal from the aLIGO (green) and a combination of the aLIGO and Virgo detectors (dark green), the Fermi GRB signal (dark blue), and the resulting optical discovery from the Swope 1 m telescope 10.9 hours after the initial signal. For reference, the same area of sky is shown 20 days prior to the signal arriving from the DLT40 collaboration to show the difference [52].

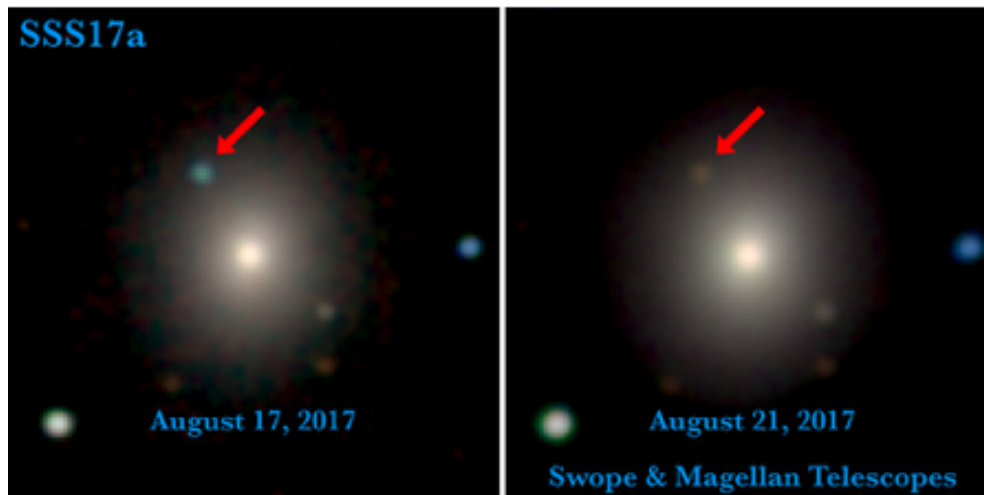


**Figure 1.16:** An optical (left) and near infra-red (right) view of the optical counterpart to GW170817 (labelled SSS17a). Photo credit: 1M2H/UC Santa Cruz and Carnegie Observatories/Ryan Foley.

As of writing this thesis, the third observing run (O3) is currently underway with LHO, LLO and Virgo with KAGRA due to join the observing run by 2020. Public alerts for candidate events are now in effect sending notifications out to the public within minutes of the signal being detected [55]. The number of candidate events found in O3 alone has so far surpassed the total number of events found prior to O3, with a gravitational wave catalogue detailing the events

to be released once O3 has finished. These detections would not have been possible had it not been for the various upgrades that the LIGO detectors went through to get them to their second generation state of aLIGO. The following section will detail one of the key upgrades that was carried out, which will be relevant for several investigations carried out in this thesis.

## 1.5 Overview of the aLIGO four-stage quasi-monolithic suspension system

One of the key upgrades that occurred between initial LIGO and aLIGO was the installation of the four-stage quasi-monolithic suspension to suspend the test masses [56] [57] [58], shown in figure 1.17 [59]. A comparison of the initial LIGO and the final stage aLIGO suspension systems is shown in figure 1.18 [56].

As the aLIGO detectors have to be able to measure a distance change of the order of a thousandth of the diameter of a proton, the test masses that are moved as a gravitational wave passes have to be isolated by all local perturbations. This is achieved through the use of a four-stage pendulum system to suspend the test mass. The concept of a multiple stage suspension system was first investigated and tested at the GEO 600 detector [60]. The system installed at aLIGO sits in an active seismic isolation chamber to combat the seismic noise, while the four-stage system combats this noise passively. The top three stages consist of cantilever blades to minimise any vertical motion of the test mass. These blades are made of maraging steel to support the weight of the entire pendulum system, with each stage attached to the end of the blades with steel wire.

The final stage of the pendulum system is the monolithic fused silica suspension. Fused silica was specifically used for its strength and thermal noise properties, which will be discussed in the following section. This final stage consists of a penultimate test mass (PUM) and either an ITM or ETM, depending on the location in the interferometer. For the purpose of this section, the suspended test mass will be referred to as the ETM. Both the PUM and ETM are 40 kg fused silica mirrors with a diameter of 34 cm and a thickness of 20 cm [56] [6]. This is a 29.3 kg increase in mass from initial LIGO test mass. The face of the ETM consists of several layers of extremely low loss, highly reflective coating layers of amorphous silica and tantalum pentoxide [61].

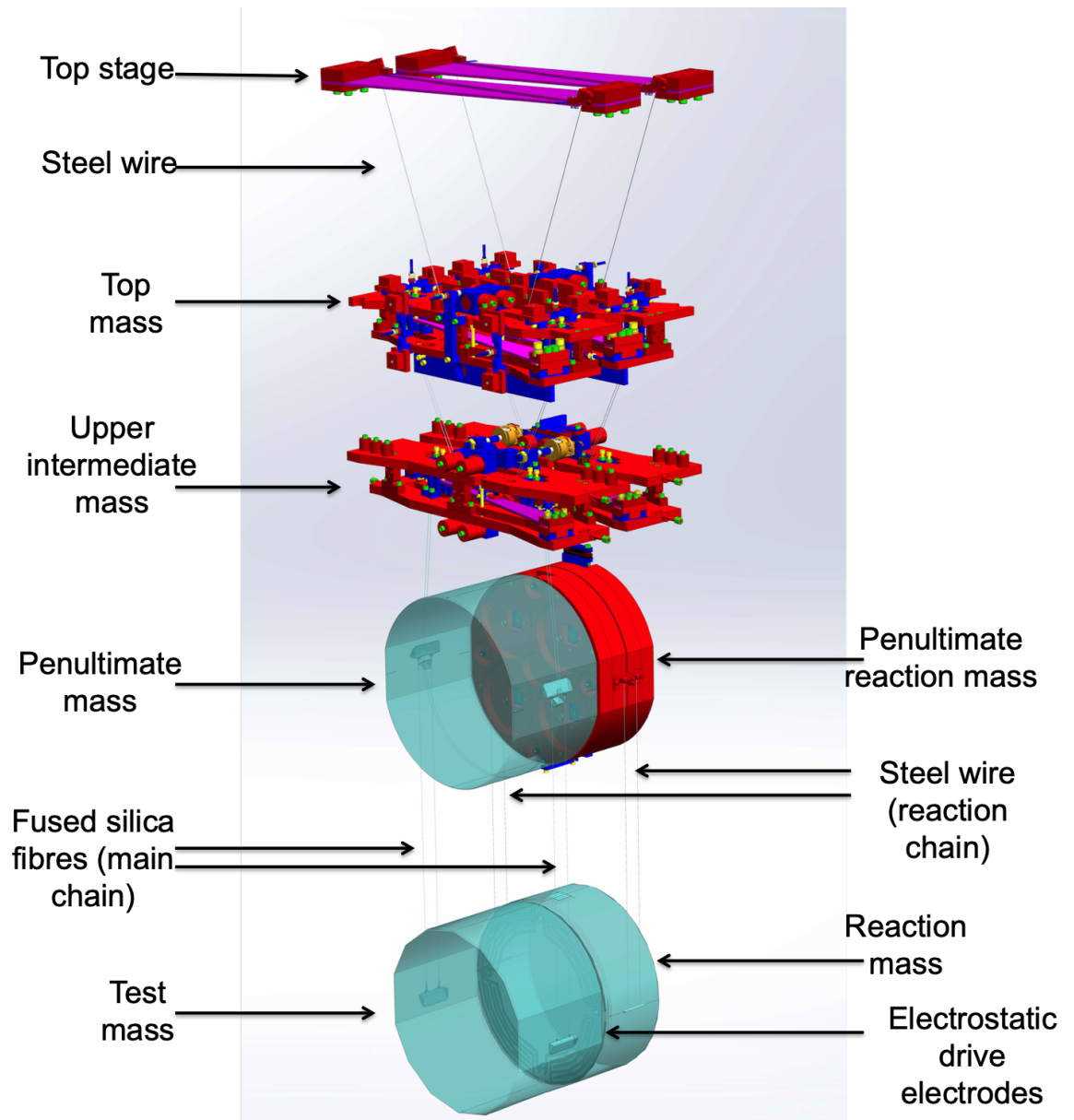


**Figure 1.17:** The layout of the four-stage suspension system for the main chain (front suspension) and the reaction chain (rear suspension) [59]. Within the top and upper intermediate mass are cantilever blades similar to that on the top stage.

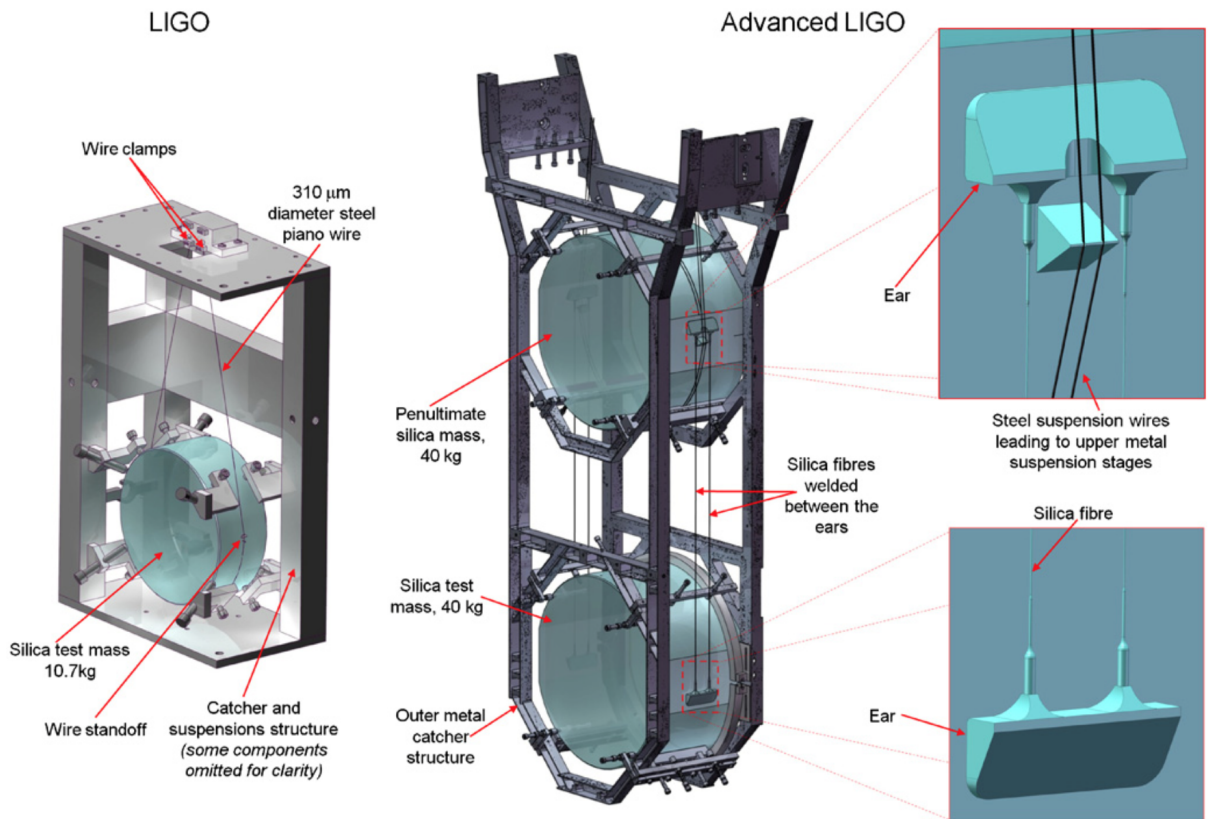


**Figure 1.18:** Comparison between the initial LIGO suspension and the aLIGO suspension systems.

The ETM is suspended from the PUM by fused silica fibres. This was a significant change to the single  $310\ \mu\text{m}$  diameter steel wire loop that was used for initial LIGO. These fused silica fibres start off as  $3\ \text{mm}$  rods and are heated by a  $\text{CO}_2$  laser to approximately  $2000^\circ\text{C}$  [62]. This stock is initially pulled down to  $800\ \mu\text{m}$  in diameter, followed by pulling down to  $400\ \mu\text{m}$ . The diameter then increases again to  $800\ \mu\text{m}$  before the pull concludes. They are approximately  $57\ \text{cm}$  long and are attached to the test mass through fused silica ears [63]. Further characterisation and details on the production of the fibres will be described in chapters 2 and 3. These ears are bonded onto the side of the test mass through hydroxide catalysis bonding [64] [65] [66] which creates a glass-like bond between the ear and the test mass. With four fibres attached to the two masses, this equates to the fibres taking a load of  $10\ \text{kg}$  and a stress of  $780\ \text{MPa}$ . It is extremely important that the final stage of the suspension is quasi-monolithic for optimal noise performance, which will be discussed in the following section.

The design of the whole suspension system was made to reduce several noise sources that were limiting the initial LIGO sensitivity. This was achieved for the start of the aLIGO observing run in 2015 allowing for the detection of numerous gravitational wave events to date. There is always a desire to further reduce the limiting noise sources in the interferometer to make the detector more sensitive, which would result in an increase in detection events. However, lowering these noise sources presents a significant challenge.

## 1.6 Noise sources

Prior to detecting any gravitational waves, a huge problem for the LIGO and Virgo interferometers was getting the required noise performance to distinguish a gravitational wave signal from the total noise of the interferometer. Noise budgets, shown in figure 1.19, were simulated to show what the target sensitivity of the device was going to be, and several science runs were carried out in the years prior to aLIGO and Advanced Virgo coming online to determine the limiting noise sources researchers were faced with to getting to their second generation target noise. Figure 1.20 shows the current sensitivity of all four operating gravitational wave detectors during O3. It is possible to subtract these noise sources once the signal is obtained [67], but the aim is to always make them more sensitive to limit the need to do any post-signal noise subtraction.

Gravitational wave interferometers operate within a vacuum to ensure optimal noise performance. Should the interferometer operate in-air, particles of dust and air molecules can interact with the laser beam and the test masses, resulting in noise in the detector output. Should a dust particle land on the face of the test mass, this can then scatter the laser beam creating noise, or burn into the coating on the face of the test mass, further introducing noise into the signal. Air molecules could also influence the movement of the test mass in the interferometer. This section will discuss various noise sources associated with a gravitational wave detector.

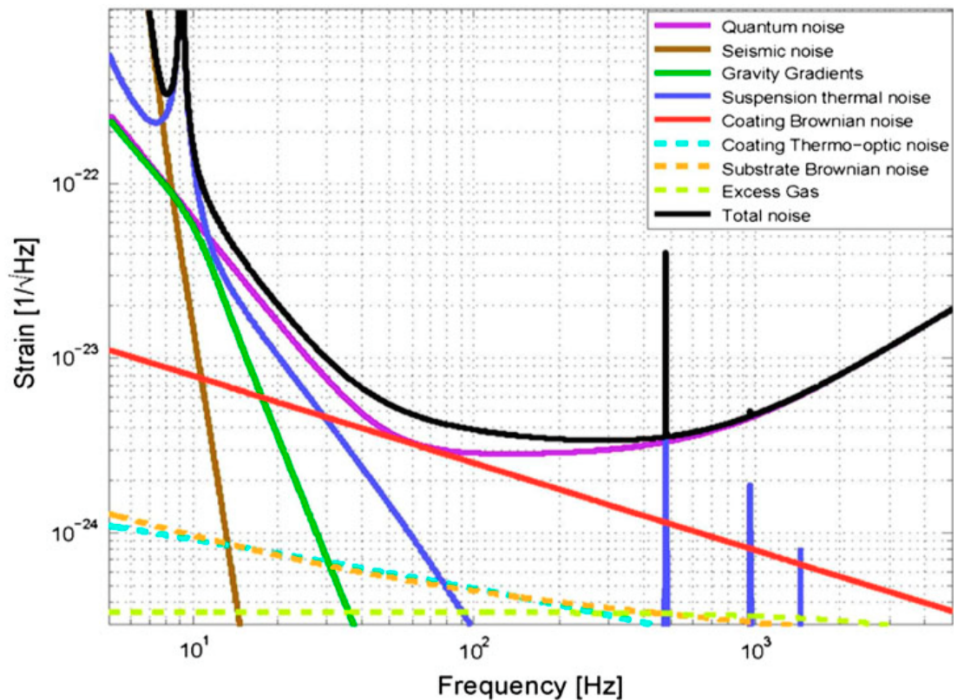


**Figure 1.19:** The aLIGO noise budget showing the various noise sources that limit and affect the interferometer [68].

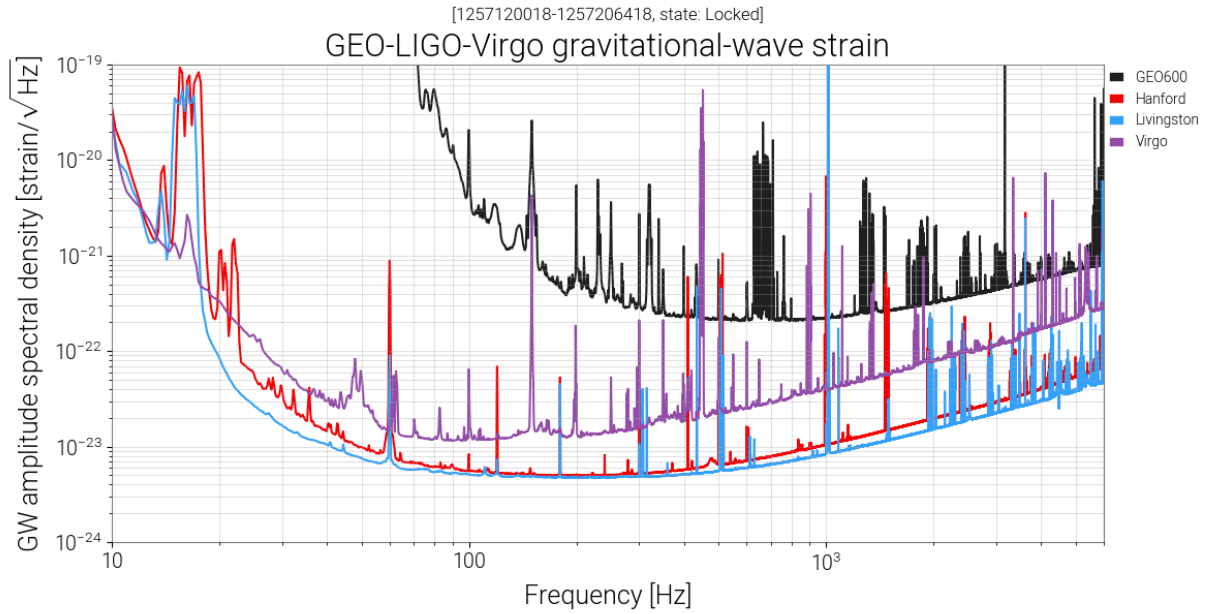


**Figure 1.20:** The current differential arm length (DARM) signal of the two aLIGO interferometers (LHO and LLO), Virgo and GEO600 during O3 [69].

### 1.6.1 Quantum noise

An example of a noise source that can affect the performance of a gravitational wave detector is quantum noise. In particular, there are two noise sources that fall into this category: photon shot noise and radiation pressure noise. Together, they create what is known as the Standard Quantum Limit (SQL). Figure 1.21 shows the effect that both of these noise sources have on the detector.

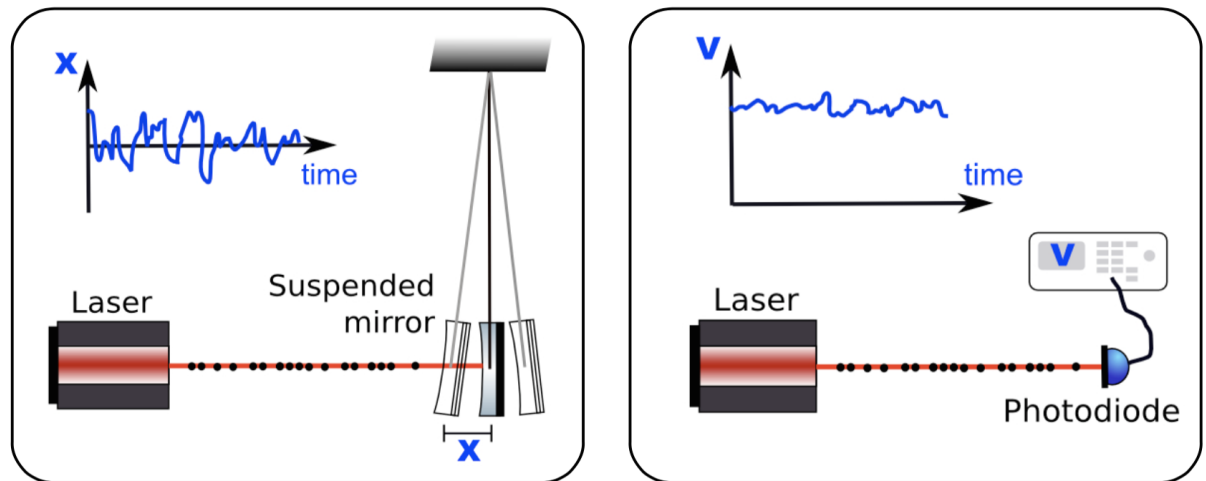


**Figure 1.21:** Illustration of the fluctuation experienced with radiation pressure noise on a test mass (left) and photon shot noise on the output photodiode (right) [70].

Photon shot noise is a result of the photons from the input laser following a poisson distribution instead of being equal over time. The uncertainty in the number of photons,  $N$ , within the time,  $T$ , can therefore be described as  $\sqrt{N}$ . The amplitude spectral density of photon shot noise,  $h_{SN}(f)$ , which indicates the level at which the interferometer is sensitive to this noise can be calculated via [70]:

$$h_{SN}(f) = \frac{1}{L} \sqrt{\frac{\hbar c \lambda}{2\pi P}} \quad (1.7)$$

where  $L$  is the interferometer arm length,  $\lambda$  is the wavelength of the laser,  $c$  is the speed of light,  $\hbar$  is the reduced Planck constant, and  $P$  is the laser power. From equation 1.7, it can be seen that to reduce the shot noise, the laser power can simply be increased. This however, has a knock on effect.

Radiation pressure noise comes from the transfer of momentum from photons to the test mass when they are reflected off the surface. This transfer of momentum therefore applies a force onto the test mass causing it to move a distance,  $x$ , as illustrated in figure 1.21. The magnitude of this position movement is affected by the Poisson distribution of the photons onto the test mass from the laser. This means that the laser power can not simply be increased to reduce the photon shot noise, as this will have the knock on effect of increasing the radiation pressure noise. The amplitude spectral density for radiation pressure noise,  $h_{RP}(f)$ , can be calculated via [70]:

$$h_{RP}(f) = \frac{1}{mf^2L} \sqrt{\frac{\hbar P}{2\pi^3 c \lambda}} \quad (1.8)$$

where  $m$  is the mass of the test mass,  $f$  is the frequency of the gravitational wave, and all other symbols hold their prior definitions. As mentioned previously, increasing the laser power to reduce the photon shot noise will increase the radiation pressure noise, but this could be mitigated by increasing the weight of the test mass, but the design of the detector dictates the value of  $P$  when in operation and therefore, these need to be balanced. This means having  $h_{SN}(f)$  equal to  $h_{RP}(f)$ . This is known as the Standard Quantum Limit (SQL).

The SQL is analogous to the Heisenberg Uncertainty Principle; should the power of the laser increase to make the detector more sensitive at higher frequencies due to the reduction of photon shot noise, the detector will then lose sensitivity at low frequencies due to the increase in radiation pressure noise, and vice versa. The SQL is a limiting noise source in a Michelson interferometer such as aLIGO, however the introduction of a technique called ‘squeezing’ [71] [72] has been proven to reduce this quantum noise limit at the GEO600 observatory [26] [73] [27] and has been installed at LHO and LLO for O3 [74]. Squeezing involves reducing the quantum noise in either the amplitude or phase quadrature of the laser beam in the interferometer, while increasing the quantum noise in the other. For example, if it were desirable to increase the sensitivity in the phase of the laser light, the light can be ‘squeezed’ such that the quantum noise in the phase quadrature decreases, while increasing in the amplitude quadrature.

## 1.6.2 Gravity gradient noise

Gravity gradient noise is a dominant noise source that plays a major role in the sensitivity of the detector at low frequencies [75]. Also known as Newtonian noise, this noise source is due to the changes in density and surface waves of the ground below the suspensions. Figure 1.22 shows the effect a surface wave has on the motion of a test mass. As a surface wave sits underneath the test mass at a peak or a trough, the gravitational pull on the test mass will be perpendicular to the face of the test mass. Once the wave passes, a gradient will occur as the mass is attracted to the direction the surface wave is influencing. Current ground based detectors use gravity gradient models to subtract the Newtonian noise from the signal by measuring the activity of seismometer arrays placed around the observatory [75] [76]. To minimise the effect of surface waves, building an underground detector can push the noise budget further down in frequency [77]. This is one of the motivations for building the Einstein Telescope underground where the low frequency interferometer will be limited by Newtonian noise at 7 Hz and below, which is an improvement to the current 10-12 Hz of current generation detectors [36] [37].

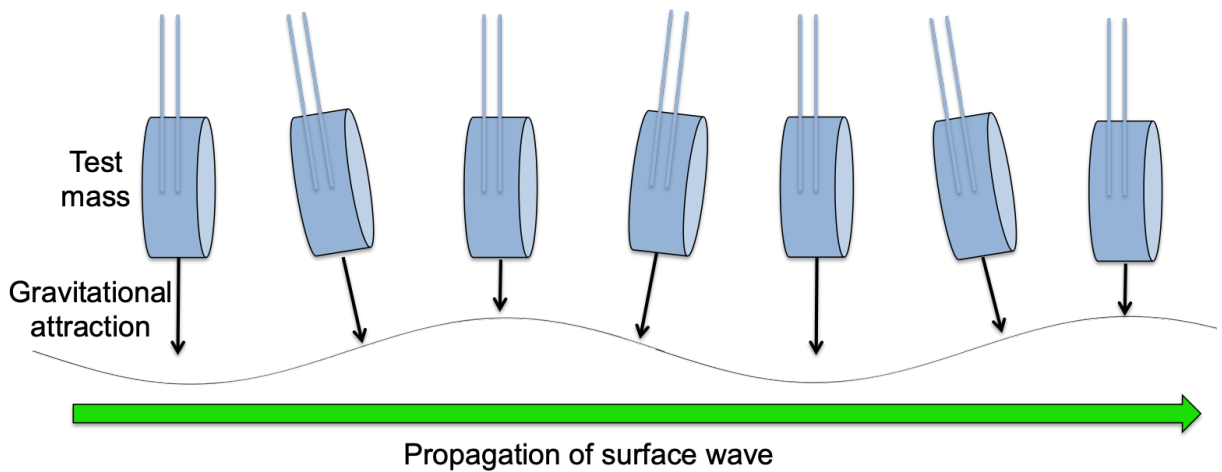


**Figure 1.22:** The effect a propagating surface wave has on a suspended test mass.

## 1.6.3 Seismic noise

Seismic noise is another noise source that is dominant in the low frequency region of current gravitational wave detectors. An example of the seismic noise spectrum at LLO is shown in figure 1.23 [78]. Seismic noise can arise through several different sources such as local weather, world wide earthquakes, local human activity both at the observatory and in the surrounding area. Earthquakes around the world can have a significant impact on the performance of the interferometer. An example of an earthquake approaching LHO is shown in figure 1.24. An earthquake anywhere around the world that measures 7 and above on the Richter scale will knock the interferometer out of lock and out of observing mode. The proximity of the interferometer to the epicentre of the earthquake can also affect the time it takes for the interferometer to

come back online and their resulting sensitivity. An example of this can be found from July 6th 2017 where a 5.8 magnitude earthquake occurred in Montana, USA, where the low frequency sensitivity was still being affected by the earthquake several weeks later [79].

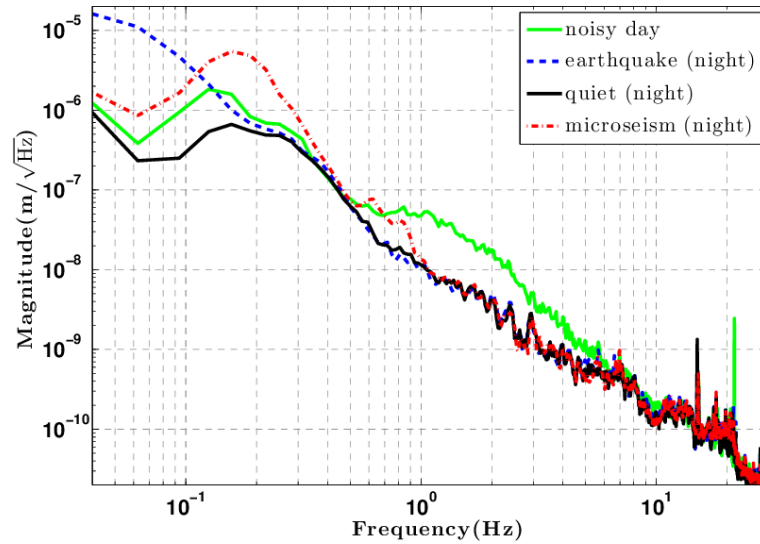


**Figure 1.23:** Seismic noise spectrum obtained for LLO under various scenarios [78].

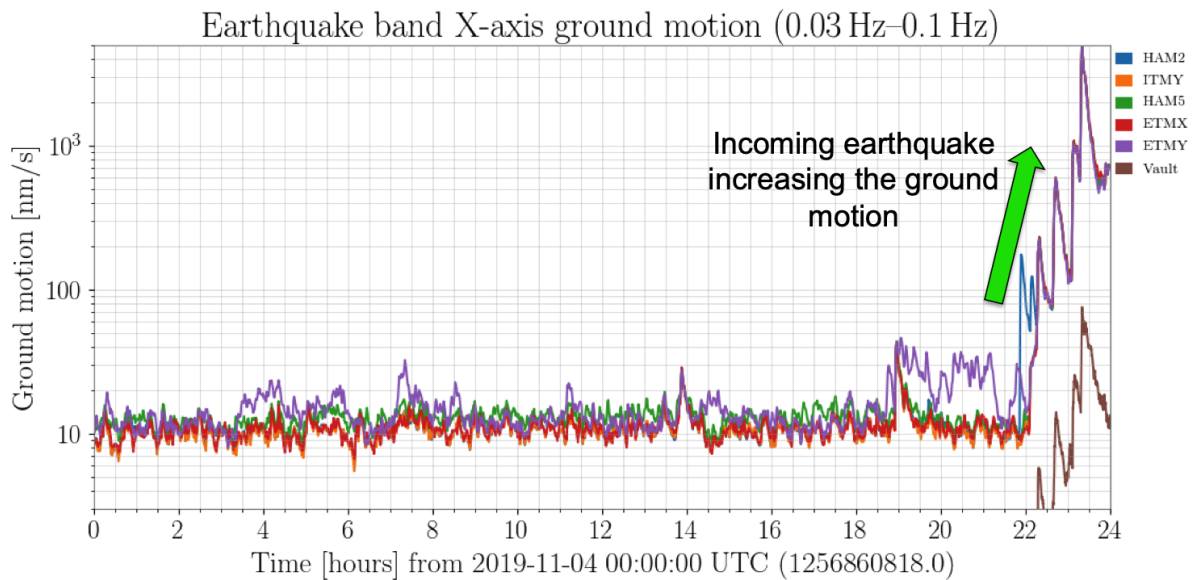


**Figure 1.24:** An incoming earthquake being picked up by the seismometers at LHO [69].

Human activity can also be a factor that has to be considered when the detectors are in observation mode. Figure 1.25 shows an example of the daily noise during a weekday at LHO. In this figure, several different artefacts can be picked up that are attributed to the human activity at LHO, which includes the morning rush hour of heavy goods vehicles, as well as the working hours where most people are on site.

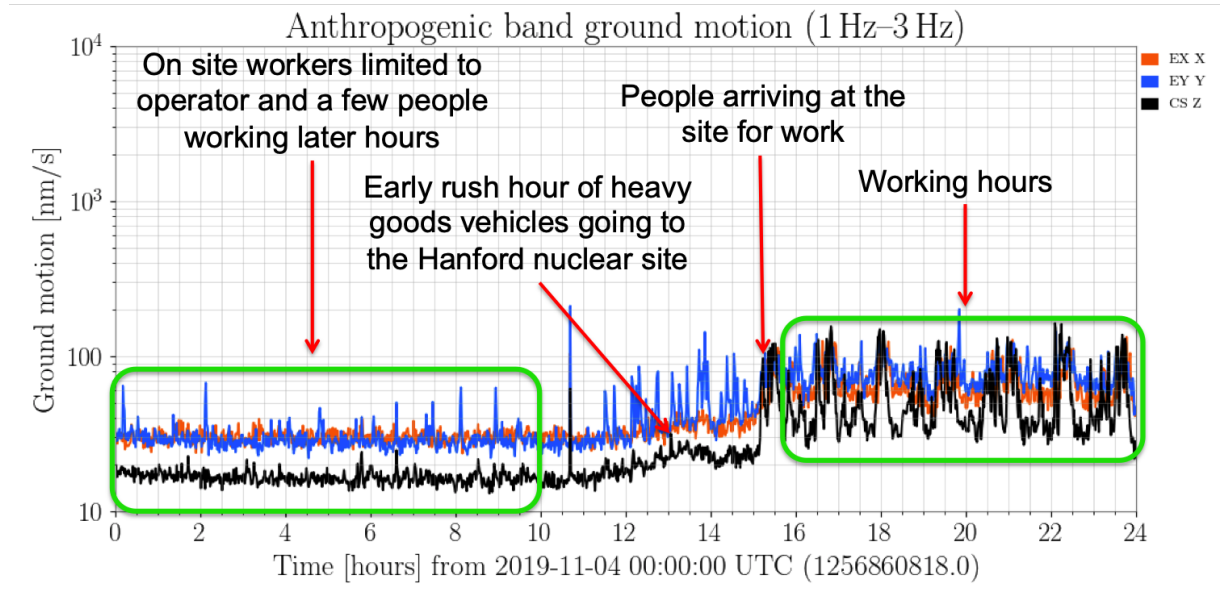


**Figure 1.25:** An example of the noise human activity has on seismometers at LHO [69].

To combat seismic noise in the interferometer, a multiple stage pendulum system had to be developed to satisfy the seismic noise performance required for the aLIGO and Virgo detectors [56] [24] [80]. A similar system is also installed at KAGRA [29]. As shown previously in figure 1.17, a multiple stage pendulum system was installed into the current generation of gravitational wave detectors to limit the horizontal and vertical motion of the test mass. The use of a pendulum system exploits the fact that the transfer function of a pendulum above resonance frequency follows  $\frac{1}{f^2}$  for the horizontal component. For a test mass with a mass of  $m$ , suspended on a spring with a spring constant,  $k$ , and damping constant,  $b$ , the transfer function between the ground motion,  $x_g$ , and the motion of the test mass,  $x_m$  is:

$$\frac{x_m}{x_g} = \frac{\omega_0^2}{\sqrt{(\omega_0^2 - \omega^2)^2 + \omega^2 \gamma^2}} \quad (1.9)$$

where  $\omega_0$  is the resonant angular frequency equal to  $\sqrt{\frac{k}{m}}$  and  $\gamma = \frac{b}{m}$  is a constant [68]. From equation 1.9, low frequencies show that  $\frac{x_m}{x_g} \approx 1$ . This means that the pendulum system would act as one system where the movement at the bottom of the spring will follow the movement at the top. However, for high frequencies,  $\frac{x_m}{x_g} \approx \frac{\omega_0^2}{\omega^2}$ . This means that very little motion is transferred to the test mass. This same principle applies for the vertical component of the cantilever blades. Active isolation is utilised in the form of the hydraulic external pre-isolator (HEPI) and the internal seismic isolation (ISI) system [81]. The HEPI isolates the chamber and is the first line of defence against the environmental noise using hydraulic actuators in combination with data from ground seismometers and position sensors. The ISI platforms utilise position and vibration sensors to damp out various environmental vibrations at local-specific tuned frequencies. The

active isolation reduces the noise down to approximately  $10^{-13}$  m. The combination of both the passive seismic isolation system, in combination with the active isolation system of the suspension chamber, allows for the sensitivity target of the seismic noise to be achieved.

### 1.6.4 Thermal noise

Thermal noise is a dominant noise source at  $\leq 100$  Hz and at a range of narrow band frequencies in the hundreds to kilo-hertz region as shown in figure 1.19, and is associated with the test mass suspensions installed in the detectors. This noise source is a result of statistical movement of atoms due to the thermal energy each atom has. This is known as Brownian motion [82]. Robert Brown observed pollen grains floating in water moving in random motions, which Einstein would later find was the result of the pollen grains interacting with the thermally driven water molecules [83]. As the pollen moved in the water, the pollen grains experienced a fluid resistance that dissipated the pollen's kinetic energy. A result of the statistical movement of atoms due to the thermal energy of each atom is the water molecules becoming thermally influenced. The random nature of the movement of the pollen was due to the number of collisions between the water molecules and the pollen. This is known as the Fluctuation-Dissipation theorem [84]. The Fluctuation-Dissipation theorem can be expressed as [85]:

$$S_f(\omega) = 4k_B T \Re[Z(\omega)] [N^2 Hz^{-1}] \quad (1.10)$$

where  $S_f(\omega)$  is the power spectral density of the thermal driving force,  $k_B$  is the Boltzmann constant,  $T$  is the temperature and  $\Re[Z(\omega)]$  is the real part of the mechanical impedance of the system, known as the dissipation where

$$Z = \frac{F}{v} \quad (1.11)$$

where  $F$  is the applied force and  $v$  is the velocity. Equation 1.10 can be re-arranged to include the admittance,  $Y$ , and to express the power spectral density for displacement:

$$S_x(\omega) = \frac{4k_B T}{\omega^2} \Re[Y] [m^2 Hz^{-1}] \quad (1.12)$$

For a low thermal noise performance, a material that shows a low dissipation behaviour, as well as high strength characteristics, was needed: fused silica.

One of the low thermal noise properties of fused silica is its thermoelastic loss performance. This occurs when there is a temperature gradient within the material when it is bending. An example of thermoelastic loss within the gravitational wave detector is within the fibres that suspend the test mass in the suspension system. Consider a fused silica fibre that is bending. This will induce a temperature gradient within the fibre that results in a heat flow between the compressed side and the stretched side. This gradient can be determined by the thermal

expansion coefficient,  $\alpha$ :

$$\alpha = \frac{1}{l} \frac{dl}{dT} \quad (1.13)$$

where  $l$  is the length of the fibre,  $dl$  is the change in length and  $dT$  is the change in temperature.

The thermoelastic loss,  $\phi_{thermoelastic}$ , is [86]:

$$\phi_{thermoelastic} = \frac{YT}{\rho C} \alpha^2 \left( \frac{\omega\tau}{1 + \omega^2\tau^2} \right) \quad (1.14)$$

where  $Y$  is the Young's modulus,  $T$  is the temperature,  $\rho$  is the density of the material,  $C$  is the specific heat capacity,  $\omega$  is the angular frequency and the characteristic time for heat to flow across the fibre,  $\tau$ , is:

$$\tau = \frac{\rho C d^2}{13.55k} \quad (1.15)$$

where  $d$  is the diameter of the fibre and  $k$  is the thermal conductivity.

Research has shown that the thermoelastic loss in a fibre can theoretically be nullified by applying a certain stress on the fibre due to the Young's modulus of fused silica increasing with temperature [87]. For a fused silica fibre, the thermoelastic loss is:

$$\phi_{fibre} = \frac{Y_0 T}{\rho C} \left( \alpha - \alpha_0 \frac{\beta}{Y_0} \right)^2 \left( \frac{\omega\tau}{1 + \omega^2\tau^2} \right) \quad (1.16)$$

where  $Y_0$  is the Young's modulus at room temperature,  $\alpha_0$  is the static stress on each fibre and  $\beta = \frac{1}{Y_0} \frac{dY}{dT}$ . From equation 1.16, should  $\alpha_0 = \frac{\alpha Y}{\beta}$ , the thermoelastic loss for a fibre is zero. This characteristic was exploited for the aLIGO monolithic stage to cancel the thermoelastic loss in the system. This was done by having an 800  $\mu\text{m}$  diameter region in the fibre which requires a stress of 195 MPa to be nullified, and is known as the thermoelastic nulling region. It however was not possible to have the entire fibre 800  $\mu\text{m}$  as this would have an effect on resonant modes that appear in the suspension system such as the bounce and violin modes.

As the test mass is suspended using a multiple stage pendulum isolation system, the majority of the energy in the test mass is in the form of gravitational potential energy [88]. For a test mass of mass,  $m$ , suspended on a single fibre, the force on the fibre is:

$$F = mg \quad (1.17)$$

where  $g$  is the acceleration due to gravity. Displacing the test mass horizontally will result in a restoring force attempting to bring the mass back to an equilibrium, with the bending region being located at the top of the fibre. Equating equation 1.17 with the restoring force,  $F_{restore} = kL$ , where  $L$  is the length of the fibre gives:

$$k_{grav} = \frac{mg}{L} \quad (1.18)$$

where  $k_{grav}$  is the spring constant equivalent in a gravitational field. The energy stored in the fibre is:

$$E_{stored\ in\ fibre} = \frac{1}{2}k_{fibre}x^2 \quad (1.19)$$

where  $k_{fibre}$  is the spring constant of the fibre and  $x$  is the horizontal displacement of the test mass. The fraction of loss in potential energy,  $\varepsilon$ , due to the internal friction at the top of the fibre when the test mass is displaced per cycle is:

$$E_{lost\ per\ cycle} = \varepsilon \frac{1}{2}k_{fibre}x^2 \quad (1.20)$$

The quality factor,  $Q$ , can be defined as:

$$Q = 2\pi \frac{E_{stored\ in\ fibre}}{E_{lost\ per\ cycle}} = \frac{1}{\phi_{fibre\ loss}} \quad (1.21)$$

and can be rearranged to give the loss in the fibre,  $\phi_{fibre\ loss}$ :

$$\phi_{fibre\ loss} = \frac{\varepsilon}{2\pi} \quad (1.22)$$

The total potential energy stored in the pendulum is:

$$E_{stored\ in\ pendulum} = \frac{1}{2}(k_{fibre} + k_{grav})x^2 \quad (1.23)$$

where  $k_{grav}$  is the effective spring constant associated with the gravitational field. Therefore:

$$\phi_{pendulum\ loss} = \frac{\varepsilon k_{fibre}}{2\pi(k_{fibre} + k_{grav})} \quad (1.24)$$

The ratio of losses between that of the fibre and the pendulum is therefore:

$$\frac{\phi_{pendulum\ loss}}{\phi_{fibre\ loss}} = \frac{k_{fibre}}{k_{fibre} + k_{grav}} \quad (1.25)$$

Since  $k_{grav} \gg k_{fibre}$ ,

$$\phi_{pendulum\ loss} = \phi_{fibre\ loss} \frac{k_{fibre}}{k_{grav}} \quad (1.26)$$

The dilution factor,  $D$ , which is the factor that the mechanical loss in the pendulum is reduced over the mechanical loss in the fibre is therefore:

$$\frac{1}{D} = \frac{k_{fibre}}{k_{grav}} \quad (1.27)$$

For aLIGO, the dilution is approximately 91 [58].

As the monolithic stage of the suspension is all made out of fused silica, which as previously

stated has a low mechanical loss value, the concentration of energy in the system is at the resonant modes. This means away from the resonant modes, the thermal noise is decreased. This can be seen in figure 1.26.

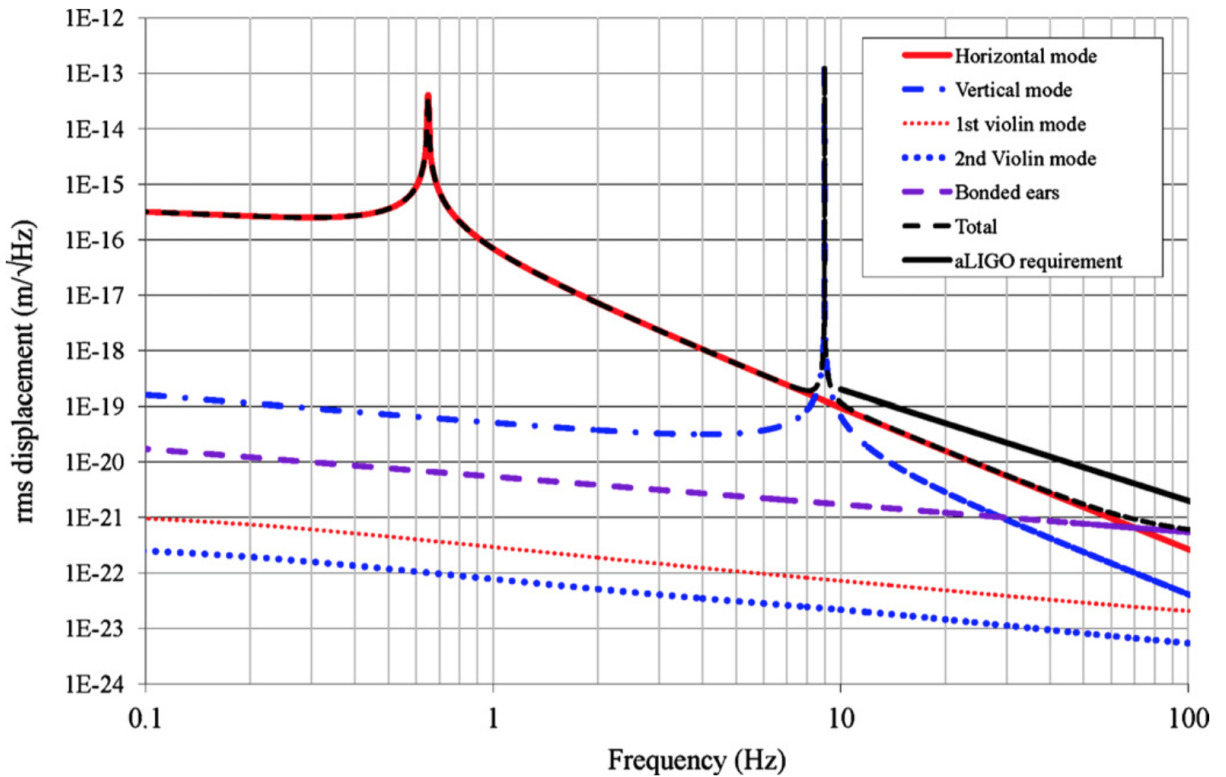


**Figure 1.26:** The horizontal and vertical modes of an aLIGO suspension. It can be seen that the bulk of the noise occurs at the resonant frequency as a sharp spike [57].

Examples of resonant modes in the aLIGO suspension systems are the pendulum, bounce and violin modes. The quadruple pendulum has 24 pendulum modes, 22 of which range between 0.4-5 Hz and are damped out by damping the top mass [89]. This arises from the movement of the test mass incident to the laser in the cavity. This results in a change in the laser path length which affects the output of the interferometer. This can be moved to a lower frequency through the use of longer and thinner fibres. The other two modes are the bounce and roll modes. The bounce mode occurs at approximately  $\leq 10$  Hz and the roll mode at approximately 18 Hz [89] [6]. As previously mentioned, the thermoelastic nulling region of the fibre is 800  $\mu\text{m}$  in diameter. If this length was carried out throughout the entire length of the fibre, the bounce mode would occur at approximately 18 Hz [58]. It is possible however to move this mode further down in frequency through the use of thinner fibres to increase the applied stress. For example, the A+ upgrade proposal of using 300  $\mu\text{m}$  fibres to suspend the test mass will move the bounce mode from 10 Hz to approximately 7 Hz [90]. Violin modes are also determined by the stress that is applied to the fibre, but occur at multiple harmonic frequencies. The first violin mode occurs at approximately 500 Hz, and the second at approximately 1000 Hz [56]. Similar to the

18 Hz bounce mode scenario, with a fibre diameter of 800  $\mu\text{m}$  along the entire length, the violin modes would occur at approximately 250 Hz [58]. The A+ upgrade however would increase the frequency of the violin modes with the first fundamental mode occurring at approximately 750 Hz [90]. Due to the fact that fused silica is an ultra low loss material, any excitation of the violin modes will result in an extremely long ring down time, of the order of days. An active damping system is therefore needed to reduce this ring down time as the excitation of this mode can affect the detector sensitivity greatly [91].

Thermal noise is one of the most critical noise sources that limits the sensitivity of the second generation detectors. Extensive research and development had gone into lowering this, and the previously mentioned noise sources, to lower them to the point where gravitational waves could finally be detected. Even though gravitational waves have been detected, the aim is to always make the detectors even more sensitive to allow for a greater rate of detections, as well as from sources yet to be found. For the next generation of gravitational wave detectors, upgrades such as going underground, into space, cryogenic detectors and longer baselines will hopefully achieve these goals.

## 1.7 Thesis outline

The content of this thesis will focus on various aspects of fused silica fibres that are used in aLIGO suspensions, as well as for fibres used for other gravitational wave related research associated with the University of Glasgow and the Albert Einstein Institute in Hannover, Germany. Chapter 2 will focus on the alignment process of the aLIGO fibre pulling machine to detail how the pulling machine should be aligned to maximise the efficiency of fibre production. This will apply to both pulling machines that are at Glasgow and LHO. Chapter 3 will present an investigation into angular misalignments that can be introduced into the fused silica fibres during the production process. This chapter will detail methods that will result in angular misalignments and how to mitigate this, as well as investigating what effect these misalignments have on the ultimate strength of the fibres. Chapter 4 continues the research of aLIGO fibres by investigating what is known as stress fatigue in aLIGO fibres. This research was carried out in parallel with a fellow PhD student at the time of the investigation, Dr Lee, with both sets of data accompanying each other [92]. Chapter 5 moves on from aLIGO fibres to discuss ultra-thin diameter fibres that are related to the Sagnac speedmeter and 10 m prototype investigations that are currently being carried out at Glasgow and Hannover, respectively. This chapter presents the development of a dedicated fibre profiler for these fibres, as well as upgrades to the fibre strength tester. Chapter 6 carries on the investigation of stress fatigue, but with ultra-thin fibres to accompany the data obtained in chapter 4. Chapter 7 presents an investigation into the Young's modulus of ultra-thin fibres, which is a follow up investigation to research previously carried out [93], but with the new equipment that was presented in chapter 5.

# Chapter 2

## Alignment of the aLIGO fibre pulling machine.

### 2.1 Introduction

The production of fused silica fibres for aLIGO suspensions has been well established for more than a decade [62] [56]. A bespoke fused silica fibre pulling machine was designed and developed at the University of Glasgow and has been replicated at Virgo to produce fibres for the Virgo detector and at LHO to produce all the fibres used at both the LIGO Hanford Observatory (LHO) and LIGO Livingston Observatory (LLO) [62].

During this PhD, time was spent by the author at LHO on two separate occasions during the commissioning period between aLIGO's second and third observing run specifically to produce fused silica fibres for the monolithic fused silica suspensions [56] for both LHO and LLO. During this time the author also assisted with the installation of fibres to one of the monolithic suspensions at LHO, shown in figure 2.1. In order to produce fused silica fibres for these suspensions, the fibre pulling machine had to be properly aligned prior to any production to ensure the fibres that were produced fall within the manufacturing tolerances. Such requirements include the ability to produce fibres with a diameter tolerance of  $400\pm 20\ \mu\text{m}$  in the thin middle section,  $800\pm 80\ \mu\text{m}$  in the thermoelastic nulling region, polishing the fused silica stock without vapourising too much material (less than  $100\ \mu\text{m}$  of stock material) and no mechanical induced offset in the stock when heating is applied. Further details of these tolerances will be discussed in further detail in chapter 3.

At the time of these two visits to LHO and as of writing this thesis, there is no dedicated document detailing a procedure to correctly align the pulling machine. This can lead to an inconsistent alignment procedure depending on the user. This chapter will serve as a detailed procedure that should be followed to ensure consistent alignment of the pulling machine. The procedure that is detailed out in this chapter was used extensively during these two visits as well as in the research that was carried out in chapters 3 and 4.

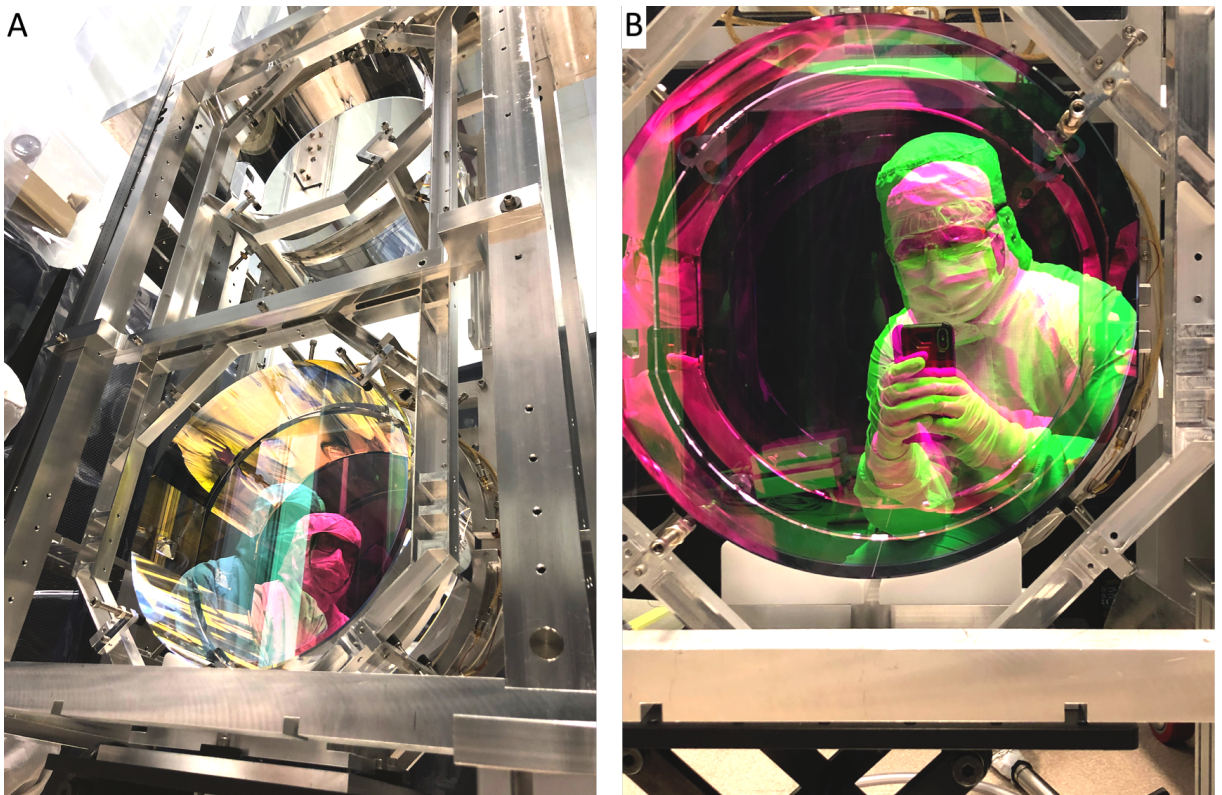


**Figure 2.1:** A: The monolithic fused silica suspension at LHO that had fibres installed during one of the two fibre pulling visits by the author. B: The coated front face of the fused silica test mass.

## 2.2 Pulling machine layout

The pulling machine, shown in figures 2.2 and 2.3, utilises a  $10.64\ \mu\text{m}$   $\text{CO}_2$  laser to heat up a rod of fused silica held securely in place via clamps. Using a  $\text{CO}_2$  laser allows for accurate control over the distribution and delivery of the heat to the fused silica. A  $45^\circ$  mirror rotating at approximately 60 Hz spreads the beam around a conical mirror. This creates a cylindrical beam as it is reflected up towards the second conical mirror, known as the feed mirror. This is illustrated in figure 2.4. The laser is focused onto the rod, also known as the stock, from the feed mirror. A fibre is then drawn out from the molten region by moving the top stage, known as the pulling stage, via a custom built LabVIEW program [62] that reads in motor voltage values to send to the motors controlling the stages. To ensure there is always material available to draw the fibre from, the feed mirror is also on a motorised stage and runs slowly down the stock during the pull to melt fresh material.

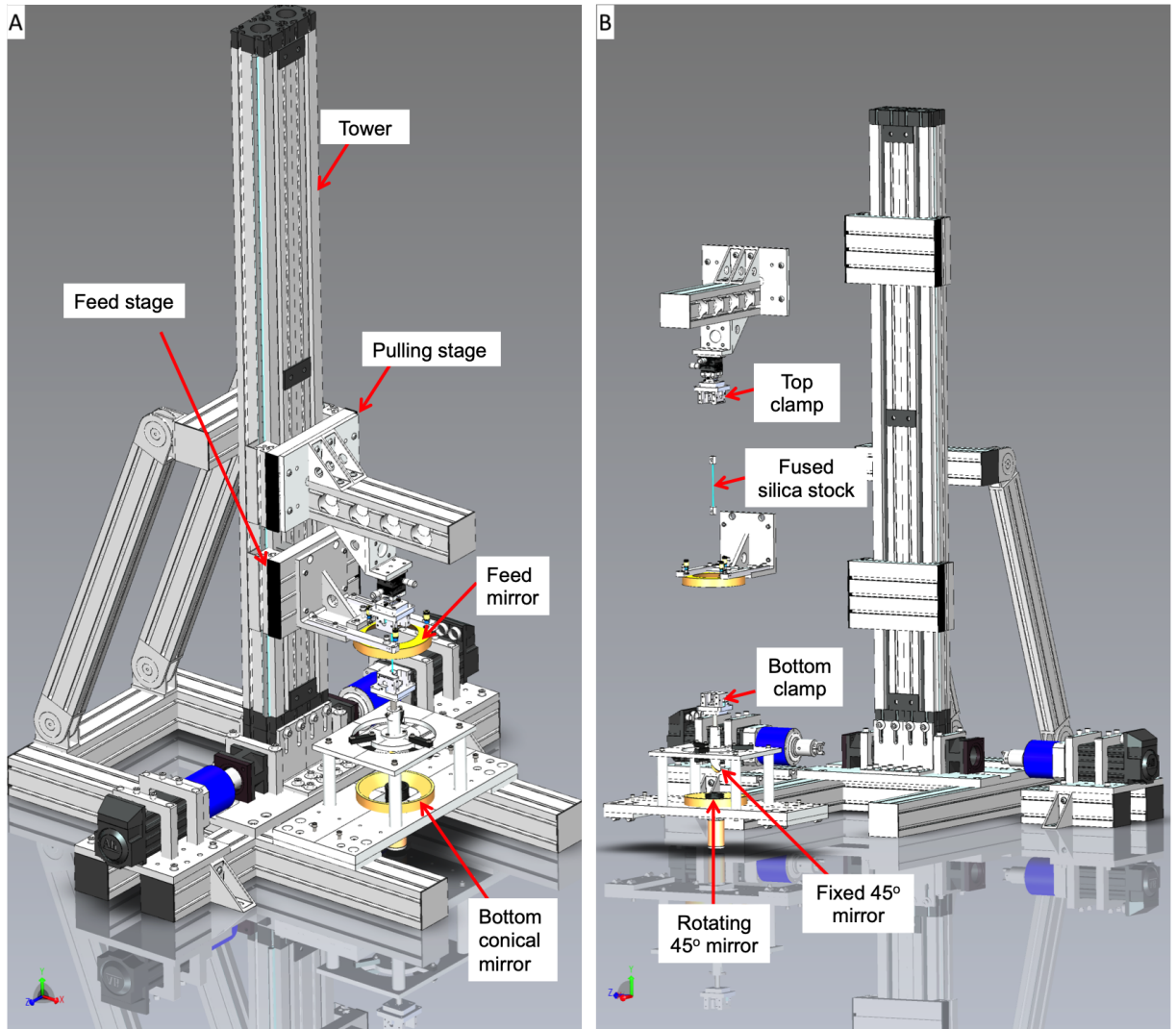


**Figure 2.2:** Solidworks rendering of the fibre pulling machine [94]. A: The full pulling machine assembly, and B: exploded view of the pulling machine to clarify labeled components.

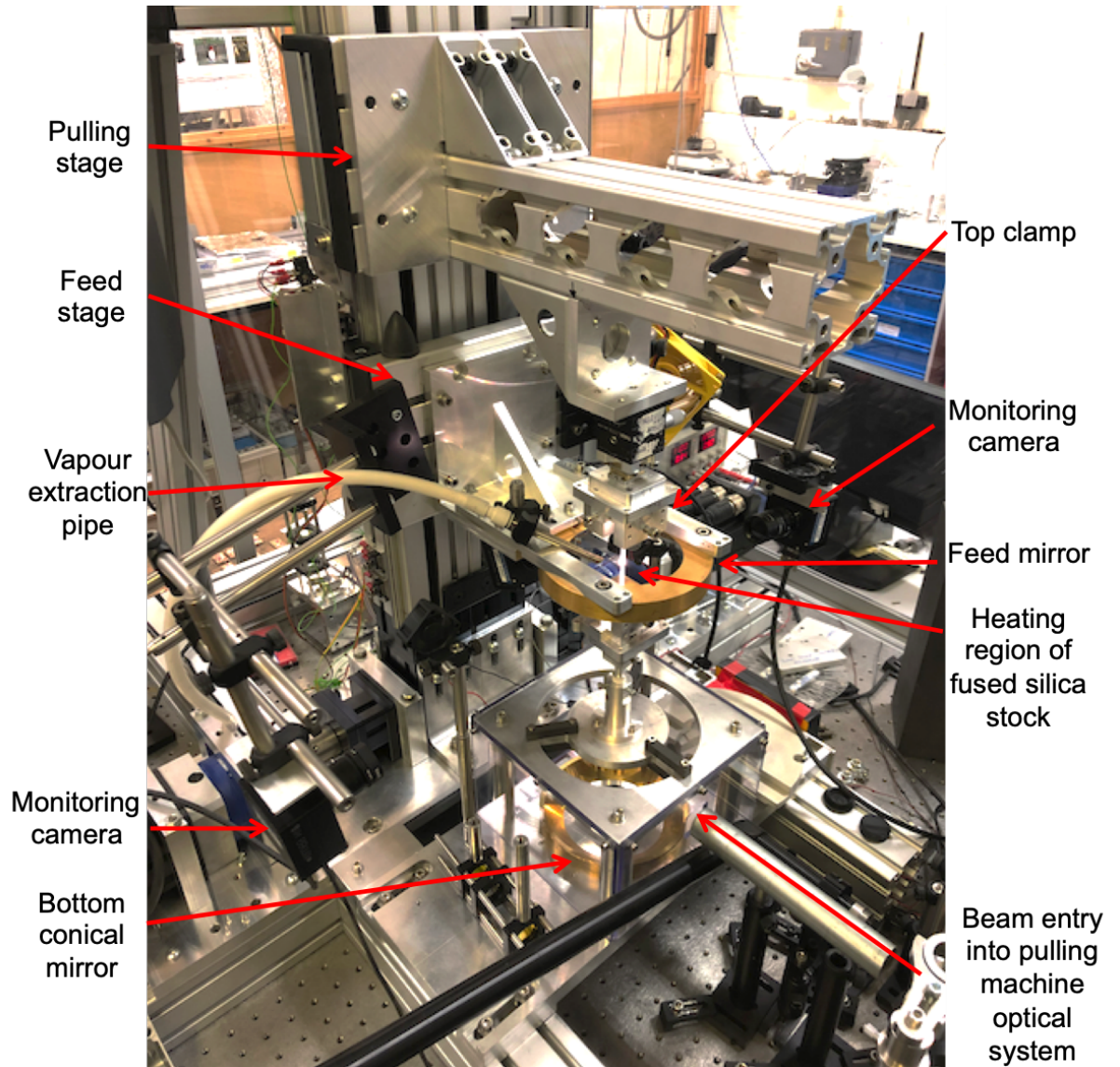


**Figure 2.3:** The current state of the fibre pulling machine at the University of Glasgow as of writing this thesis.

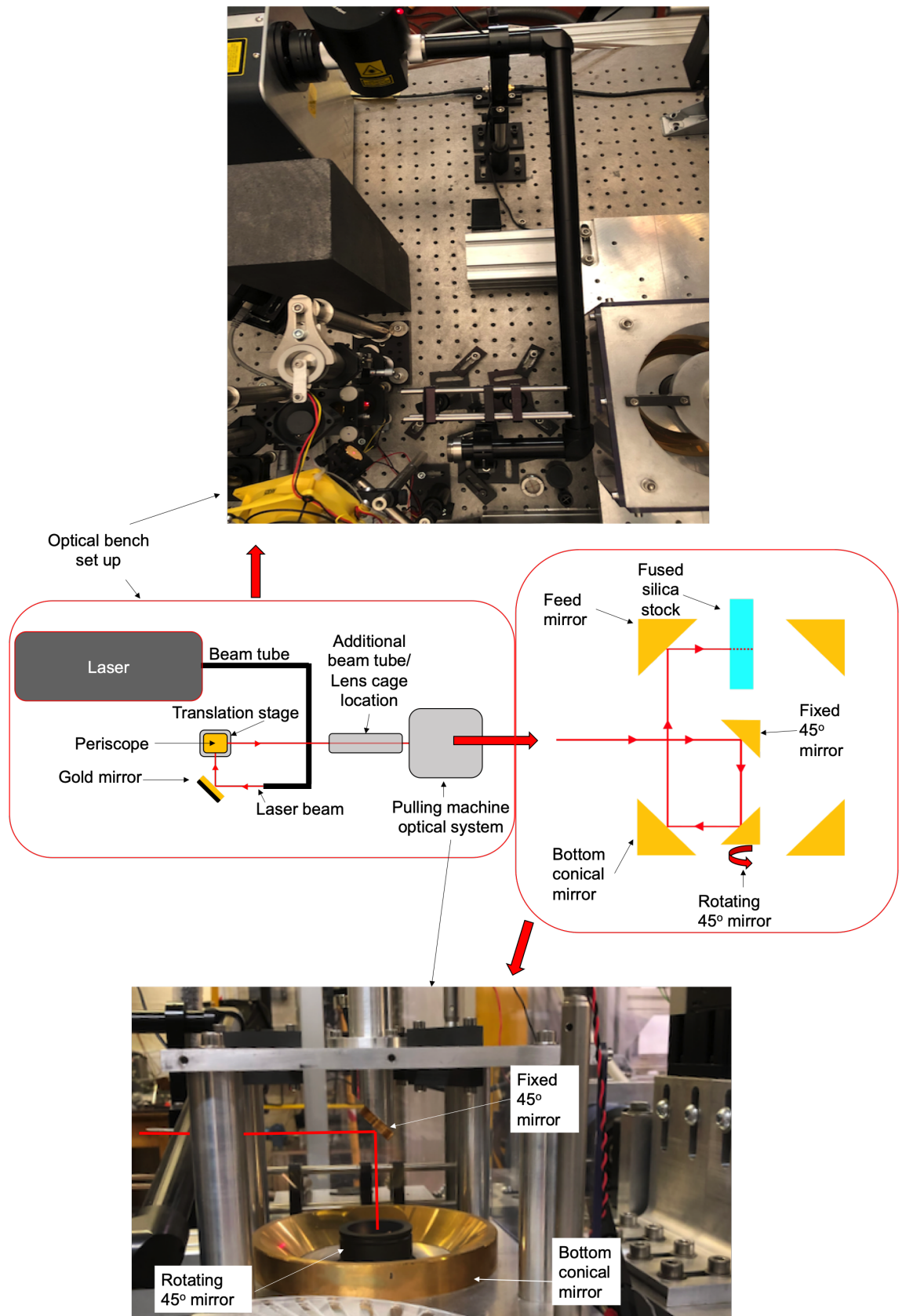


**Figure 2.4:** Illustration of the beam path for the pulling machine at Glasgow with a side-view cross section of the optical path within the optical system of the pulling machine.

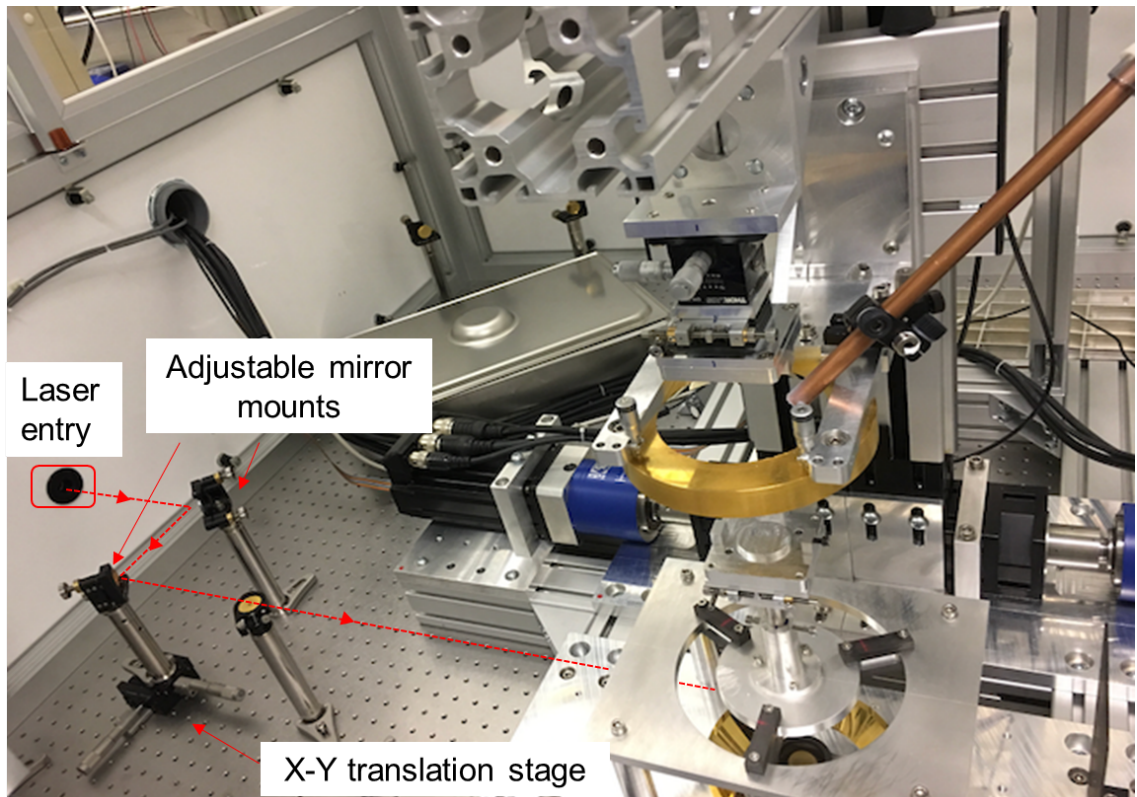


**Figure 2.5:** The beam path and optical set up on the pulling machine at LHO. Note there is no periscope in the beam path compared to the Glasgow pulling machine in figure 2.4.

Previous research [95] has shown that fused silica fibres can be strengthened through a technique called laser polishing. This is a process that has now become the standard procedure for any fused silica fibres that are to either be installed to an aLIGO monolithic suspension, or for any strength test investigations. This process involves heating the fused silica stock with the laser to the point where it is molten (approximately  $2000^{\circ}\text{C}$ , and then slowly moving the feed mirror down the fused silica stock, at approximately  $0.0275\text{ mm s}^{-1}$ . The feed mirror travels for a distance set by the user, before traveling back up to the start position at the same velocity. Moving the feed mirror down and back up the fused silica stock at a slow velocity ensures that at every point between the start and finish positions, the stock has been molten. This removes artefacts such as surface cracks that may have been present in the fused silica stock that could potentially have an impact on the ultimate strength of that fibre. Figure 2.6 shows a photo of a rod of fused silica during the polishing procedure. It is clear from this image to see the part of the stock material that has been polished as there are no surface artefacts and is transparent. Any surface dirt is removed by a three stage wipe down of the stock prior to polishing. This wipe down procedure consists of using Anticon Gold Wipes [96] to clean the stock with methanol, then with acetone and then with methanol a second time [97].

It is therefore essential to ensure the pulling machine is well aligned so that the laser during the polishing and pulling process is equally distributed along the stock material. Failure to do so

could result in the beam being concentrated in areas for prolonged periods of time, vapourising stock.

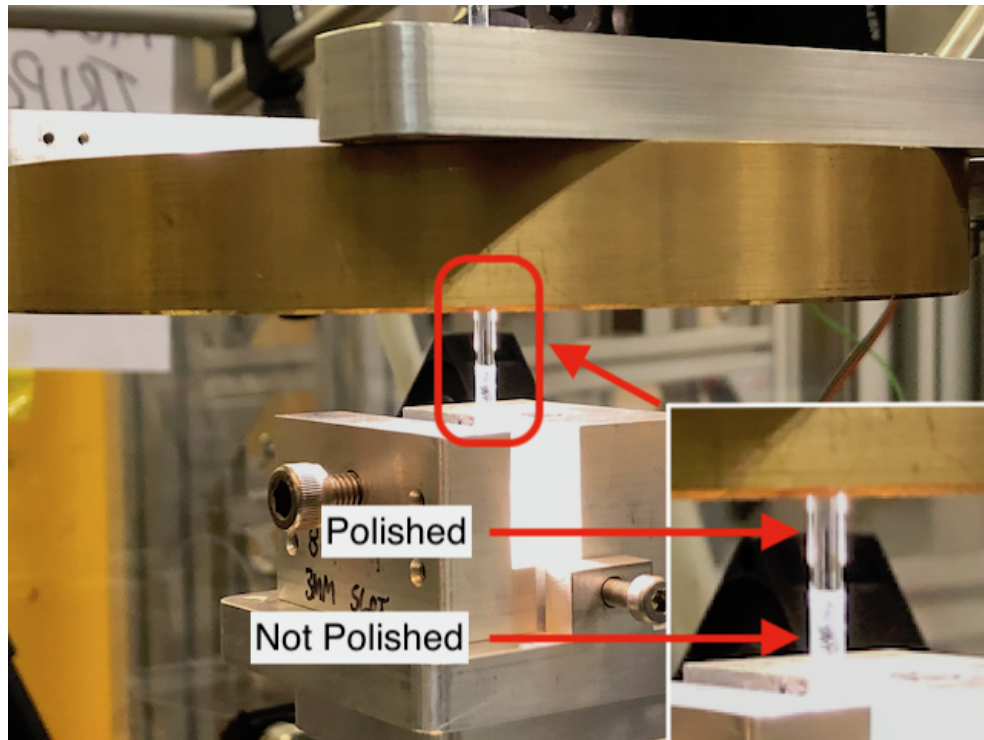


**Figure 2.6:** Rod of fused silica undergoing laser polishing. The difference between the unpolished and polished stock material can be clearly seen in the insert in the bottom right where the unpolished region is visibly more opaque than the clear polished region.

In the following sections, the alignment of the pulling machine will be discussed in the order the procedure should be carried out. The following procedure is written with the assumption that the pulling machine has been previously assembled according to the documented specifications [94].

The alignment procedure has two main stages:

- Mechanical alignment of the pulling machine core components
- Alignment of the laser beam

It is important that the alignment procedure is carried out in this order. Reversing the order of alignment by aligning the laser first prior to mechanical alignment can result in further misalignment of the pulling machine. This would result in compensating for a mechanical misalignment with a misalignment of the laser distribution. While this can be a quick fix for a short term pulling demonstration environment, this is not an ideal situation for batch production of fibres for aLIGO suspensions or any proper investigation and can lead to material being wasted on imperfect fibres.

It should be noted that the mechanical alignment of the core components, such as the tower baseplate and conical mirror holders, should only need to be set once and never touched again. Components associated to the laser beam alignment, such as mirror mount knobs and posts, will however need frequent checks during usage. Checks on the core mechanical components should still be carried out prior to the production of fibres that will be used in a monolithic suspension. The rest of this chapter will describe in detail the procedure to aligning all of the above components.

## 2.3 Pulling machine mechanical alignment

### 2.3.1 Bench, tower and baseplate

A first check to be made is to ensure that the bench the pulling machine is sitting on is level to the floor. This ensures that the natural user assumption of using the optical bench as a reference point, is valid. Adjustments to the bench legs should be made following the manufacturer's manual [98]. All alignment checks from this point assume a level bench that is perpendicular to local gravity.

The tower can be checked with spirit levels to ensure that it is perpendicular to the bench. This is essential as a tower that is not perpendicular to the bench will not pull fibres along an axis that is perpendicular to the bench. This could lead to misalignment artefacts as both the feed and pulling stages move along the tower off the central axis of the stock material. Adjustments can be made to the back arms that hold the tower in place, shown in figure 2.7. How well the tower is aligned can be judged through the use of the previously mentioned spirit levels with tools such as a set square.

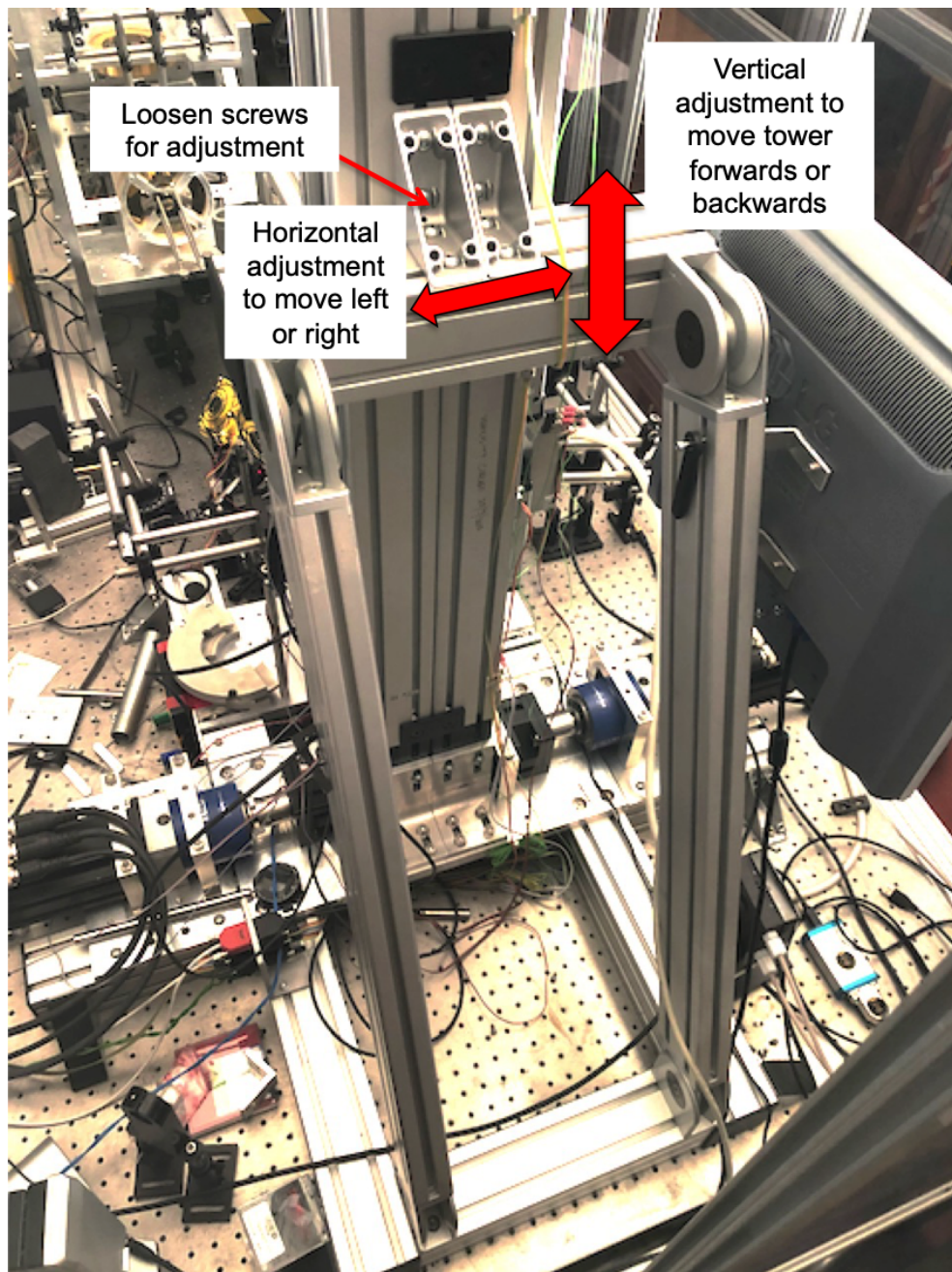


**Figure 2.7:** Arm connector for the tower.

A feature that was installed in the Glasgow machine and later installed at LHO during this PhD were reference plates for the base of the pulling machine. A reference plate in this case is a block of aluminium that has been manufactured to have a width and length with a tight tolerance. It is designed to sit in the space in between the baseplate and the tower baseplate shown in figure 2.8. When installed against the tower baseplate, the baseplate can then be positioned against this reference plate to ensure that the distance between the baseplate and the tower baseplate was of a known absolute distance. Prior to their installation, the LHO conical mirror baseplate did not have any marked reference points on the Bosch frame that the baseplate was sitting on to check this. An inspection of the position of the opposite edges from the base plate to the back plate

showed that the baseplate was offset by a few millimetres, also shown in figure 2.8.

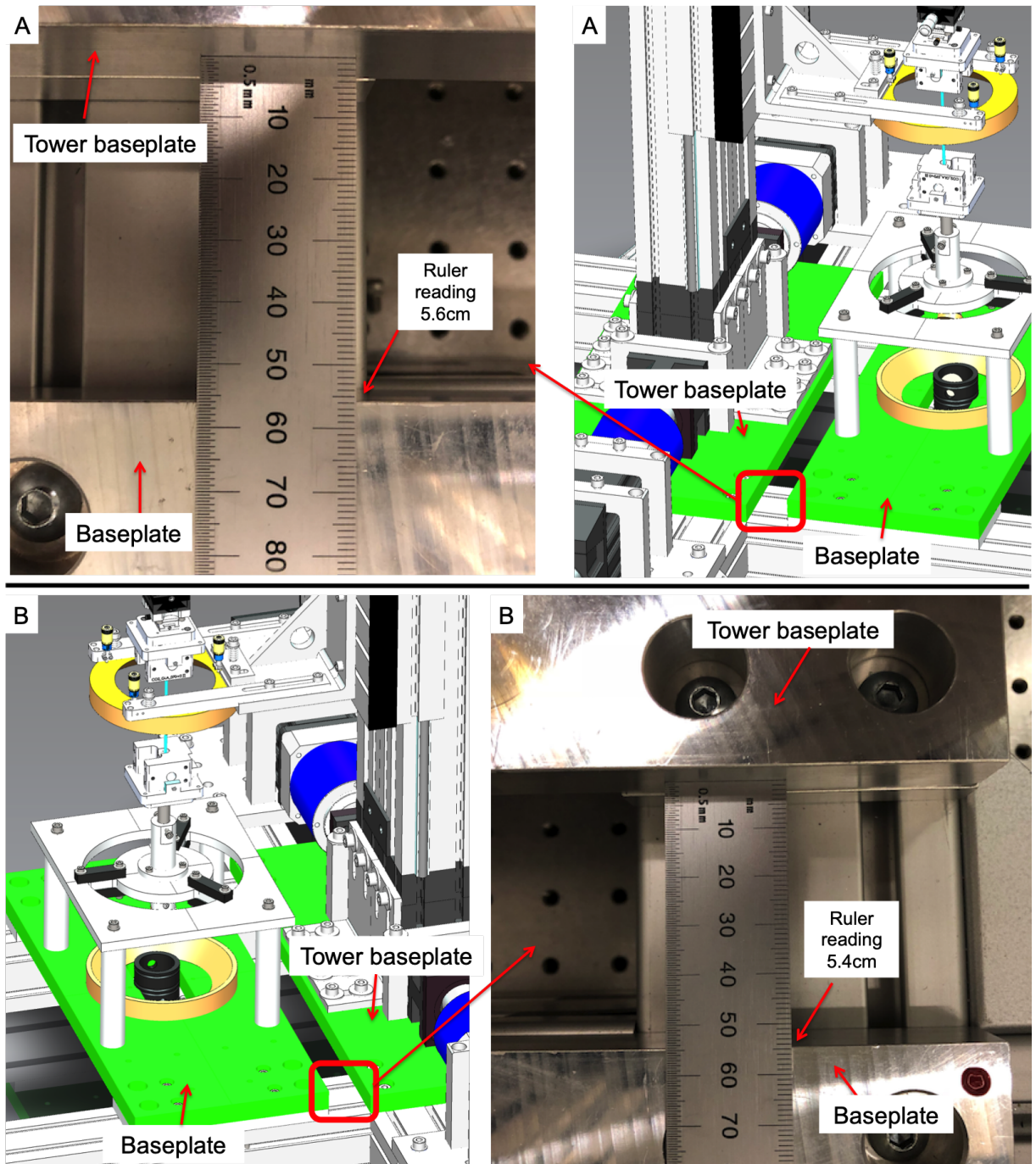


**Figure 2.8:** Offset of the baseplate to the tower baseplate. A: Offset of left side. B: Offset of right side.

Previous research [93] [99] has shown that the position of the conical mirrors of a fibre pulling machine is critical to ensuring uniform heating distribution of the laser beam. In the aLIGO pulling machine, the bottom conical mirror is in a fixed position on the baseplate. The fixed position is such that the rotating  $45^\circ$  mirror is in the centre of this mirror. Also concentric to this mirror are the post and post holder of the bottom clamp.

In total, three reference plates were installed to the pulling machine to ensure the baseplate was sitting in the correct position. This included two plates to reference against the tower of the pulling machine [100], shown in figure 2.9 and one side plate [101] to ensure the base plate was sitting flush to the edge of the frame. This means that the bottom conical mirror, and therefore the fixed and rotating  $45^\circ$  mirrors, were sitting in their ideal positions, and could then be referenced to carry out the next steps in the alignment. This will be discussed in the following subsection.

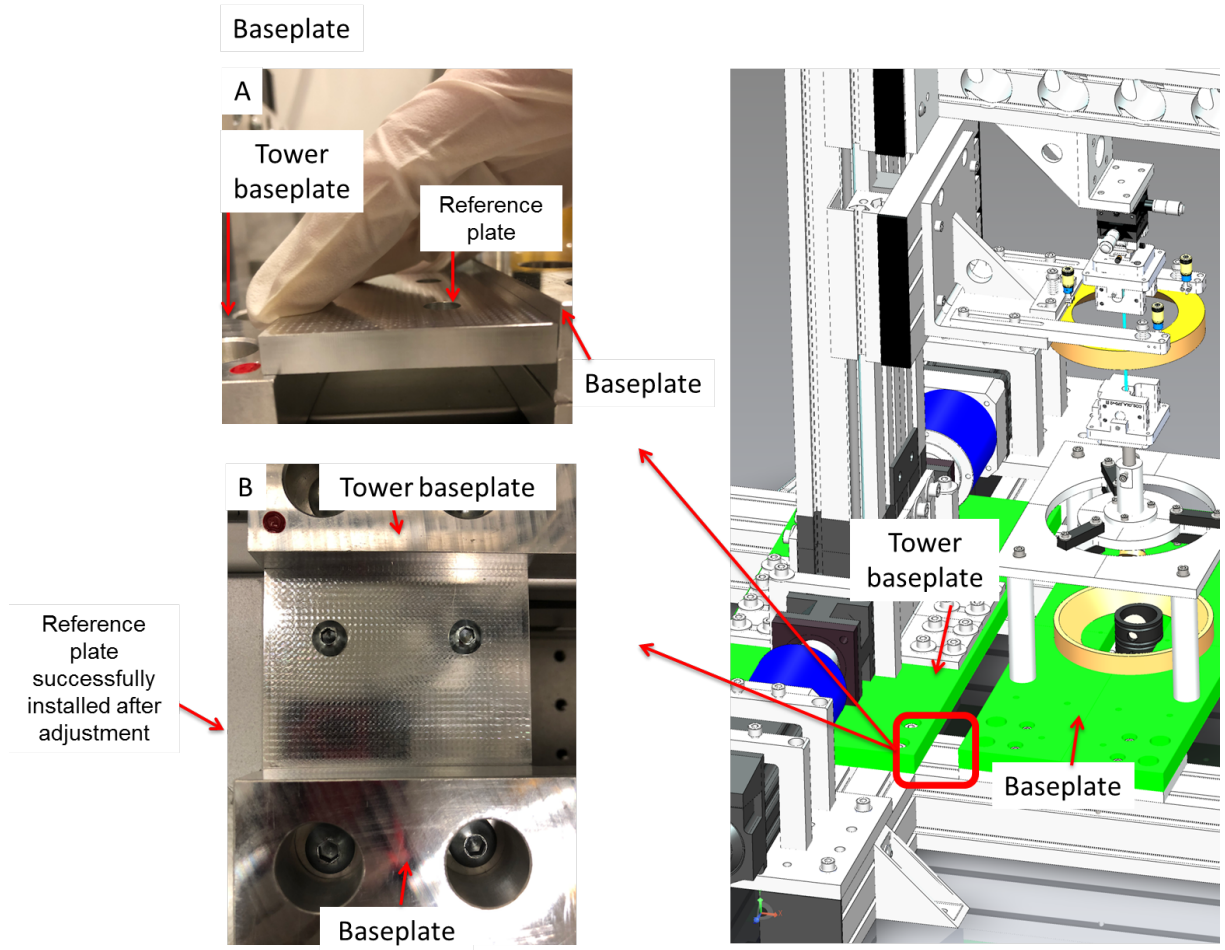


**Figure 2.9:** Installation of the reference plate to align baseplate to the tower baseplate. A: Reference plate prior to installation. B: Reference plate after installation.

### 2.3.2 Conical mirrors

In an ideal scenario, the feed mirror would be able to run down the tower until it is just in contact with the bottom conical mirror to check that both mirrors are concentric. Due to the design of the pulling machine, this is not possible due to the frame that is holding the bottom post holder. The feed mirror instead should be run down to the top of the bottom post holding plate without making contact with the plate.

Two checks should be carried out at this stage. Firstly, to check the attachment plate, shown

in figure 2.10 of the feed mirror to the feed stage on the tower is level to the motor stage on the tower. This is then followed by checking the feed mirror holder and the feed mirror itself. Any offset at this point would suggest two potential scenarios:

- The feed mirror face is not flush to the face of the holder.
- The feed mirror holder is not flush to its attachment plate.

Previous experience had shown material between the contact faces of the holder and mirror which resulted in the feed mirror failing to sit flush to its holder and therefore this should be checked. This material can be anything from a bit of dirt, which can then be wiped away with methanol, to leftover material during manufacturing of the aluminium parts. This can be resolved by filing away the leftover material until the drilled hole is flush with the rest of the face. Ensure this is carried out in an appropriate environment and not in the clean lab. Checks to all screws should also be carried out to ensure no movement occurs to the mirror or mirror holders when a small amount of force is applied by hand.

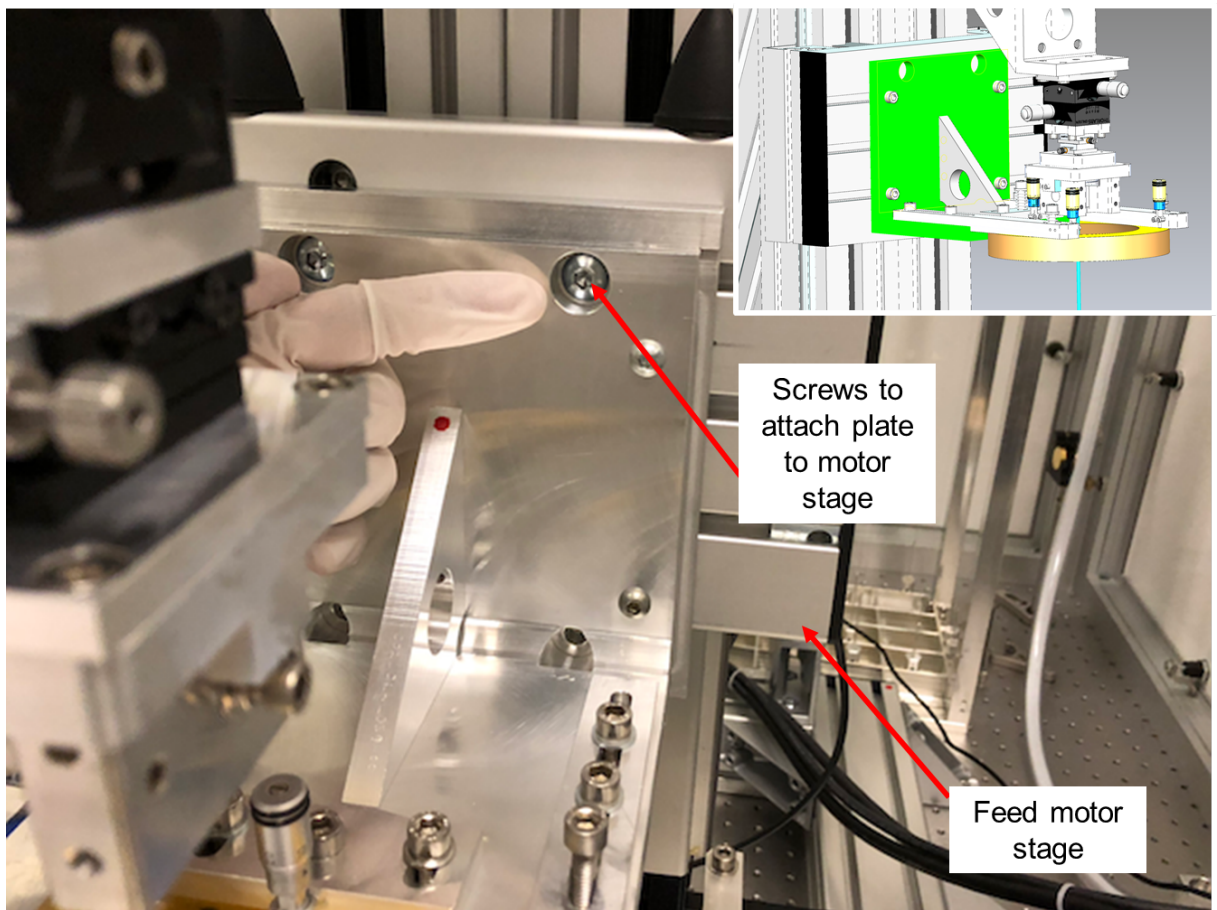


**Figure 2.10:** The back plate that connects the feed mirror holder to the feed mirror stage on the tower. The finger in the image is pointing to one of the screws that attach the plate to the tower that should be checked for tightness. Inset shows SolidWorks rendering with attachment plate highlighted in green.

A plastic alignment reference tool [102] can then be installed flush around the bottom post. This tool has the outer circumference of the conical mirror grooved onto the surface. The feed mirror can then be aligned up to the circular alignment grooves on the tool by loosening the screws on the feed mirror holder and sliding the holder until aligned. The alignment of the feed mirror to the alignment plate grooves can be done by eye as long as the mirror is inspected from all angles.

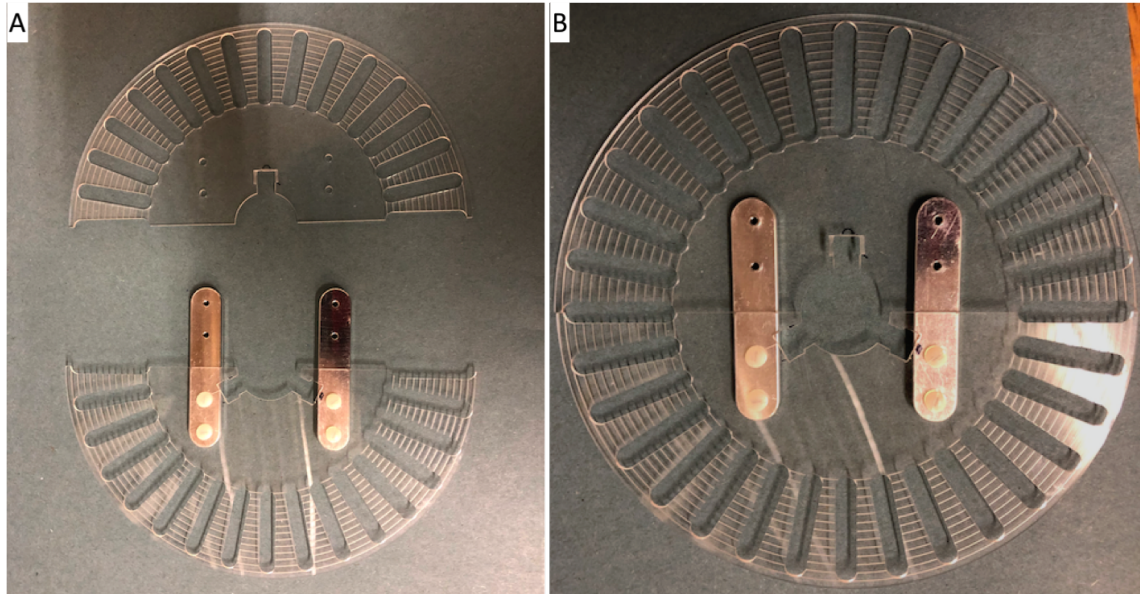


**Figure 2.11:** Disassembled (A) and assembled (B) conical mirror plastic alignment tool.

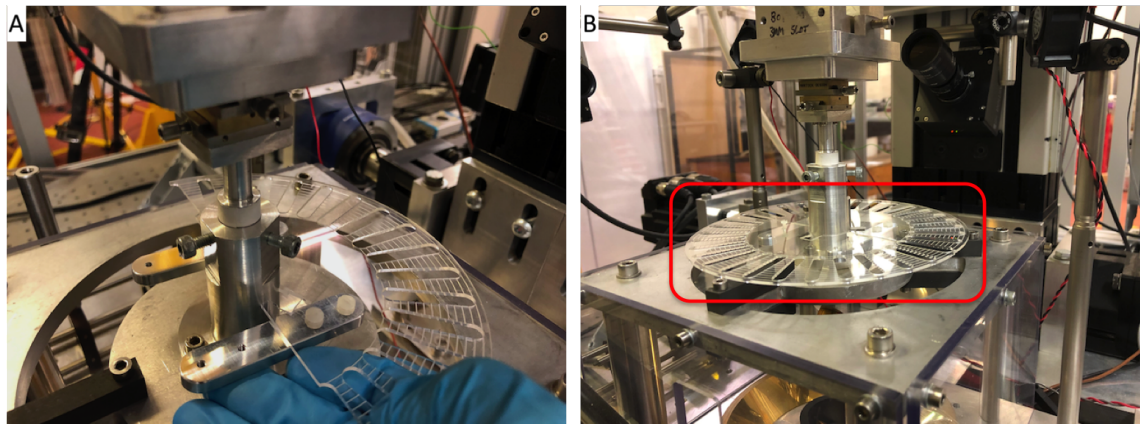


**Figure 2.12:** Installation of the conical mirror plastic alignment tool (A) and an installed alignment tool highlighted in the red box (B).

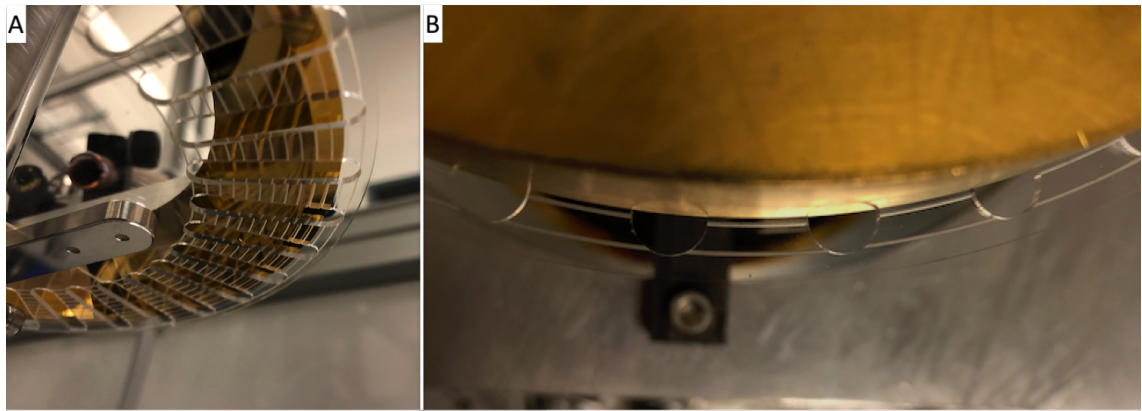


**Figure 2.13:** The groove on the plastic alignment tool to align the feed mirror. A: underside of feed mirror. B: Topside of feed mirror.

The feed mirror should then run back up to its start position followed by a final spirit level check. There should be no change in how level the feed mirror is sitting during this positional change and serves as a "double check". If there is a significant change between the two points, this would suggest that the feed mirror is not travelling along the central axis of the conical mirror. This could indicate another issue such as the tower was not properly aligned and not set perpendicular to the bench. This would have to be revisited and the previous processes repeated once fixed.

### 2.3.3 Top and bottom basic clamps

An offset between the top and bottom clamps where the fused silica stock sits is obvious to spot. Should there be an offset, the moment the fused silica stock becomes molten, the stock will move in a horizontal direction. This is due to the force that is being applied on the stock due to the offset. An example of this is shown in figure 2.14.

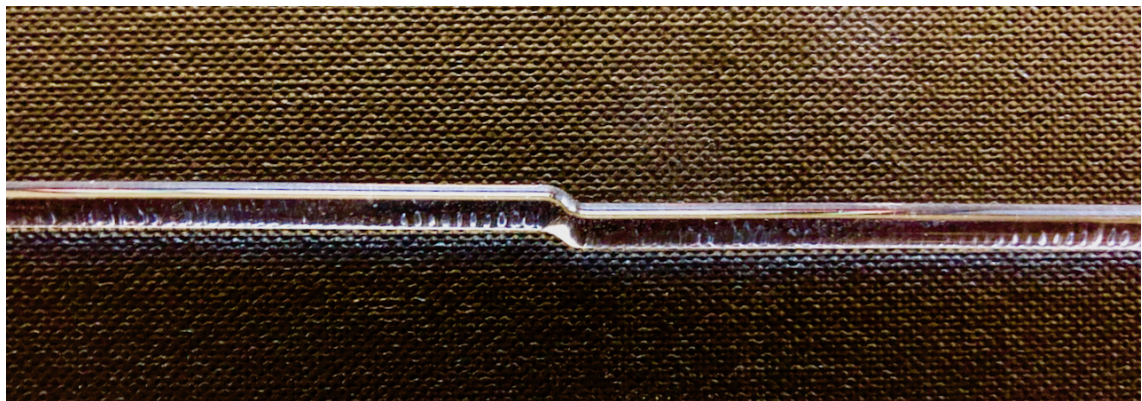


**Figure 2.14:** Horizontal offset of a piece of fused silica stock.

If there has been a significant period since the last alignment of the pulling machine, or is the first alignment prior to a batch of production fibres, it is recommended to use the basic clamps

for this procedure. An example of basic clamps is shown in figure 2.15. The second type of clamp, known as fuse clamps, will be discussed in the following subsection. The bottom clamp should be aligned first to ensure that the stock is held concentric to the conical mirrors. Firstly, the post that the bottom clamp holder is attached to, shown in figure 2.16, should be checked to ensure it is at the right height and position. This can be carried out by adjusting the post within the holder and tightening the screws to secure it in place. Markers can be marked on both the post and the holder for future reference if desired.

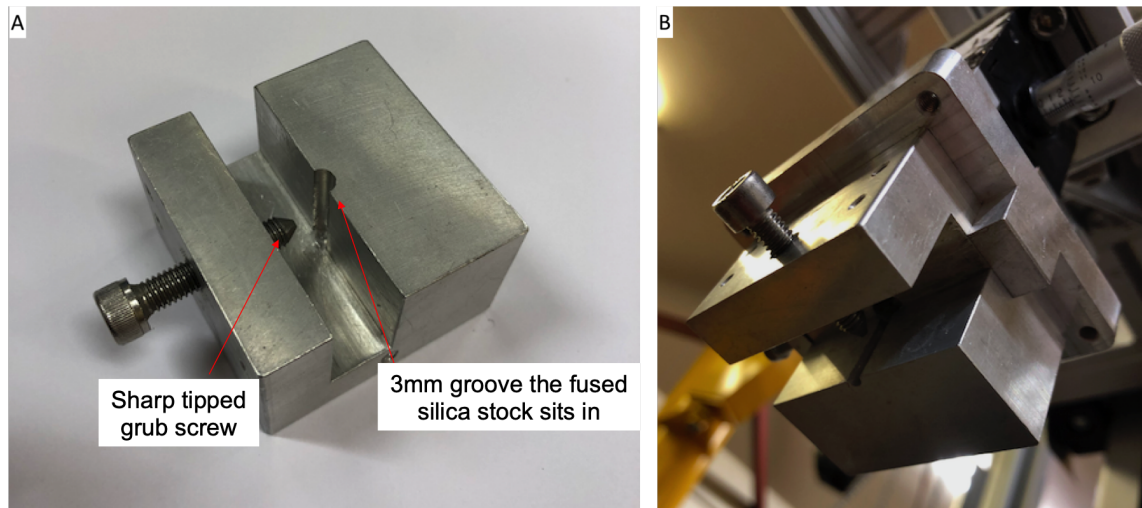


**Figure 2.15:** A: A basic clamp. B: Top basic clamp attached to its holder.

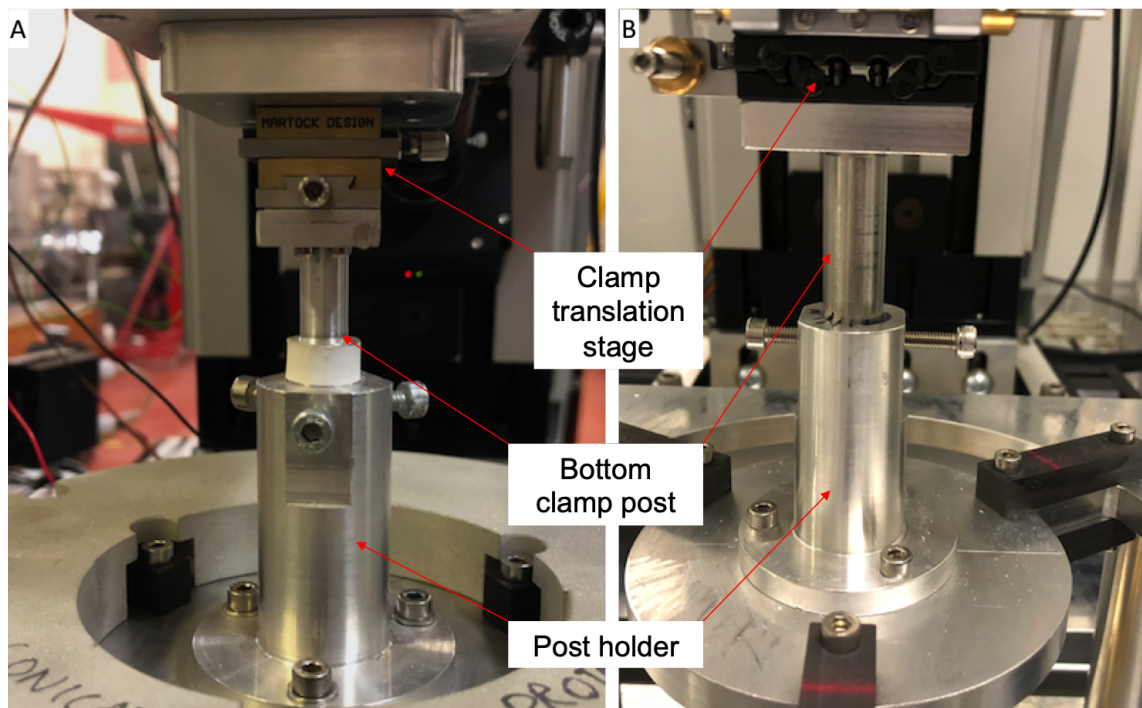


**Figure 2.16:** The centre post that holds the bottom clamp holder at Glasgow (A) and LHO (B).

To check that the semi-circular groove in the clamp is concentric to the conical mirrors, an alignment tool, shown in figure 2.17, was developed for use on the Glasgow pulling machine to aid the alignment of the clamps [103]. This aluminium plate can be slid onto the top of the feed mirror. The lip on the plate will come into contact with the outside circumference of the feed mirror resulting in the opposite edge sitting exactly half way along the feed mirror. This side has a  $3\pm 0.1$  mm wide groove in the middle where the fused silica stock would slot into should the stock be perfectly in the centre of the feed mirror.

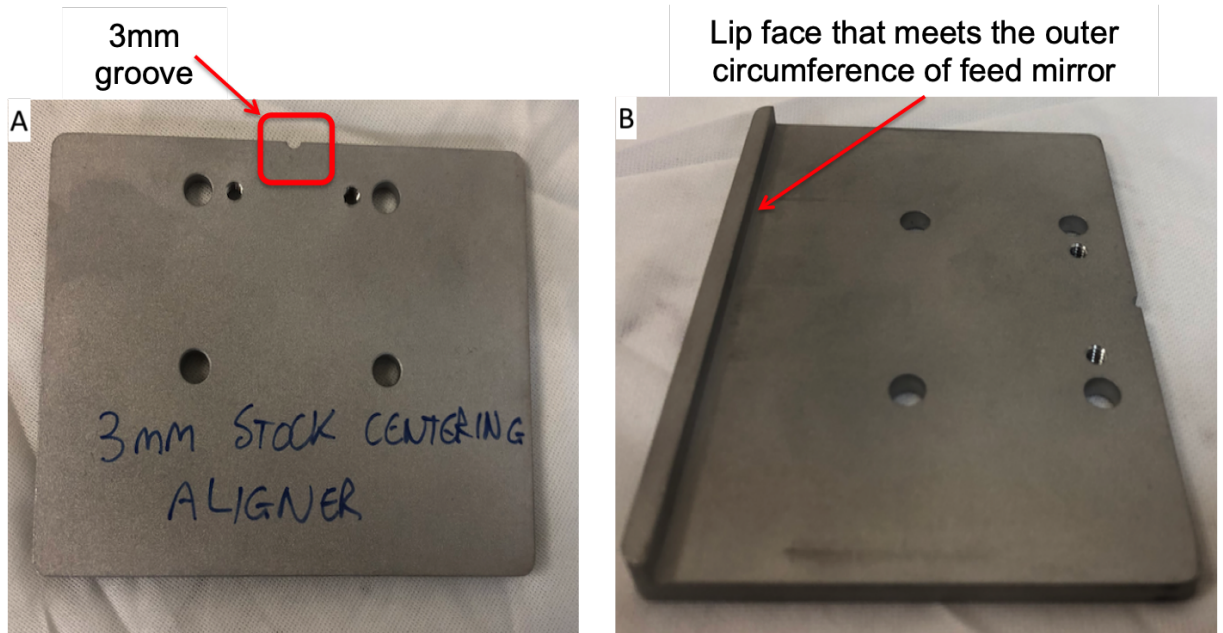


**Figure 2.17:** Aluminium alignment plate, D1800247, used to align the clamps to the centre of the feed mirror.



**Figure 2.18:** Zoomed view of the 3mm groove on the alignment plate.

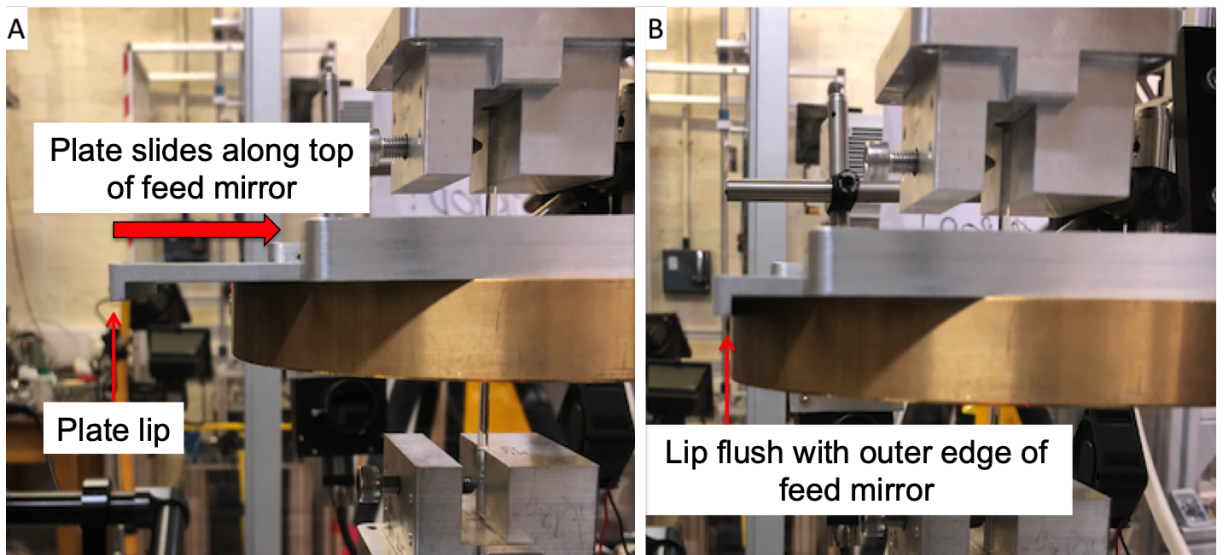


**Figure 2.19:** Aluminium alignment plate to check fused silica stock is in position.



**Figure 2.20:** Alternate angle of aluminium alignment plate to check fused silica stock is in position.

Using this tool, a rod of stock can be inserted into the bottom clamp with the feed mirror as far down as possible without going past the bottom clamp. The X-Y translation stage that the clamp sits on is then adjusted until the stock material is sitting in the groove. This process is then repeated for the top clamp with the feed mirror at the reset position.

Once aligned, the stage holding the top clamp is moved down as close to the bottom clamp as possible without touching, as shown in figure 2.21. A check can then be made to ensure that the sides of the top and bottom clamps and clamp holders are parallel with each other and that the clamps are coaxial. An offset in the clamp or clamp holders can result in issues with extracting the fibre cartridge from the pulling machine where the clamps can twist and catch on the holder when trying to advance the top stage.

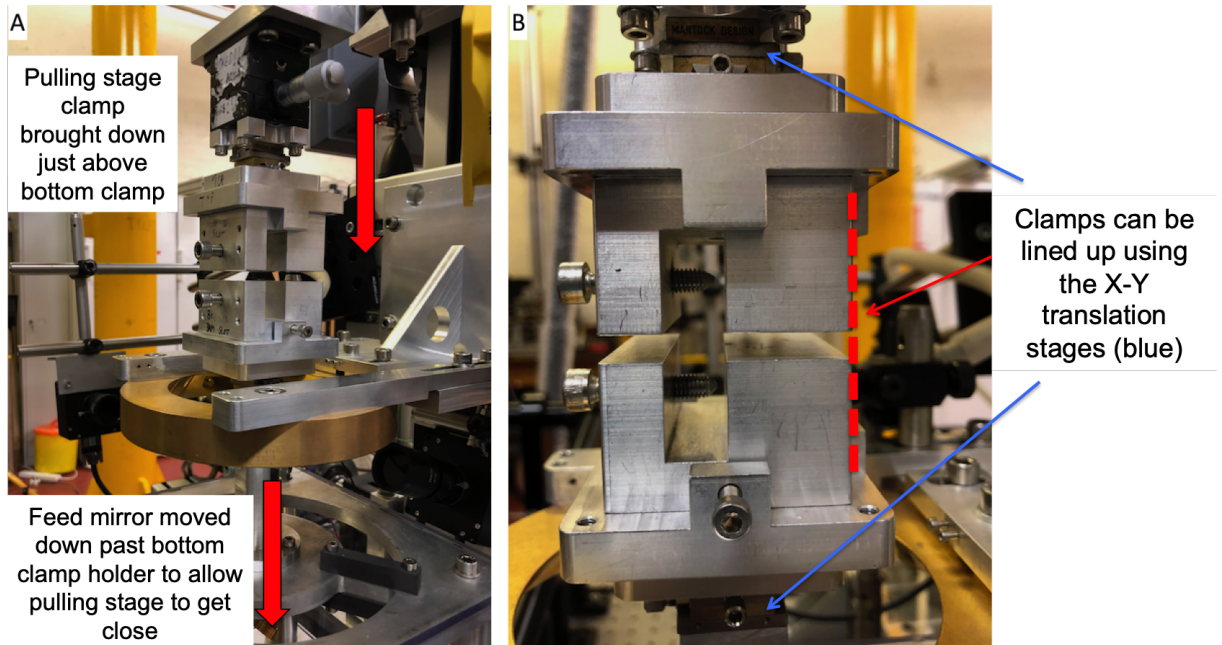


**Figure 2.21:** The top and bottom clamps brought close to contact with each other to align the clamp holders.

The top stage can then be moved up to its starting position. A final check is made by using

the aluminium alignment plate with a piece of fused silica stock in the top clamp and with the feed mirror at its reset position.

### 2.3.4 Top and bottom fuse end clamps

When producing fibres for use in monolithic suspensions, lengths of fused silica stock are prepared with what are known as fuse end attachments. The process of attaching fuse ends to the fused silica stock will be described in greater detail in chapter 4. Fuse ends are aluminium attachment blocks that allow handling and securing of the fused silica stock without physically handling the actual stock material. This is shown in figures 2.22 and 2.23.

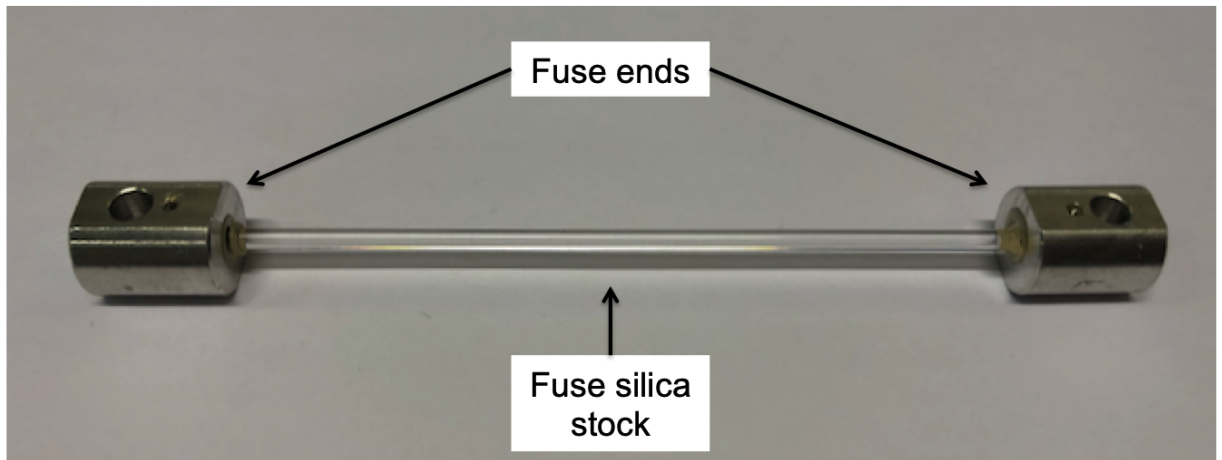


**Figure 2.22:** Fused silica stock with fuse end attachments.

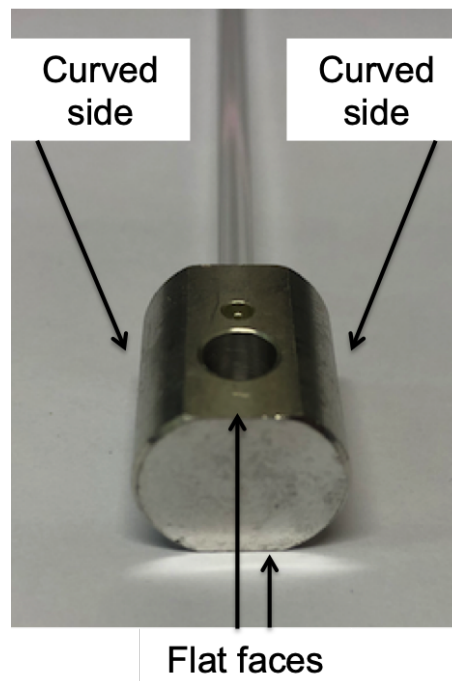


**Figure 2.23:** Fuse end attachment showing the two flat faces and two curved sides.

Alignment of fuse end clamps, shown in figure 2.24, is in principle, the same as the basic clamps. There is however an additional factor to consider when using fused silica stock with fuse end attachments. An example of a fuse end within a fuse end clamp is also shown in figure 2.24.

The important factor to take into consideration when using fuse ends is the accidental torque imparted to the fused silica stock during attachment to the clamps. Examples of this are shown in figures 2.25 and 2.26.

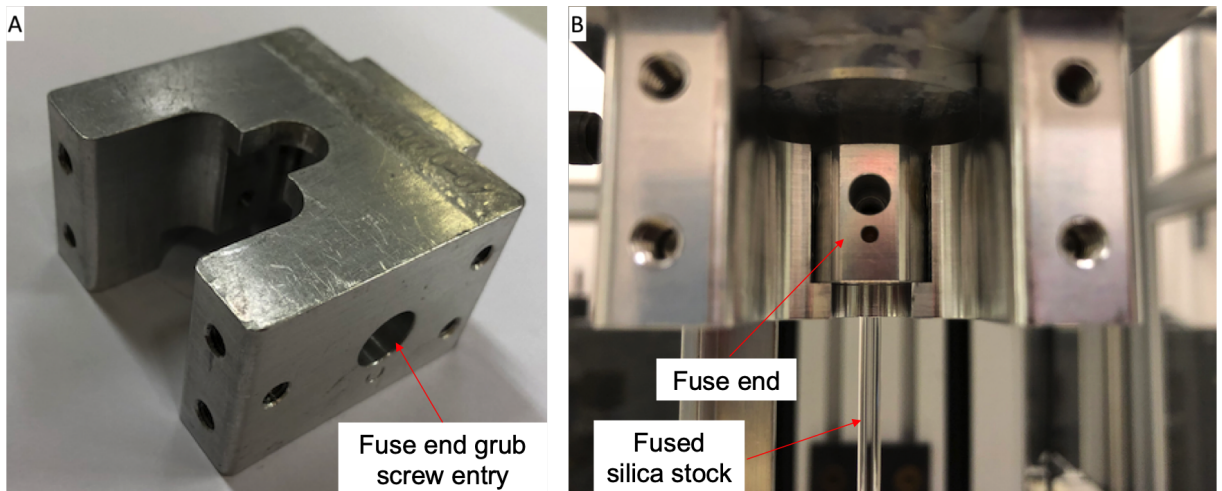


**Figure 2.24:** A: A fuse end clamp. B: A fused silica stock rod with a fuse end sitting in the top fuse end clamp in the fibre pulling machine.

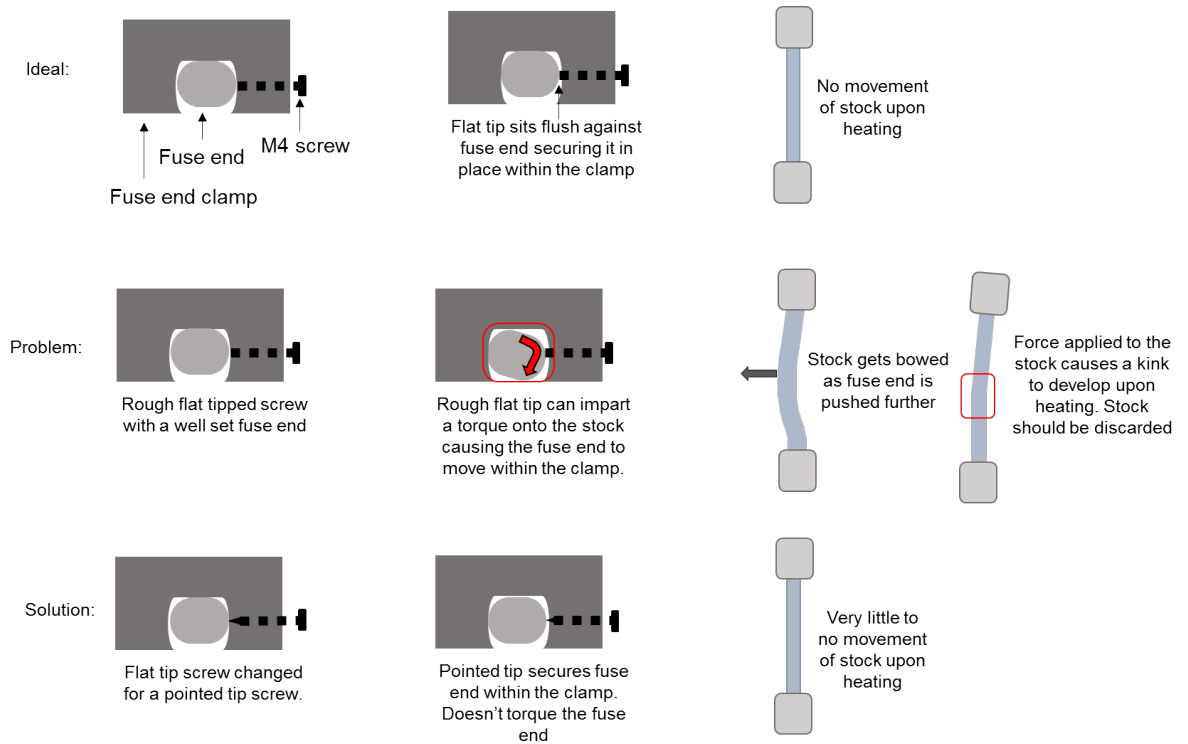


**Figure 2.25:** Top row: ideal scenario of a fuse end sitting in a fuse end clamp.  
 Middle row: Top down view of a well aligned fuse end sitting within a fuse end clamp with an angle induced by a flat tip screw with the resulting stock shape after heating.  
 Bottom row: Well aligned fuse end with a pointed tip screw used instead of a flat tip screw.

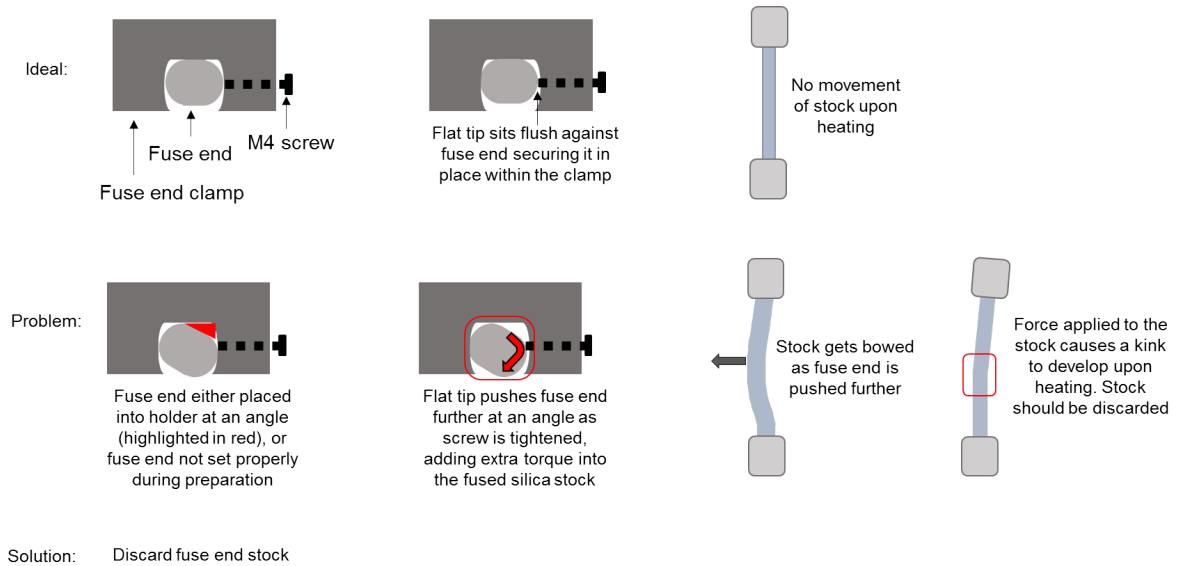


**Figure 2.26:** Top row: ideal scenario of a fuse end sitting in a fuse end clamp.  
 Bottom row: Top down view of a fuse end sitting within the fuse end clamp at an angle with the resulting stock shape after heating.

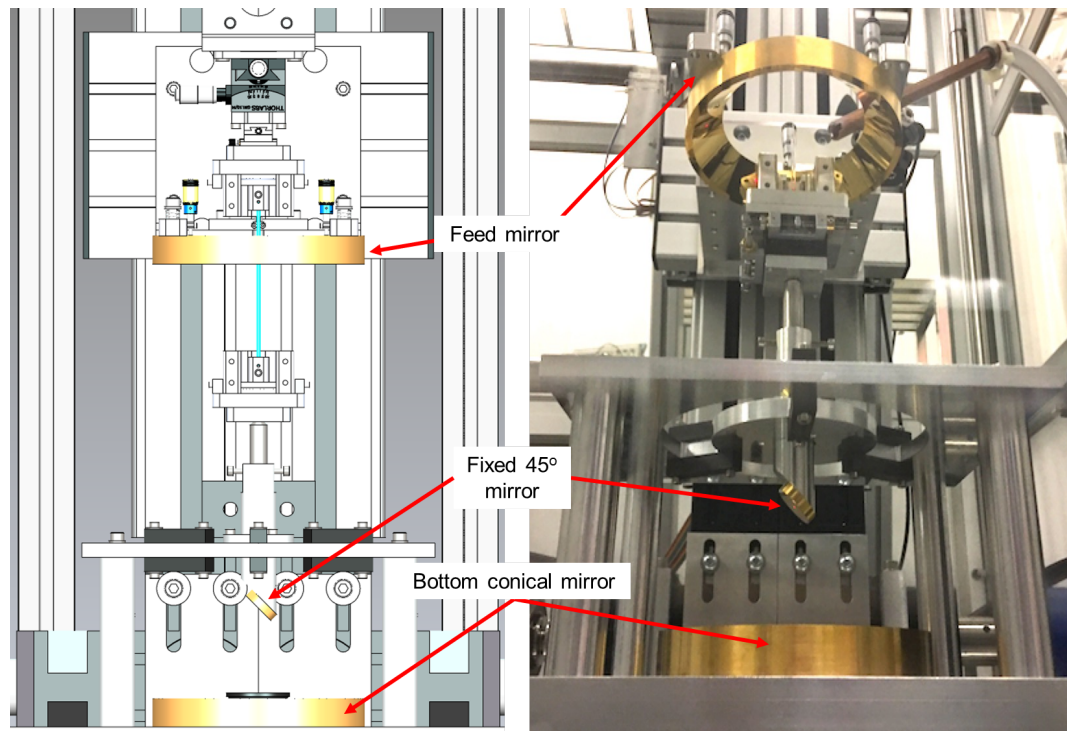
By necessity, there is some clearance in the clamps to allow for the installation of fused silica stock with fuse ends. This can result in slight movement of the stock within the clamp. This movement, combined with tightening the flat tipped screws that are not perfectly flat, but "rough" flat, can result in the fuse end being pushed to the other side, twisted or both. This can easily be misinterpreted as the clamps not being coaxial. To minimise this issue, extra care must be taken to ensure there is no significant movement of the fuse end when tightening the screws. Movement of the fuse end during tightening can be seen by eye. It is possible to significantly reduce the issue caused by flat tip screws by using sharp tipped screws. This is an upgrade that will be made in the near future prior to production of fibres for A+ [90].

This issue can also arise from a fuse end that has been misaligned during the preparation process, which can also contribute significantly to this issue. Therefore any fuse ends that are not properly aligned during the production process should be discarded from production fibres. This will be discussed in more detail in chapter 4.

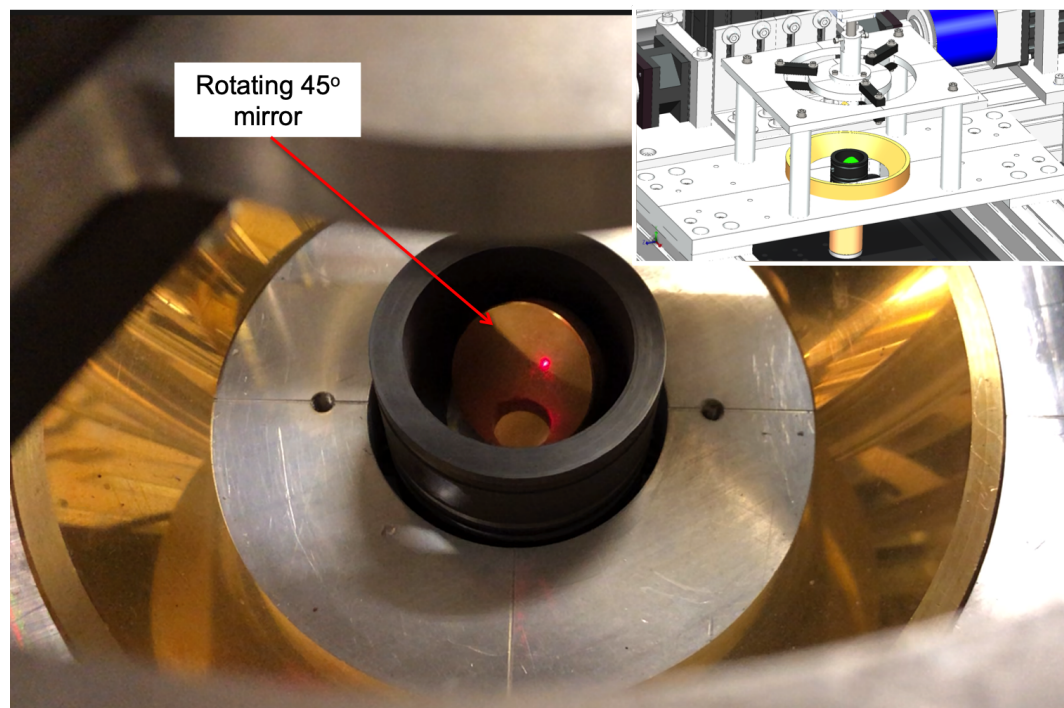
## 2.4 Laser beam alignment

Once the mechanical alignment has been completed, the laser alignment can be carried out. It is absolutely essential to ensure the laser is properly aligned when producing fibres for aLIGO suspensions. The mechanical alignment of the core components described previously should only need to be carried out once at the start of a fibre production period and should not need to be carried out again in the near future. Laser beam alignment should be carried out at the start of every day when producing production fibres. It is likely that in between days of producing fibres, only slight minor adjustments will need to be made the next day. The initial alignment at the start of the production period however might require significant adjustments. Proper alignment of the laser beam is essential as misalignment of the beam during the pulling process can produce fibres that fall outwith the tolerances of the fibre specifications.

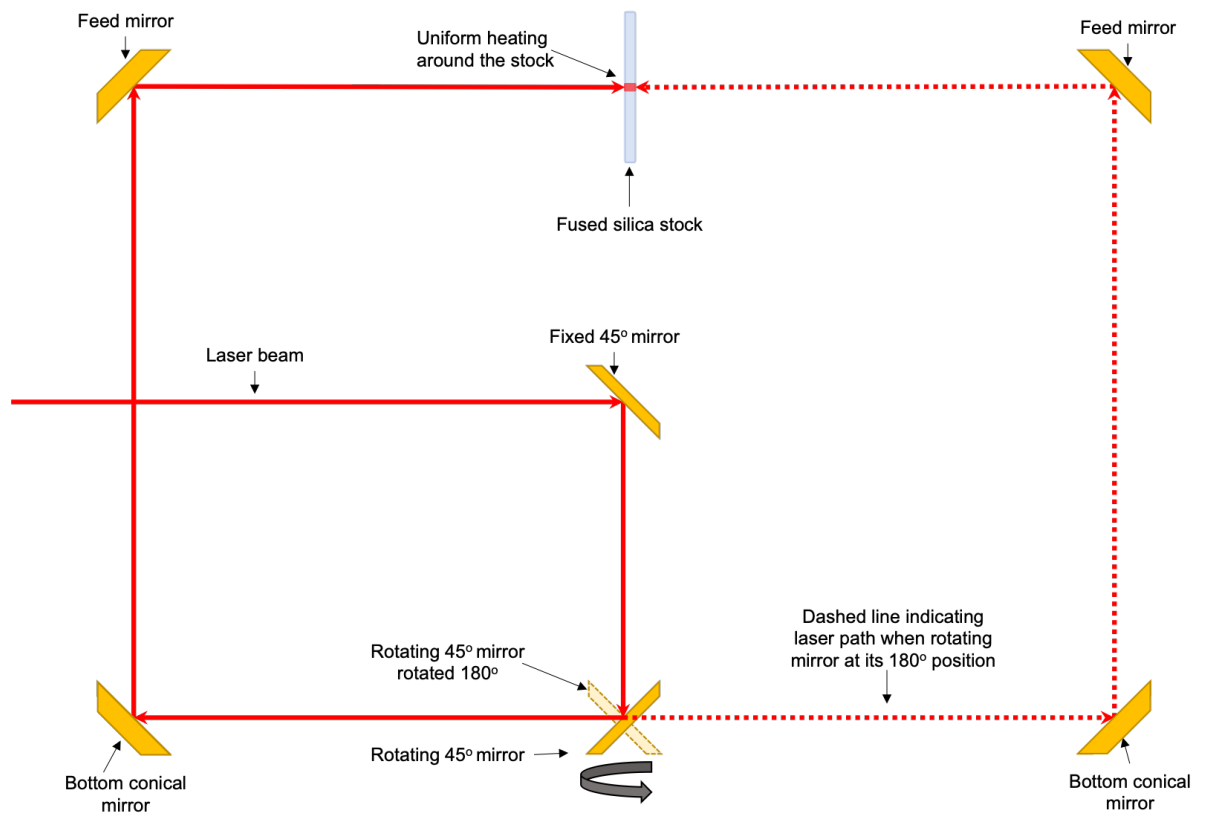
Figure 2.27 shows a SolidWorks rendering and an image of the optical setup within the fibre pulling machine. Figure 2.28 shows the location of the rotating 45° mirror within the bottom conical mirror. Figure 2.29 shows a cross-section of the beam path within the pulling machine optical set up when the laser is theoretically perfectly aligned.



**Figure 2.27:** SolidWorks rendering and an image of the optical setup within the fibre pulling machine.

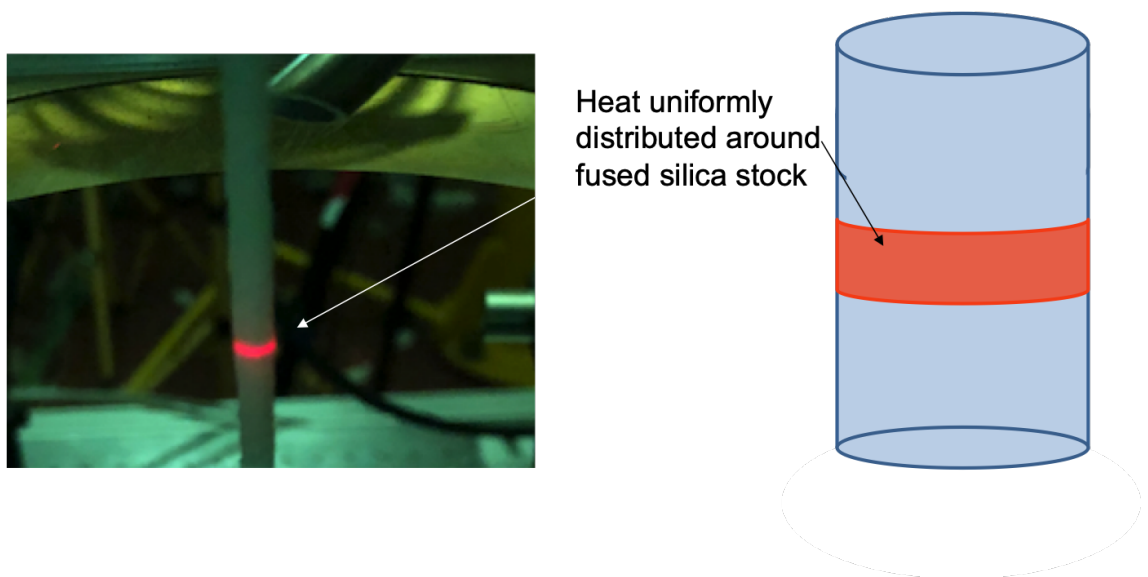


**Figure 2.28:** Rotating 45° mirror at the centre of the bottom conical mirror. Inset shows location in the SolidWorks rendering, highlighted in green.



**Figure 2.29:** Cross section of beam path for an aligned pulling machine to the fused silica stock.

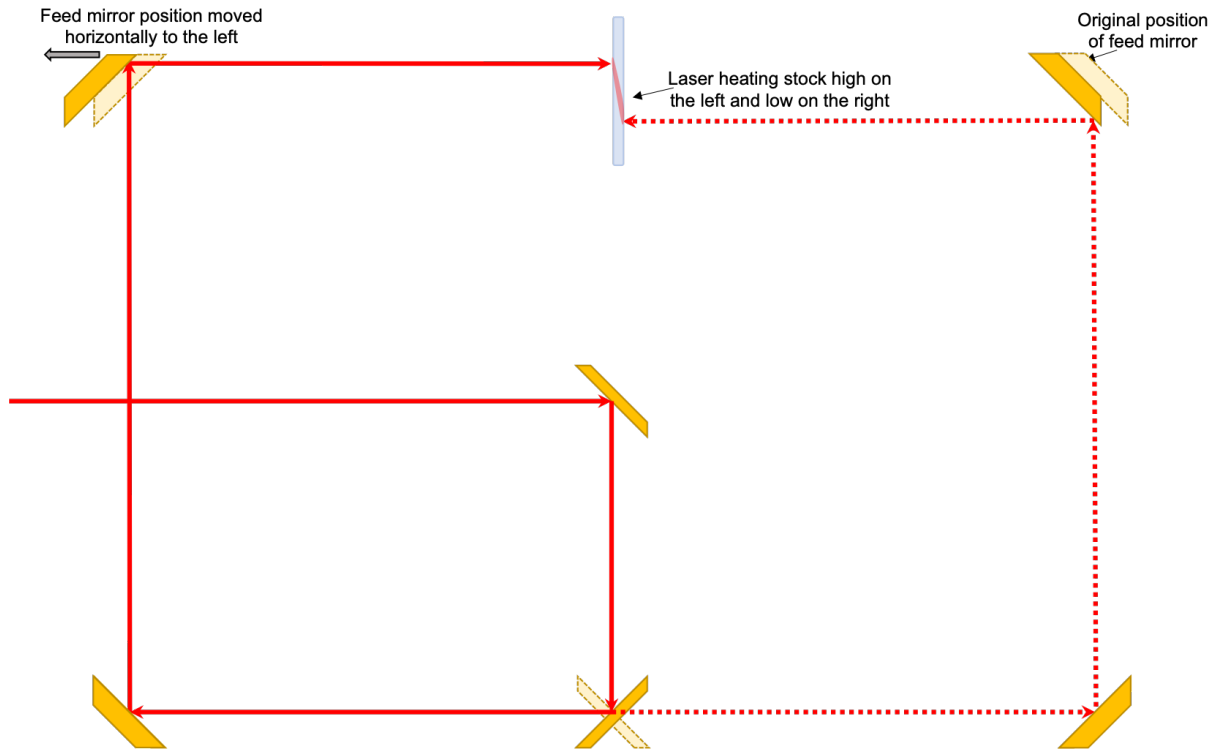
Figure 2.30 shows the beam distribution around the fused silica stock for an aligned pulling machine. This is the ideal scenario of the pulling machine for producing fibres as the laser beam is uniformly distributed around the fused silica stock.



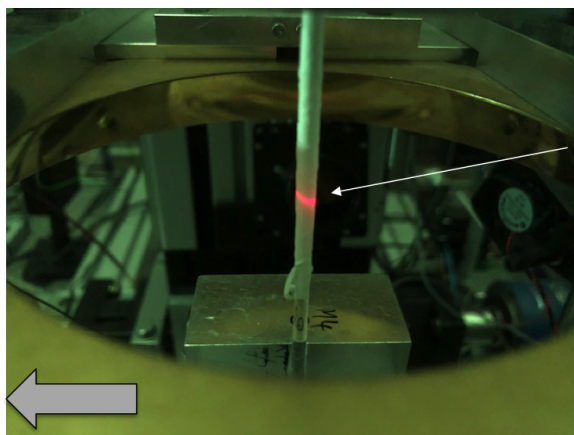
**Figure 2.30:** Distribution of beam around fused silica stock for an aligned pulling machine.

Figure 2.31 shows the resulting cross section of the beam path where there is a mechanical offset misalignment of the feed mirror. Figure 2.32 shows the beam distribution around the fused silica stock with this misalignment. Resulting effects of this type of misalignment will be discussed in the following chapter.

At this point in the alignment set up, this should have been solved during the mechanical alignment process that was described prior to this subsection.



**Figure 2.31:** Cross section of beam path for a mechanical misalignment of the feed mirror.



Feed mirror moved horizontally to the left

Heat distributed around an angular circumference. Higher power needed to heat region to same intensity as aligned distribution

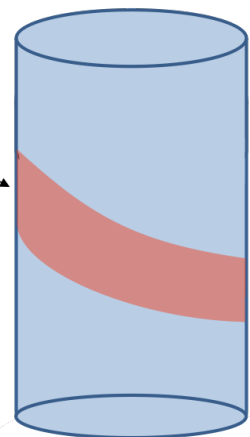


**Figure 2.32:** Distribution of the beam around fused silica stock for a feed mirror mechanical misalignment.

### 2.4.1 Red alignment beam

Initial checks should be made to ensure that the visible alignment beam is aligned with the CO<sub>2</sub> laser as the majority of the alignment will be checked with this alignment beam. As of writing this thesis, there are two different CO<sub>2</sub> lasers being used for the LHO and Glasgow pulling machines:

- LHO - Synrad Firestar f100 100 W [104]
- Glasgow - Synrad Firestar i401 400 W [105]

Both of these lasers have different visible alignment beam units, but both work on the same alignment principle: near and far field alignment. Low power tests can be carried out with a temperature-sensitive target cards [106]. An example of one of these cards is shown in figure 2.33. These cards change colour when exposed to a higher temperature than its surrounding. To carry out near and far field alignment, a target card should be placed in a far field position and a second removable one placed in the near field. Far field in this case should be at least the maximum path length the beam would be expected to travel in the optical set up of the pulling machine. If possible, a greater distance than this would be beneficial to the alignment process. Near field would be as close as possible to the alignment unit that still allows for visible inspection of the target card. A flip mirror may be required to place in the beam path to direct the beam away from the near field card to the far field card. The cards should be positioned such that the CO<sub>2</sub> beam is hitting the centre of the target. This is achieved by using a low laser power, to ensure the beam does not burn the card, and observing the change in colour around the target on the card. Care should be taken not to move the card while the laser is on.

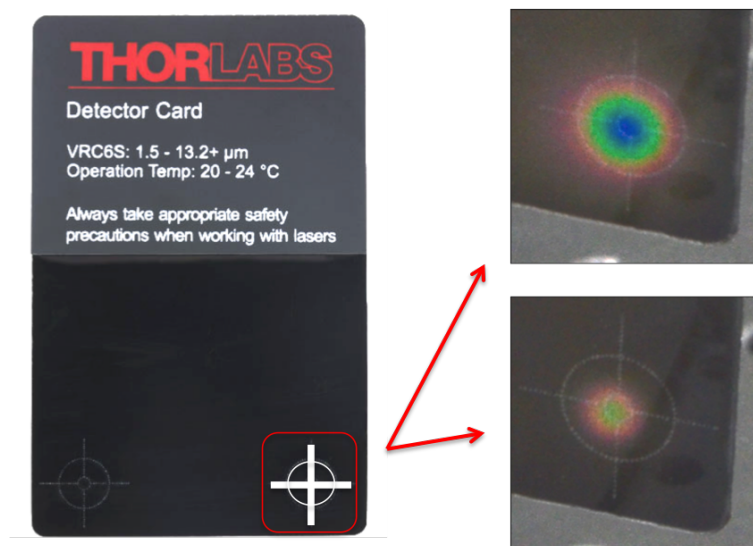


**Figure 2.33:** A Thorlabs VRX6S temperature-sensitive target card that can be used for laser alignment [106]. Bottom right target highlighted for clarity.

Once both cards are in place, the red alignment beam is observed on the near field target. Should there be a difference between the position of the alignment beam and the CO<sub>2</sub> beam, the near field adjustments on the alignment beam unit should be turned until the beam is in the middle of the target. The same process is then carried out for the far field target.

This process is repeated until the alignment beam is hitting the centre of the target on the cards for both near and far field. A final check is made by turning the CO<sub>2</sub> laser on to ensure that both the CO<sub>2</sub> and visible beams are overlapping each other. As this check is carried out by eye, a tolerance of 0.5 mm from the centre of the target is acceptable.

It is important that this process is carried out due to the infrared nature of the CO<sub>2</sub> not being visible by eye. The distribution of the red alignment beam is the visible counterpart of the CO<sub>2</sub> beam and is therefore key to all visible alignment inspections of the beam path and distribution to the CO<sub>2</sub> beam. Failure to carry this alignment will result in the red alignment beam giving false information as to the true whereabouts and distribution of the CO<sub>2</sub> beam, and is a safety hazard.

## 2.4.2 Optical bench mirror mounts

The CO<sub>2</sub> beam is directed around the optical bench by reflecting off multiple gold coated 1" mirrors [107] held in 3 way kinematic mirror mounts [108]. Standard laser safety practice states that the beam should be travelling parallel to the bench while travelling in between mirrors in the horizontal axis. This can be achieved simply by using an iris on a post sitting at the desired height at that point in the beam path, or simply with a 0.5 mm division ruler that can be visibly inspected by eye.

At this point on, there are four key degrees of freedom that determine the distribution of the beam around the fused silica stock:

- Horizontal translation
  - Horizontal directional movement of the beam across the fixed 45° mirror.
- Vertical translation
  - Vertical directional movement of the beam across the fixed 45° mirror.
- Pitch
  - Beam entering the pulling machine optical system at a vertical angle.
- Yaw
  - Beam entering the pulling machine optical system at a lateral angle.

Any combination of the four above listed factors can result in non-uniform heating of the fused silica stock. Unlike the mechanical alignment of the core components of the pulling machine, optical components used to direct the beam into the pulling machine optical system will need regular alignment checks. This is due to the heat transfer from the laser beam. Figure 2.34 shows the periscope set up on the Glasgow pulling machine. This periscope has all the adjustments needed to correct the above misalignment factors. This periscope set up will be installed at LHO as part of the future A+ upgrades to the fibre pulling machine.

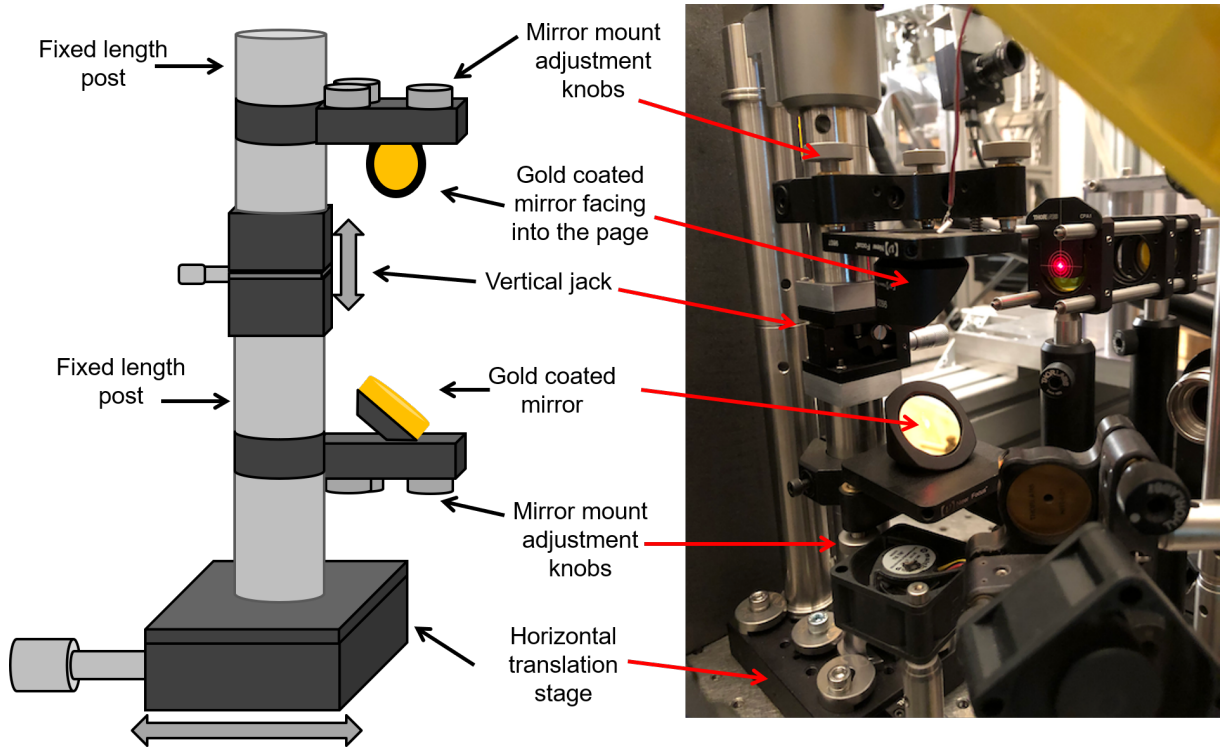


**Figure 2.34:** Periscope system currently installed on the Glasgow fibre pulling machine.

An example of a pitch misalignment can be seen in figure 2.35 and the beam distribution around the stock shown in figure 2.36. A yaw misalignment has the same characteristics, but with the distribution pattern moved  $90^\circ$  around the stock. There is a clear difference in beam intensity around the stock between figures 2.32 and 2.36. Figure 2.32 intensity is uniform along the points of contact on the stock, whereas figure 2.36 the intensity visibly changes along the points of contact with the stock.

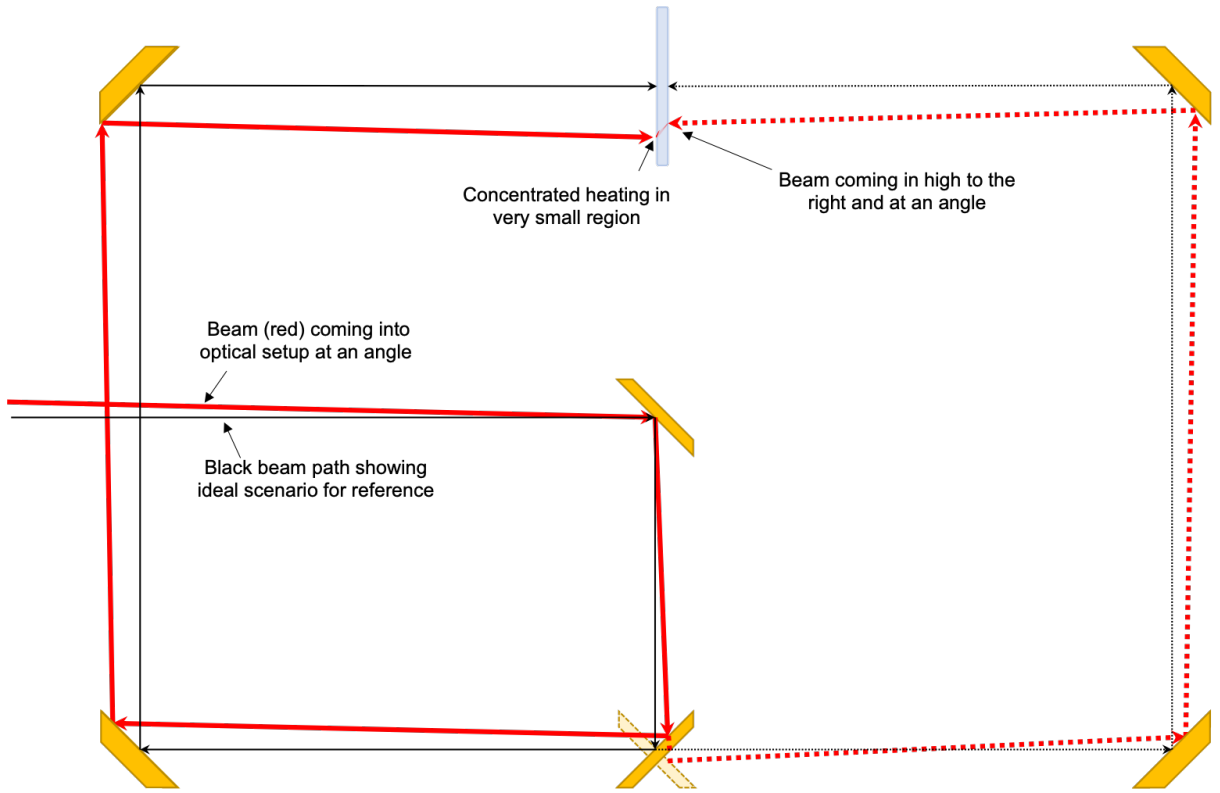


**Figure 2.35:** Cross section of beam path with the laser coming into the pulling machine optical system at an angle.

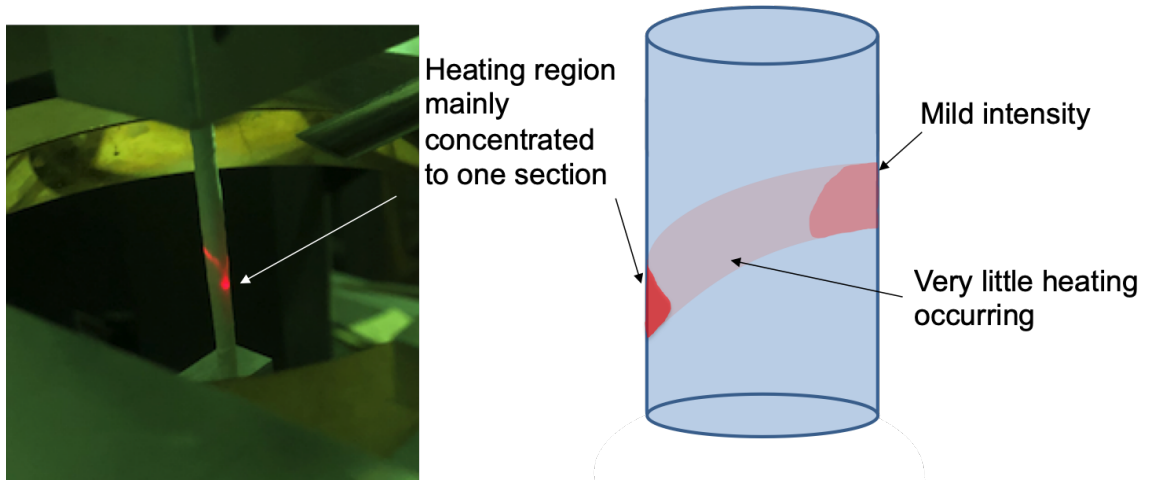


**Figure 2.36:** Distribution of beam distribution around the fused silica stock with an angular misalignment.

Figure 2.37 shows the path the laser beam takes around the surface of the stock in this scenario. The beam appears to concentrate itself at the lower most point, where the intensity is greatest. This concentration of heat is caused by the beam turning back on itself as the 45° mirror rotates. This can be seen in figure 2.38 where 10 frames from a video recording shows

the beam follow the path drawn out in figure 2.37. This can be seen when using the pulling machine by lowering the voltage supply to the rotating 45° mirror which will slow down its rotation speed.

These are clear indications to separate the two different scenarios between figures 2.32 and 2.36.

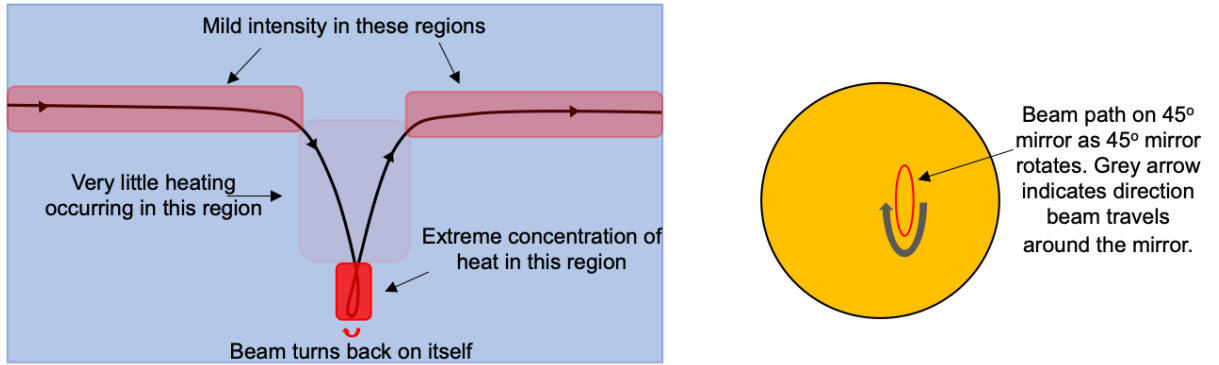


**Figure 2.37:** A: The path of the laser beam across the 2D surface of the fused silica stock. B: The beam path of the laser on the rotating 45° mirror with an angular misalignment.

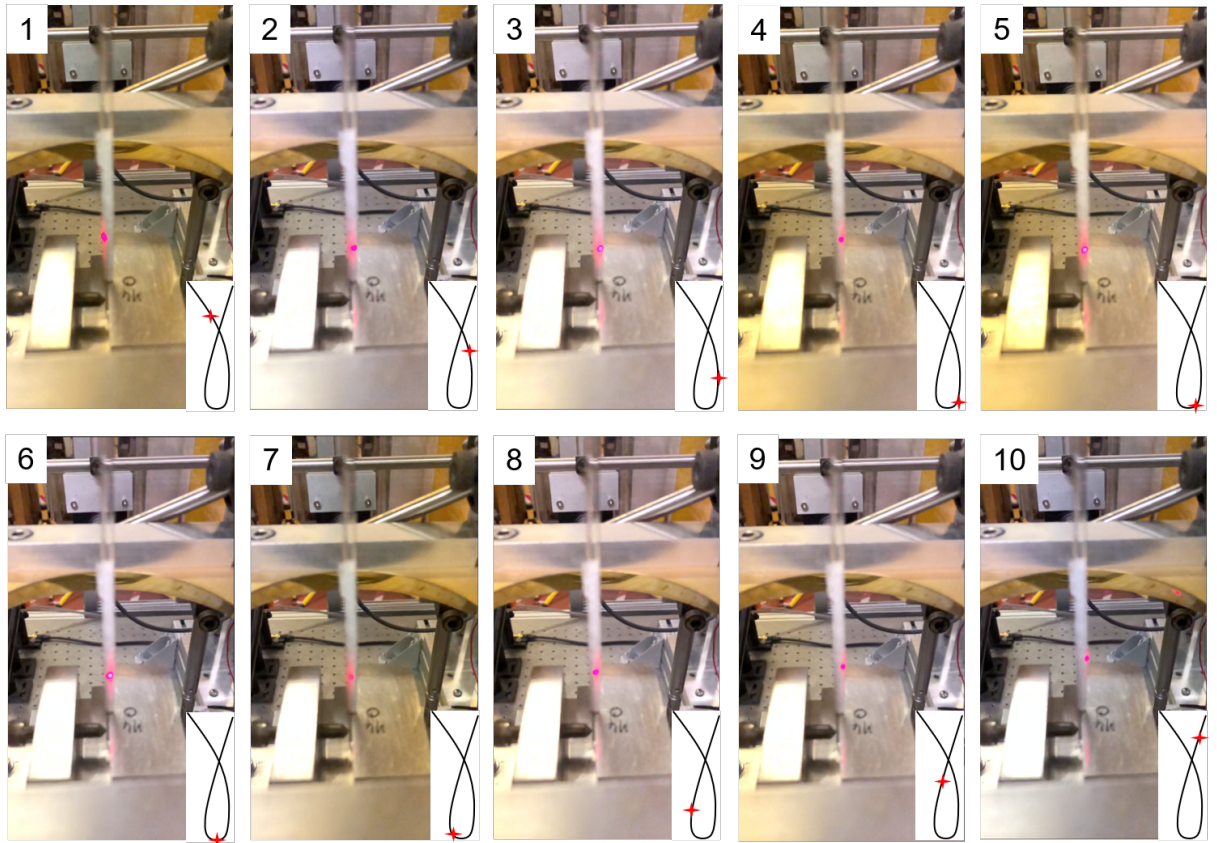


**Figure 2.38:** 10 frames from a slow motion video plotting out the path of the beam around the fused silica stock. The red + that is shown in the bottom right inset of each frame is the position of the beam along the path that it travels. This path is the same shape as shown in figure 2.37.

It is therefore critical to ensure that the beam is level with the bench after the final mirror before entering the optical system of the pulling machine. The final mirror in this scenario would be the top periscope mirror. This can be carried out by placing irises along the optical path to check that the beam is passing through the hole. Ideally, an iris should be placed soon after the final mirror and another just before the entry to the optical system of the pulling machine. The irises should be at the height of the fixed  $45^\circ$  mirror within the pulling machine set up. Care should be taken to ensure the irises are placed in a straight line between the last mirror outside the pulling machine and the entry point into the pulling machine enclosure. Care should also be taken to ensure that the irises are placed perpendicular to the fixed  $45^\circ$  mirror. This can be achieved by measuring the distance of each side of the iris with respect to the face of the enclosure at which the beam would enter. This would ensure that the beam is not entering at a lateral angle.

Should adjustments be required to pass the beam through the irises, knob adjustments to the mirror mounts on the periscope should be made. The bottom mirror mount adjustments should be used to direct the beam through the first iris, and the top mirror mount adjustments should be made to pass the beam through the second iris, and then iterate between the two until the beam passes through both irises.

Once the beam is level to the bench, the mirror mount knobs should not be adjusted. Any adjustments to direct the laser beam should now be carried out with the horizontal and vertical translation stages.

### **2.4.3 Beam position within the pulling machine**

The next step is to check the alignment of the beam within the pulling machine set up. The beam should be hitting the centre of the fixed and rotating  $45^\circ$  mirror before spreading the beam out to the bottom conical mirror. Figure 2.39 shows the effect of a vertical misalignment coming into the optical set up of the pulling machine. A lateral misalignment has the same characteristics, but with the distribution pattern moved  $90^\circ$  around the stock. Note that the beam is coming in level to the pulling machine, but results in the similar beam situation as previously described in figures 2.31 and 2.32.

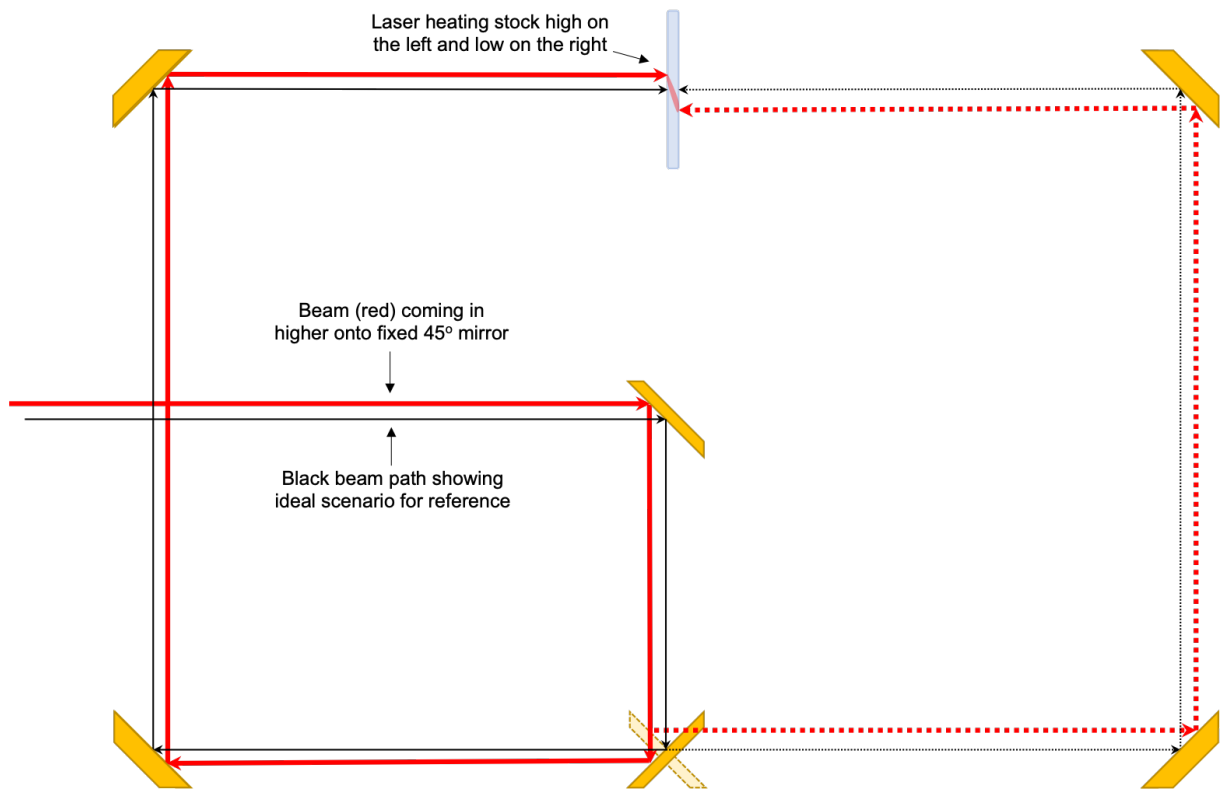


**Figure 2.39:** Cross section of the beam path coming in high on the fixed 45° mirror.

A target cover, similar to the target shown in figure 2.40, can be modified and used as a guide to position the beam to the centre of the mirror.



**Figure 2.40:** A Thorlabs LMR1AP target cover that can be modified to sit on top of the rotating 45° mirror [109].

The plastic tool used for the alignment of the conical mirrors can then be used to check the laser alignment. This is shown in figure 2.41. There is an array of concentric grooves on the tool that line up with the beam as it is reflected off the bottom conical mirror. Adjustments at this

point should only be made with the horizontal and vertical translation stages, previously labeled in figure 2.34, that the mirror posts are sitting on until the beam is lying on the same line around the tool.

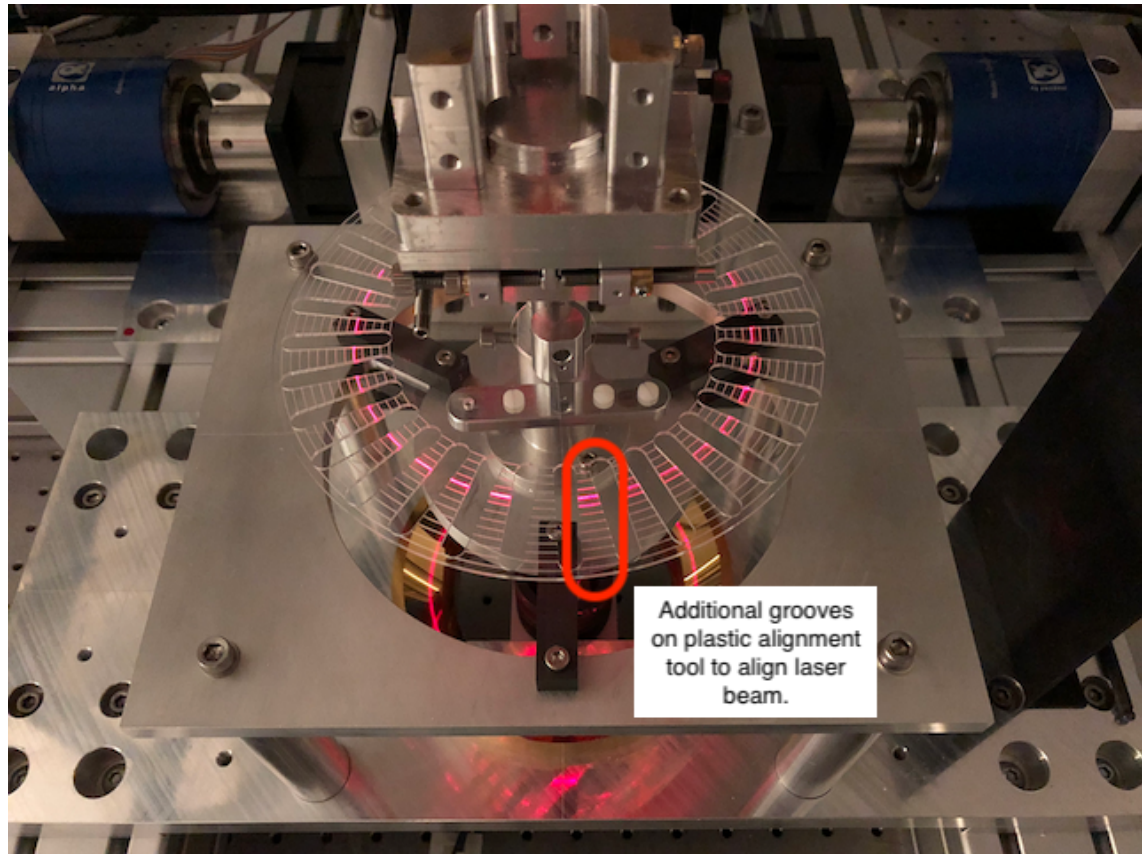


**Figure 2.41:** Plastic alignment tool for laser alignment check.

A piece of fused silica stock wrapped in teflon tape, or any other opaque thin layer, should then be installed into the clamps. This makes it easy to see the alignment beam distribution on the fused silica stock. Slight final adjustments of the X-Y stages should only be needed at this point. A burn test can be carried out if desired with a piece of fused silica stock wrapped in masking tape. Ensure that the laser power is low enough to only just burn the tape.

For the pulling machine at LHO, a final test can be carried out by heating up a piece of fused silica stock until just molten. The beam distribution can then be observed around the stock through highly tinted welding goggles that are available in the fibre lab. In Glasgow, the same process can be carried out, but observing the distribution of the beam around the stock via the installed cameras with ND filters on the fibre pulling LabVIEW program [92] [110]. This upgrade was installed on the LHO fibre pulling machine during the first quarter of 2020 in preparation for A+.

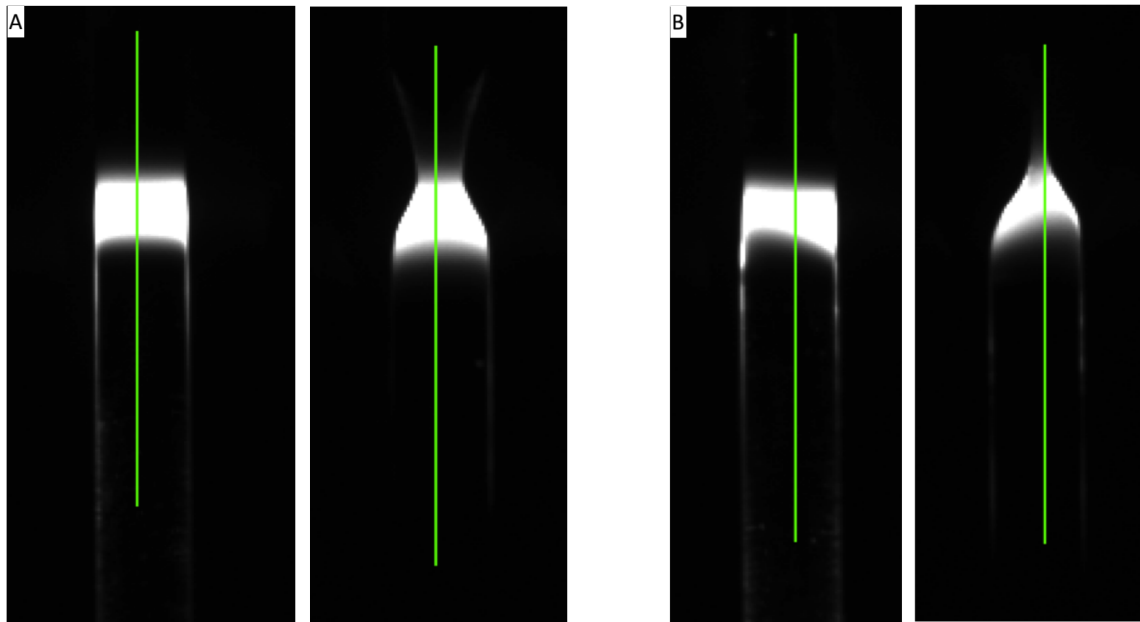


**Figure 2.42:** A: Well aligned laser distribution around the stock during polishing and pulling, respectively. B: Misalignment of the same situation.

The camera system allows greater accuracy viewing the beam distribution that is not possible with just welding goggles. With welding goggles, the enclosure set-ups at both LHO and Glasgow can make it tricky to get close enough to the molten stock material to see the beam distribution in detail. As the alignment of the beam also relies on the eyes of the user, there is less control on the degree of alignment as this would be subjective to each user. A camera monitoring system can reduce this subjectiveness, as shown in figure 2.42. Currently, 3 cameras are installed onto the pulling machine to view the beam distribution from both sides and the rear view of the fused silica stock. The rear view in particular is critical as it is not possible to get this view through welding goggles.

In the future, image templates could be made to ensure that the alignment on the camera feed match what the expected beam alignment should be. This would remove any inconsistencies from the alignment process.

#### 2.4.4 Lens system

Installation of a lens system in the pulling machine will reduce the beam size at the point the beam focuses onto the fused silica stock. It allows for greater headroom of the laser power as less power is needed to heat the stock material to its molten point. Currently, fibres are pulled with the f100 laser at 85% power. This is effectively full power as the difference between 85% and 95% is approximately 5 W. With a lens system, this power can decrease to approximately 50% [111]. The decrease in beam size also means that there is potentially greater control on the shape of the necks due to less material being heated during the pulling process.

There are currently no lenses set up in the optical path for either Glasgow or LHO's pulling machines to alter the beam size when producing fibres using 3 mm stock. There has previously been a lens system installed at Glasgow, as shown previously in figure 2.4, so this subsection is added in the future case that a lens system is again installed on one of the pulling machines.

Installation of the lens system should be the final task done, with the rest of the pulling machine alignment set as described in this chapter so far. Therefore, the lens system should just be put in the correct position along the optical path. Care has to be taken to ensure proper alignment. The lens cage system should be installed first without any lenses in the holders. To ensure the beam passes through the centre of the lenses, various targets or irises can be installed onto the lens cage. Shirt targets, shown in figure 2.43, can be used as a first order check to check the cage is coaxial to the beam. Targets can then be installed in the lens holders to observe where the beam is passing for that holder.

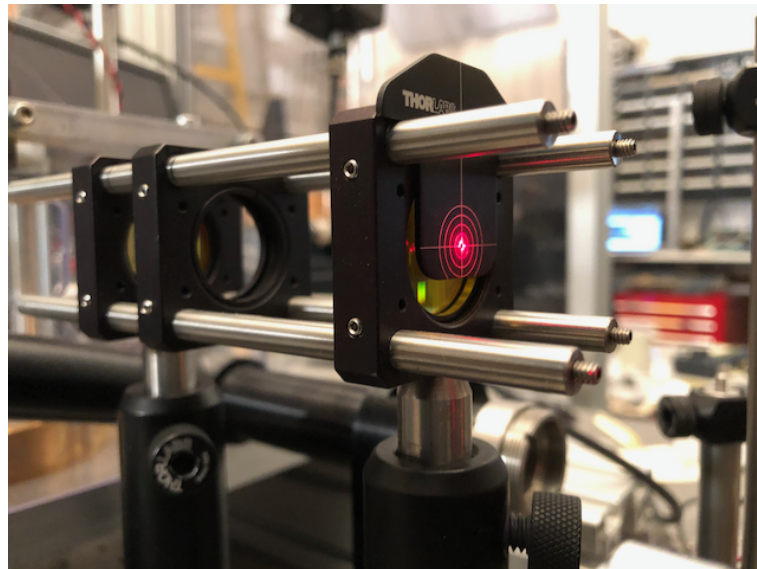


**Figure 2.43:** Shirt target attached onto the lens cage to check alignment.

Ideally, the lens posts should be of a fixed length to minimise any drop in height over time that would occur if the post was sitting in a holder. If a holder has to be used, ensure that the post height is marked on the post with a permanent marker, or a scribe, and is secured in place by tightening the knob with an allen key. Figure 2.44 shows a lens cage with both a fixed length post and a post sitting in a post holder to show the two different options.



**Figure 2.44:** Example of a lens cage with both a fixed length post and a post within a post holder.

Once installed, beam distribution checks should again be carried out to check the beam alignment.

## 2.5 Conclusion

This chapter sets out the procedure that should be followed when aligning any of the fused silica fibre pulling machines in their current state. This chapter will be also written into a LIGO DCC document that can be updated with versions when any hardware changes have been carried out. Ensuring the pulling machine is at its optimal alignment increases the efficiency of producing fibres that fall within the aLIGO fibre tolerances and minimises any wastage of material. Having a written procedure also eliminates the subjectivity of the alignment procedure which could potentially be different for individual users. This also acts as a guide to solving possible alignment issues that a less experienced user might come across.

The following two chapters will describe use of both the Glasgow and LHO pulling machines to produce fused silica fibres, along with other characterisation apparatus. These machines were used to extensively investigate two separate aspects relating to properties of fused silica fibres. During these investigations, the alignment procedure detailed in this chapter was carried out on both machines.

# Chapter 3

## Angular defects of fused silica fibres used in aLIGO monolithic suspensions

### 3.1 Introduction

In 2018, the two aLIGO detectors underwent a commissioning period between observing runs ‘O2’ and ‘O3’. During this commissioning period, there were a total of 8 monolithic assemblies replaced to install new test masses. This included all ETMs at both detectors, as well as two ITMs at LHO and new annular reaction masses. There were several reasons for all these replacements, which include better transmission for green light used for calibration and locking of the interferometer, as well as reducing scatter and the removal of an optic with a significant point absorber on the surface [112]. Unfortunately, there were three incidents where there was a suspension fibre failure at some stage shortly after the replacement process. These included an ETM on the x arm (ETM<sub>x</sub>) at LHO and an ETM on the y arm (ETM<sub>y</sub>) at LLO which had two separate failures. ETM<sub>x</sub> at LHO had a total hang time of approximately 1 week, where as the two failures at ETM<sub>y</sub> at LLO occurred during one of the final stages of the fibre installation process and 4 weeks after installation, respectively.

An investigation was carried out to determine the root cause of these failures [112] [113] [114]. One of the various suggested contributors to the failures in this investigation was from angles that appeared in the top thermoelastic nulling region (TNR) of the aLIGO fibre. These angles would have been introduced into the fibre during the fibre production process. Figure 3.1 shows a photograph of one of the installed fibres into the monolithic assembly that had a visible angle in the stock-to-TNR region of the fibre. This was the region where the fibre diameter reduces from 3 mm to 800  $\mu\text{m}$ . The fibre selection process has since been updated to only allow fibres with an angle between the stock and TNR region of under  $1^\circ$ . The reason this was chosen was because angles greater than  $1^\circ$  could be visibly seen by eye to allow for quick visual inspection. It was therefore decided that an investigation into what effect angles in these TNR regions have on the ultimate strength of the fused silica fibres and whether or not an upper

limit of  $1^\circ$  was a safe value to use for the selection process.

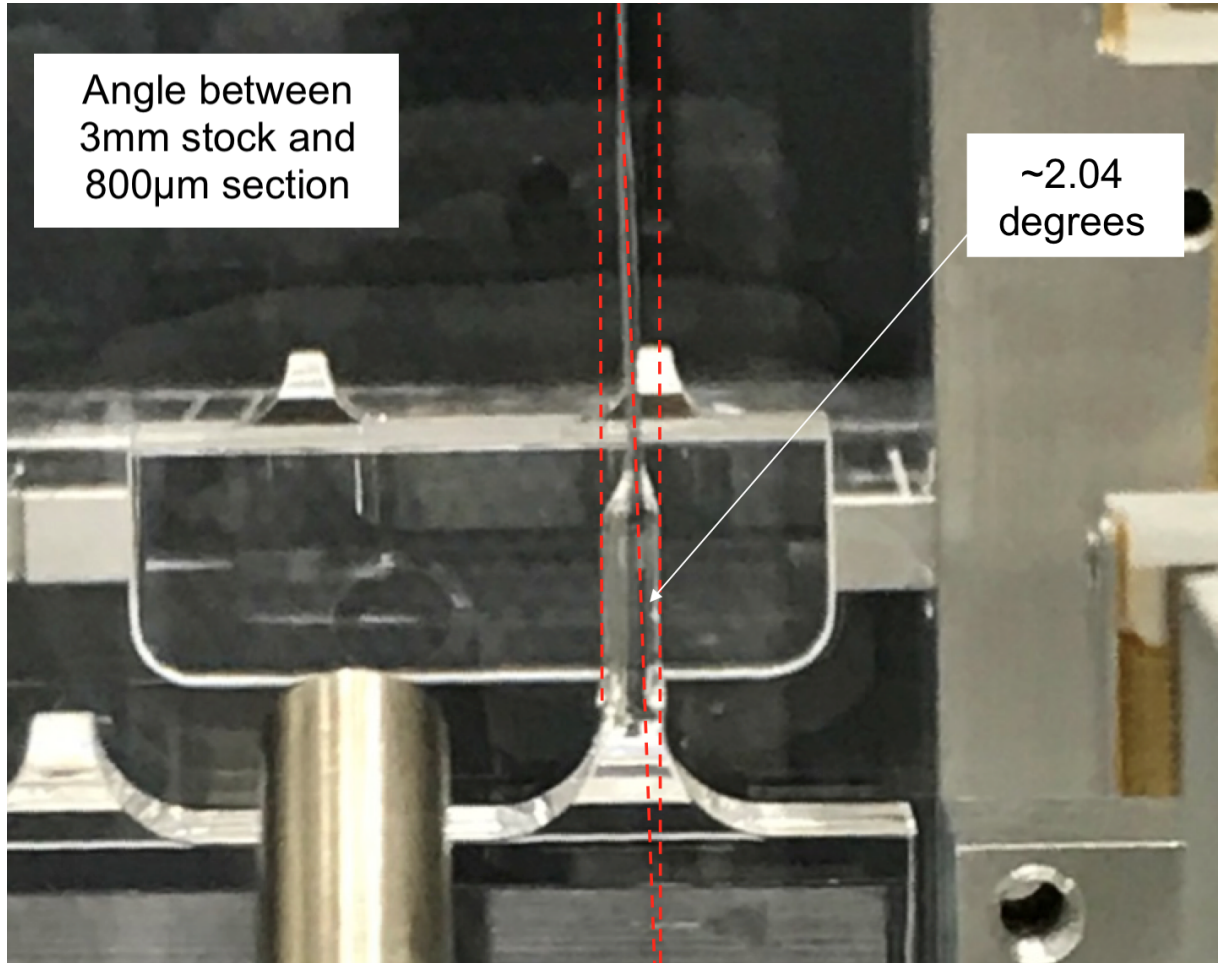


**Figure 3.1:** A photograph of a fibre that was installed into ETMx at LHO that shows a visible angle in the fibre. The labeled angles were calculated from pixel analysis of the photo [114].

This chapter discusses the process behind producing aLIGO fibres using the fibre pulling machine previously discussed in chapter 2, followed by an investigation into producing fibres with angular misalignments and their subsequent ultimate strength performance. Fibres discussed in this chapter aimed to fall within the tolerance of  $400 \pm 20 \mu\text{m}$  to be considered suitable for an aLIGO suspension.

## 3.2 Fibre production

### 3.2.1 Fibre production

Producing fibres for this investigation to be as close to the same conditions as in LHO was essential to understanding how angles could appear during the pulling process. Therefore, the

laser stabilisation feature, previously mentioned in chapter 2 [92], that has been installed on the Glasgow pulling machine was not used during the production process. A different laser, a Synrad Firestar i401 400 W [105], was used as this was the laser currently installed on the Glasgow pulling machine. The power used to produce fibres was set to match the power of the laser that was used in LHO, which was approximately 113 W from previous power measurements (discussed in chapter 4.2.1).

The pulling profile used in this investigation was a modified version of a profile that was previously used for production of fused silica fibres for the aLIGO suspensions, named "LHO15" [115]. The modification to this profile was to reduce the speed of the thin middle section of the fibre by 10%, and is shown in figure 3.2 to allow for the production of fibres with diameters within the aLIGO specifications. "LHO15" will be used in a future investigation that will be discussed in chapter 4.2.1. This change in pulling profile was not significant as several pulling profiles have been developed to produce aLIGO fibres [115].

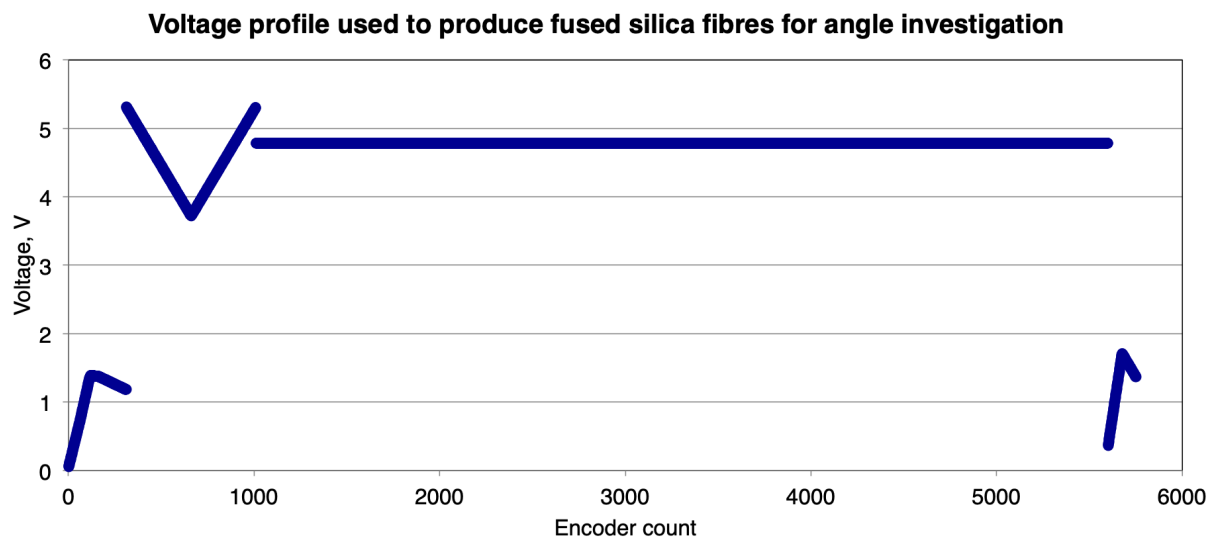


**Figure 3.2:** Graph of fibre pulling profile used to produce the fibres in this investigation.

All fibres in this chapter were produced without fuse ends. Lengths of fused silica stock were cut to 11.5 cm and wiped down following the aLIGO cleaning procedure [97]. They were then inserted into the basic clamps with a 3 mm groove to sit in and secured with a pointed tip screw, as described in chapter 2.3.3. The polishing and pulling laser duty cycle, which is the fraction of the laser period where it is on, were both set to be the same value of 27%. This equates to an output laser power of 125.5 W. This was on par with the laser power output of the CO<sub>2</sub> laser at LHO. The polishing distance was set to 50 mm with the motor voltage set to 0.25 V. This equates to a velocity of 0.0275 mm s<sup>-1</sup> and a total polishing time of 3636 seconds.

After production, the fibres were stored in a storage fridge, shown in figure 3.3. This unplugged fridge has been adapted to allow the storage of fibres on aluminium rails. The fridge was also thoroughly cleaned with isopropanol and the shelves were filled with desiccant to minimise

the humidity within the fridge.

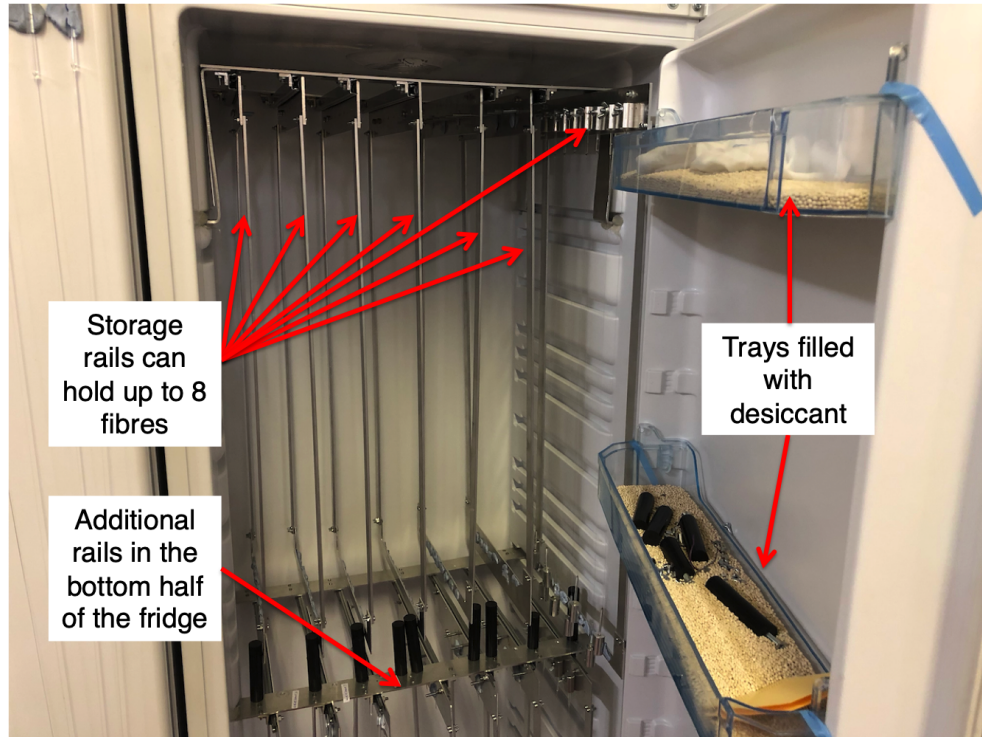


**Figure 3.3:** The fibre storage fridge used to store the fibres when not in use at Glasgow.

### 3.3 Fibre bonding

Previous investigations used cardboard and copper stock holders instead of fuse ends when carrying out strength tests [97] [95] [92]. This allows for a secure grip to be obtained between the clamp and the face of the copper without damaging the stock material, and also due to there not being enough surface area when using fuse ends to secure the stock in place when exerting loads greater than 20 kg onto the fibre. A schematic of how the cardboard and copper was used is shown in figure 3.4. The bonding procedure consists of two main procedures, repeated for both ends of the fibre:

- Bonding copper and cardboard together.
- Bonding the cardboard to the stock.

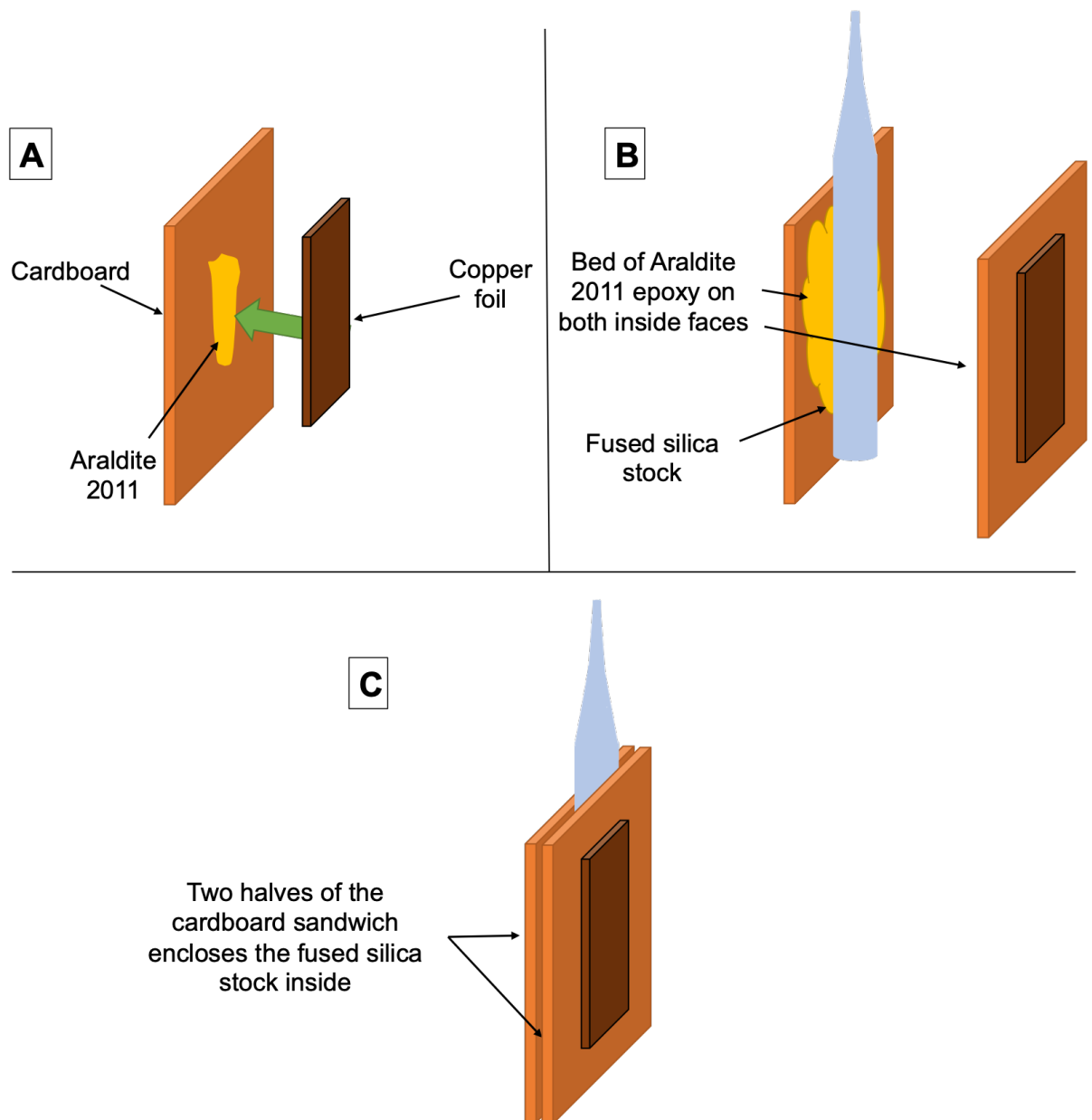


**Figure 3.4:** A schematic of the bonding procedure. Cardboard and copper were first bonded together (A), before two halves were bonded together with fused silica stock in between and left to cure (B) and the final product for testing (C).

### 3.3.1 Cardboard-copper bonding

Cardboard and copper rectangles of rough dimensions  $5 \times 3$  cm and  $3 \times 1.5$  cm, respectively were cut out, as shown in figure 3.5A. Copper was used to increase the grip the clamp has to the fibre being tested to minimise the chance of slippage within the clamps [92]. The dimensions do not need to be exact, just as long as the cardboard was big enough so the copper sheets may be attached. The cardboard was then flattened with a 1 kg mass used as a rolling pin to maximise flexibility of the cardboard. This makes the insertion of the fused silica described later an easier process.

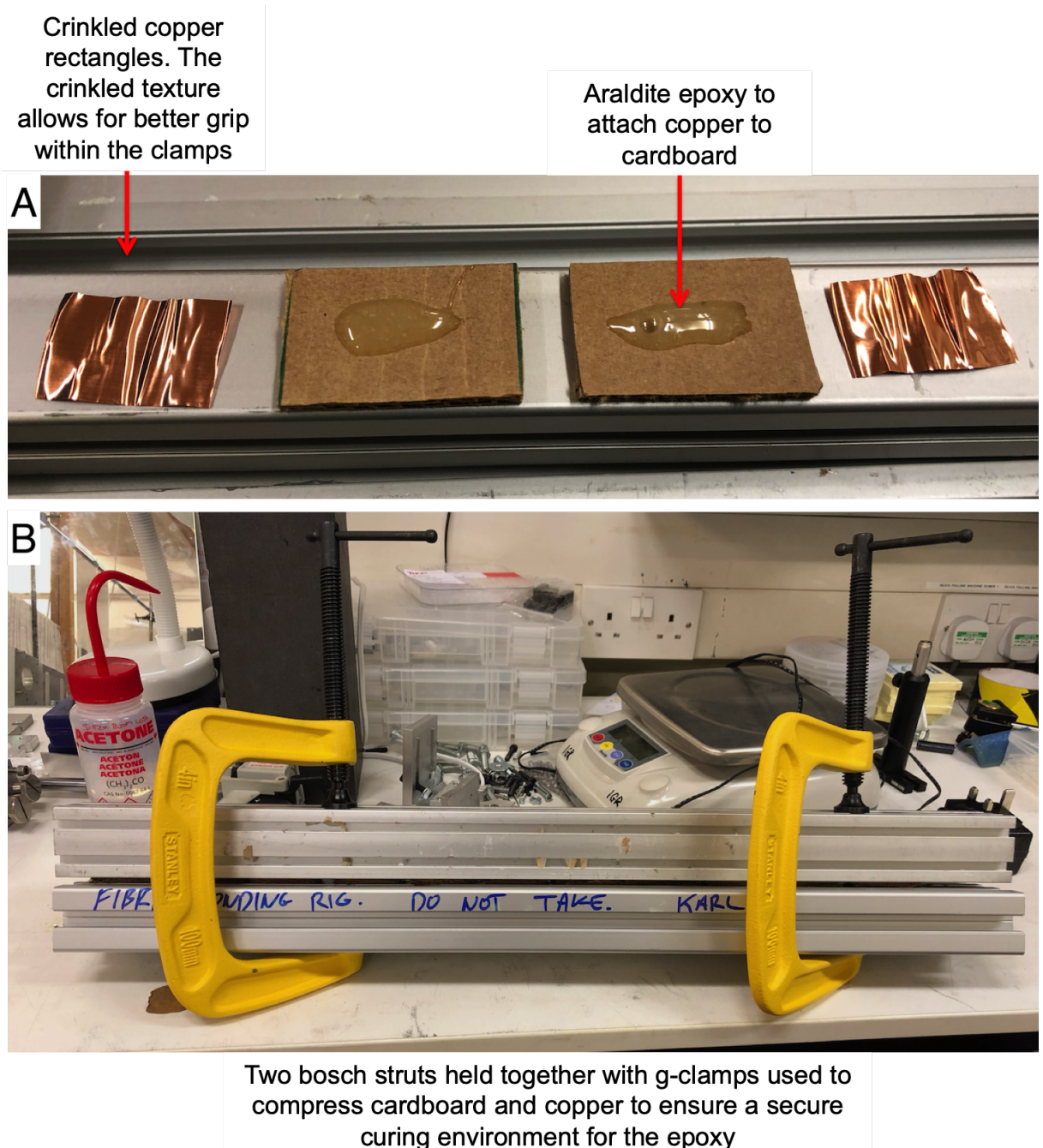


**Figure 3.5:** Cardboard and copper rectangles used to create the cardboard holders

Cardboard rectangles were placed onto a flat surface such as a bosch strut, as shown in figure 3.5A. A 2-part epoxy, Araldite 2011 [116], was then mixed together and a finger nail size pasted onto the cardboard. It should be noted that the use of Araldite is only appropriate for in-air tests and not vacuum tests due to its outgassing nature when in vacuum. The copper rectangles were then placed onto the area with epoxy and then compressed with another bosch strut. The two struts were then clamped together with G-clamps and left to cure for at least 12 hours, as shown in figure 3.5B. Once cured, the clamps were removed and the top strut was removed. The newly bonded cardboard-copper halves could then be removed from the bottom strut. If too much epoxy was applied, they could get stuck to the bosch and will be difficult to remove by hand. If this was the case, tweezers could be wedged into the grooves on the bosch struts to lever out the cardboard-copper halves. This is shown in figure 3.6. For each end of the fibre, two of these cardboard-copper halves were needed. Therefore, four of these halves need to be produced per fibre.

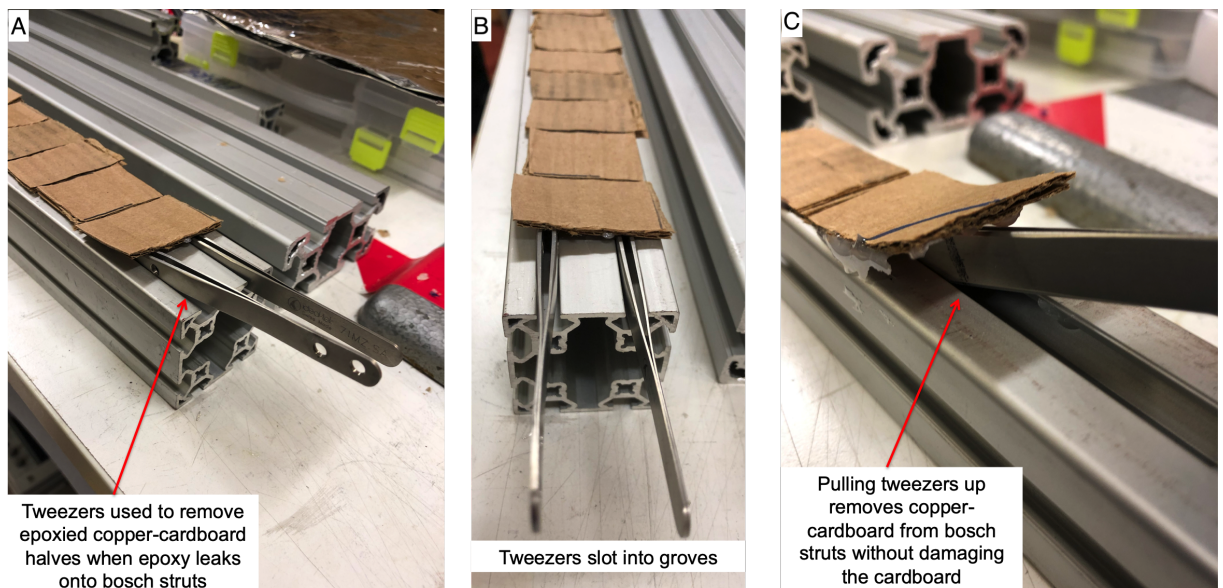


**Figure 3.6:** The method to remove the cardboard-copper sheets when epoxy overflows onto the bosch struts.

### 3.3.2 Cardboard sandwich

There was a lot of handling of the fibre during this procedure so care was taken to ensure nothing comes into contact with the thin section of the fibre, which could compromise the strength of the fibre causing it to fail at a lower load than expected. The bonding procedure to attach the two pieces of cardboard-copper sheets to the fibre to create what will be referred to as a "cardboard sandwich" must be carried out in two separate steps:

- Bottom stock

- Top stock

The order as to which end must be bonded first was not important. Both ends however must not be done simultaneously as this could lead to epoxy running along the stock and potentially onto the fibre itself. The fibre would then have to be discarded. Figure 3.7 illustrates the process carried out to bond the two cardboard-copper halves together to the fused silica stock. Figure 3.7A-D shows the process being carried out.

Prior to installation of the cardboard sandwich, the fused silica fibre was attached to a horizontal rail with blu-tack. This is shown in figure 3.8B. The height of the rail was chosen such that when the top stock was attached to the blu-tack on the rail, the bottom stock just sits below the length of bosch that sits underneath the rail. Two cardboard-copper halves were each attached to a metal plate with a small piece of blu-tack, as shown in figures 3.7A. This keeps the cardboard-copper half in place while handling the metal plate. The two metal plates that were used are attached together with corresponding screws and holes. The plate with the hole could be placed over the screws and secured with wing nuts.

Araldite 2011 2 part epoxy [116] was mixed onto a clean surface and applied to both inner pieces of cardboard-copper halves. There needs to be enough epoxy applied to keep the stock within the cardboard sandwich during testing, but not too much that the epoxy overflows out of the cardboard sandwich and onto the aluminium clamp. This could cause problems with removing the clamp once the epoxy cures, potentially putting that fibre at risk of being damaged. The amount of epoxy that should be applied could be roughly described as thumb size amount.

Once the epoxy was applied to both halves, the back plate was brought around the back of the bottom stock with one hand, while the other hand holds the bottom stock. The pinky finger of the hand holding the plate was placed at the bottom of the plate in line with the applied epoxy. The hand holding the stock then places the stock gently into the epoxy, with the bottom of the stock resting on the pinky finger to help keep it in place. This could be seen in figure 3.7C. The plate might need to be held at a slight angle to keep the stock in contact with the epoxy. Care should be taken to ensure awareness of the fibre at all times so that no contact was made with any object.

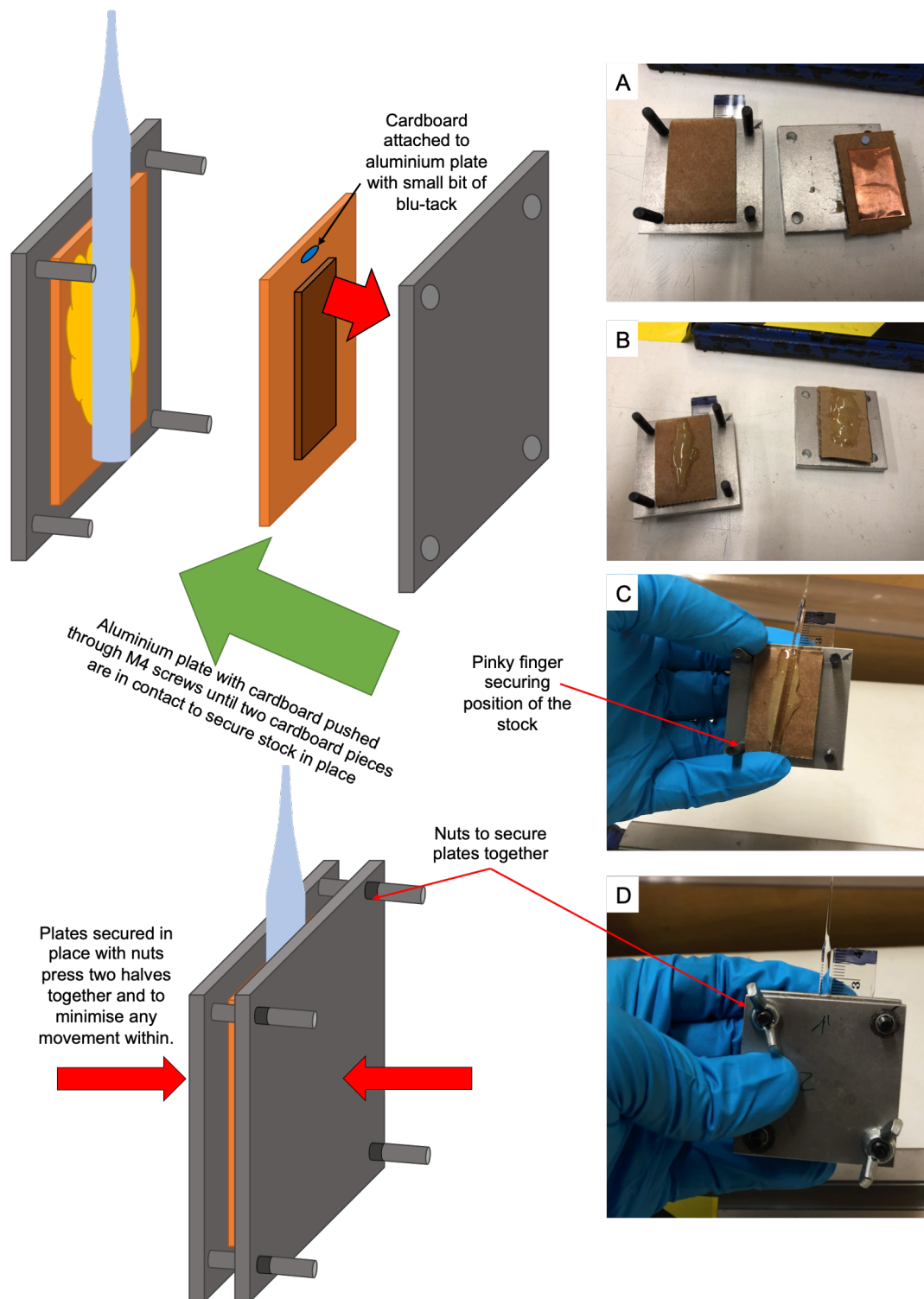


**Figure 3.7:** Illustration of the bonding process to produce the cardboard sandwiches. Photo inset A: Cardboard-copper halves attached to the metal plates with blu-tack. Photo inset B: Araldite 2 part epoxy applied to each cardboard half. Photo inset C: Fused silica stock placed into the epoxy. Note that the plate with the screws was used for this stage. The pinky finger was used to secure the stock in position to minimise movement within the epoxy during handling. The ruler attached to the plate was used at a reference for the length of stock within the cardboard. Photo inset D: Second plate attached by passing screws through the holes and attached with wing nuts. These were tightened as far as possible.

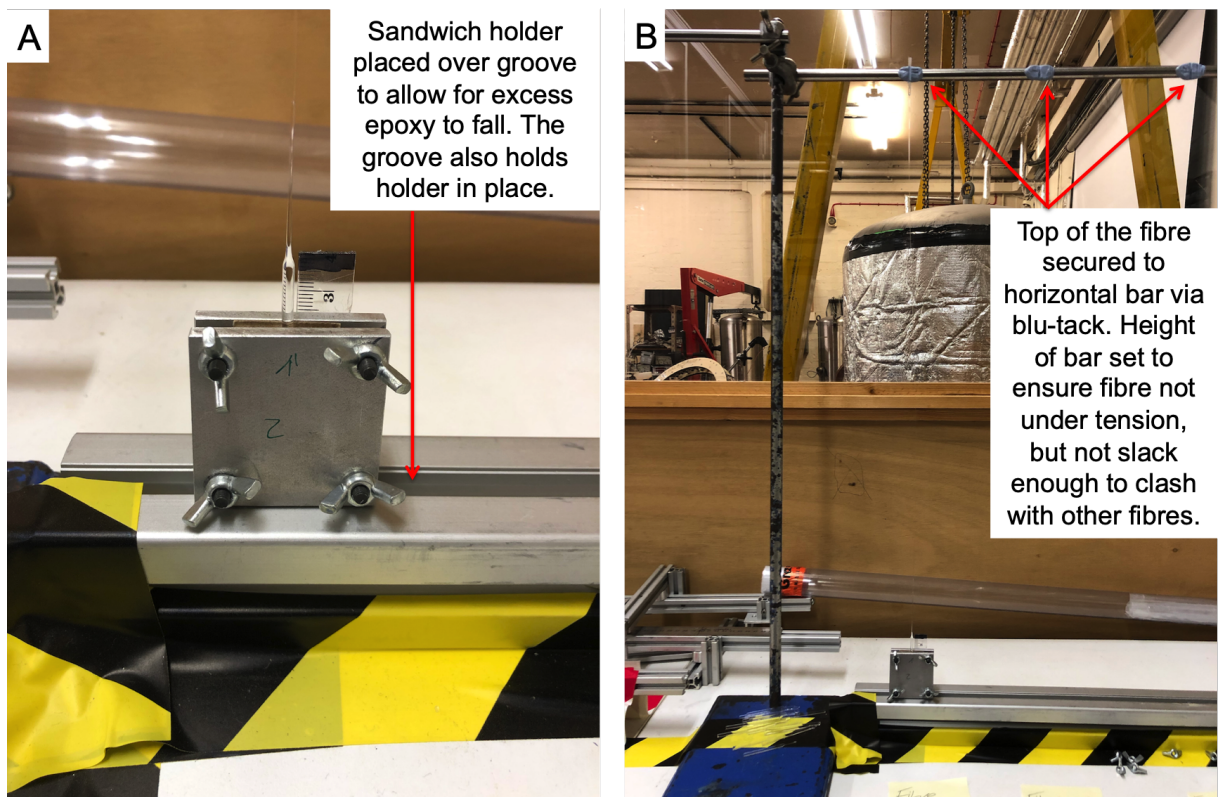


**Figure 3.8:** A: The metal bonding plates sitting on the Bosch strut. B: The cardboard sandwich bonding rail set up. Note that there was no shield or anything protecting the fibres from the surrounding lab environment.

The front plate was then placed through the screw holes and pressed onto the stock. While the plates were pressed together, the wing nuts were then screwed on to secure the plates together to create the clamp. The clamp was then sat on the bottom length of the bosch, sitting within the groove to ensure that the fibre was not under tension during curing. This process was then repeated for the rest of the fibres in the fridge, or until all the spaces were filled up on the rails. The Araldite epoxy data sheet recommends a cure time of 7 - 10 hours when curing at room temperature [116]. Due to this cure time, each clamp was left to cure overnight. This means that the bonding time for one fibre in total was approximately two days.

To remove the clamps, the four wing nuts were removed to allow the front plate to slide out of the screws. The back plate could then be removed, taking care not to hit the stock or fibre with the screws that were attached. The fibre was then flipped such that the bonded bottom stock was attached to the blu-tack on the top rail. The same process as the first bond was then carried out on the top stock.

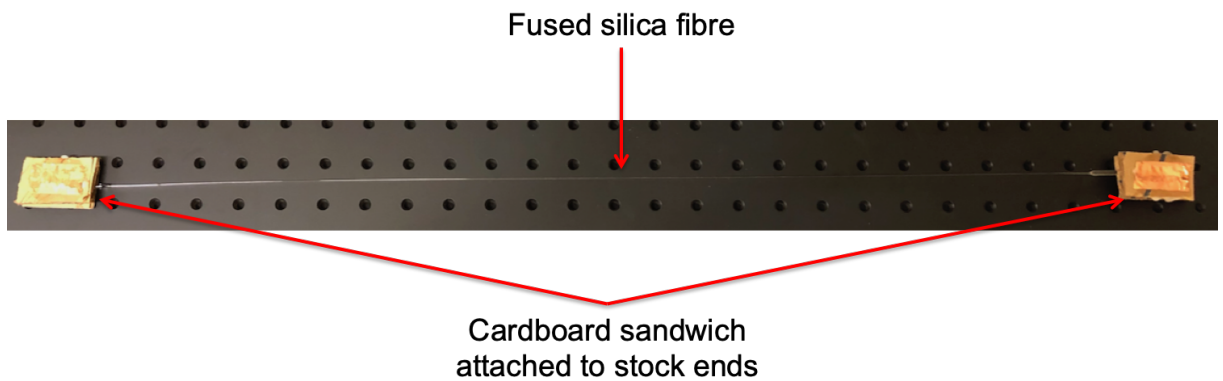


**Figure 3.9:** A fully bonded fibre ready for strength testing. Note that the fibre in this figure was not used for testing and was placed on a table for illustration purposes.

### 3.4 Strength tester

To carry out the destructive testing of the fused silica fibres, the aLIGO fibre strength tester [117], shown in figure 3.10, was used. This strength tester was conservatively rated at 100 kg load, which was more than sufficient for this test. The strength tester consists of two stages:

- Fixed load stage
- Bottom pulling stage

The fixed load stage was attached to an Omega S Beam load cell [118] connected to a digital output reader. This output reader has several readout settings that could be chosen. For this investigation, the ‘record maximum load’ setting was used. This setting shows the maximum load applied to the load meter at all times, until the reset button was pressed. The bottom pulling stage was pulled down via a Parvalux PM10C permanent magnet motor with a double worm gear. The velocity of the motor could be set by the variable speed control potentiometer on the motor controller box. Kill switches were wired to the pulling stage to avoid the possibility of the stage clashing with any components from running too far down during pulling, or too far up during resetting the stage position.

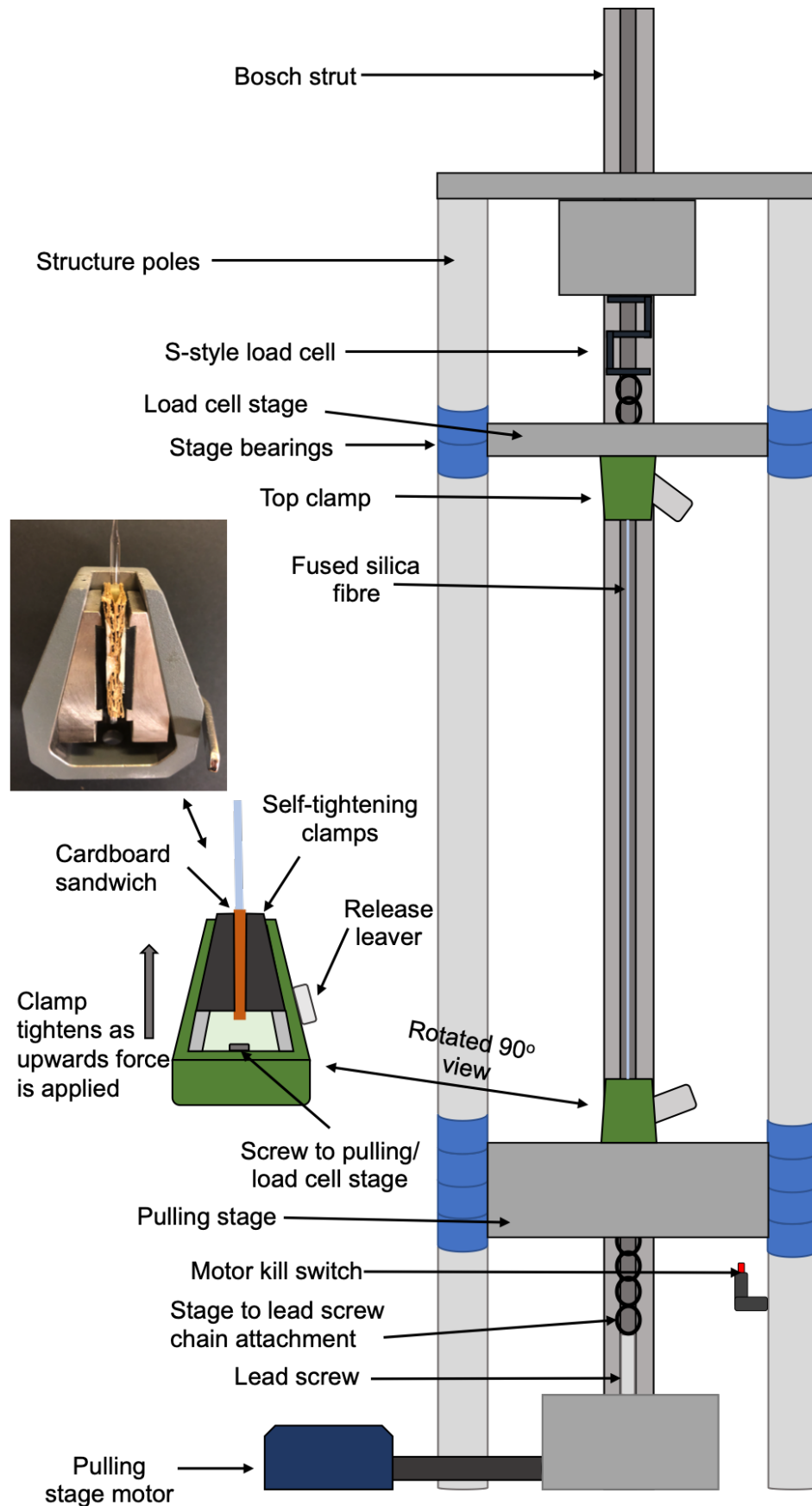


**Figure 3.10:** The experimental set-up of the fused silica fibre within the aLIGO fibre strength tester. Photo inset: Self tightening clamp with cardboard sandwich within.

To secure the fibre in place, self tightening wedge grip clamps were used. These clamps, illustration shown in figure 3.10, have been previously used for strength testing of both fused silica ribbons and fibres, and have a maximum force capacity of 2.5 kN. Care was taken to ensure that both clamps were positioned coaxial to each other. To achieve this, the top stage was moved down to the bottom stage to first check that the plates to which the clamps would be attached to were aligned. The clamps were then installed and position checks were carried out before returning the top stage to the desired position.

The orientation of the clamps was such that the width of the cardboard sandwich would be parallel to the front of the of the strength tester enclosure door. This orientation was chosen so that data could be obtained to see if there was any movement of the fused silica stock inside the clamps during testing. Movement of the stock within the cardboard would have been significant as it would not be mimicking the conditions of a welded fibre in an aLIGO suspension where the stock material was unable to move in this form.

### 3.5 High speed camera

In this investigation, the location of the failure of the fibre was a key area to fully understand. Previous research [92] had shown that the fibre will break at its minimum diameter as this was theoretically the region that was going to experience the most stress. For this investigation, a high speed Phantom VEO 410L camera [119] was set up to record the fibre breaks. The settings used to record the fibre breaks is shown in table 3.1 and the set-up shown in figure 3.11.

Due to previous experiments damaging the enclosure door obscuring the view into the enclosure, a viewing window had to be cut into the door to make it easier for the strength tester to see the fibre. Six halogen lights were used to illuminate the fibre to help the image quality on the high speed camera. A significant amount of time was spent ensuring that the lights were in the optimal position for the camera. If a light was not in an optimal position, the fibre on the camera will have a shadow or a bright reflection appear over it which could result in parts of the fibre not being clearly visible. ‘Phantom Camera Control 3.3’ was used to record the data and control the camera settings and CineViewer 3.3 was used to analyse the recorded footage [120]. To record the data, the trigger delay setting was used. The camera would continually record data over a 5 second window until the fibre breaks. The moment the fibre breaks, the user presses the trigger button which then saves the last 2-3 seconds of data, depending on the setting. The recorded data could then be analysed to find the breaking point on the fibre.

**Table 3.1:** The high speed camera settings used in this investigation.

Setting	Value
Frames per second	17000
Exposure	70 $\mu$ s
Trigger delay	1 s

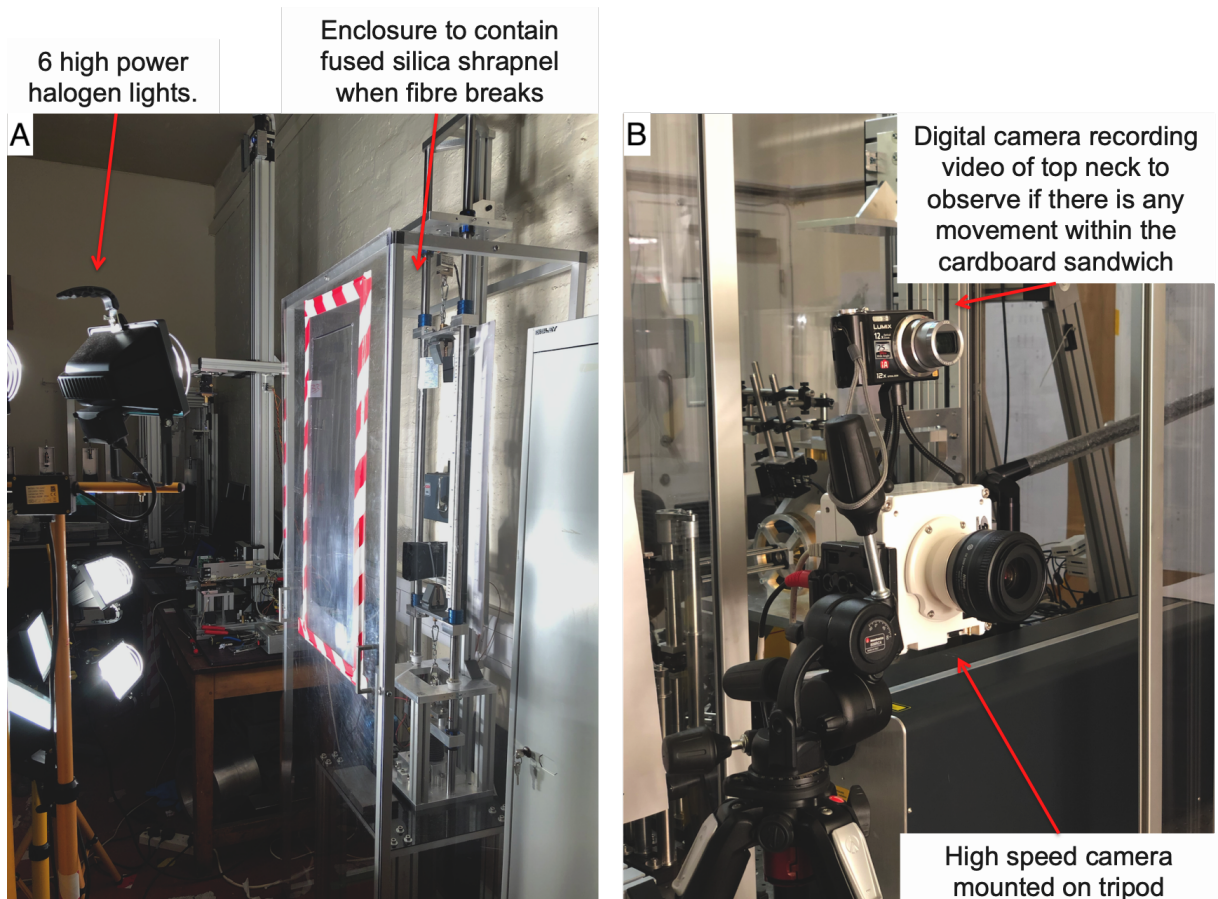


**Figure 3.11:** A: The enclosure around the strength tester to contain the aftermath of the destructive testing. The halogen lights were used to provide enough light to the fibre to be seen in the high speed camera. B: The high speed camera used for this investigation with the digital camera placed on top that will be utilised later in this chapter.

### 3.6 Beam misalignment

As mentioned previously, the current condition set out in the selection process was to discard any fibre that has an angle between the stock and the Thermoelastic Nulling Region (TNR) greater than  $1^\circ$  degree [112]. Prior experience with pulling aLIGO fibres indicated that the most likely cause of angular misalignments in the production process was from the non-uniform distribution

of heat around the fused silica stock. To test this hypothesis, two types of fibres were produced:

- Fibres with an aligned beam
- Fibres with a deliberately misaligned beam

Judging the severity of the misalignment of the beam distribution around the fused silica stock by eye was difficult. Through welding goggles, the beam distribution could look near enough perfect, when in reality it could still have some level of deformity. Also due to laser safety and the layout of the bench, the user could not get up close to inspect the heated region. The advantage of carrying this investigation out on the Glasgow pulling machines was the addition of two up close monitoring cameras with ND filters [92], as previously described in chapter 2.4.3. These filter out the vast majority of the brightness from the radiated heat, allowing the heating region to be monitored in a more precise, repeatable and quantified way. This is seen in figure 3.12 where the beam distribution appears uniform on both images.

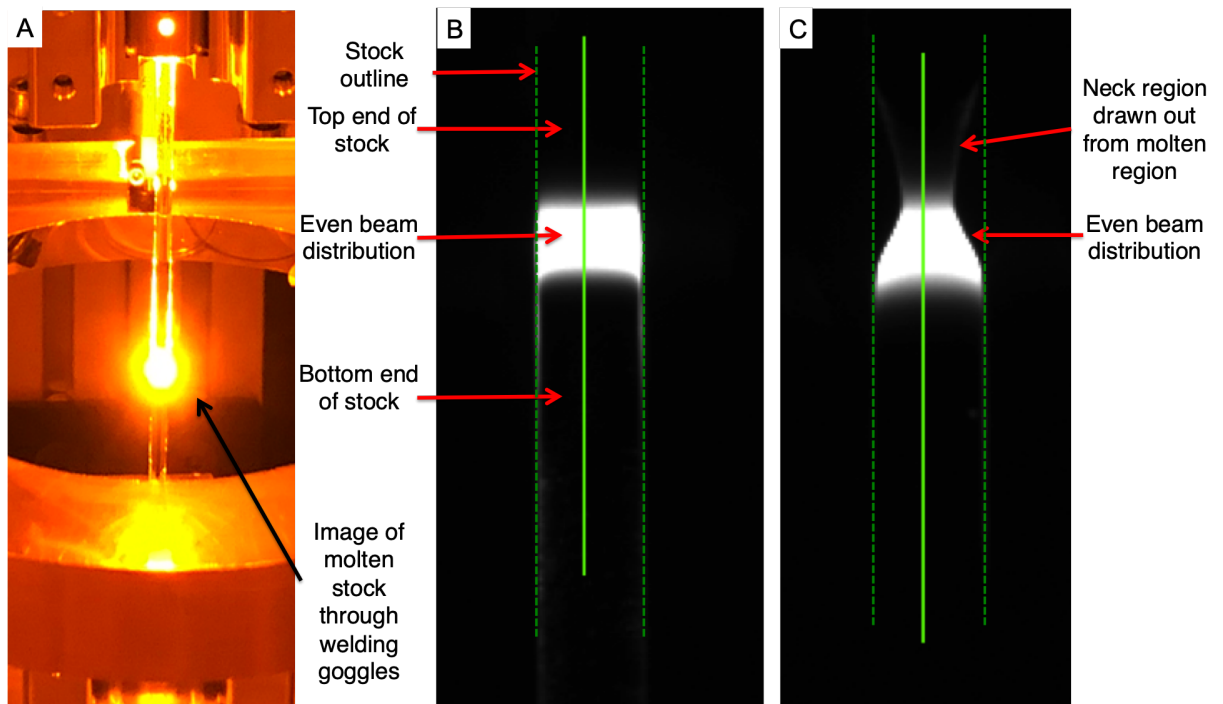


**Figure 3.12:** A: A view of the molten fused silica through welding goggles to show the difference in intensity that was viewed. B: Screenshot of the beam distribution of an aligned beam around the fused silica stock during initial heating. C: Aligned beam around the fused silica stock during the start of the pull.

Figure 3.13 shows an example of a misaligned beam distribution around the fused silica stock. This particular example shows a non-uniform distribution around the stock when compared to figure 3.12C.

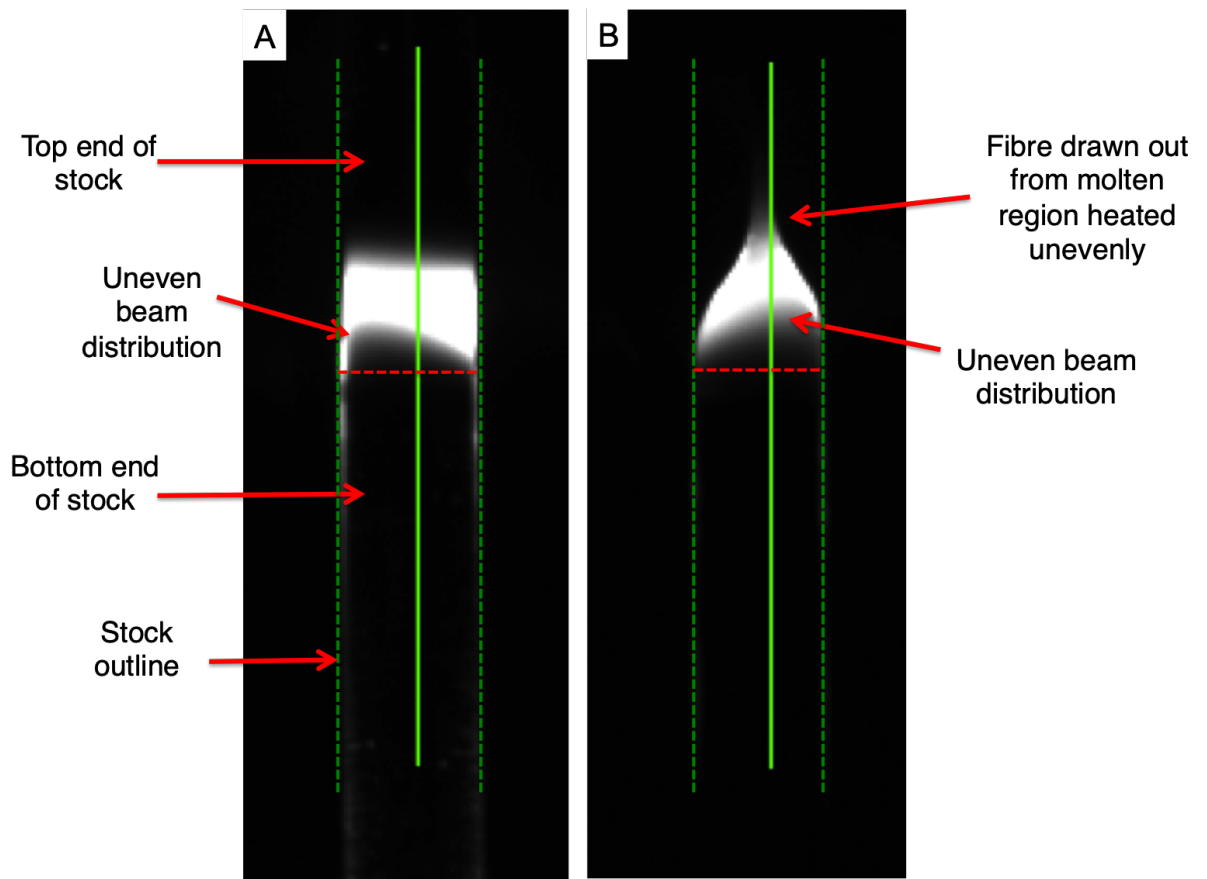


**Figure 3.13:** Screenshot of the misaligned beam distribution around the fused silica stock. A: Misaligned beam around the fused silica stock during initial heating. B: Misaligned beam around the fused silica stock during the start of the pull.

The procedure at LHO for pulling fibres was that the pulling machine was aligned at the start of the day before fibre production. As mentioned previously in chapter 2, the alignment process of the pulling machine at LHO could be very subjective due to the fact it was carried out visually instead of through a camera system. Since this investigation wanted to look at the effect of misalignment, the pulling machine was misaligned at the start of the day before production fibres were pulled. As the pulling machine will naturally, ever so slightly, misalign itself through a day, a batch of polished fibres would be produced through the day without making any attempt to fix the alignment. This gradual misalignment was the result of the laser heating up the kinematic mounts holding the mirrors, as well as the temperature within the lab which could increase when the laser, vapour extractor and laser cooler were running for long periods. This temperature change in the kinematic mounts causes the screws holding the mirrors, as well as the position of the mount to move over time as the material heats and cools down when the laser was on and off, respectively. The mirror mounts delivering the laser beam to the pulling machine used in this investigation have small fans pointed to the mirror mounts that help reduce the amount of heat dissipated into the mounts. Previous investigations [111] have shown that the mirror mounts could get as hot as  $110^{\circ}\text{C}$  with the laser at full power, but

with the fans on, this temperature falls to approximately 60°C. As of writing this thesis, fans were not installed onto the mirror mounts at LHO, but were planned to be installed in the future.

At the start of each pulling day, the machine was "aligned" prior to fibre production. As the hypothesis was that the beam distribution was the cause of the introduction of angles during the production process, the daily alignment consisted of deliberately misaligning the beam. To do this, a fused silica stock length wrapped in teflon tape was placed into the clamps to observe the beam distribution. The main adjustment made was through the vertical jack on the periscope mirror system, and the top kinematic mirror mount on the top mirror of the periscope (as shown previously in chapter 2.4.2). To get a beam distribution with enough asymmetry to introduce an angle into the fibre, it only took as little as half a turn on the micrometer adjustments on either the vertical jack or the kinematic mount. This equates to approximately 0.25 mm travel to give the misalignment shown in figure 3.13.

The production of fibres that achieved the criterion of having angles less than 1° criteria had to involve constant alignment checks during polishing, and initial heating before the pull commenced. No alignment of optical components occurred once the pulling process was initiated due to laser safety, though this has been tested and shown to help matters [111]. In total, 58 fibres were produced for this investigation.

## 3.7 Results and analysis

### 3.7.1 Fibre profiles

The resulting dimension of the fibres were measured using the aLIGO fibre profiler [121] [122], shown in figure 3.14. This apparatus measures the diameter of the fused silica fibre all along the length of the fibre, as well as the shape of the fibre at the top and bottom of the fibre that includes the stock, TNR and part of the thin regions. It consists of two perpendicular Unibrain Fire-i digital board monochrome cameras [123] that were attached to a motorised stage. Attached to the camera was a lens system that gives a magnification of  $\times 1.75$  and  $\times 1.9$ . The two cameras will be referred to as 'camera 1' and 'camera 2' for their respective magnification values. Opposite the cameras were high powered LEDs directed at the fused silica fibre in the profiler. The fibre creates a shadow that was cast upon the camera sensor. The custom LabVIEW program [122], utilises an edge detection algorithm to determine where the edge of the shadows were on either side. A pixel distance measurement between these two locations could be carried out to determine the width of the fused silica fibre. This pixel count could be converted to micrometres by calibrating the profiler with a  $(500.00 \pm 0.12 \mu\text{m})$  slip gauge. The motorised stage moves the cameras along the entire length of the fibre at set intervals. These intervals were measured using a SIKO MSK320 magnetic encoder [124] which measures counts along a magnetic strip and converted to millimetres through the LabVIEW program. Details on how this encoder works is

discussed later in chapter 5.2.2.

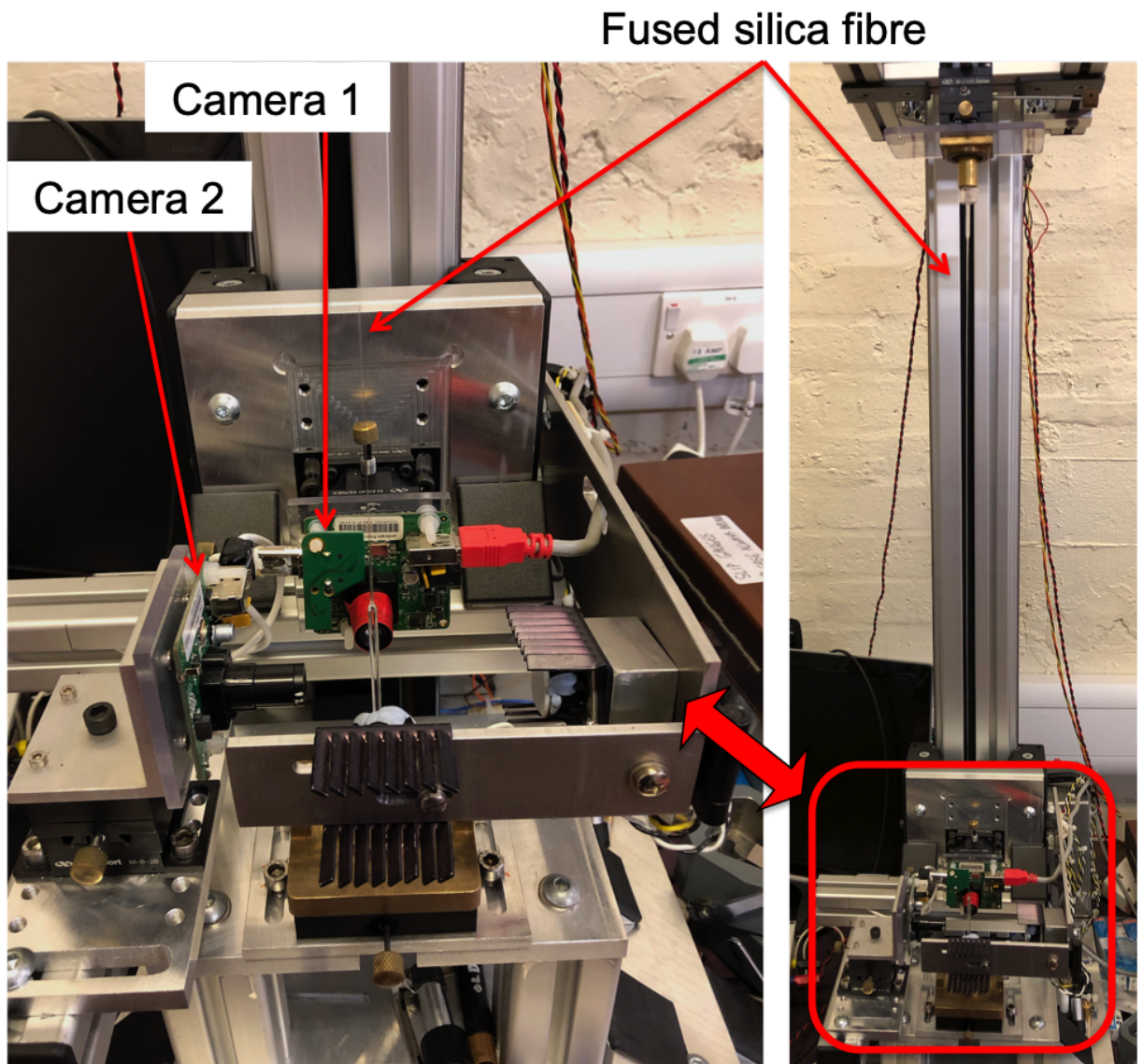


**Figure 3.14:** The aLIGO fibre profiler at Glasgow used to profile the fibres used in this investigation.

The files for the profile of a fibre were created in three different stages:

- Bottom neck
- Middle
- Top neck

The bottom and top neck scans the entire length of the fibre that was captured on the screen. This length was typically 4 mm. The stage then moves 0.3 mm before the repeating the process. This allows more detail to be obtained in this region as the camera scanned over every pixel

where an edge was observed. The value of 0.3 mm also allows for an overlap of data points after each stage movement to ensure that no section of the fibre was not profiled. The middle section only takes 6 data points at a position before taking an average of the 6 diameter values. The files could then be combined into one Excel spreadsheet. The settings used in this investigation for the profiler are in table 3.2.

**Table 3.2:** Values for profiler settings used during this investigation.

Setting	Value
Bottom neck scan steps	800
Top neck scan steps	720
Middle scan steps	20
Calibration tool	500 $\mu\text{m}$ slip guage
Calibration camera 1	57.572
Calibration camera 2	84.654

Both bottom and top neck scans comprise of taking diameter readings along the entire length of the image on the screen. The position of the the pixels that were measured were also recorded. This was important when it comes to measuring the angle alignment of the fibres, and will be discussed in detail in the following subsection. Once a measurement was taken, the motorised stage moves up 0.3 mm before repeating the process. The distance over which this was carried out over was pre-determined by the user prior to starting the LabVIEW program. For the middle scan, an average of 6 measurements was taken to measure the diameter of the fibre at that section. Once taken, the motorised stage moves up a pre-set distance that was also set prior to starting the LabVIEW program. Table 3.3 shows the distance values, in counts (1 count = 0.1 mm), that were used for profiling fibres in this investigation:

**Table 3.3:** aLIGO fibre profiler settings that were used for profiling fibres in this investigation.

Variable	Value (counts)
Bottom neck scan total distance	800
Middle scan total distance	230
Top neck scan total distance	720

### 3.7.2 Python 3 fibre analysis script

There were two particular areas of interest at each end of the fibre that were investigated for angular misalignments:

- Angles between the stock and the TNR of the fibre, referred to as ‘stock-to-TNR’.

- Angles between the TNR and the thin section of the fibre, referred to as ‘TNR-to-thin’.

Figure 3.15 shows the regions of the fibre labeled with their corresponding part as ‘stock’, ‘TNR’ and ‘thin’. As mentioned previously, fibres with stock-to-TNR angular misalignments greater than  $1^\circ$  were discarded from selection for aLIGO suspensions [112]. This applies to both perpendicular camera angles. Therefore, fibres produced in this investigation with angles less than  $1^\circ$  were considered to be fit for purpose and will be assigned as ‘control’ fibres. In this scenario, fibres that fall into the control group could have angles between the TNR-to-thin greater than  $1^\circ$ , as this section was not part of the criteria.



**Figure 3.15:** A fibre profile of the top end (TE) scan of fibre 58 with corresponding labels to indicate the different regions of the fibre.

The fibre profiler records fibre alignment data during the bottom and top neck scans. As discussed previously, this involves scanning across the length of the edge of the fibre on the screen before moving position to the next point. The pixel that detects the edges of the fibre on either side was converted to the equivalent distance from the edge of the sensor in micrometres. This data could then be plotted against the position of the profiler stage to show the shape of the fibre that was obtained during that scan. All the data from these scans could be combined and plotted to give the plot shown previously in figure 3.15. Due to interest in calculating angles in the two listed areas above, this resulted in scanning a much larger distance at both ends of the fibre to cover both full necks and start of thin fibre section than standard aLIGO fibres would scan over, by almost a factor of 2. The consequence of this was that each neck file for the two sets of camera data contain between 80,000 - 100,000 data entries per column. With 8 columns of data total, each file consisted of between 640,000 - 800,000 individual data points.

A Python script was developed to deal efficiently with large datasets by the author to process this data. This script was written in Python 3 [125] through Jupyter notebooks [126] (see appendix A). This script carries out several different tasks related to analysing and characterising the fused silica fibres. The script works through the following stages:

- Imports the data from the Excel files produced from the fibre profiler.
- Assigns the columns of data to variables.
- Finds the minimum diameter of the fibre and its corresponding location along the length. The uncertainty in the minimum diameter is stated to be 1.3% [121] [122].

- Creates various plots of the top, middle and bottom sets of data. For the top and bottom sections, this includes plotting the alignment of the fibres.
- Calculates the angles between the stock and the TNR region, and the TNR and the thin region using both profiler cameras for both top and bottom ends.
- Calculate the maximum stress value at the minimum diameter location of the fibre.
- Calculates the stretch of the fibre under a given load. This load would be the maximum load that would be obtained from the strength tester at point of failure.
- Creates a new fibre profile for when the fibre was stretched to its maximum extension.
- Allows the breaking region to be highlighted and locations compared between breaking region and minimum diameter region.
- Calculate the breaking stress value at the location of the breaking region which was obtained through the high speed camera footage.
- Saves all plots produced as .png files, as well as creating a .txt file with all the relevant diameter and angle information within.

Figures 3.16 and 3.17 show an example of the bottom and top end data sets that were obtained from the two cameras.

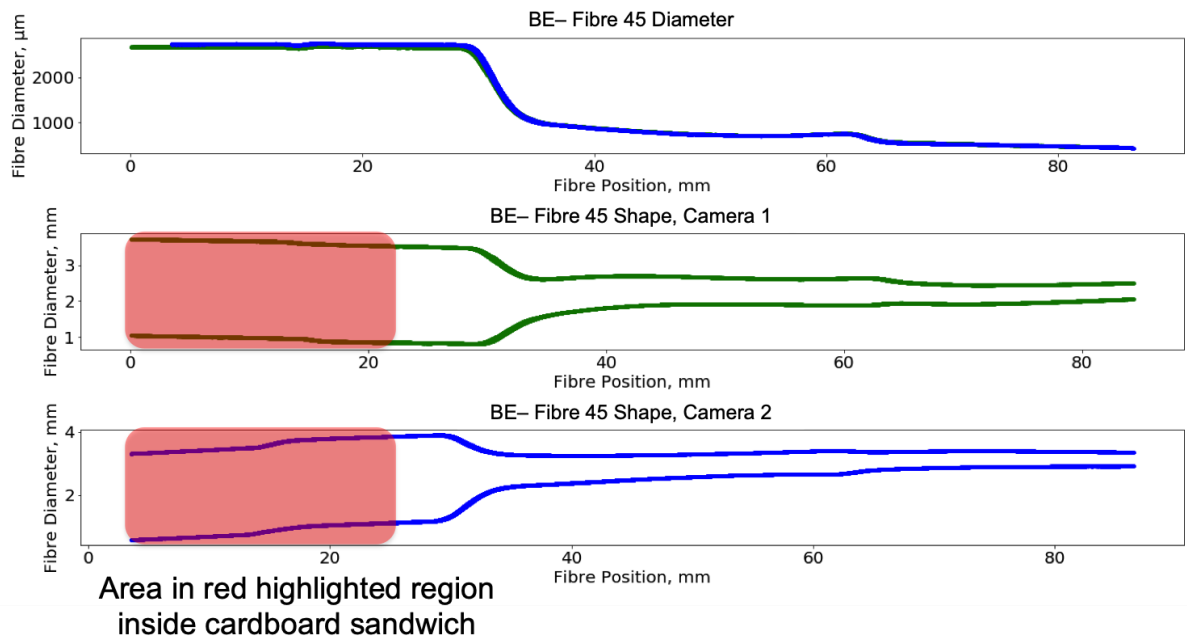


**Figure 3.16:** The bottom end (BE) scan profile for cameras 1 and 2 of a selected fibre. Note the bottom two graphs contains the data used to calculate the angles within the bottom end of the fibre. The highlighted region indicating the section within the cardboard sandwich was determined through the use of a ruler attached to the aluminium plates during the bonding process. The cardboard sandwiches were attached after the profiling process was completed.

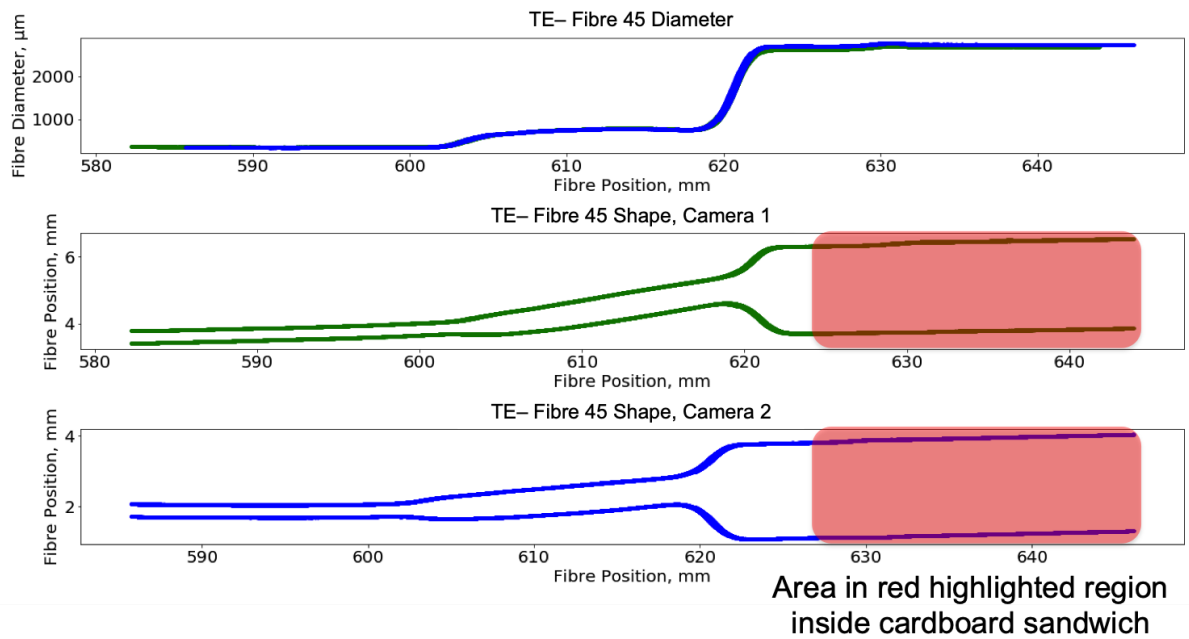


**Figure 3.17:** The top end (TE) scan profile for cameras 1 and 2 of a selected fibre.

### 3.7.3 Fibre angle calculations

To calculate the angle from the plotted data, the data from the neck files were sliced into 6 different sections for both the top and bottom ends:

- Edge 1 and edge 2 of the stock section
- Edge 3 and edge 4 of the TNR section
- Edge 5 and edge 6 of the thin section

An example plot of this data is shown in figure 3.18. The edge label format in this figure, 'Edge (1-2).(1-6)' indicate camera 1 or 2, and an edge 1-6.

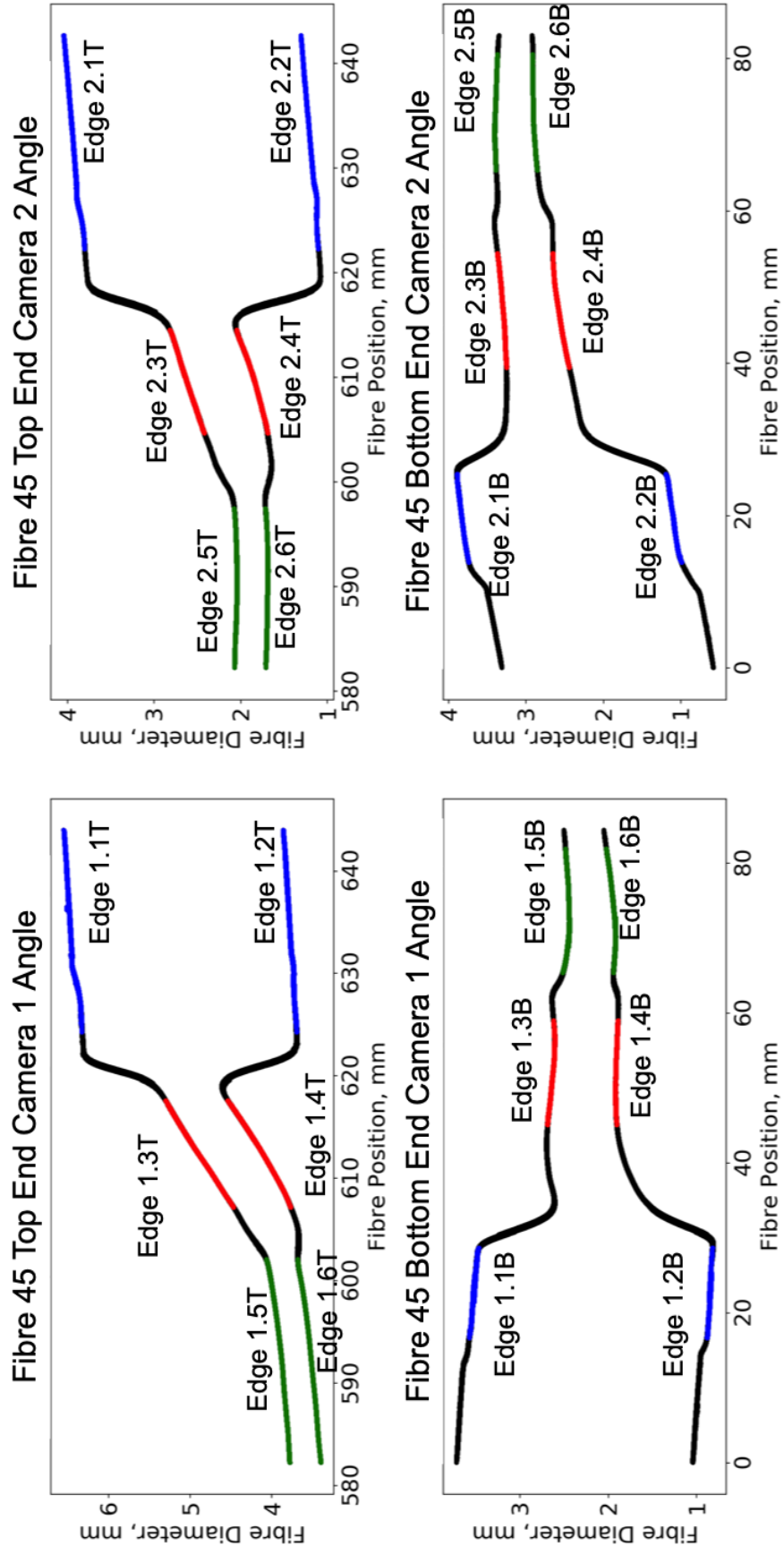


**Figure 3.18:** An example of the 6 different sliced sections of the profiler data, with the full fibre profile of this region in black.

Each of these edges contained anywhere between 10000 - 40000 data points depending on the length of the edge. A line of best fit was then calculated for each edge section using the `scipy.stats.linregress` function [127]. This was a function from the SciPy package in the Python script that calculates a linear least-squares regression. The gradient of the fit, as well as the standard error in the fit could be obtained through this function. Angles between the stock-to-TNR and TNR-to-thin section were then calculated. Using the following example of edges 1 and 3, the angle between the stock and TNR were calculated by:

$$\theta = \tan^{-1} \left( \frac{m1 - m3}{1 + (m1 \times m3)} \right) \quad (3.1)$$

where  $m1$  and  $m3$  were the gradients of the best fit lines for the edges 1 and 3 respectively. This equation was derived from the  $\tan(A \pm B) = \frac{\tan(A) \pm \tan(B)}{1 \mp \tan(A)\tan(B)}$  identity to calculate the angle between two gradients, shown in figure 3.19. This was repeated for the opposite side of the fibre and both values were averaged to obtain the angle between the stock-to-TNR region. This was repeated for the TNR-to-thin region and for the second perpendicular camera angle. The uncertainty in the angle calculated can be extracted from the `scipy.stats.linregress` function. Though it differs slightly for every fibre, the uncertainty was of the order  $0.01^\circ$ . An example of a top fibre end with labelled angles is shown in figure 3.20, with a photograph comparison shown in figure 3.21. The slight difference between the angles between these two figures was due to the fact that the photograph angles were plotted out along the edge by hand, instead of through a fitting function. The two values however were very similar, showing that the fitting in the Python code was calculating the angles correctly.

The largest angles on the fibres were always at the top end of the fibre. The bottom end of the fibre would rarely result in an angle greater than  $1^\circ$ . This could be due to the fact that the pull at the start has more material to heat and draw the fibre from, which was not as greatly affected from the beam misalignments as the end of the pull where the angles occur. The number of fibres obtained for various ranges of angles between the stock and TNR region are shown in table 3.4, where fibres were designated to an angle range corresponding to its maximum angle from either camera perspective.

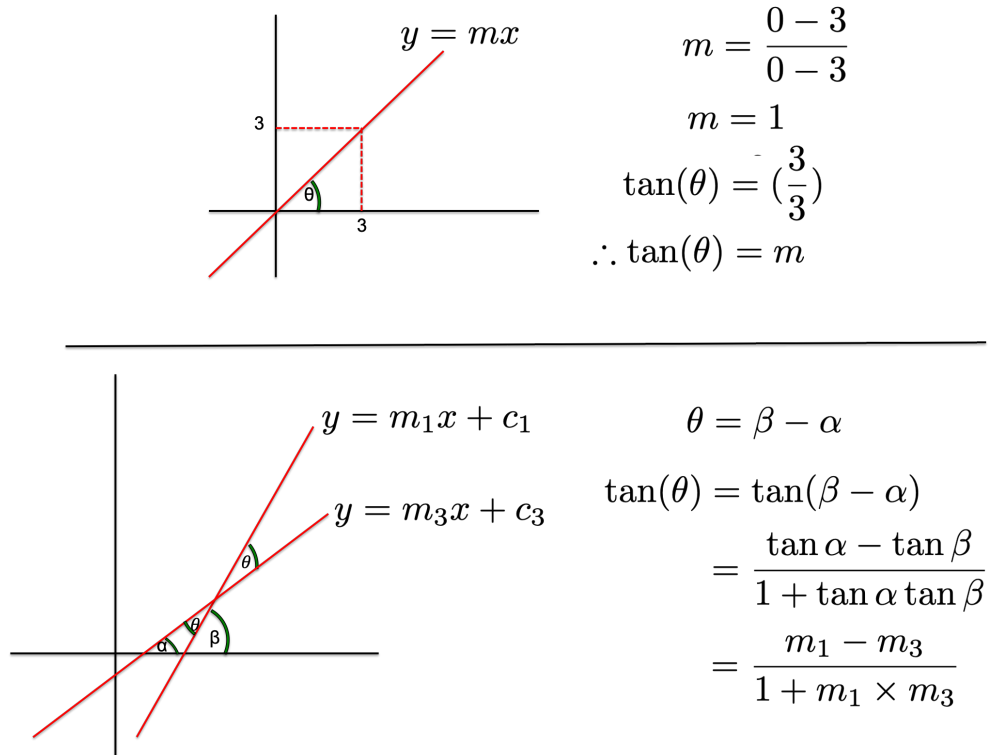


**Figure 3.19:** Illustration showing how the angle between two lines could be calculated using the  $\tan(A \pm B)$  identity.

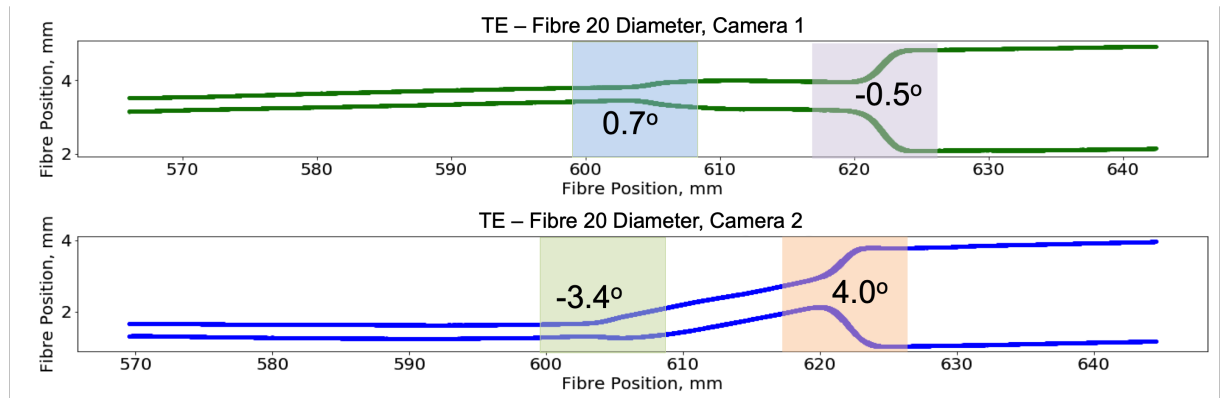


**Figure 3.20:** Annotated angle profile of fibre 20 that was tested in this investigation.

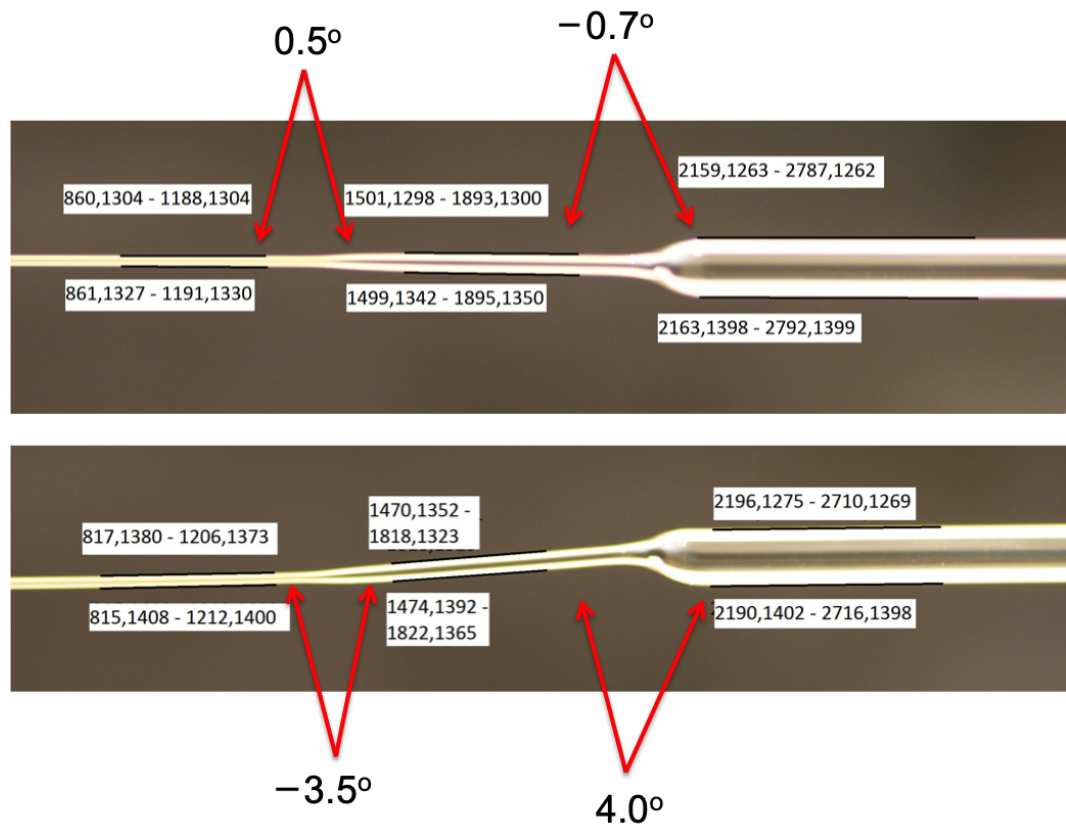


**Figure 3.21:** Photograph of fibre 20 in figure 3.20 showing the coordinates of the edge lines used to calculate the angle in the fibre end for comparison to the angles obtained from the Python script.

**Table 3.4:** The quantity of fibres obtained with various stock-to-TNR angles. Note these were all top fibre end measurements as that was where the maximum angles occur.

stock-to-TNR fibre angle, $^\circ$	Quantity
0 - 1	15
1 - 2	15
2 - 3	8
3 - 4	3
4 - 5	2
5 - 6	1

**Table 3.5:** The quantity of fibres obtained with various TNR-to-thin angles.

TNR-to-thin fibre angle, °	Quantity
0 - 1	6
1 - 2	21
2 - 3	10
3 - 4	4
4 - 5	2
5 - 6	1

**Table 3.6:** The quantity of fibres obtained with various net angles.

Net fibre angle, °	quantity
0 - 1	42
1 - 2	2

From table 3.4, 15 of the 44 successfully tested fibres would satisfy the criteria of having a degree less than  $1^\circ$  between the stock-to-TNR region. There were less fibres  $> 3^\circ$  due to production restrictions. To get angles greater than  $3^\circ$ , a significant beam misalignment was needed around the stock. This resulted in a higher laser power, up to approximately 200 W, being needed to heat the fused silica stock up to the required temperature. This was approximately 80 W greater than the maximum LHO laser power at the time of writing this thesis. The misalignment needed also meant that the CO<sub>2</sub> beam was getting physically close to the edges of the rotating and conical mirrors within the optical system of the pulling machine. This was determined via observation of the position of the red alignment beam. In the interest of safety and to keep pulling conditions as close to aLIGO specifications, which would not have had such severe misalignment as it would be visible by eye and discarded, it was decided to minimise the number of fibres with angles greater than  $3^\circ$ .

### 3.7.4 Strength tests and breaking locations

An intensive investigation was carried out to locate the breaking locations of the fibres that were tested. To do this, the high speed camera footage for each fibre was analysed frame by frame to locate where the fibre broke. It was key to know what to look for when locating the breaking location. Figure 3.22 shows three consecutive frames from the high speed camera data. Frame A shows the frame immediately prior to the fibre breaking, which is shown in frame B. Frame C was the frame immediately after the fibre breaking frame. Initially, it was easy to misinterpret the fibre breaking at the TNR due to the explosive nature of the failure. This was actually due to the shockwave that travels through the fibre from the breakage and reaching the neck where the

diameter change from 400-800  $\mu\text{m}$  occurs. The key indication as to where the fibre breaks was to observe the direction towards which the fibre debris travelled in from either side of the breaking region. When the nature of the direction was established, the break location could be found by zooming into the fibre in that area and analysing the footage frame by frame. Depending on the timing of the break, the break location could vary from a narrow to a wide spread depending on when the frame on the high speed camera takes the image. An example of a wide and narrow spread is shown in figures 3.23 and 3.24, respectively.

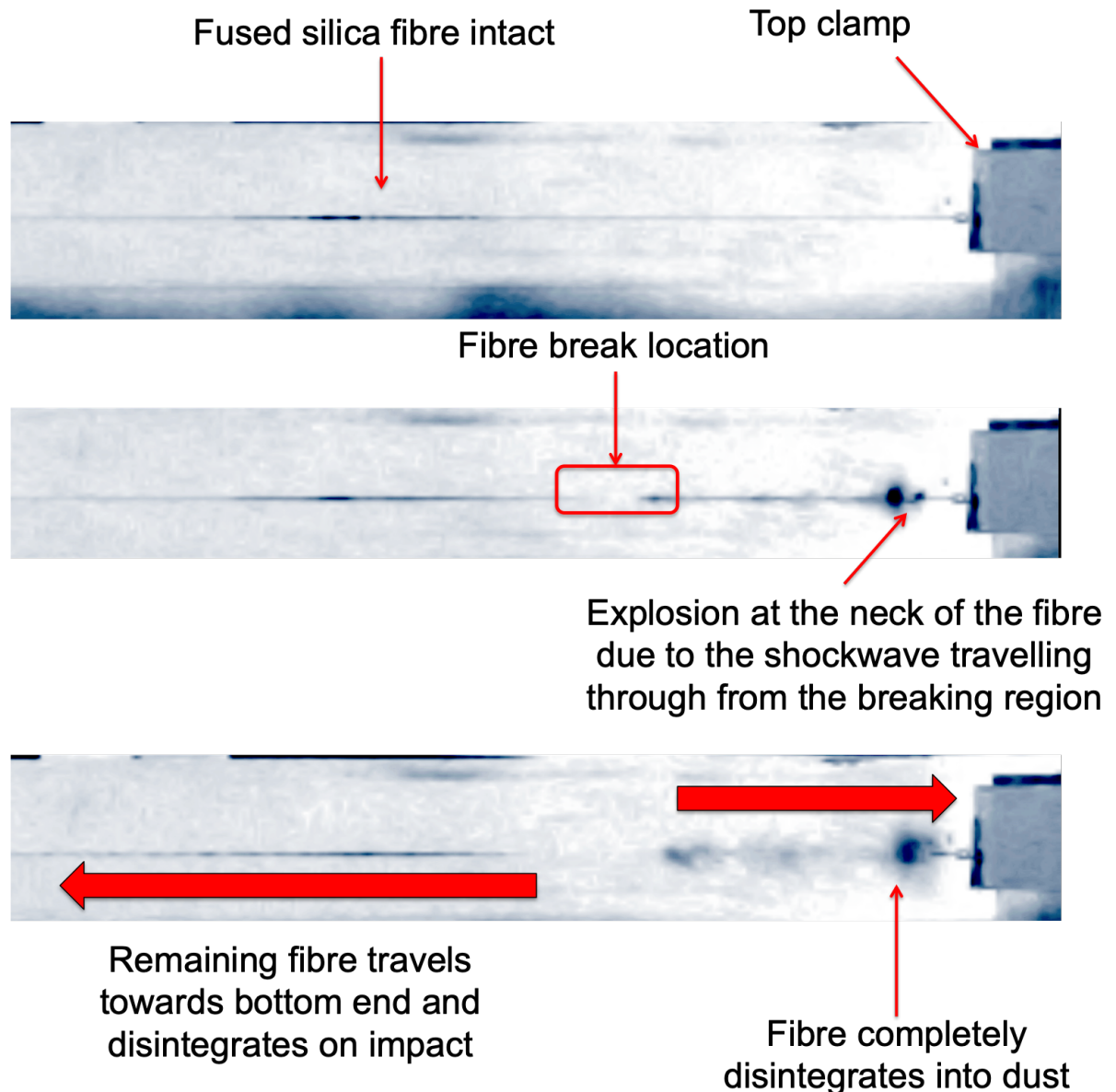


**Figure 3.22:** Three consecutive frames from the high speed camera footage of a fibre breaking. Note the image colour has been inverted to make it easier to observe the fibre. Top: Frame prior to the fibre breaking. Middle: Frame fibre breaks. Two artefacts of interest in this frame were the explosion for the TNR, which could be misinterpreted as the breaking region, and the actual breaking region highlighted in the red box. The break in the fibre in this region could clearly be seen. Bottom: Frame after fibre break. Remaining fibre from the left side of the break travels towards the bottom neck. Fibre on the right side of the break has disintegrated.

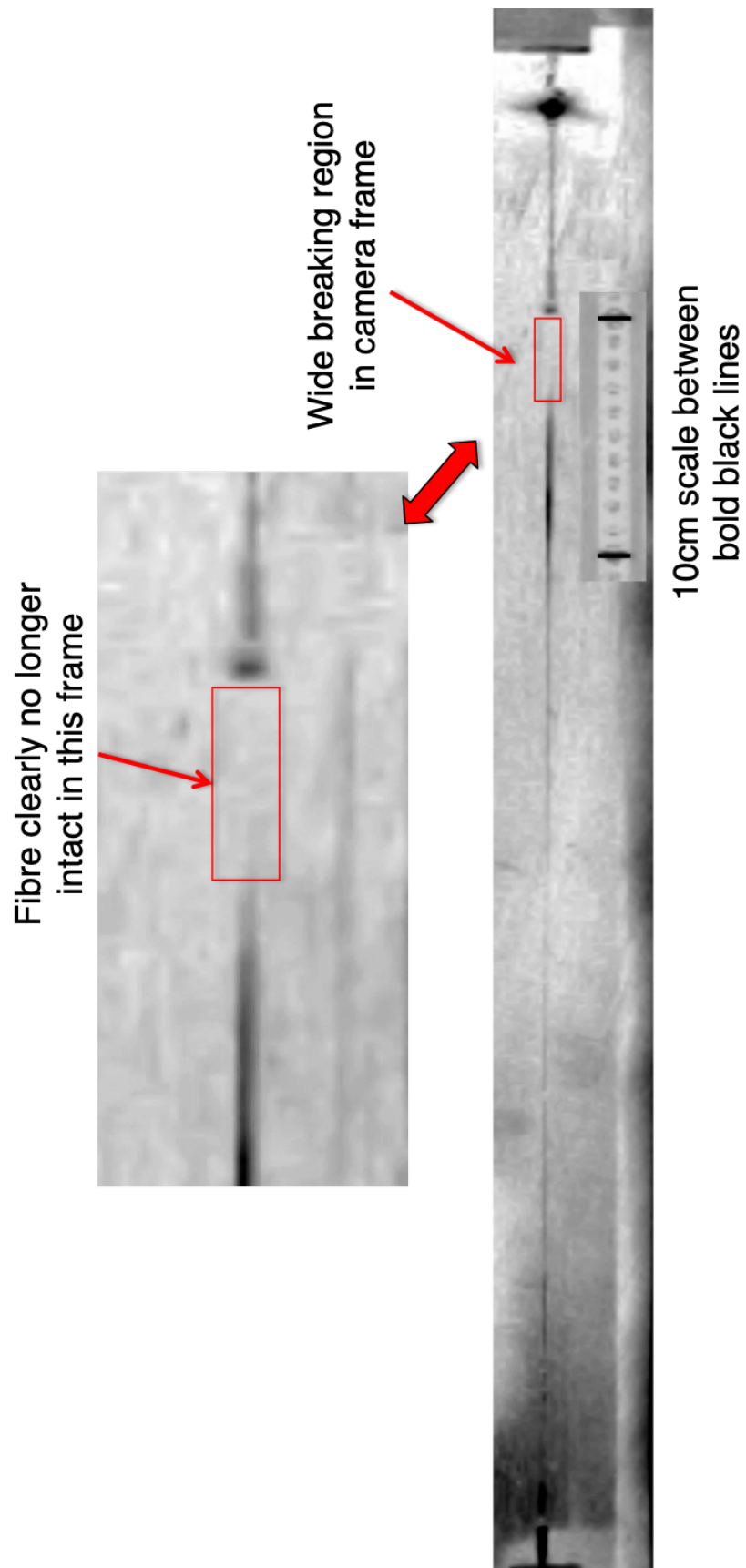


**Figure 3.23:** An example of a wide spread break location from the high speed camera footage. Note that this was the first frame where the fibre appears to break.

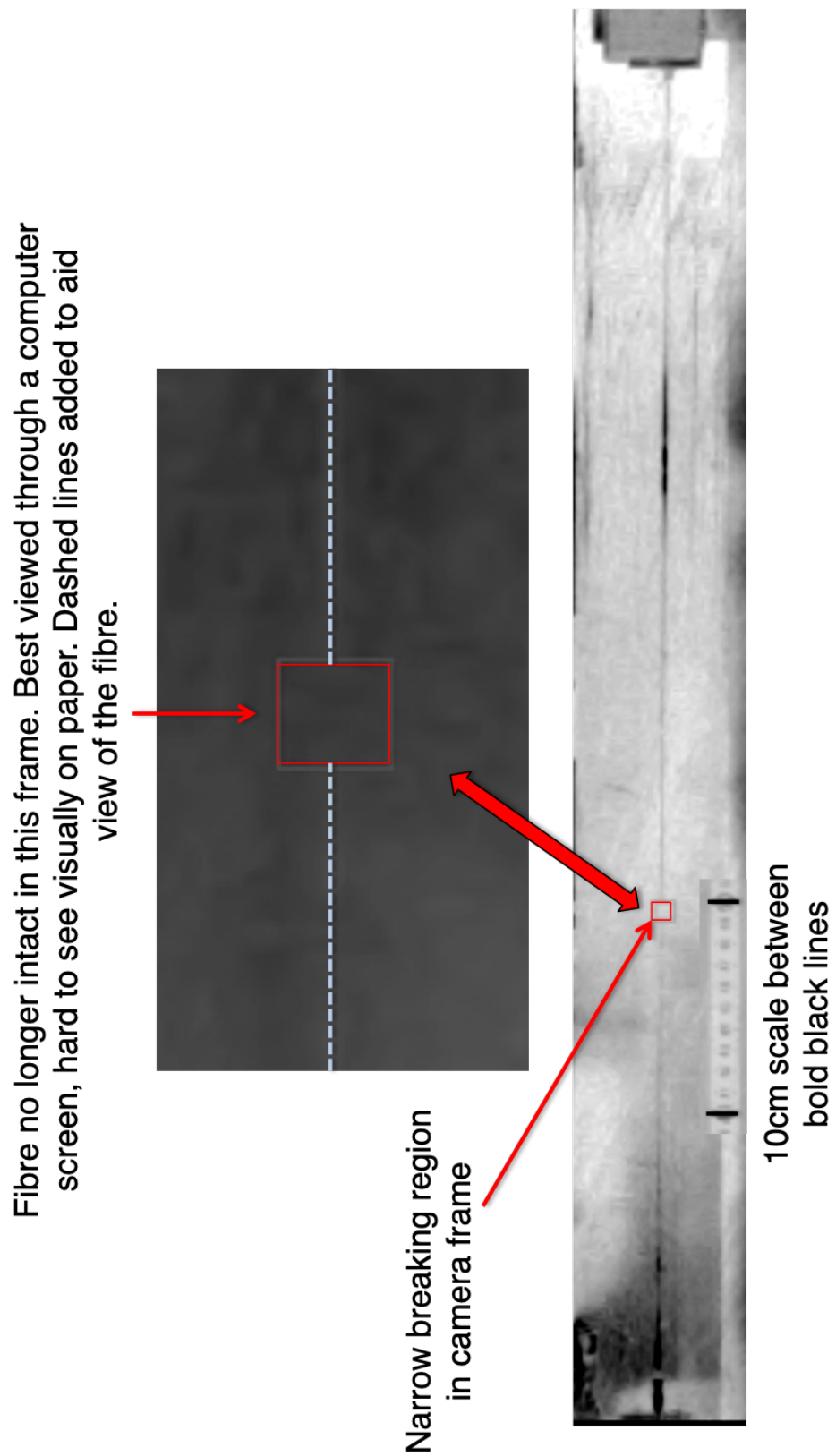


**Figure 3.24:** An example of a narrow spread break location from the high speed camera footage. Top zoom frame colour not inverted due to lack of clarity in image when inverted.

Once the breaking location was established, the next stage was to locate where this point lay on the fibre profile. A reference point had to be established on the high speed footage to determine the distance from that point to the breaking location. The reference point used was the transition point from the top stock and the top neck. This is indicated in figure 3.25.

### Top stock-neck transition point used as a reference location

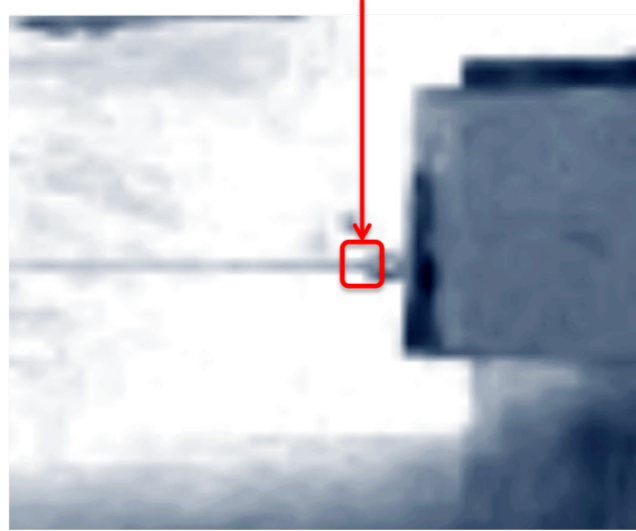


**Figure 3.25:** Zoomed in image from a high speed frame of the top stock reference point that was used to determine the distance of the fibre break.

A calibration tool within the high speed camera software was used to determine the distance of the break from this reference point. The calibration used was a ruler that was lined up alongside the fibre during testing. Using the built in software in the high speed camera program, the calibration tool counts the number of pixels within a 10 cm region along the ruler to determine the number of pixels per mm. The pixel distance between the reference point and the break location allowed the location to be located initially from the profile data. The error associated with locating the reference point was taken into consideration and given a value of  $\pm 2$  mm. This was obtained through the mm per pixel calibration tool on the camera software.

The stretch of the fibre during testing then has to be taken into account when locating the breaking location on the fibre profile. The total stretch could be calculated by the following relation:

$$\sum_{i=1}^n \Delta L_n = \sum_{i=1}^n \frac{L_n F}{Y A_n} \quad (3.2)$$

where  $\Delta L_n$  is the stretch of a segment of a fibre profile,  $L_n$ ,  $F$  is the breaking force,  $Y$  is the Young's modulus of bulk fused silica and  $A_n$  is the cross sectional area of segment  $L_n$ . A new stretched profile could then be plotted and used to locate the fibre break location. This is shown in figure 3.26. The calculated stretch could be up to 3 cm for fibres that were breaking at approximately 4.5 GPa.

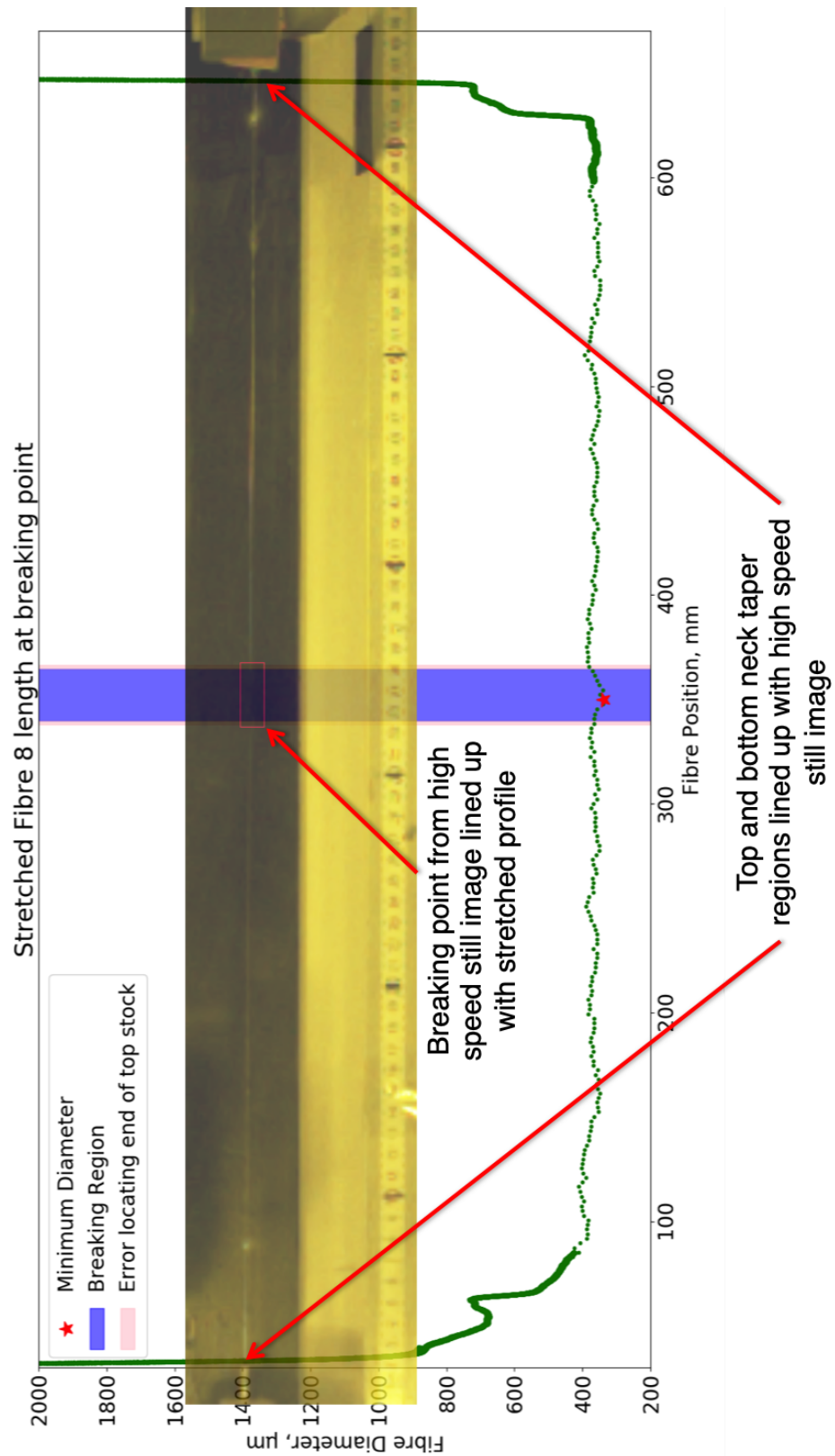


**Figure 3.26:** A stretched fibre profile lined up with the breaking frame of the high speed footage.

Previous research [92] has indicated that typically the breaking location would be at the min-

imum diameter location of the fibre. Figure 3.27 shows the location of the minimum diameter region on the fibre and how wide the spread was of the breaking region from the high speed camera frame that the fibre breaks.

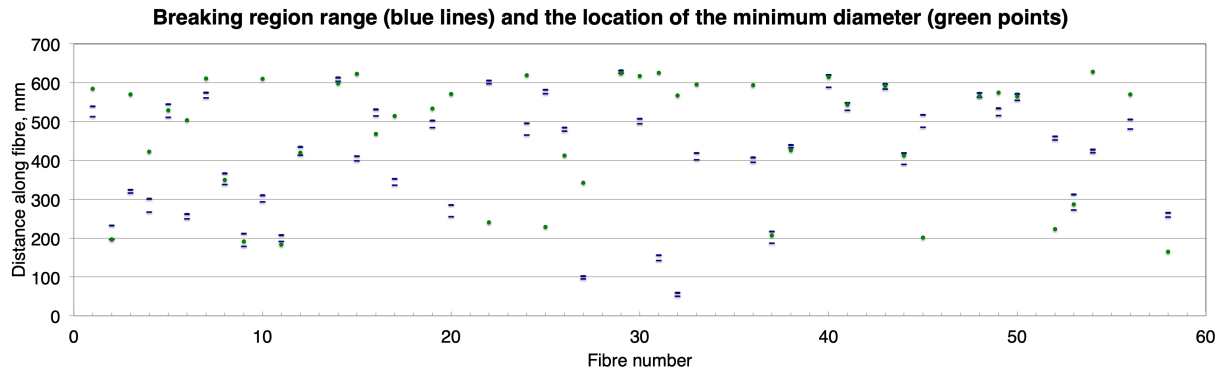


**Figure 3.27:** Location of the minimum diameter region on the fibre and the spread of the breaking region from the high speed footage. From this image, the number of fibres that have a minimum diameter within the breaking region could be observed.

From figure 3.27, it was clear that the breaking location of the fibres were not consistently at the minimum diameter. An example of a fibre that did not break in the minimum diameter location is shown in figure 3.28. Combining the data from these graphs and analysing the data from the high speed footage, only 32% fibres broke in the region where the minimum diameter was located. Previous research [92] has shown that for fibres breaking at stresses greater than 4 GPa, this figure should be approximately 80% and above. Further investigation into the breaking locations needed to be carried out.

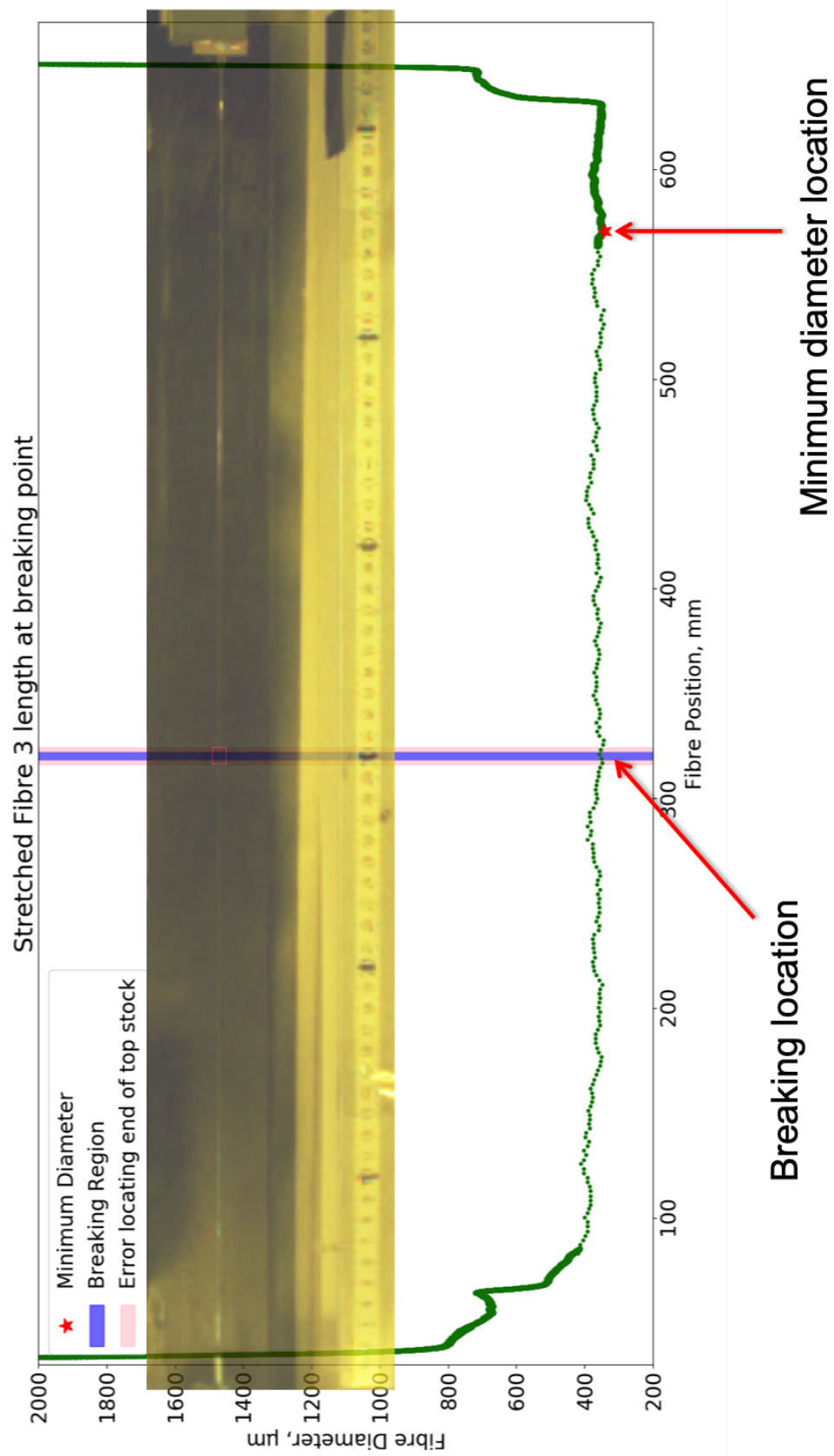


**Figure 3.28:** A stretched fibre profile lined up with the breaking frame of the high speed footage. In this example, the breaking region was not near the minimum diameter location.

## 3.8 Discussion

### 3.8.1 Fibre failures due to cardboard sandwich failure

8 fibres failed during this investigation due to the stock coming out of the cardboard sandwiches. Confirmation of this was also achieved through the high speed camera footage where the stock could clearly be observed to have come out the holder. An example of this is shown in figure 3.29 where the top end of the fibre has been pulled out of its holder. The fibre clearly could be seen to still be intact as the top stock material was pulled to the ground.

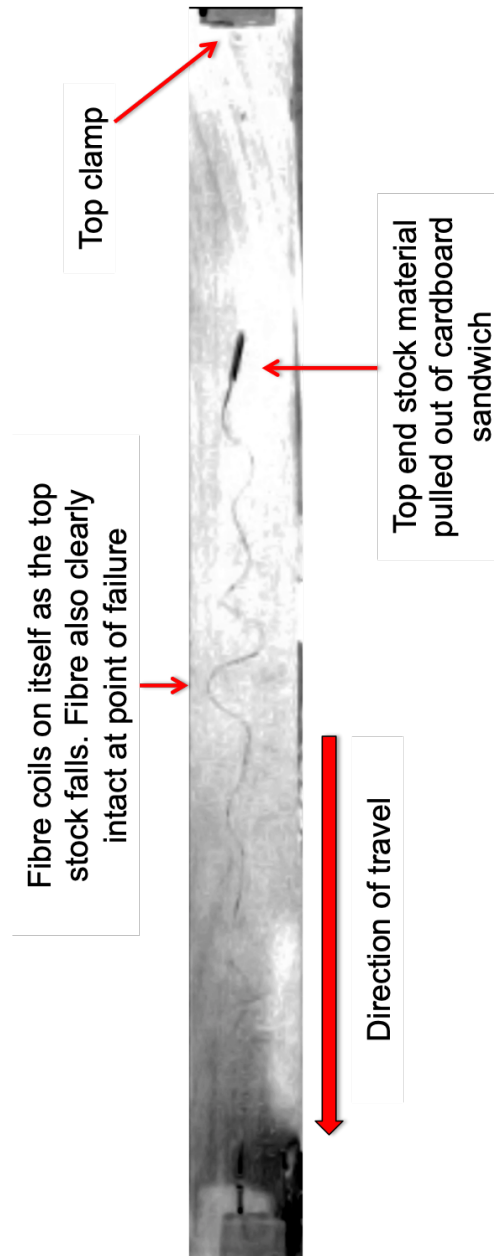


**Figure 3.29:** Screenshot of a fused silica fibre where the top stock was pulled out of the cardboard sandwich holder. It could be seen from this image that the thin section of the fibre was still intact as the top stock was falling to the ground.

Figure 3.30 shows a comparison between a fibre that had a higher likelihood to fail through this method, and the aftermath of a successfully tested fibre. From figure 3.30A, a gap could be clearly seen between the two halves of cardboard next to the fused silica stock. In figure 3.30B, this gap was filled with epoxy to the point where it slightly overflows from the sandwich and around the exposed stock. All the fibres that failed due to pulling out of the cardboard sandwich did not have this overflow feature.

During the epoxy process, the overflow could appear at the initial attachment of the two halves, but as the cardboard sandwich was cured vertically, this results in some of the epoxy naturally sliding down the inner sides of each half. To get around this, extra epoxy could be applied to the top of the bond region next to the exposed stock to fill in the gaps. Care should be taken when applying this extra epoxy to ensure that no part of the TNR or fibre was touched during this procedure. The epoxy could be applied with a small and thin stick of cardboard, or a cocktail stick, for example. Ensuring that the two aluminium plates were as tight as possible also helps limit the amount of epoxy that could slide down on the inside.

After each successful test, the cardboard ends were inspected to observe if there was any slippage within the cardboard sandwiches. No ends showed any visible signs of slippage during testing.

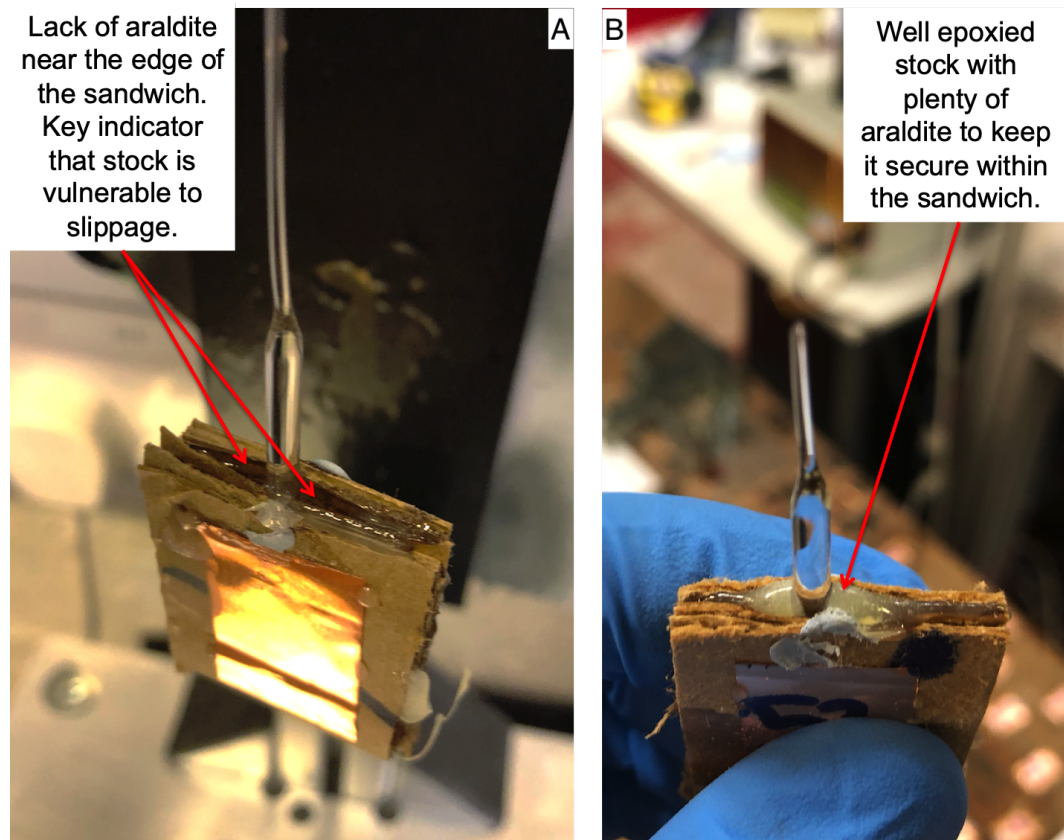


**Figure 3.30:** A: An example of a cardboard sandwich that was likely to have the fused silica pulled out of it during testing. This was determined from the lack of epoxy around the stock at the edge of the cardboard sandwich. B: An example of a cardboard sandwich with a sufficient amount of epoxy to keep the stock in place.

An additional digital camera was set up to record the top clamp during testing to see if there was any observation of slippage of the cardboard sandwich within the clamps, as well as monitoring the stock to see if there was any movement of the stock within the cardboard sandwich to ensure the test was mimicking the environment of the stock being welded in place. This camera could be seen in the previously shown figure 3.11. Figure 3.31 shows an example of the result of the footage obtained from this camera for one fibre. A frame from the very start of the strength test and just before fibre failure were overlaid on top of each other to see if there was any noticeable difference in the cardboard sandwich position. No slippage or movement was observed in any of the footage that was obtained within the cardboard. This test was carried out for multiple fibres and all showed the same behaviour.

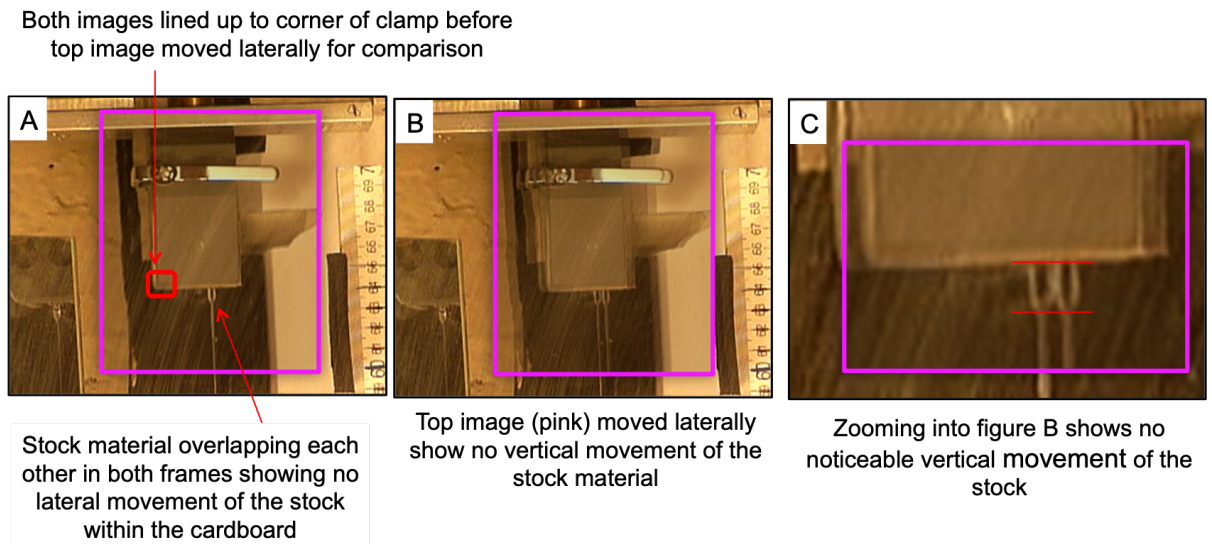


**Figure 3.31:** A: An overlay of two frames from the start of the strength test procedure (black border frame) and just before the fibre fails (pink border frame) observe if there was any slippage of the cardboard sandwich in the clamps. It could be seen from this image that there was no obvious visual movement of the stock between the two images. B: Pink border frame moved laterally over the black frame image to observe if there was any vertical movement of the stock. C: Zoomed in view of B.

### 3.8.2 Breaking location

A major focus of this investigation was to inspect the location of the fibre breaking to determine whether or not the angles introduced into the fibres would have a greater influence to where the fibre would break. Having angles in the TNR would increase the amount of stress in the TNR region of the fibre. The stress applied to the TNR could then result in the fibre failures occurring at the TNR region instead of the minimum diameter location in the thin section of the fibre should the stress in this region be sufficiently high enough.

From the breaking position analysis, it was found that while no fibres broke at the TNR region where the fibre angle was at its greatest, the majority of the fibres that were tested did not then break at the expected minimum diameter location. In total, only 14 out of 44 (32%) fibres

broke at the minimum diameter region. 30 fibres did not break around their minimum diameter location. This result is in contrast with previous research that previously found that fibres would break around the minimum diameter region with sample sizes of 70 and above [128] [92]. When carrying out investigations with fused silica fibres, the assumption that the fibre would break at the minimum diameter region was made when there was no high speed camera available to monitor the breaks. This was because the stress should theoretically be at a maximum at this point using the following equation:

$$\sigma_{max} = \frac{F_{break}}{A_{min}} \quad (3.3)$$

where  $\sigma_{max}$  was the maximum stress applied to the fibre,  $F_{break}$  was the breaking force applied from the strength tester when the fibre fails and  $A_{min}$  was the minimum cross-sectional area of the fibre at its thinnest point. Figure 3.32 shows the difference between the stress in the breaking region and in the minimum diameter region for all the fibres tested, with the stress at the actual breaking point being lower than the minimum diameter stress as expected.

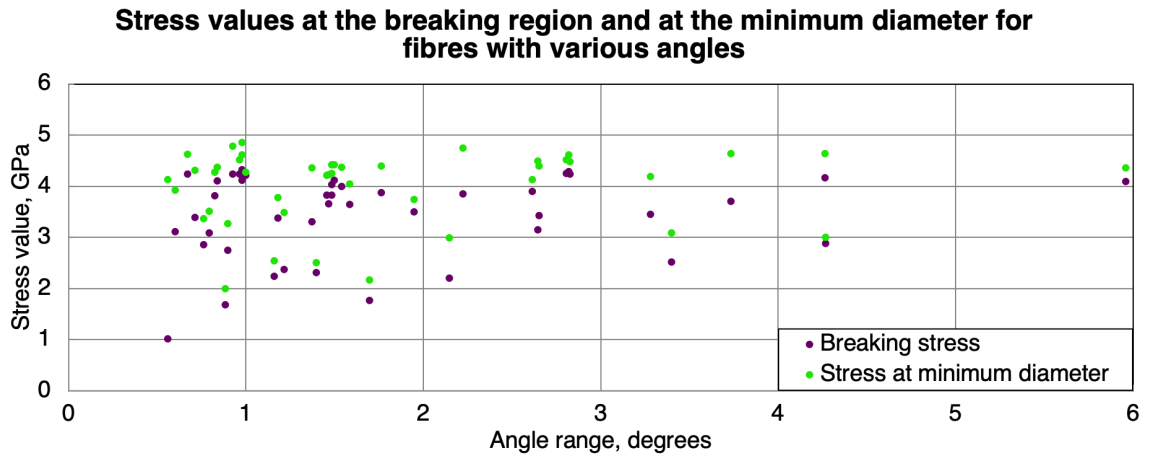


**Figure 3.32:** The stress in the fibre in the location where the fibre broke and at the minimum diameter region for all the fibres tested in this investigation.

To further investigate why the majority of fibres did not break at their minimum diameter, the fibre profiles were examined to see if there were any features around the breaking region that may have contributed to the breaking location. Previous research during the installation of the laser stabilisation system on the fibre pulling machine had shown that features on the fibre such as dips in diameter in the thin region could have an effect on the ultimate strength of the fibre [92]. Figure 3.33 shows a fibre profile with the minimum diameter location (red star) and the observed breaking region of the fibre. It could be seen that the breaking region was in a dipped region where the diameter decreases by approximately  $20\ \mu\text{m}$ . An artefact such as this, or in a region where there was a steady change in diameter (either decreasing or increasing) was only observed in 13 fibres out of the 30 fibres that did not break at the minimum diameter. Figure 3.34 however shows a fibre that, again, did not break at the minimum diameter region, but also did not break in a location where there was any obvious visual artefacts.

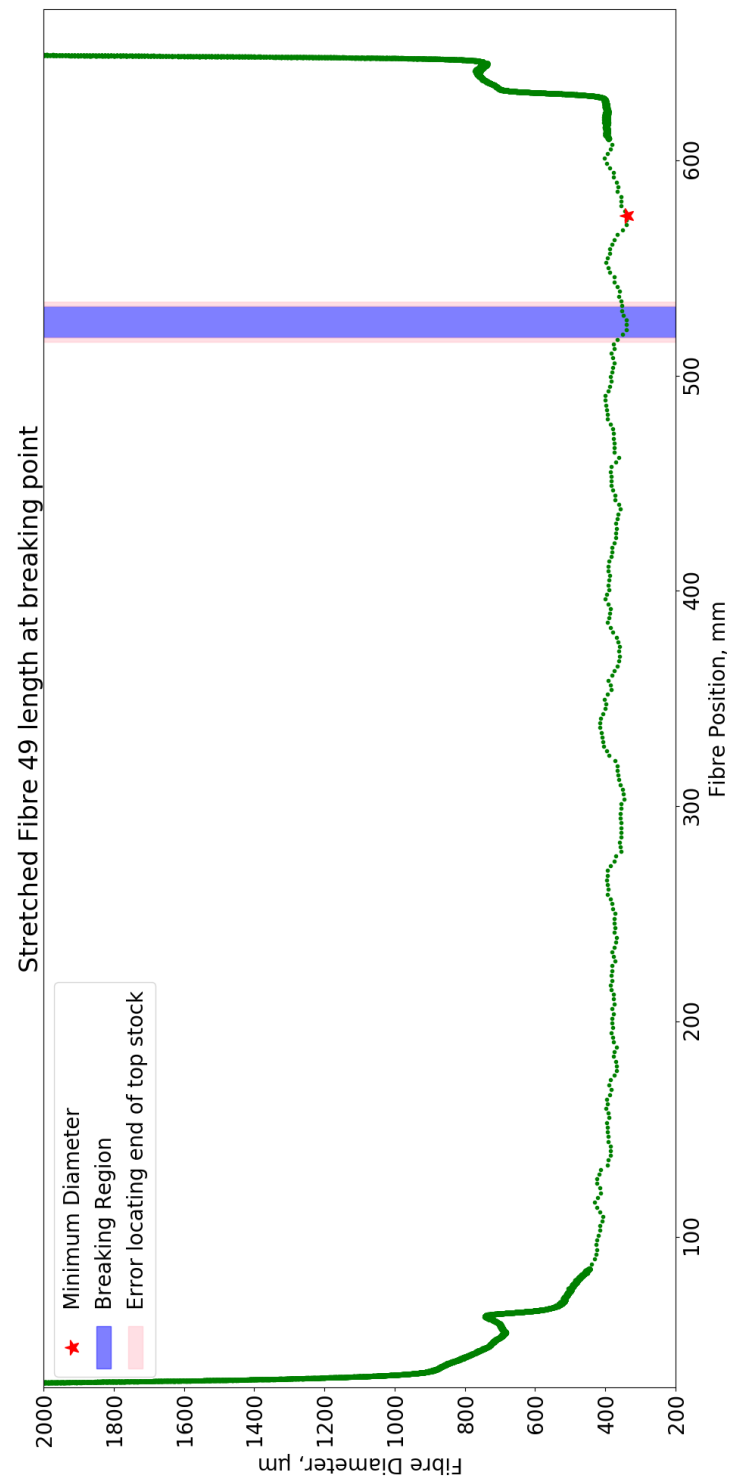


**Figure 3.33:** Fibre profile that shows the breaking region sitting in a location where there was a dip in diameter. This fibre was of particular interest as the difference in profiler diameter data between the minimum diameter of the fibre and the minimum diameter of the breaking region was  $0.6\ \mu\text{m}$ . Therefore the stress in both of these locations would be extremely close. This was the only fibre that had this scenario.

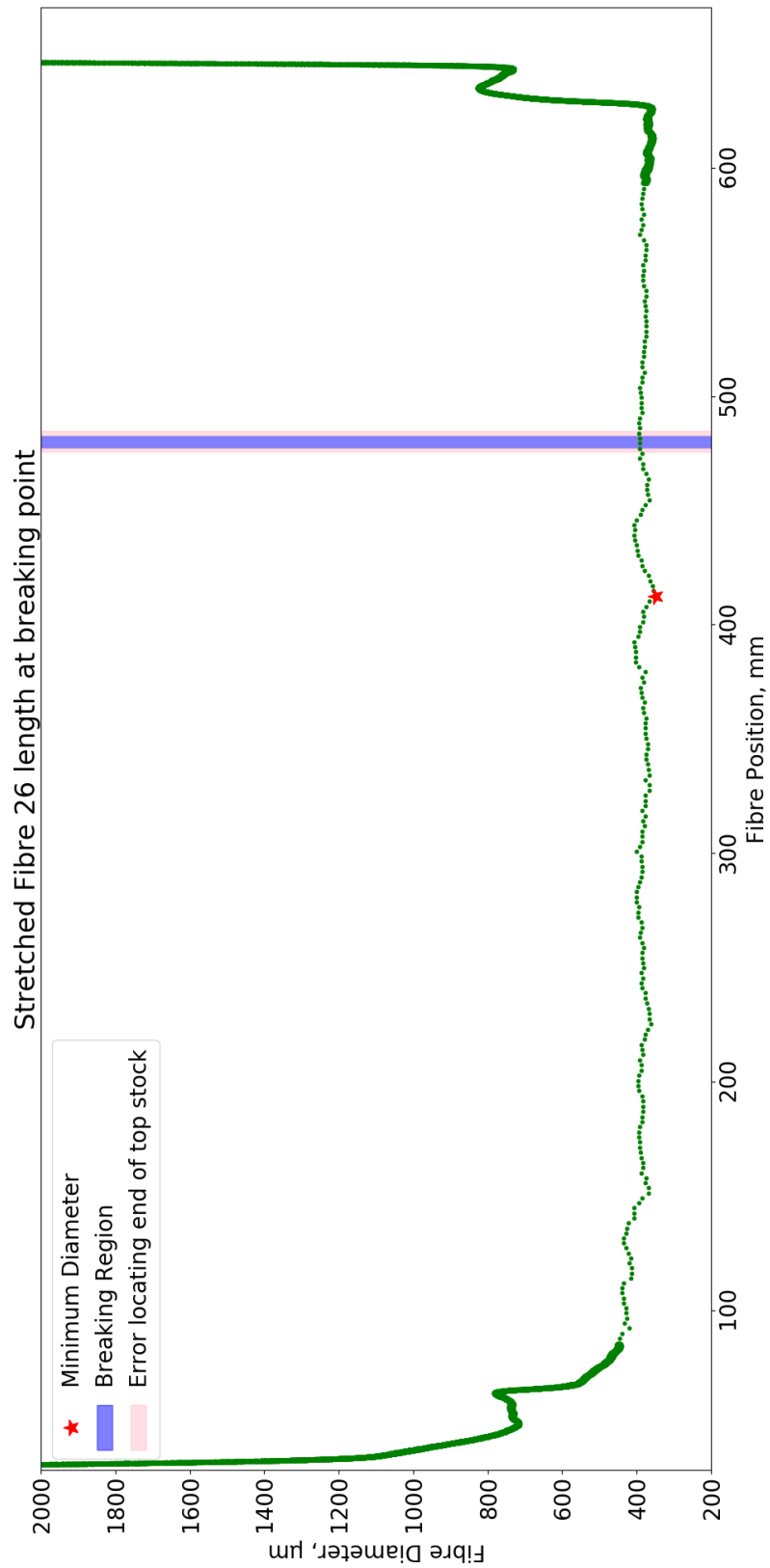


**Figure 3.34:** Fibre profile that shows the breaking region sitting in a location where there was no visual artefact in the breaking region.

If the fibres that did break in the region where the minimum diameter value was included in the artefact observation tally, this number would increase from 13 to 24. This equates to more than half of the successfully tested fibres. It was unclear why the remaining fibres broke in a location where there was no artefact. Looking only at the 17 fibres that showed this behaviour, 9 fibres showed a breaking stress that could be considered weak. This involves having a breaking stress below 3 GPa, as defined in previous research [128]. Two of the 9 fibres tested had a breaking stress under 2 GPa. One of these fibres broke under a load of 44.3 kg, which correlates to a maximum stress at the minimum diameter of 4.1 GPa. This would generally be considered to be a very strong fibre, but the breaking region was in the bottom TNR, which resulted in the low breaking stress at the breaking point. There were no obvious defect in the fibre profile in this region to suggest why it broke at this point and was the only fibre that was tested in this investigation that broke in the TNR. The maximum angle observed in the bottom end of the fibre was  $0.5^\circ$ . It could be possible that during the bonding process that a bit of apparatus came in contact with this  $800\ \mu\text{m}$  region, but could not be said for certain. The possibility that additional thermal stress could have been added during the pulling process at this point through the misalignment of the beam could not be ruled out either though a recording of the beam power and distribution during the pull would need to be obtained and analysed. There were a further 6 fibres that broke with a breaking stress of under 1 GPa which were not included in the presented data. These 6 fibres were touched at some point prior to testing and failed take more than 10 kg of load, meaning that these fibres would have failed the proof test that fibres go through prior to installation into a suspension.

During the bonding of the cardboard sandwiches to the fibre, the fibre itself was out of its storage area and in the lab bonding jig for up to 48 hours. This was a significant period of time in a non-cleanroom, active lab environment. It could not be said for certain that absolutely nothing came in contact with the fibres during this period as that would require 24 hour surveillance. Small dust particles carried in the air current would not be expected to cause damage to the fibres, though it was not something that would be desired.

As previously stated, the laser stabilisation system on the pulling machine was not used to make the fibre production as identical as possible to those produced on the LHO machine. Future tests repeating this investigation with fibres that were produced with the laser stabilisation enabled could lower the number of dipping artefacts that could occur in the fibre profile, and therefore limit the number of fibres that would break in these regions. As there will be a laser stabilisation system installed at LHO by the start of 2020, this would give another opportunity to carry out a comparison test between the Glasgow and LHO pulling machines (a separate investigation comparing these two machines will be discussed in the following chapter).

### 3.8.3 Effect angles have on ultimate strength of fibre

As discussed in chapter 3.8.3, a wide range of angles between the stock-to-TNR and TNR-to-thin were obtained. Figure 3.35 shows the maximum angle observed in the fibre and the corresponding breaking stress that was obtained from all the fibres that were tested. The angles represented in figure 3.35 is the maximum angle found on the fibre out of all the stock-to-TNR and TNR-to-thin at both ends. Fibres with angles under  $1^\circ$  between the stock and TNR region of the fibre, which was the criteria to be suitable for aLIGO suspension installation, mostly showed very good performance. This includes the strongest fibre that was tested which broke at 4.3 GPa. In total, there were 14 fibres that were tested that satisfy the criterion for aLIGO suspensions that had angles under  $1^\circ$  specifically in the top neck stock-to-TNR.

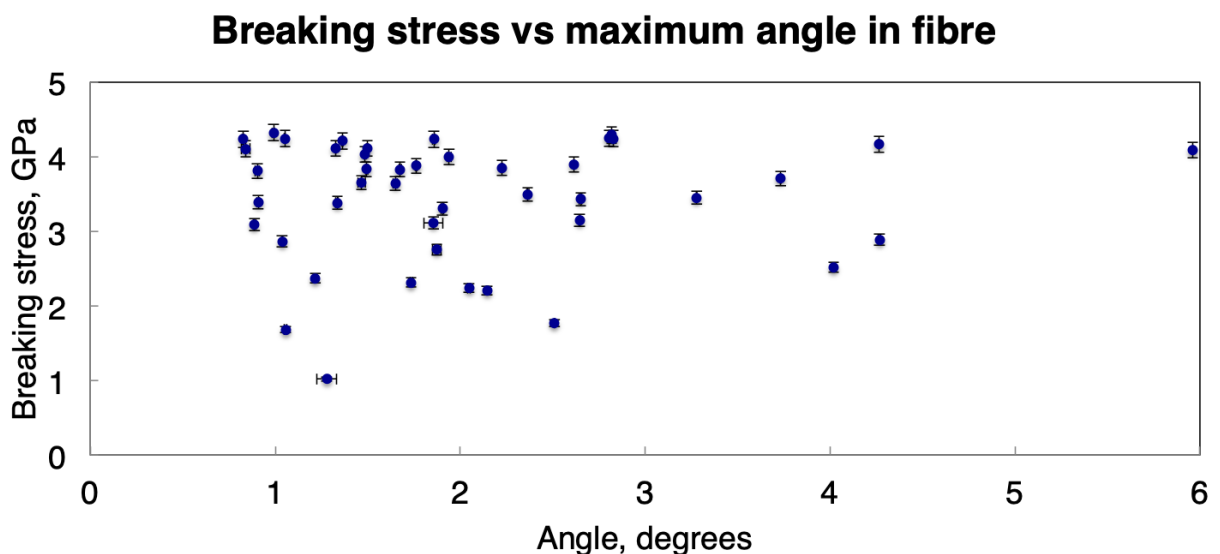


**Figure 3.35:** The maximum angle (left Y-axis) in both the stock-TNR and TNR-thin, and the breaking stress (right Y-axis) of the fibres that were tested in this investigation

From figure 3.35, only 11 fibres out of 44 showed a performance where the breaking stress was under 3 GPa. All 11 of these fibres contain angles in a range between  $0.7 - 2.5^\circ$ . There does not appear to be any correlation showing that the more extreme the angle defect is, the worse the ultimate strength performance is. An interesting follow up investigation would be to test the lifetime of these fibres hanging a load at a range of stress values. This was discussed in section 3.10, with a similar, but non-related investigation carried out in chapter 4.

During the previous analysis regarding the fibre failures during the commissioning break, there was some finite element analysis (FEA) that was carried out by members in the suspensions working group (SWG) within the LIGO Scientific Collaboration (LSC) to observe what the applied stress on the TNR region would be if angles were inserted into the models [129]. Prior to this investigation starting, it was thought that the angles found in the fibres could have a significant effect on the ultimate strength of the fibres. The results presented in this chapter have

shown that this hypothesis was not the case. For example, the fibre with the greatest angle,  $5.96^\circ$ , that was investigated for example had a breaking stress of 4.1 GPa, which could be considered as very strong. From figure 3.35, it could be seen that the majority of fibres that were tested with an angle between  $1-3^\circ$  were found to have breaking stresses between 3.5-4.3 GPa.

However, the fibre models in this FEA were based on an ideal fibre of uniform diameter in the stock, TNR and thin regions of the fibre. For this FEA model to be considered an accurate representation, importing a fibre profile of a real fibre that has been tested was essential and would need to be carried out to give an accurate comparison to the model and experimental data. A key component in accurately portraying the fibre in these models was to correctly import the radius of the bend in the fibre where the angle occurs. This would ensure that the stress values calculated in the model were as accurate as possible.

It could also be concluded that if, for example, a fibre was installed into a monolithic suspension with angle greater than  $6^\circ$ , there would need to be an additional contribution through the welding procedure to observe an angle this severe. Since no fibres with angles greater than  $4^\circ$  were obtainable without exceeding the laser power available at LHO, any fibre that would be installed to the monolithic assembly, previously shown in chapter 1.5, would have to be welded into the ears poorly to give an overall angle of approximately  $6^\circ$  or more. Theoretically, the de-stress procedure [97] should eliminate any angle introduced into the stock-horn weld region. However, if this process was not carried out correctly, it could have the detrimental effect of giving an additional contribution to the overall angle. An investigation could be carried out in the future where the stock at both ends of the fibre were welded to an ear and tested to see the strength performance and how angles in the weld region effect the suspension.

### 3.9 Future research

A follow-on investigation could look into a different mechanism of testing. Instead of misalignment of the beam through adjustments on the mirror mounts, misalignment of the clamps within the pulling machine could be investigated to see how feasible it was to introduce angles into produced fibres with the beam well aligned. Chapters 4 and 6 focus on an investigation related to the stress fatigue of suspension fibres. In these investigations, the angle alignment of the fibre was not investigated. This investigation focused on the strength of the fibres with angles in them due to the suspension failures that had occurred during installation into the detector chambers. The fibres at the time of failure were under a set stress for a period of time before failing. For example ETMx at LHO hung for approximately 1 week and ETMy at LLO hung for approximately 4 weeks. Data that was obtained in the investigation that will be explained in chapter 4 of this thesis, which was used in the investigation surrounding the failures [112], showed that the fibres would have been under a stress of approximately 2.5 - 2.7 GPa. As this was a different mechanism of investigation where the lifetime of the fibre was investigated under various loads

instead of ultimate strength of the fibre, it would be interesting to see if fibres with deliberate angle defects would perform with respect to stress fatigue. The equipment and set-up needed to carry out this investigation was already made and available to suit aLIGO length fibres due to previous research that was carried out [92].

An additional factor that was highlighted in the previous report into the fibre failures during the commissioning break was the stock offset on the horn of the ear on the side of the test mass. This offset could be introduced during the welding process when the stock material was not aligned properly when driving stock into the molten region in the horn. An example of this is shown in figure 3.36. This could be an area that could be investigated in parallel with the previous suggestion. An offset in the stock material could be easily done by misaligning the X-Y translation stages that the clamps on the pulling machine were sitting on and would replicate an offset of the stock on the ear.

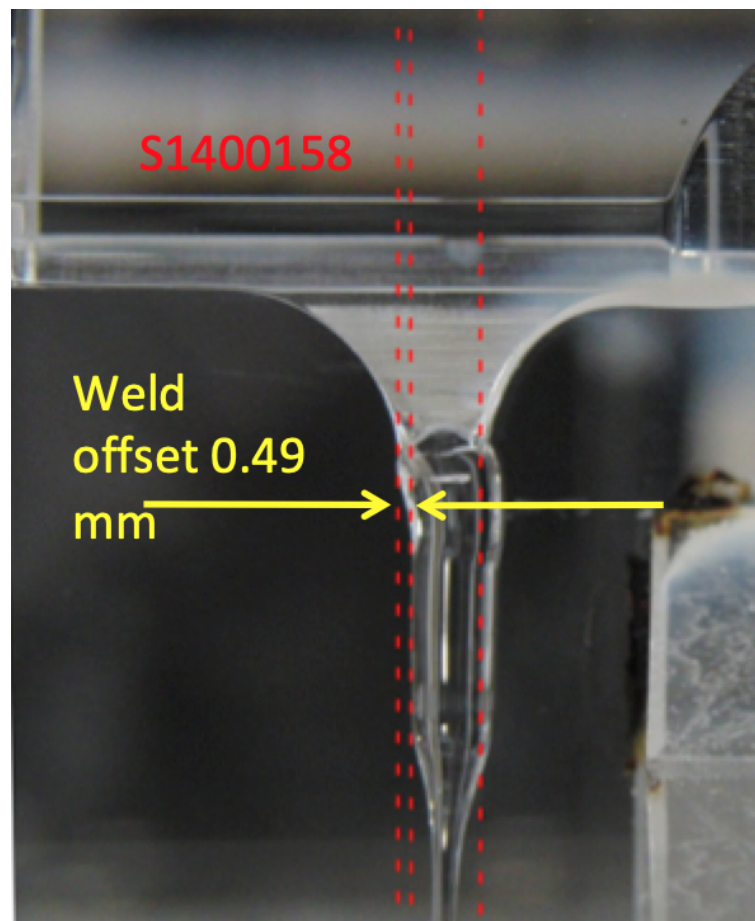


**Figure 3.36:** An offset of the stock material relative to the horn on the ear attached to the test mass [114].

Finite element analysis modelling of these fibres would help quantify the increase in stress that was actually applied to the TNR regions of the fibres where the angles were located with profiles of fibres that were tested experimentally. This was attempted in the early stages of this

investigation, but due to time constraints, it had to be set aside as future work. Difficulties were found when it came to producing accurate models of the fibres with angles accurately placed into ANSYS (a finite element analysis program) [130]. It was decided that time was better spent obtaining the experimental results, but building on the work that had been carried out by LSC colleagues [129] to accurately model a real angled fibre that had been tested will help understand how great of a stress increase was observed in the TNR.

All three of these investigations listed above will require a significant period of research time and effort, but could yield results beneficial to our understanding of what were the ultimate limitations the aLIGO fibres that could be installed into a suspension, as well as enhancing more general understanding of fused silica as a structural material. It would be a recommendation by the author that these investigations were picked up within the research group in the near future to feed into future projects that will use fibres such as A+, Einstein Telescope and LIGO Voyager.

### 3.10 Conclusion

This investigation set out to investigate the potential adverse effect that angular defects have on the ultimate strength of fused silica fibres. This was motivated due to incidents that occurred during the aLIGO commissioning break in between O2 and O3 where there were several suspension failures during installation of new test masses. During the root cause analysis report [113] into these failures, one of the possible reasons for these failures was angles that had been introduced into the fused silica fibre during the fibre production process. The outcome of this investigation was that all fibres that showed an angle between the stock and the TNR of the fibre greater than  $1^\circ$  were to be discarded from selection for aLIGO suspensions. An investigation into finding out what could cause these angles to be introduced during the production process, and the subsequent effects these angles have on the ultimate strength of the fibre was carried out.

The investigation consisted of firstly confirming that the angles had been introduced through the misalignment of the laser beam. Previous experience with aLIGO fibre production indicated that this could be the possible reason, but could not confirm due to the difficulty of determining the severity of the beam misalignment. This was due to the fact that the beam distribution would be inspected by eye through heavily tinted welding goggles through a laser safe enclosure window. This enclosure, as well as general laser safety protocols, made it difficult to inspect the beam up close to the heating region at an appropriate view to determine the beam distribution around the stock. At the time of this investigation, this was how the beam distribution was observed at LHO. On the Glasgow pulling machine, there was a camera monitoring system installed that allowed the close up inspection of the CO<sub>2</sub> through the LabVIEW program controlling the fibre pulling machine. This upgrade will be installed onto the LHO pulling machine by 2020 in preparation for the A+ upgrade. It was confirmed that a reliable way to introduce fibres into the production process was to misalign the CO<sub>2</sub> beam on the stock material through

the adjustments that were available on the periscope. This caused the CO<sub>2</sub> beam to enter into the pulling machine optical system at an angle. Ensuring the beam was well aligned onto the fused silica stock would produce fibres that satisfied the aLIGO criteria of having angles under 1° between the stock and the TNR.

A key component on estimating the stress values to which the fibres were exerted, and the lifetime before failure, was based on an investigation that was carried out by the author while at LHO. This investigation focused on the stress fatigue of aLIGO fibres where a mass was attached to the fibre and the hang time was recorded. The result of this investigation is presented in the following chapter.



## Chapter 4

# Stress fatigue in fused silica suspension fibres

### 4.1 Introduction



**Figure 4.1:** An arial photograph of LIGO Hanford Observatory while descending for landing at the Tri-Cities Airport.

During this PhD, there was an opportunity to work on a Long Term Attachment (LTA) at the LIGO Hanford Observatory (LHO) in Washington, USA for four months between March-July 2017. During the four month fellowship, one of the main projects that was worked on was related to the Suspensions Working Group (SWG) within the LIGO Scientific Collaboration (LSC). An investigation was set up to understand the expected lifetime of fused silica fibres at a higher stress range than what is currently used in the aLIGO suspensions in preparation for future upgrades to the suspensions. Fibres investigated in this chapter ranged in diameter between 183-208  $\mu\text{m}$ . The results of this investigation will be discussed within this chapter.

### 4.1.1 Motivation

Current upgrade plans to the aLIGO detectors, A+, involve the use of thinner fibres in the monolithic suspensions [72] [90]. This change in design will result in a greater load being applied to the fused silica fibres suspending the test mass. The maximum increased stress can be calculated by:

$$\sigma_{max} = \frac{F_{max}}{A_{min}} \quad (4.1)$$

where  $\sigma_{max}$  is the maximum stress of the fibre at the thinnest point on the fibre,  $F_{max}$  is the force applied to the fibre and  $A_{min}$  is the area of the fibre at its thinnest diameter. In the current monolithic design [56], the fibres were under a stress of 780 MPa. The proposed plans for A+ is to increase the stress to 1.2 GPa [90]. This increase will move the resonant modes, known as violin modes, from approximately 500 Hz, to 650 Hz for the first harmonic in the aLIGO sensitivity curve. The vertical mode of the suspension, known as bounce modes, will also move, but in the opposite direction from approximately 10 Hz down to 7 Hz. These upgrades, along with the possibility of increasing the stock and fibre length to increase the dilution factor will overall lower the thermal noise and increase sensitivity in the detector [58] [72].

Designs for the next generation gravitational wave detectors also suggest the use of heavier test masses in their suspension design with an increased stress figure [90] for the suspension compared to current aLIGO. It was therefore essential to understand what impact increasing the stress has on the expected lifetime of the fused silica fibres.

Previous research by Proctor et al [131] investigated properties of fused silica with fibres that were 15-80  $\mu\text{m}$  in diameter. These fibres were produced with Vitreosil fused silica through the use of a gas flame with both single pulls and what was described as a ‘double-draw’ technique. It was not possible to trace the exact data sheet to observe the properties of the Vitreosil fused silica. The latter involves pulling a new thin portion from the initial stock, followed by pulling the actual thin fibre from this new region. This technique was used to produce ultra thin fibres that will be described in both chapters 6 and 7. The stock material ranged from being treated with a chromic acid wash, followed by flame polishing, whereas the stock material in aLIGO

fibres were treated with acetone and methanol followed by laser polishing. These fibres were placed under a range of stresses both in air and in vacuum. As the fibres that were tested were of a diameter 10 times thinner than what is currently used in aLIGO suspensions, it was decided it would be beneficial to investigate if there was an observable difference between Proctor's fibres and fibres that could be produced with the aLIGO fibre pulling machine.

Research within this chapter was carried out in parallel with research that was going on at the University of Glasgow by then PhD student, Dr Kyung Ha Lee. The fibres that were investigated at LHO were all in air tests, which have been shown to show lower strength than that in vacuum [131]. Dr Lee's work [92] looked at a slightly similar stress range in air (2.5-4.2 GPa), as well as in vacuum tests at a lower stress range (2.3-2.9 GPa) as the set-up at Glasgow allowed for vacuum tests. Though the aLIGO monolithic suspensions were under vacuum when installed into the detector, they could spend more than two years in storage before installation, as well as 2-3 months in air after installation onto the test masses while the quadruple suspension system is installed into the chamber. While in storage, the fibres were under no tension, but locked in place within a fibre cartridge (discussed in chapter 4.2.1). Though this investigation did not allow for the testing of fibres that had been in storage for that amount of time, carrying out in air tests was still relevant as this would give a lower bound to the fibre safety margin. In addition, carrying out similar research that produces fused silica fibres with identical pulling machines at two separate locations also allows for a test of reproducibility to see if both sets of data match.

To ensure the investigation was carried out to aLIGO conditions, the fibres produced were pulled and characterised following aLIGO fibre pulling procedures. This is detailed in the following subsection.

## 4.2 Experimental method and set-up

### 4.2.1 Fibre production and characterisation

The fused silica fibre pulling machine, shown in figure 4.2 was functionally the same as that described previously in chapter 2. All fibres produced in this chapter followed the procedure detailed in the LIGO document, E1000366 [97], the official aLIGO fibre production procedure. The fused silica stock used was Heraeus Suprasil 2 [132], as used in aLIGO.

This procedure has slight differences compared to the procedure that was carried out in the fibre production in the previous chapter. The main difference was the introduction of 'fuse ends' attachment holsters and fibre cartridges into the fibre production and characterisation set-up [133]. The fuse ends are aluminium blocks that were attached to either end of the fused silica stock to interface with the fuse end clamp installed into the pulling machine. This also gave the user a contact point to handle the stock without actually touching the stock. A SolidWorks

rendering of the final product is shown in figure 4.3 [134].

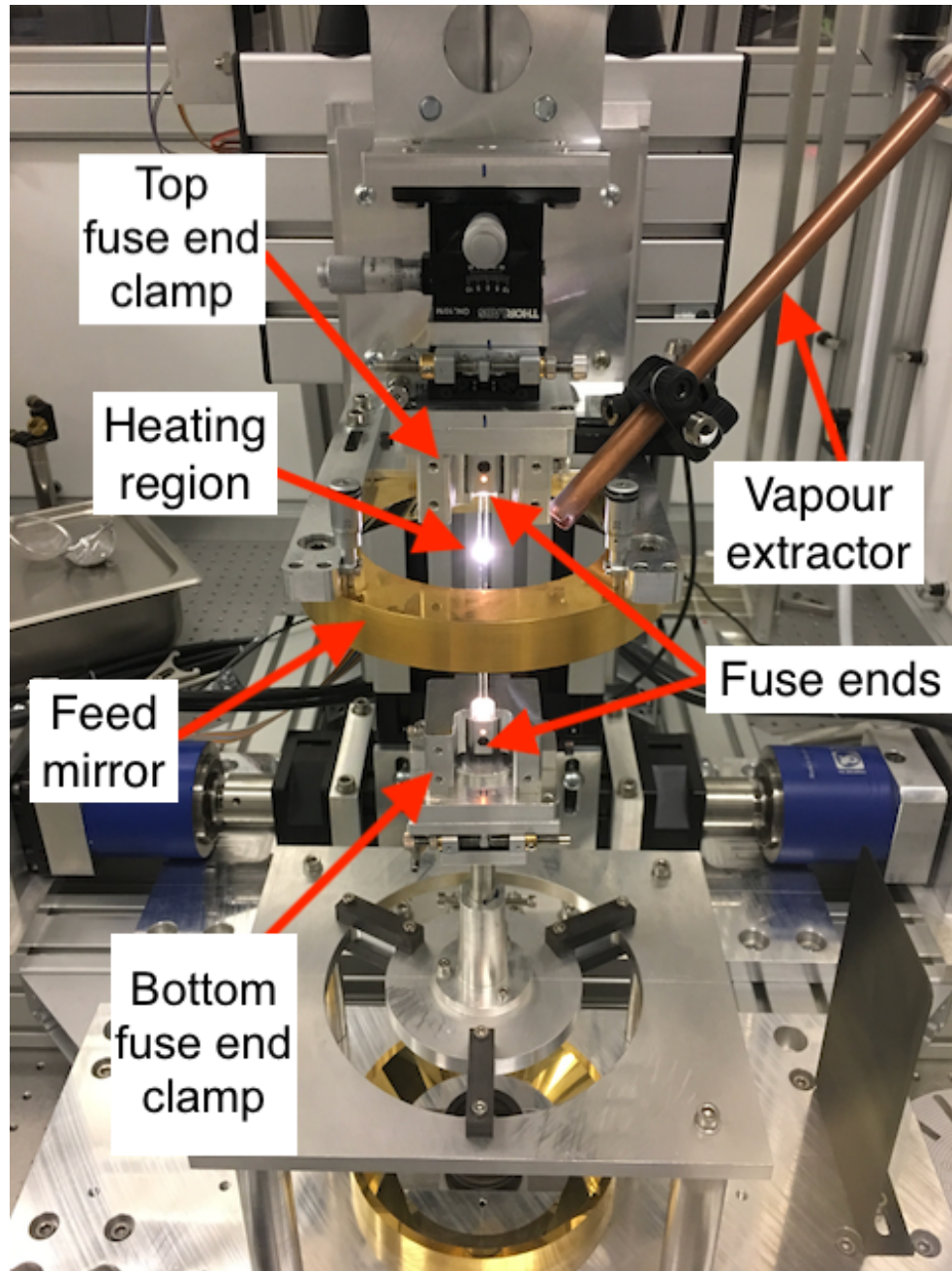


**Figure 4.2:** The fibre pulling machine at the LIGO Hanford Observatory with a rod of fused silica installed and being heated to the point where it was molten.

Lengths of 11.5 cm fused silica stock were cut and cleaned prior to installing the fuse ends. The cleaning process consisted of three stages of wiping down with Anticon gold wipes [96] doused with methanol, then acetone then methanol again to remove any surface dust. The fuse ends were attached to the fused silica stock with 2 part Araldite epoxy [116]. The assembly was then placed into an aluminium holding plate [135] that ensured the fuse ends were sitting in the correct position on the stock and properly aligned with each end. This holding plate was then placed on a hotplate at 80°C for 30 minutes, as seen in figure 4.4. The stock was then ready to

install into the pulling machine fuse end clamps.

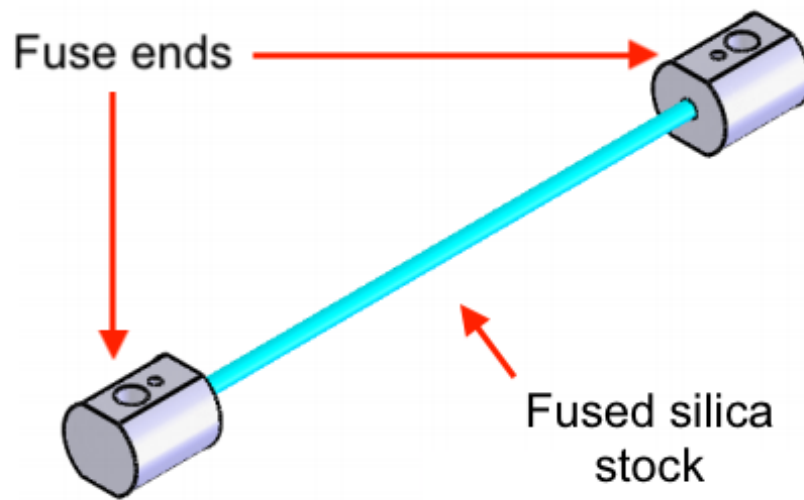


**Figure 4.3:** SolidWorks rendering of a fused silica stock with attached fuse ends [134].

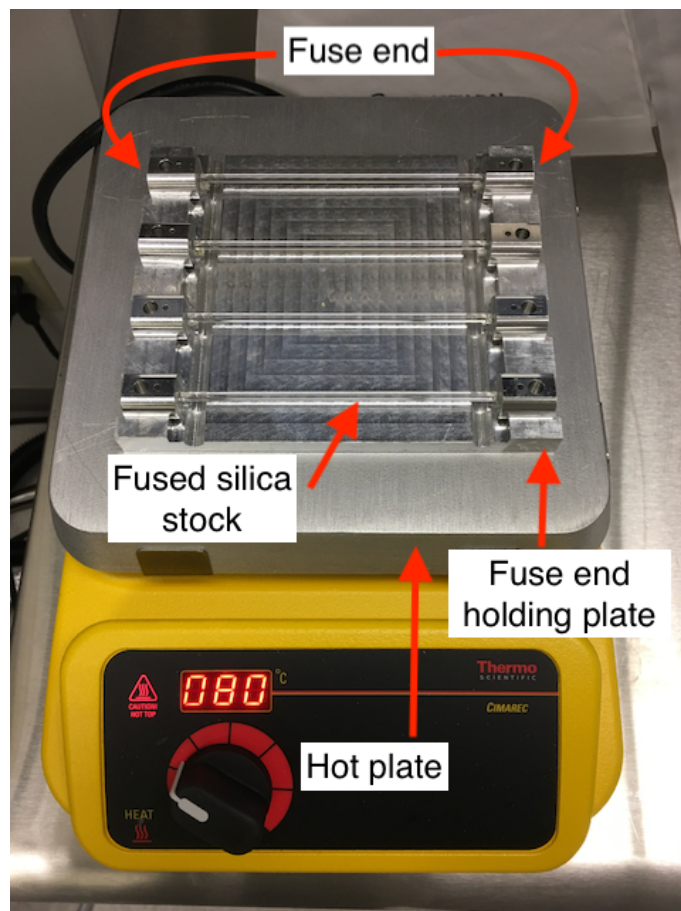


**Figure 4.4:** Assembly of a fused silica rods with fuse ends attached curing on a hotplate at 80°C.

The laser polishing process for the fused silica stock of these fibres was the same as that in the previous chapter: 50 mm distance down and up with the feed mirror stage voltage set to 0.25 V. The 100 W CO<sub>2</sub> laser [104] was turned on at the start of each day of fibre production with the shutter closed to ensure that the laser was sufficiently warmed up before fibre production. This minimises the power fluctuation that could be experienced from a cold start, which could be up to 10% [104]. This fluctuation could potentially vaporise stock material during the pulling process. This was because as the fibre was drawn, more heat was concentrated onto a smaller surface area. A sudden increase in power during this stage could therefore vapourise material leading to a thinner diameter in that region. Stock material could also be vapourised during the polishing process from these fluctuations if the power were to increase. As the polishing process involves moving the feed mirror at a slow speed along the length of the stock, excess heating could occur in a region due to an increase in power. This would lead to the stock material getting too hot and vapourising away. This would leave the polished stock having an uneven diameter. This was an artefact that could be observed by eye without using the fibre profiler, meaning it could be of the order of approximately 100 µm or greater.

Prior to any production, the laser output power was checked. This consisted of placing a fan cooled laser power meter at the path length such that the power reading would be approximately this value at the point the fibre was focused onto the stock. At 85 % duty cycle, the power meter gave a reading of 113 W and at 95 %, a reading of 118 W. This was typical of the performance of the laser [104] [92].

It was essential that prior to the production of fibres, a diameter, and therefore stress range, was decided for this investigation. Previous research carried out by Proctor [131] found the following relationship between stress and failure time:

$$(\sigma - \sigma_0) = \frac{1}{n} \ln(K) - \frac{1}{n} \ln(t) \quad (4.2)$$

where  $\sigma$  is the stress on the fibre in  $kg/mm^2$ ,  $\sigma_0$  is the fatigue limit,  $t$  is the time to failure and  $n$  and  $K$  are constants  $4.7 \times 10^{-2}$  and  $8.13 \times 10^3$ , respectively. The fatigue limit is the maximum stress that could be applied without causing fatigue failure in the material, such as cracks. Rearranging equation 4.2, the predicted hang time,  $t$  could be calculated:

$$t = Ke^{-n(\sigma - \sigma_0)} \quad (4.3)$$

This equation was used to determine what stress range should be investigated during this LTA, with the preference being fibres that would break in under a day to maximise the number of data points that could be obtained. Using equation 4.3, a range between 3-5 GPa was the aim of values to be investigated that gave time values that fitted the desired hang time.

Equation 4.3 could therefore be used to calculate the estimated hang time of a fibre under a specific stress. The pulling process was similar to that described in chapter 3. A voltage profile

was uploaded to the custom LabVIEW program to control the velocity of the pulling and feed stages to draw the fibre. In total, three different pulling profiles were created in this chapter to produce fibres with a minimum diameter range between 183-208  $\mu\text{m}$ . This range was chosen by calculating the stress values that could be applied with the available masses, and calculating the predicted hang time of the fibre with equation 4.3 to maximise the number of fibres that could be investigated during this visit.

These profiles originated from the pulling profile that was already used for previous aLIGO fibre production, namely the profile "LHO15" [115]. The main change that was made to this pulling profile was to make the velocity of the pulling stage be maximum during the middle section of the fibre pull. This was achieved by setting the voltage of the stage to its maximum value of 10 V. This is shown in figure 4.5. The aim of this was to obtain thinner fibres by maximising the velocity of the pulling stage, and determine whether or not that velocity was too fast, or not sufficient enough.

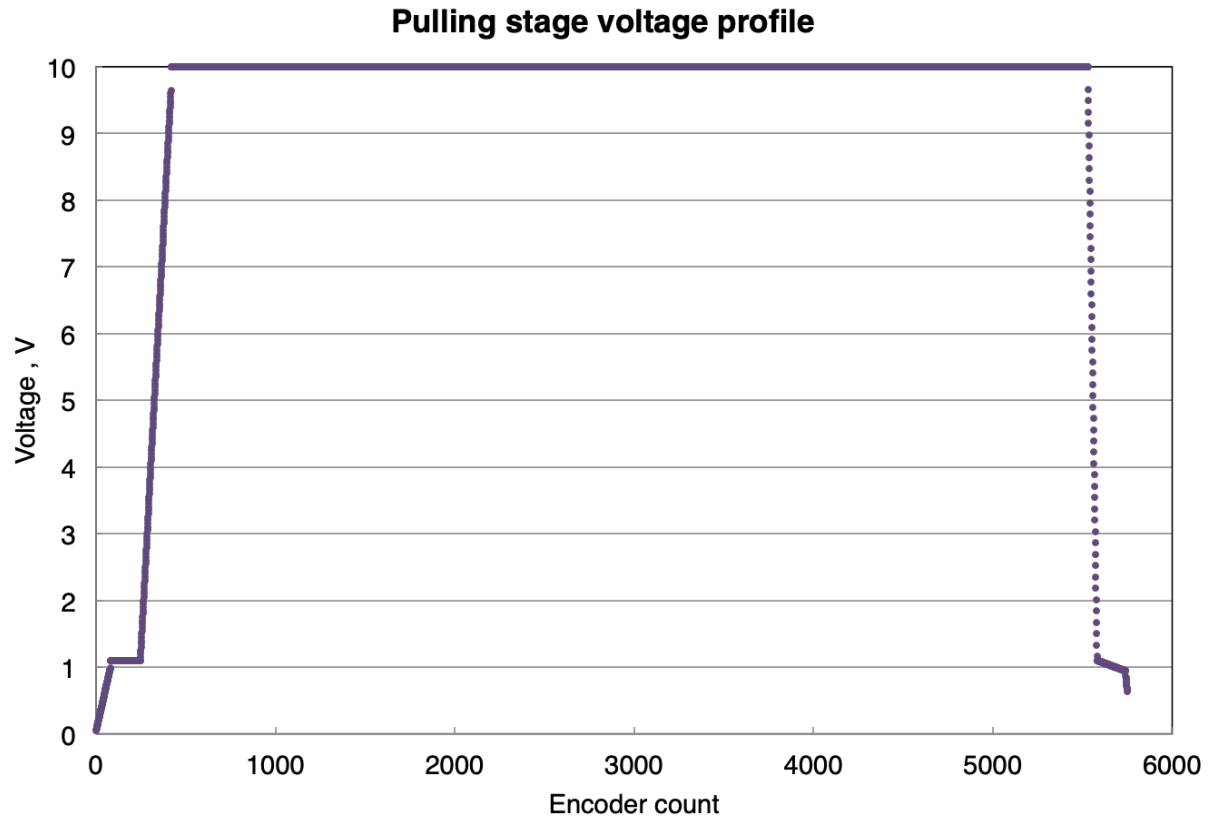


**Figure 4.5:** The pulling voltage profile used to produce the fibres that were investigated within this chapter.

This voltage profile, combined with the feed stage voltage profile 1 shown in figure 4.6, gave fibres that lay in the lower region of the previously mentioned diameter range. To produce fibres that were slightly thicker, the feed stage voltage had to be increased. Increasing the velocity of the feed stage means that more material could be fed into the production of the fibre. Feed

voltage profiles 2 and 3 shown in figure 4.6 produced the fibres that filled out the rest of the previously mentioned diameter range.

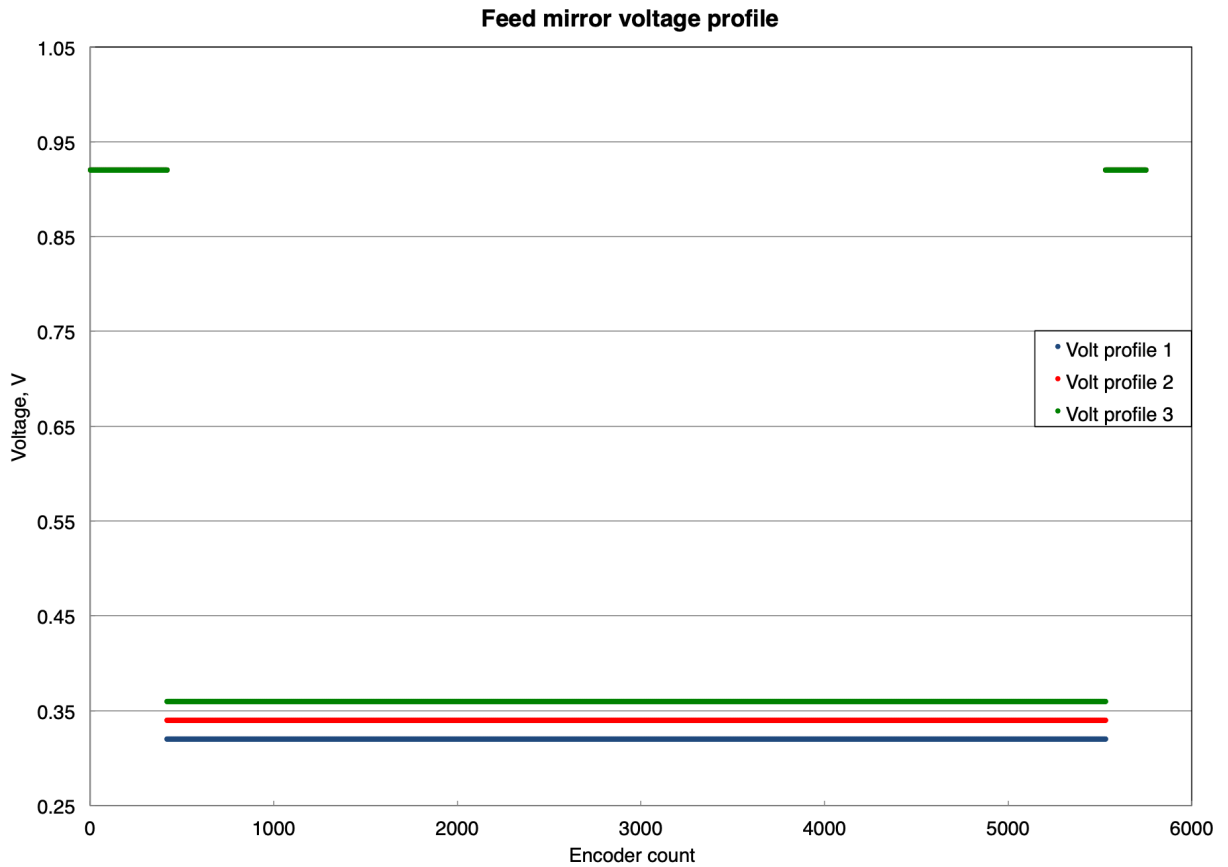


**Figure 4.6:** Feed stage voltage profile used to produce the fibres that were investigated within this chapter. Note that the data points at  $0.9\text{V}$  is there for all 3 profiles, therefore only voltage profile 3 is shown due to the overlay of points.

Unlike the fibre puller at Glasgow, there was no camera feedback installed to monitor the alignment of the beam around the fused silica stock [92]. Alignment of the beam distribution around the fused silica stock was carried out with the use of a welding mask and heavily tinted laser goggles. This reduced the visible brightness enough to allow the distribution of the  $\text{CO}_2$  beam to be observed. Once the fibre has been pulled, aluminium rods were attached to the fuse end clamps to create one rigid unit, creating what was known as a fibre cartridge [136] shown in figure 4.7. The top clamp was then loosened from its holder in the pulling machine and the top stage of the puller was moved up to create space for removal of the cartridge. Once this was done, the bottom clamp could be loosened from its holder and the cartridge could be safely extracted from the pulling machine without touching the fused silica fibre.

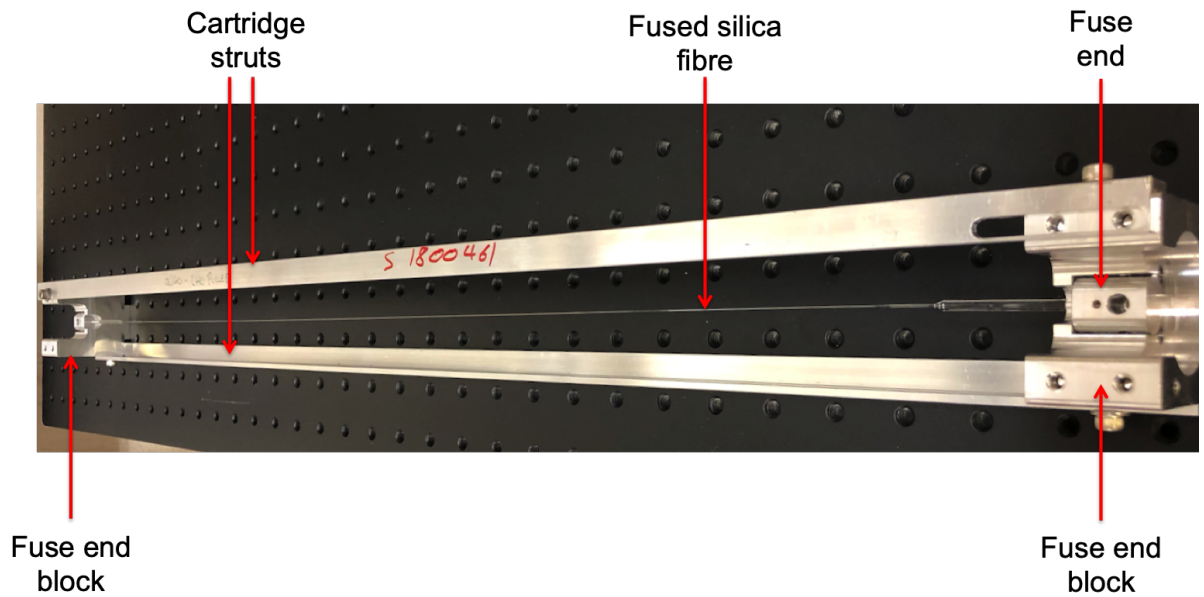


**Figure 4.7:** A fibre cartridge which allows transportation of the fibre around the lab. The blocks and struts allow for easy physical handling without touching any fused silica.

The fibre cartridge was then installed into the fibre profiler, shown in figure 4.8, to measure the diameter of the fibre [137]. Figure 4.9 shows the full profile of a fibre that was pulled using voltage profile 1. This was a combination of the three files that were obtained during the profiling procedure, as described previously in chapter 3. Figure 4.10 shows a zoomed in plot of the thin section of the fused silica fibre. Figure 4.11 and 4.12 show the profile of the bottom and top neck, respectively.

This profiler was a replica of the one developed at Glasgow that was described previously in chapter 3, however it only had one camera operational at the time of this investigation. As a result of this, no angle alignment investigation was carried out.

The dip artefact that appears in figures 4.9 and 4.11 was a common artefact that appears in the vast majority of fibres of all diameters. This occurs at the beginning of the pulling process when the pulling stage starts to draw out the fibre from the molten region. A possible reason for this could be due to the high viscosity that the molten fused silica has and the resulting slow reaction time to reach an equilibrium as the fibre was produced. As the molten region was unsettled during the initial motion of the pulling stage, the fibre was initially drawn from the molten region, before a bulk molten mass from this region was pulled out. The rest of the fibre was then drawn out from this point. In the case of aLIGO fibres, there was a criterion that the bottom and top necks sit within  $800\ \mu\text{m} \pm 10\%$ . A well aligned pulling machine will produce fibres with this artefact that fits within this criteria for it not to be a limiting issue.

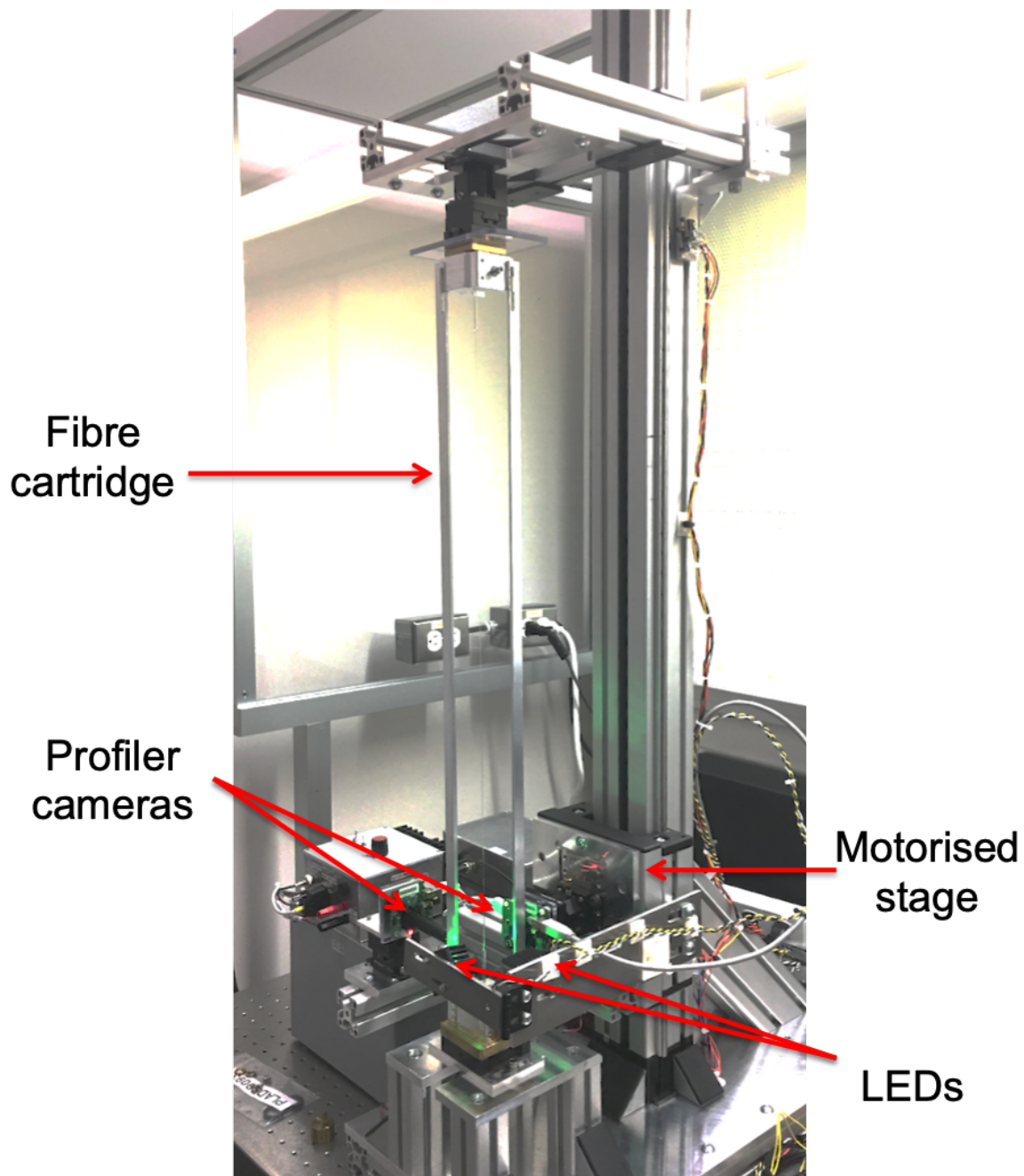


**Figure 4.8:** The aLIGO fused silica fibre profiler at LHO.

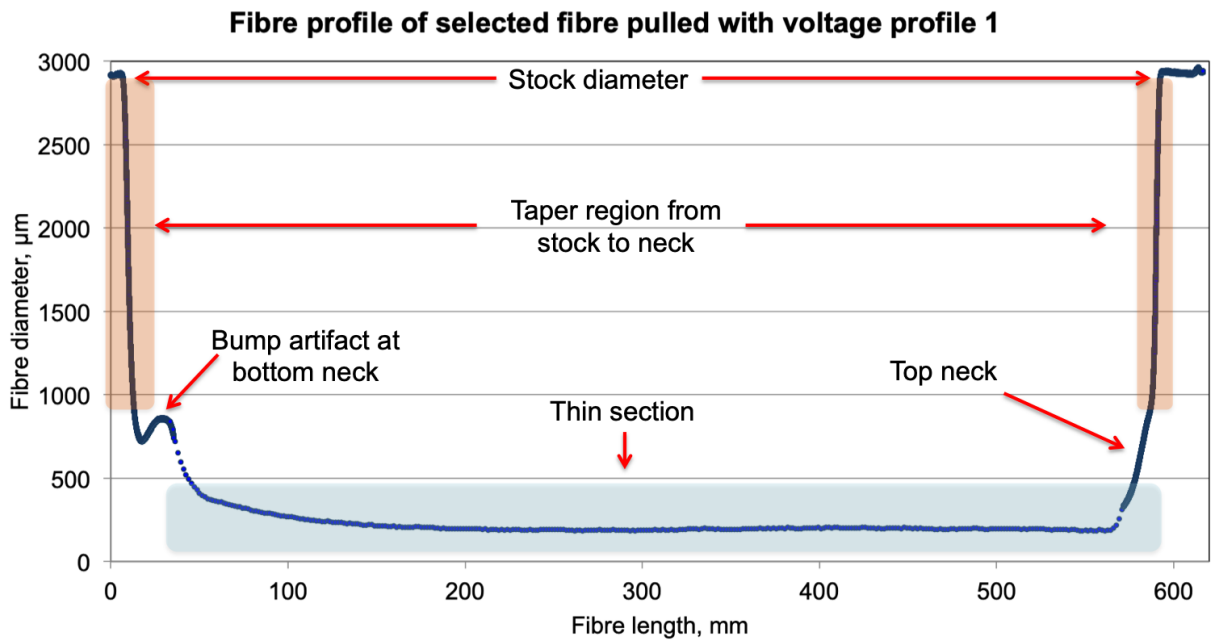


**Figure 4.9:** A full fibre profile of a fused silica fibre that was pulled with pulling voltage profile 1. This plot consists of all the data that was obtained from the three files that were saved during the profiling process as previously described.

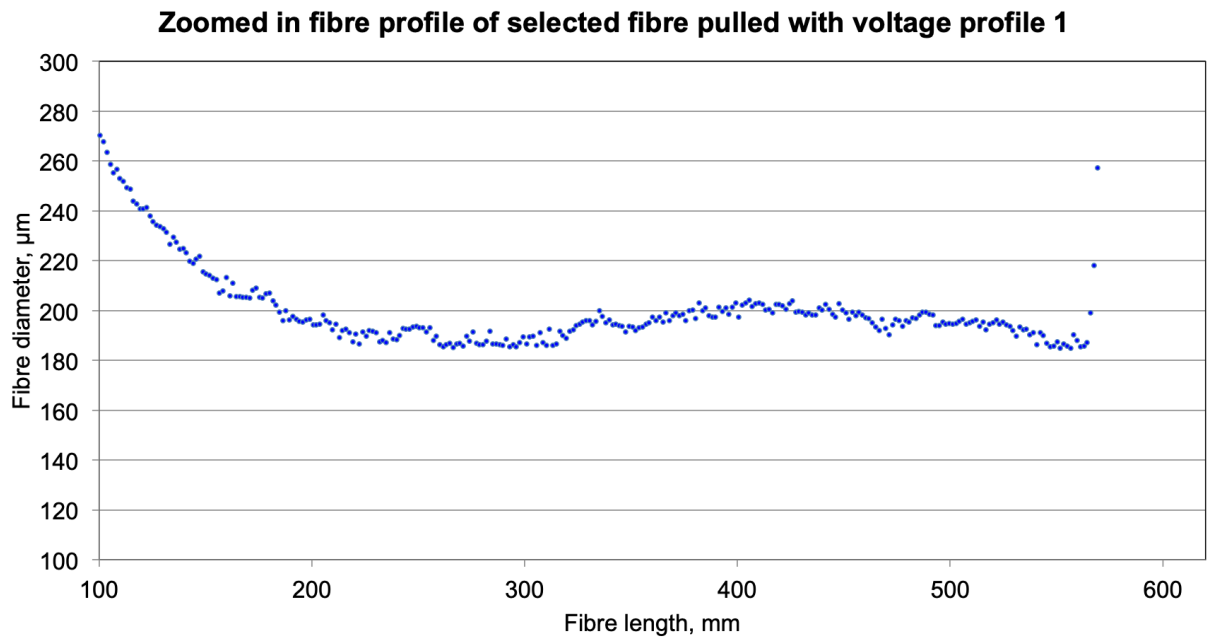


**Figure 4.10:** The thin section of the fused silica fibre in figure 4.9.

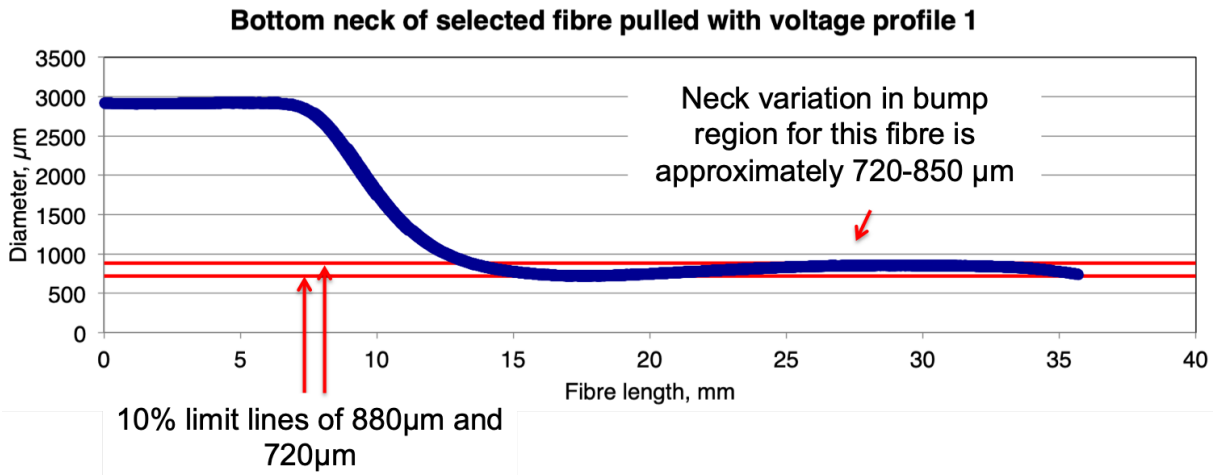


**Figure 4.11:** The bottom neck of the fused silica fibre in figure 4.9. Here, the bump artefact that was described could be seen. For aLIGO suspension fibres, a variation of  $800 \pm 80 \mu\text{m}$  was allowed in this region.

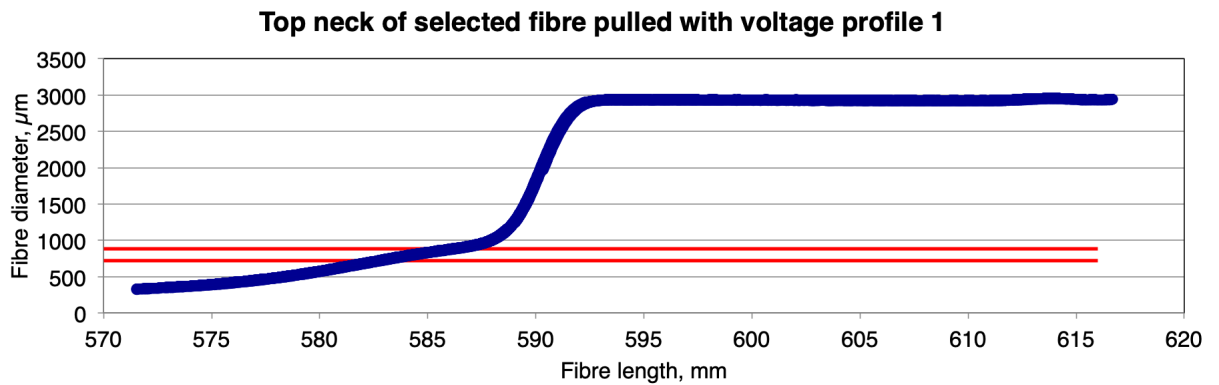


**Figure 4.12:** The top neck of the fused silica fibre in figure 4.9. Note that the neck in this fibre does not satisfy the 10% error allowed for the neck regions for suspension fibres. However, this error was not critical for this investigation and was therefore not an issue that needed to be addressed.

Once characterised, the fibres were stored in a McDry MCU-340A humidity controlled storage cabinet [138]. This kept the fibres in an environment with a humidity level of  $< 1\%$  until they were ready to use.

## 4.2.2 Method

The aim of this investigation was to observe the lifetime of a fused silica fibre under a range of stresses. In particular, stresses between 3-5 GPa. To do so, an experiment had to be developed to allow the suspension of a mass from a fibre with the ability to record the total hang time of the fibre.

For this investigation, the lifetime of a fibre under a specific stress was the key investigative point. To explore this, an experiment was set up to record the lifetime of a fibre hanging a mass in air. This was set up within the aLIGO fibre proof test enclosure, shown in the inset of figure 4.13. The enclosure consists of a solid aluminium base with 4 polycarbonate sheets as walls. These sheets were held in place by a metal frame, and another aluminium plate was attached to the top to fully enclose the space. For aLIGO suspensions, the proof tester was used to carry out an overload hang of a fibre before the installation of a fibre into a monolithic suspension [97]. The fibre was overloaded with a 15 kg mass, which was 50 % more than what it would experience in the suspension and left to hang for 15 minutes or longer. Should the fibre survive, it was considered fit for purpose. This minimises the chance of installing a defective fibre into the monolithic suspension which could result in a suspension failure and stop LIGO from obtaining data during an observing run. This was the same principle that motivated the experimental set up for this investigation.

A schematic of the experimental set up is shown in figure 4.13. The proof tester consists of an anchor point at the top of the enclosure to which the top of the fibre is attached. A motorised jack on the base of the enclosure could then raise a mass to the required height to the bottom of the fibre. The mass could then be attached to the fibre and the jack lowered until the mass was freely hanging. A timer switch, shown in figure 4.14, was then installed to run on a simple custom LabVIEW program to record the hang time of the fibre. The switch was placed next to the jack and underneath the mass so that when the fibre fails, the mass will land on the timer switch, triggering the LabVIEW program to record the hang time.

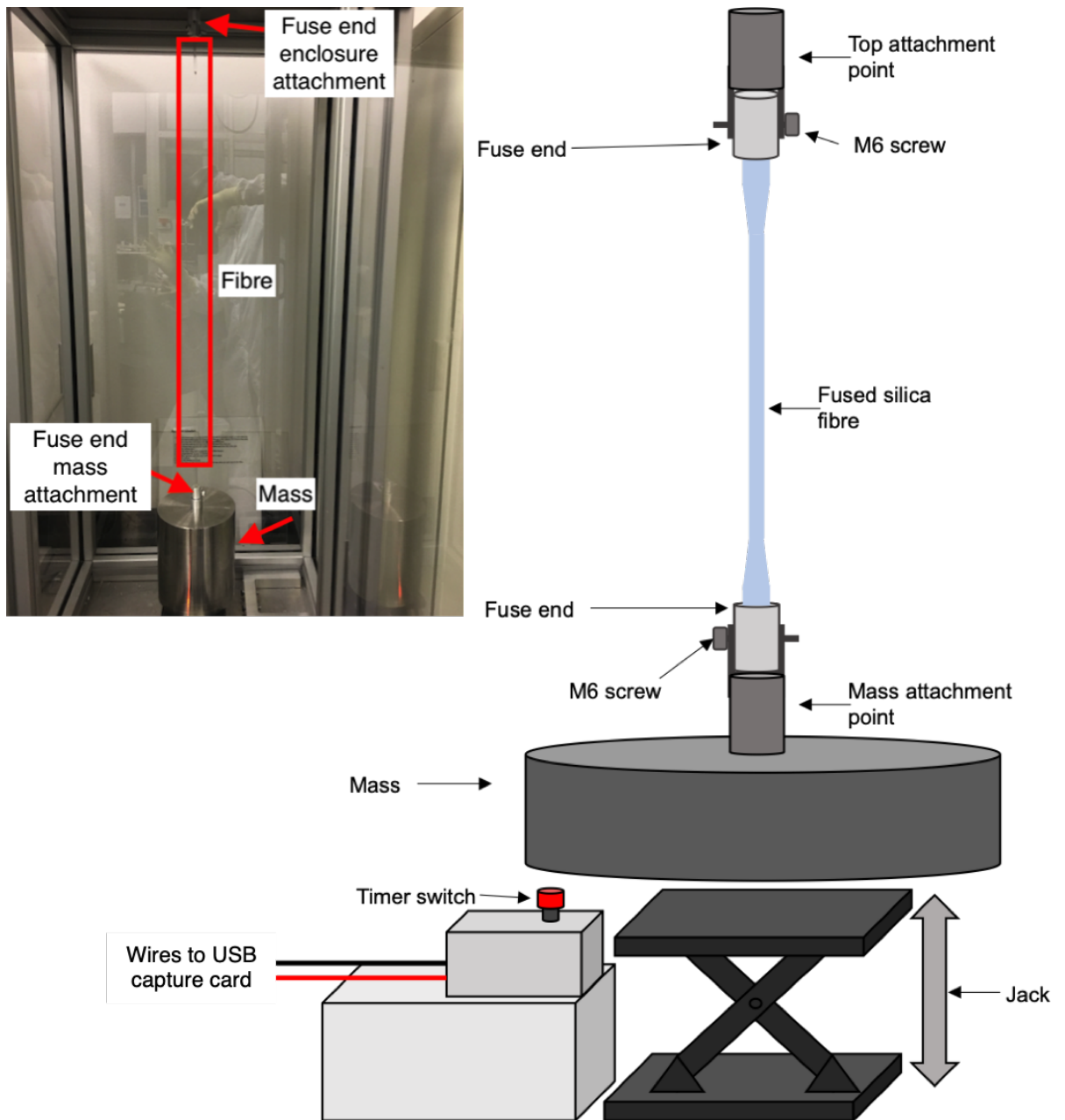


**Figure 4.13:** Schematic of the experimental set up to suspend a mass from a fused silica fibre. Inset: The proof tester enclosure with a fibre undergoing a proof test.



**Figure 4.14:** The timer switch that was used to record the total hang time of the mass.

Theoretically, the aLIGO strength tester would have allowed for any load to be applied to the fibre, and therefore allow for specific stress values to be applied with greater control. It would also have allowed for the change in stress during testing, if so desired. This apparatus however was unavailable during this investigation. As the proof tester uses fixed masses, this made it slightly more difficult to aim for specific stress values within this range. As a result, three masses were used during this investigation, weighing 10 kg, 12.5 kg and 15 kg.

The masses were attached to the fibre by interfacing the fuse-end to a bracket that was attached to the mass. Both the fuse-end and the bracket have a through-hole drilled through to allow a screw to be passed through to secure the mass to the fibre. This same technique was used to attach the fibre to the top of the enclosure. The mass was then lowered using a motorised stage until suspended. This was operated using a Thorlabs built-in stage controller that had controls to move the stage up and down.

The timer switch was a push switch encased in a metal enclosure and connected to a PC via a USB U12 Labjack capture card [139]. A custom LabVIEW program was created to count the time duration of the suspended mass. The LabVIEW counter would start once the mass was suspended and would trigger when the mass fell onto the switch. When the switch was pushed, this sent a +5 V signal to an input pin which triggers the timer to stop when received. The program would then record the hang time by subtracting the start time from the trigger time using its internal time counter.

## 4.3 Analysis

### 4.3.1 Results

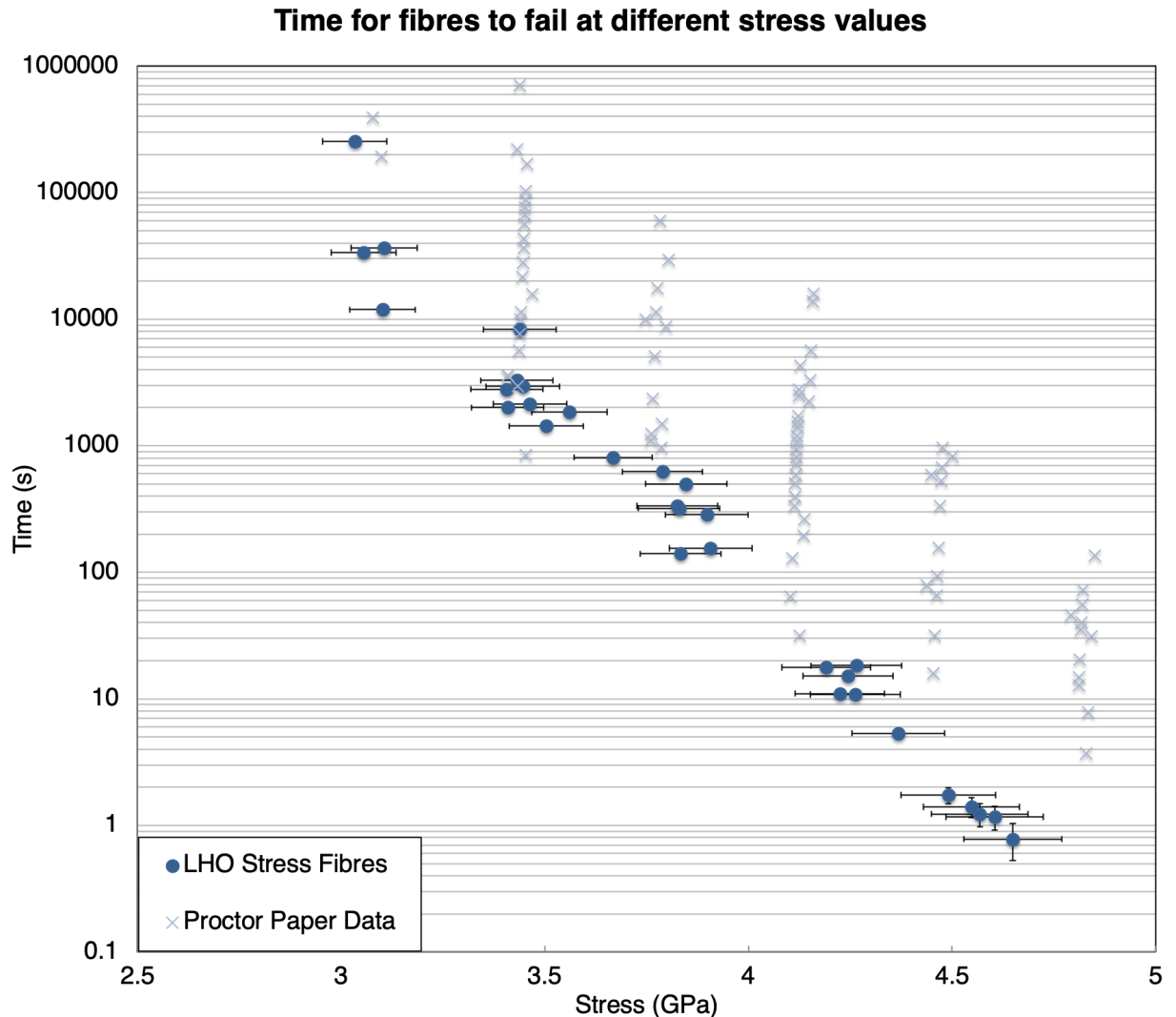


**Figure 4.15:** Total hang time of the suspended masses plotted against breaking stress values for the fibres that were tested in LHO (blue dots). The  $\times$  data points were the data points from Proctor’s in-air research for comparison [131].

Figure 4.15 shows the resulting hang time, in seconds, against the maximum stress applied to the fibre, in GPa. Figure 4.15 also shows the data from previous research by Proctor [131]. As the raw data from this research was not available, the data points were extracted from the published paper using a data plot extraction tool [140]. As this software relies on clicking on data points on an image of the original graph [131] to extract the data, an uncertainty of  $\pm 0.1$  GPa was associated with the position of the data along the x axis on figure 4.15. An assumption was made that all fibres broke at its minimum diameter along the fibre as no high speed camera was available to video the fibre breaking. The maximum breaking stress, calculated using equation 4.1, therefore uses the minimum diameter value.

Each pulling profile altered the fibre diameter significantly enough to cover the parameter space along the aimed stress range of 3-5 GPa. There were small gaps between 3.1 - 3.4 GPa and 3.9 - 4.2 GPa where there was no data. This was due to no produced fibres having a diameter that would fall into those ranges with the masses that were available. The range of minimum diameter values for each pulling profile is shown in table 4.1.

In total, 37 fibres were tested. One fibre failed due to a fuse end failure while lowering the mass. This fibre did not have sufficient epoxy applied during the preparation process, resulting in the stock pulling out. This fibre therefore was not included in figure 4.15. Five fibres failed during the lowering process. Calculations showed that these fibres would experience a maximum stress greater than 5 GPa, which was the accepted value of the ultimate tensile stress of bulk fused silica [132], therefore immediate failure was to be expected. The remaining fibres failed while suspending the mass.

**Table 4.1:** Range of fibre diameters obtained with the four pulling profiles

Pulling profile	Fibre diameter range, $\mu\text{m}$
1	$183.5 \pm 2.4 - 186.6 \pm 2.4$
2	$195.2 \pm 2.5 - 200.8 \pm 2.6$
3	$194.2 \pm 2.5 - 198.0 \pm 2.6$
4	$203.7 \pm 2.6 - 208.3 \pm 2.7$

All but one fibre that experienced a maximum stress above 3.4 GPa broke within an hour, and all those that had a maximum stress greater than 4.4 GPa broke in under 20 seconds. The fibre that experienced the lowest stress value of 3.2 GPa was the only fibre to last longer than a day, lasting a total of 70 hours 41 minutes.

### 4.3.2 Uncertainties

The main source of uncertainties in this chapter was from the diameter of the fused silica fibres from the profiler. The uncertainty in the diameter of the profiler was taken as 1.3% as stated in [121] through the quadrature sum of the random and systematic uncertainties. Calculating the uncertainties for the area therefore gives a value of 2.6%. This was the value of the stress uncertainty shown in figure 4.15.

The vertical error bars were taken as the average human reaction time of 0.2 seconds [141] as the program was started the moment the mass was suspended. The moment this happened was obvious by eye as there was movement of the mass at the moment of suspension.

### 4.3.3 Discussion

Compared to the data points obtained by Proctor [131], the majority of the fibres that were produced during this investigation lie either at the low end, or below, the spread of data points.

Both sets of data were carried out in air, however the diameter range was different. Proctor’s data consisted of fibres that were pulled between 15 - 80 μm in diameter with an uncertainty of 3.0 % [131].

Extrapolation of the data to lower value ranges could allow for predictions of the estimated hang time of a suspension under a specific stress. Table 4.2 and figure 4.16 shows the predicted life time of fused silica fibres under stress values of current gravitational wave observatories, as well as future possible stress values. The exponential relationship from equation 4.3 could be seen from this graph where fibres that would be exposed to stress of 2.0 GPa would be expected to hang for more than a year.

**Table 4.2:** Predicted in-air hang time values of four gravitational wave detector stress scenarios.

Detector	Stress, GPa	Predicted lifetime, years
GEO600 (current value)	0.3	114155
aLIGO (current value)	0.78	5700
aLIGO (proposed A+ upgrade)	1.2	340
aLIGO (potential future upgrade)	1.6	34

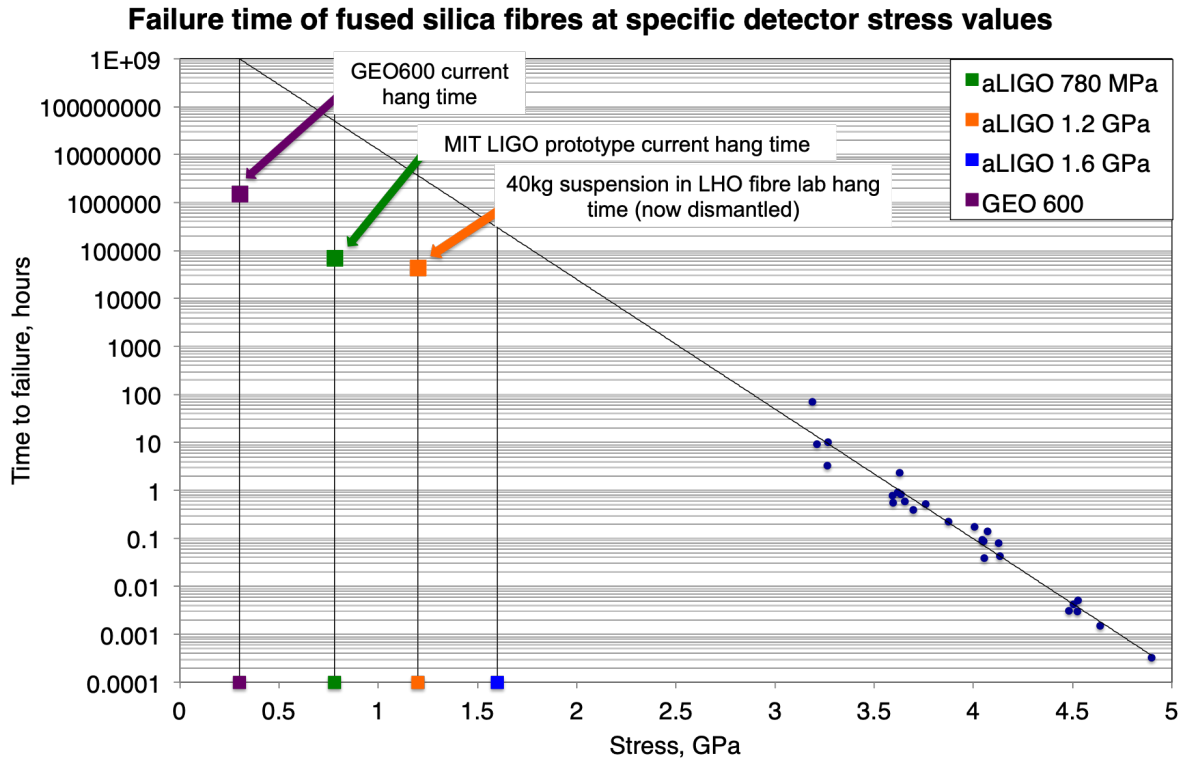


**Figure 4.16:** Predicted in-air lifetime of fused silica fibres at relevant detector stress values. Note that the highlighted points for GEO600, MIT and LHO were all experimental results. Out of the three square indicators, only the LHO fibre lab suspension has been dismantled to allow equipment use for suspension welding practice. GEO600 and MIT are still hanging.

The 1.2 GPa and 1.6 GPa stress values marked in figure 4.16 were chosen as these were two of the proposed values that were being considered at the time of this research to install into the

aLIGO suspensions for A+ [72] [90]. In figure 4.16, there was an orange block that indicates the hang time of a 40 kg suspension at the fibre lab in LHO at 1.2 GPa. This suspension was however taken down due to the need to use the set up for fibre weld training prior to the start of the third aLIGO observing run. To reach this required stress value, the fibres have to have a diameter of 300  $\mu\text{m}$ . It could also be seen from figure 4.16 that any fibres that would be under a stress of 2.0 GPa would be expected to last for more than a year.

The extrapolation of data in figure 4.16 show that the stress that aLIGO fibres were currently exposed to (780 MPa) should have an expected lifetime of approximately 5700 years before failing. For the A+ scenario of 1.2 GPa, a fibre would be expected to last approximately 340 years in air. This was a significantly sufficient lifetime for an operational detector. As it has been shown that fibres in vacuum could potentially last significantly longer by up to thousands of years [131] [92], these hang time values could be considered to be the lower expected bound to the fibre lifetime at this stress. A possible reason for the increased lifetime of fibres in vacuum could be due to the fact that the fibre is not exposed to a humidity varying environment. Research has shown that water molecules can affect the integrity of the bonds within fused silica, such that strength performance drops as the environmental humidity increases [142] [143]. This is a reason that the fibres are stored away in humidity controlled cabinets where the relative humidity is  $<1\%$ .

Increasing the stress to 1.6 GPa would give an in-air lifetime of approximately 34 years. This was still a lifetime that was suitable for use in an operational detector. A value of 1.8 GPa would bring the expected in air lifetime to approximately just under 10 years. Though there was currently no minimum lifetime set of suspension fibres in aLIGO, a value of 10 years could be seen as a possible minimum lifetime of an operational detector. This was due to the fact that within those 10 years, there would be many commissioning periods where components would be changed and replaced and the fibres could be seen as a component that could be replaced. This assumption would mean 1.8 GPa could be set as the upper limit stress value that should be applied to a aLIGO suspension fibre. It should be noted however that as previously mentioned, life time in-air was significantly less than that in-vacuum [131] [92] and should also be taken into consideration when determining what the maximum stress applied to suspension fibres should be .

A comparison of data could also be made to research that was carried out in parallel to that discussed in this chapter by a fellow University of Glasgow PhD student at the time, Dr Kyung Ha Lee [92]. The Glasgow data was from a similar experimental set up, but focusing on a lower stress range, to complement the work presented here. In this case, the range was 2.8 - 4.2 GPa. This allowed for some overlap to occur between the two sets of experiments to allow comparisons between similar stress values.

Both experiments at LHO and Glasgow were deliberately carried out simultaneously to cover a wide range of stress values due to the exponential rise in time needed for fibres to break at lower

stresses. The pulling machines that were used in Glasgow and Hanford were the same. The only differences occur on the optical bench to direct the laser beam into the pulling machine.

Due to a slight difference in the calibration between the profiler between LHO and Glasgow, a fibre that was produced in Hanford was brought back to Glasgow to be profiled. The profile data that was obtained from profiling the Hanford fibre both in Hanford and in Glasgow were then compared [92]. It was found that there was a difference between the two profiles at the 3 mm stock region of the fibre of 45  $\mu\text{m}$ . Data taken from LHO was then adjusted accordingly to match the calibration of the Glasgow profiler. This allowed a fair comparison between the Hanford and Glasgow data to be made, and is shown in figure 4.17.

Figure 4.17 shows that the tests that were carried out at LHO and Glasgow, on two different fibre pulling machines, were in agreement with each other. The fact that both sets of data were in agreement with each other show that the pulling machine performance could be considered to be consistent with each other. This means that tests on fibres produced in either location would be expected to give similar results. Interestingly, both sets of data lie either below or at the bottom of the spread for the data obtained by Proctor [131]. Up until 3.5 GPa, the majority of fibres that were tested sit in the bottom of Proctor's spread. For stresses at 3.5 GPa and above, the trend of the fibres lying below the data of Proctor continue with the Glasgow tests that were carried out. The spread of data points for both the LHO and Glasgow data together was however tighter than the observed spread from Proctor's data. This could potentially be associated with the tighter production repeatability of the aLIGO pulling machines than the flame pulled devices that were used in Proctor's data.

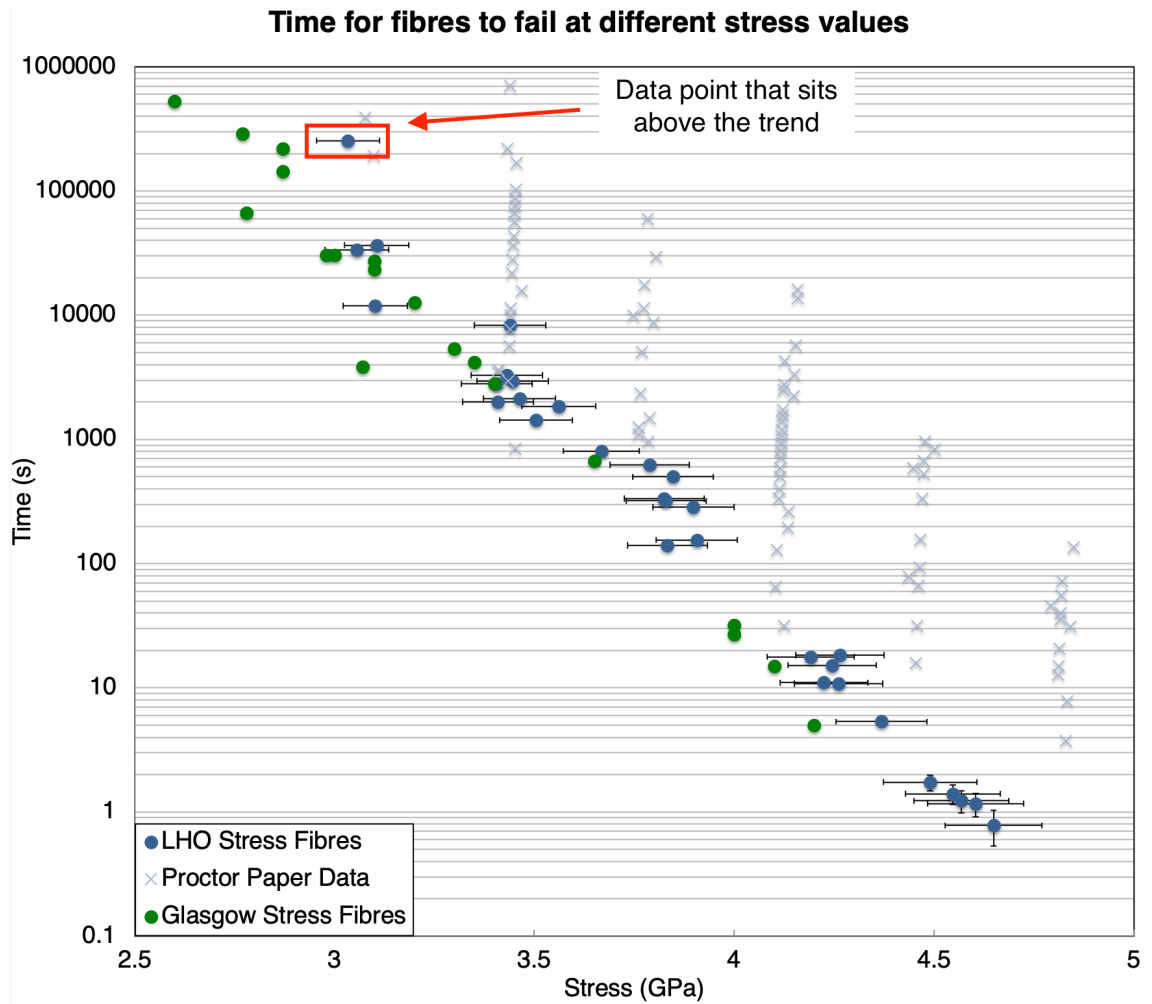


**Figure 4.17:** The comparison of results discussed in this chapter with data from Lee [92] and Proctor [131].

There was one data point at 3.0 GPa that does not follow the trend of the LHO data points and was the only fibre tested that lasted for more than 1 day. This point sits above the trend, and is highlighted in figure 4.17. This fibre hung for a total of 70.6 hours. It was not known why this fibre lasted this long in comparison to fibres that were tested to similar stress values. All fibres were subject to the same preparation and pulling procedure. The experimental set-up was regularly checked to ensure that the fibre was still suspended and that it did not fail and miss the timer switch. When the fibre eventually failed, it did land on the timer switch triggering the timer to stop. A greater number of fibres could in the future be tested to see if this one data point was indeed a true outlier, or if the greater number of tests will widen the spread of data points.

The fused silica that was used in this investigation, as mentioned previously, was Heraeus Suprasil 2 [132]. This was the same material that was used for producing fibres for the aLIGO suspensions. However, this was not the same brand of fused silica used in Proctor's investigation, for which the data sheet could not be located to confirm purity properties for comparison. It could be assumed that it was a modern high purity silica due to the high performance values

it showed. At this point in the investigation, it was not possible to determine whether or not this played a significant role in the performance of the fibres in this test. The pre-production treatments were also different in that the stock material in Proctor's investigation consisted of a chromic acid wash, followed by flame polishing. This was unlike the laser polishing carried out in this investigation.

It was possible that the reason for the difference between the aLIGO-type fibres and Proctor's fibres was the diameter of fibres tested. As previously mentioned, the fibres that were tested in Proctor's work had the diameter of 20-40  $\mu\text{m}$ . Previous research [93] has shown a difference in performance for thinner ( $< 100 \mu\text{m}$ ) fused silica fibres than thicker ( $> 100 \mu\text{m}$ ) fibres. The bottom range of Proctor's diameter range was approximately an order of magnitude smaller than the fibres that were tested in LHO. It was therefore a possibility that the thinner fibres tested could have a different performance than that of the diameter that were tested in LHO and Glasgow. It was therefore concluded that this would be the next stage in this investigation. Details regarding the pulling, characterisation and investigation of thinner fibres will be discussed in the following two chapters.

Due to the set-up of the fibre profiler at the time where only one camera was used to characterise the fibre, angle measurements in the neck regions could not be calculated. Photos of the fibre necks were not taken either as the angle artefact was not an area of interest at the time. Even though this was not investigated, no fibres were noted to have an obvious angle by eye during production as this would have been flagged at the time.

## 4.4 Improvements

Improvements could be made to this investigation to increase the spread of data points. One improvement that could be made would be to use the fibre strength tester, as previously used in chapter 3, instead of metal masses. A limitation of the metal masses was the reliance on being able to change the fibre diameter to fill in the stress values within the range that was being investigated. If the strength tester was used instead, it would mean only one pulling voltage profile would need to be made to produce the approximately the same fibre through the whole investigation. The strength tester could then be controlled to apply a specific load on the fibre that would equate to the desired stress that would be wanted. This also means that the repeatability of obtaining a data point from one specific stress value could occur in a relatively straight forward manner. An alternative to this would also be the use of a wider range of masses should the strength tester not be an available option. Tests that involve a change in stress could also be performed with the strength tester to accompany results of the static tests that were carried out in this investigation. This could include relaxing and tensioning the fibre at specific stresses to observe if this effects the life time of the fibre.

A second improvement applies to the profiling procedure and was also a previous recommen-

dation from the previous chapter on the neck angle investigation. As the fibres in this chapter were profiled with only one camera, due to the set up of the LHO fibre profiler at the time, it was not possible to see if there were angular defects in the fibre. The possibility that angular defects could have a more prominent effect during hang tests instead of destructive tests could not be ruled out at this stage.

## 4.5 Conclusion

During a LTA to LIGO Hanford, the opportunity arose to carry out an investigation into the stress fatigue of fused silica fibres in the fibre production lab at LHO. The aim of this investigation was to investigate the hang time of fused silica fibres under high stress range compared to what aLIGO suspension fibres were currently subjected to. This was in preparation for planned future upgrades to aLIGO, known as A+, and for next generation gravitational wave detectors where the stress value that the fibres in the suspensions would be exposed to was greater than what the current aLIGO fibres were exposed to. For example, current aLIGO suspension fibres were under a stress of approximately 780 MPa, but A+ is aiming to increase this to 1.2 GPa as this will move resonant modes towards the edges of the observing band.

This investigation involved looking at a stress range between 3-5 GPa as this range would yield fibres that would break in a time scale of less than a day to maximise the number of data points that could be obtained during this LTA. All tests at LHO were carried out in air in parallel to tests that were being carried out in Glasgow at a similar stress range, but both in-air and in-vacuum. The results of these investigations were then compared to an investigation by Proctor in the 1960s to see if there were any differences observed.

It was found that data from both LHO and Glasgow did not align with the data that Proctor had obtained in his investigation, but did align with each other. The alignment of the LHO and Glasgow data shows that the two separate pulling machines at each location could produce fibres that were consistent with each other. This means in the future, any investigations that were carried out at only one location could be considered to produce repeatable results at the other location.

Extrapolating the LHO data back to the stress that aLIGO fibres were currently exposed to show that a pristine fibre in air exposed to 780 MPa should have an expected lifetime of approximately 5700 years before failing. For the A+ scenario of 1.2 GPa, a fibre would be expected to last approximately 340 years in air. As it has been shown that fibres in vacuum could last significantly longer, these hang time values could be considered to be the lower expected bound to the fibre lifetime at this stress. Increasing the stress to 1.6 GPa would give an in-air lifetime of approximately 34 years. As test masses and various suspension components could potentially require changing every few years due to performance related aspects, the data obtained in this investigation could be used to judge what the upper stress bound should be for all

future suspension upgrades. A recommended maximum stress would be 1.8 GPa which would give a in air lifetime of approximately just under 10 years.

This data was also used in an investigation into recent suspension failures that occurred during the commissioning period before the third aLIGO observing run to determine whether or not the stresses that were applied to the suspension fibres due to misalignments were too high to determine the cause of failure [112].

As both the LHO and Glasgow data did not perform to the level of Proctor's data, it was decided that extending this investigation into fibres with a diameter  $50\ \mu\text{m}$  and below would be carried out to see if they would align with the LHO/Glasgow data or with Proctor. The following two chapters will detail this investigation thoroughly.

# Chapter 5

## Development of a dedicated diameter characterisation profiler and strength tester for $\leq 50 \mu\text{m}$ diameter fibres

### 5.1 Motivation

Before an investigation into looking at stress fatigue of sub  $50 \mu\text{m}$  diameter fibres could be investigated, there were several developments that had to be carried out.

Previous research was conducted to build and characterise a pulling machine to produce fused silica fibres of a much smaller diameter than what was produced for aLIGO, known as the ultra-thin fibre pulling machine [93] [99]. The ultra-thin fibre pulling machine was capable of producing fibres up to a length of approximately 30 cm, with diameters down to  $\approx 7 \mu\text{m}$ . Fibres produced from this pulling machine will here on be referred to as "ultra-thin fibres". The detail of how the fibres were produced will be discussed in detail in the following chapter. These fibres were produced for use in various investigations and experiments both in Glasgow, such as characterisation of ultra-thin fibres, Young's modulus, and the production of fibres for the Sagnac Speedmeter [144] [145] and the Albert Einstein Institute's 10 m prototype interferometer in Hannover, Germany [146].

One of the investigations carried out in Glasgow was to look into the Young's modulus of ultra-thin fibres ranging between a diameter of 10-100  $\mu\text{m}$  [93] [147]. This investigation looked at pulling fibres from three different pulling profiles to obtain three separate batches of fibres to investigate. These fibres were then installed into an ultra-thin fibre strength tester to record the breaking load and stretch at point of failure. All three of these batches obtained a wide spread of Young's modulus values.

There were two major factors that contributed to the uncertainties obtained during the Young's modulus investigation:

- Uncertainty in the diameter of the fibre during profiling.

- Uncertainty in the reading of the stretch of the fibre at point of failure.

The first of these items was related to the optical set-up of the aLIGO fibre profiler and the difficulty in accurately imaging an ultra-thin fibre. The second was related to the method the fibre extension was measured and calculated and the variability in where on the set-up the measurement was taken from. Both of which will be discussed in this chapter.

Figure 5.1 shows a screenshot of one of these ultra-thin fibres being profiled on the aLIGO fibre profiler that was approximately  $9\ \mu\text{m}$  in diameter during the above mentioned investigation. It could be seen in this case that the image of the fibre was under 6 pixels in width for a fibre with diameter of approximately  $9\ \mu\text{m}$ . This equates to each pixel measuring approximately  $1.5\ \mu\text{m}$  which placed limitations for the thin fibre imaging. The uncertainty in the diameter of the fibres tested could get as high at 10% due to the difficulty in profiling an ultra-thin fibre with the aLIGO profiler configuration.

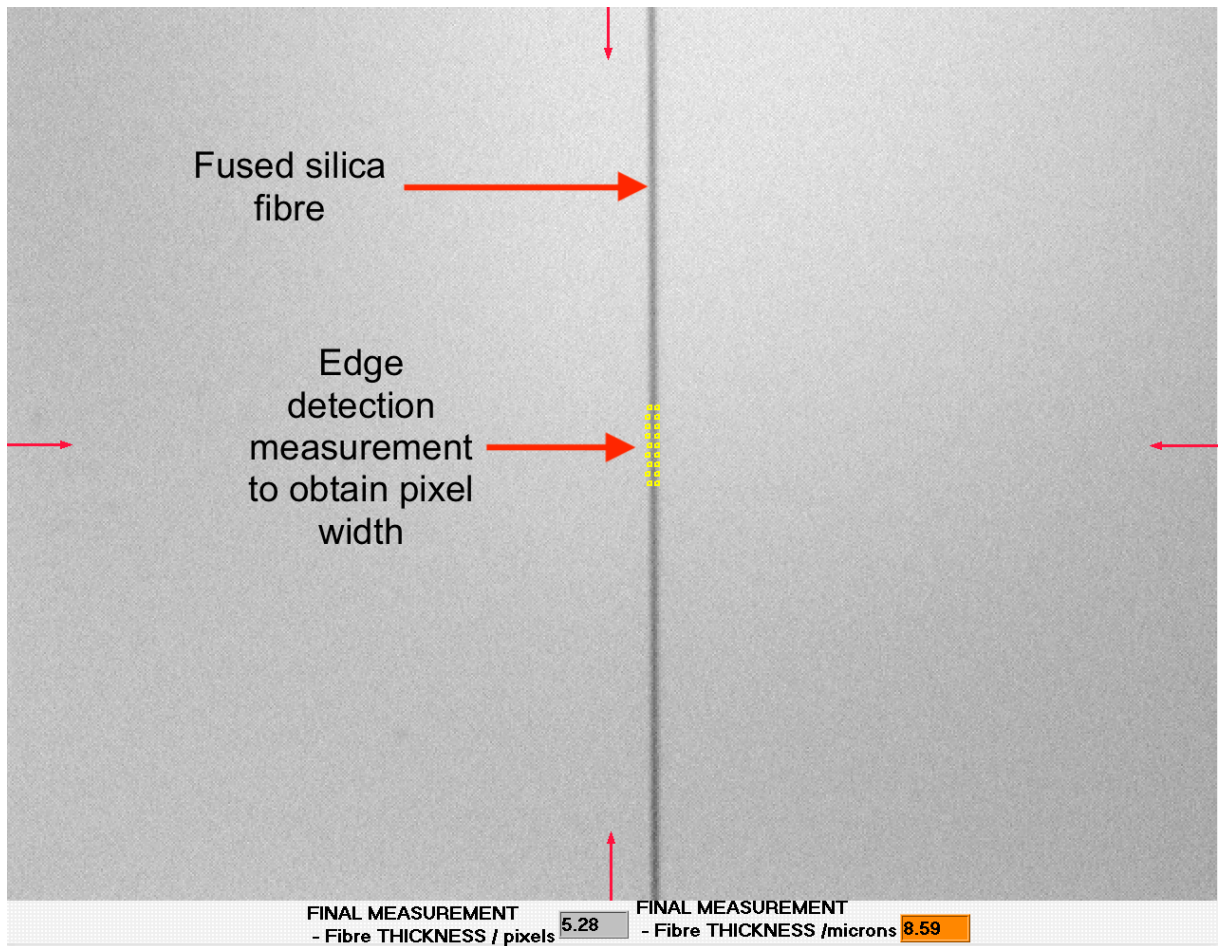


**Figure 5.1:** Screenshot of the image of an ultra-thin fibre being profiled on the aLIGO fibre profiler. .

Figure 5.2 shows an image of the strength tester during the previous investigation. To measure the extension of the fibre at the point the fibre broke, a set of digital calipers were used to

measure the distance between the baseplate and the motorised stage. The ability to measure the distance between the baseplate and the motorised stage consistently was a challenge due to the lack of reference points on the set-up to ensure the calipers would sit in the same place for every measurement. Holding the calipers at an angle and not perfectly perpendicular to the base plate could result in a greater distance measurement than the motorised stage actually travelled.

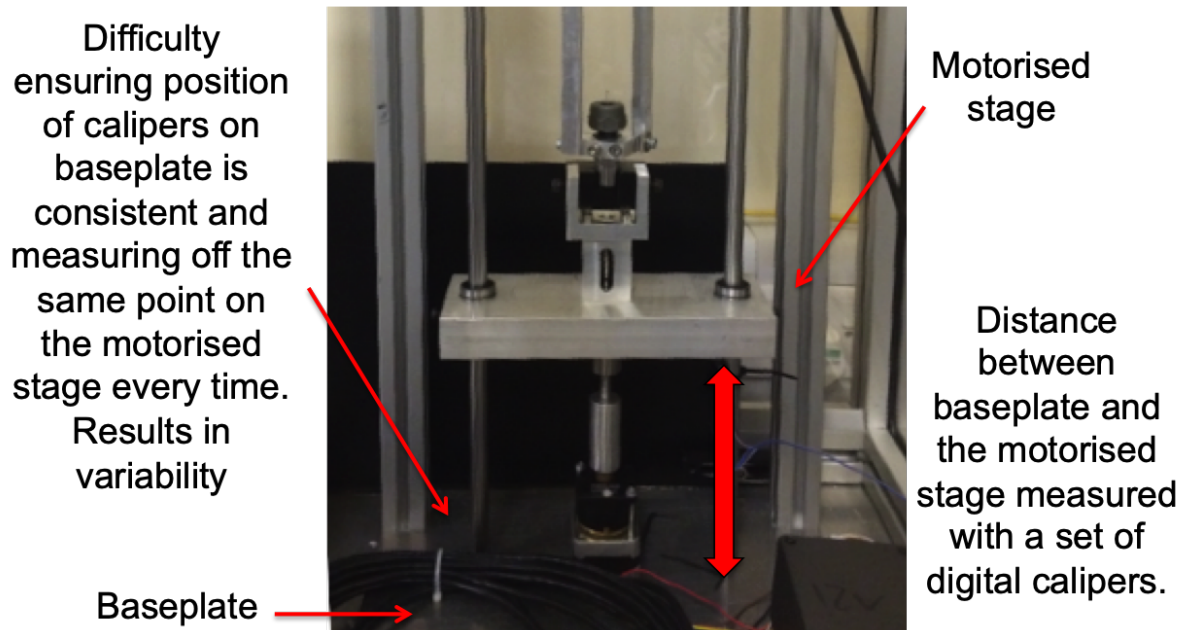


**Figure 5.2:** Highlighted issues with the previous set-up of the ultra-thin fibre strength tester.

The combination of these major sources of uncertainty resulted in values of the Young's modulus having up to a 16% uncertainty associated. For any investigation involving these ultra-thin fibres to be carried out, these sources of uncertainties had to be tackled. In the case of the aLIGO profiler mentioned previously, the stated uncertainty value for the diameter was 1.29% for aLIGO diameter fibres. For ultra-thin fibres, this uncertainty value was up to approximately 10%. The best case scenario uncertainty for measuring the stretch of the fibres was  $\pm 0.03$  mm that was associated with the digital calipers that were used. This relies on the ability to measure the stretch of the fibre from the exact same position on the motorised stage of the strength tester. As previously seen in figure 5.1, the fibre in the screenshot was only approximately  $9 \mu\text{m}$  in diameter, and takes up 6 pixels. This equates to each pixel approximately measuring  $1.5 \mu\text{m}$ , and it was this resolution that contributes to the large resulting uncertainty in the earlier mentioned Young's modulus.

This chapter will discuss the design and characterisation of a dedicated fibre profiler specifically for ultra-thin fibres, and the upgrades that were carried out to the already existing ultra-thin fibre strength tester. The goal of these developments and upgrades was to decrease the above mentioned uncertainties where the uncertainty that would be associated with the Young's modulus would be approximately 5-10%. These goals are also stated in table 5.1. This would equate to

decreasing the profiler uncertainty associated with the profiler to under 5% for ultra-thin fibres.

Work within this chapter was carried out with the assistance of two IREU summer students, with credit given where appropriate. Work within this chapter was also published in *Classical and Quantum Gravity* [99].

**Table 5.1:** The goals that were aimed to be achieved through the development and upgrades of the ultra-thin fibre characterisation apparatus in this chapter.

Requirement	Feature
Higher camera magnification than the aLIGO profiler	Increase magnification capabilities from $\times 6$ to at least $\times 16$
Reduce uncertainty in fibre diameter measurement	Higher magnification and increased camera resolution
Ability to easily change magnification for different diameter samples	Variable magnification
Remove the need to use hand held instruments to measure fibre extension	Installation of encoder to strength tester stage
Ability to strength test multiple lengths of fibres	Increase length of drive rods
Reduce the uncertainty value in Young's modulus measurements	All of the above

## 5.2 Dedicated ultra-thin fibre profiler

The current iteration of the new fibre profiler, referred to as the "ultra-thin fibre profiler" from here onwards, is shown in figures 5.3 and 5.4. It works on the same principle as the aLIGO fibre profiler [121] [122] as detailed in chapter 3. In short, a variable high magnification lens system was attached to a camera to image the fibre. A LED was used to illuminate the fibre to cast a shadow on the sensor of the camera. An ultra-thin fibre cartridge, shown in figure 5.5, was placed into a holder and a camera system moves along the length of the fibre on a motorised stage to obtain the diameter of the fibre. This stage, as well as the camera were controlled through a custom LabVIEW program based on the same program as the aLIGO fibre profiler [122]. The ultra-thin fibre cartridge and the fibre cartridge holding block that were both developed during previous investigations [93] [99], shown in figure 5.6, sit on a  $360^\circ$  rotating platform. The rotating platform allows for different perspectives of the fibre to be profiled. The holding block has the same footprint as the aLIGO profiler, which allows ultra-thin fibre cartridges to be used

on both profilers. A clear plastic shield was installed onto the front of the platform, as shown previously in figure 5.3. This was to protect the fibre from air currents as people walk by the front of the desk the profiler sits on, as the fibres were so thin that they were prone to air current disturbances.

This section will detail the key components of the ultra-thin fibre profiler.

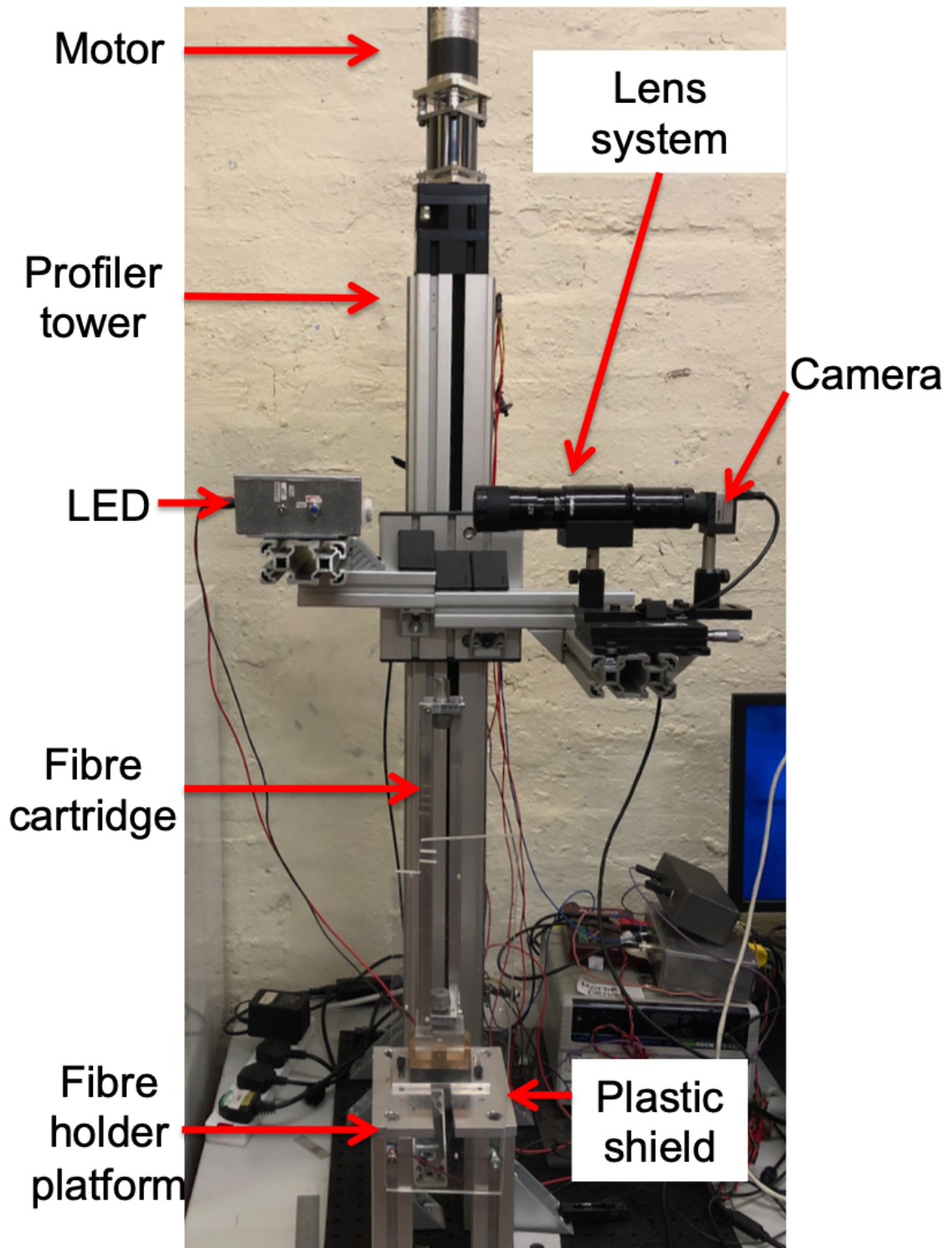


**Figure 5.3:** Current iteration of the ultra-thin fibre profiler.

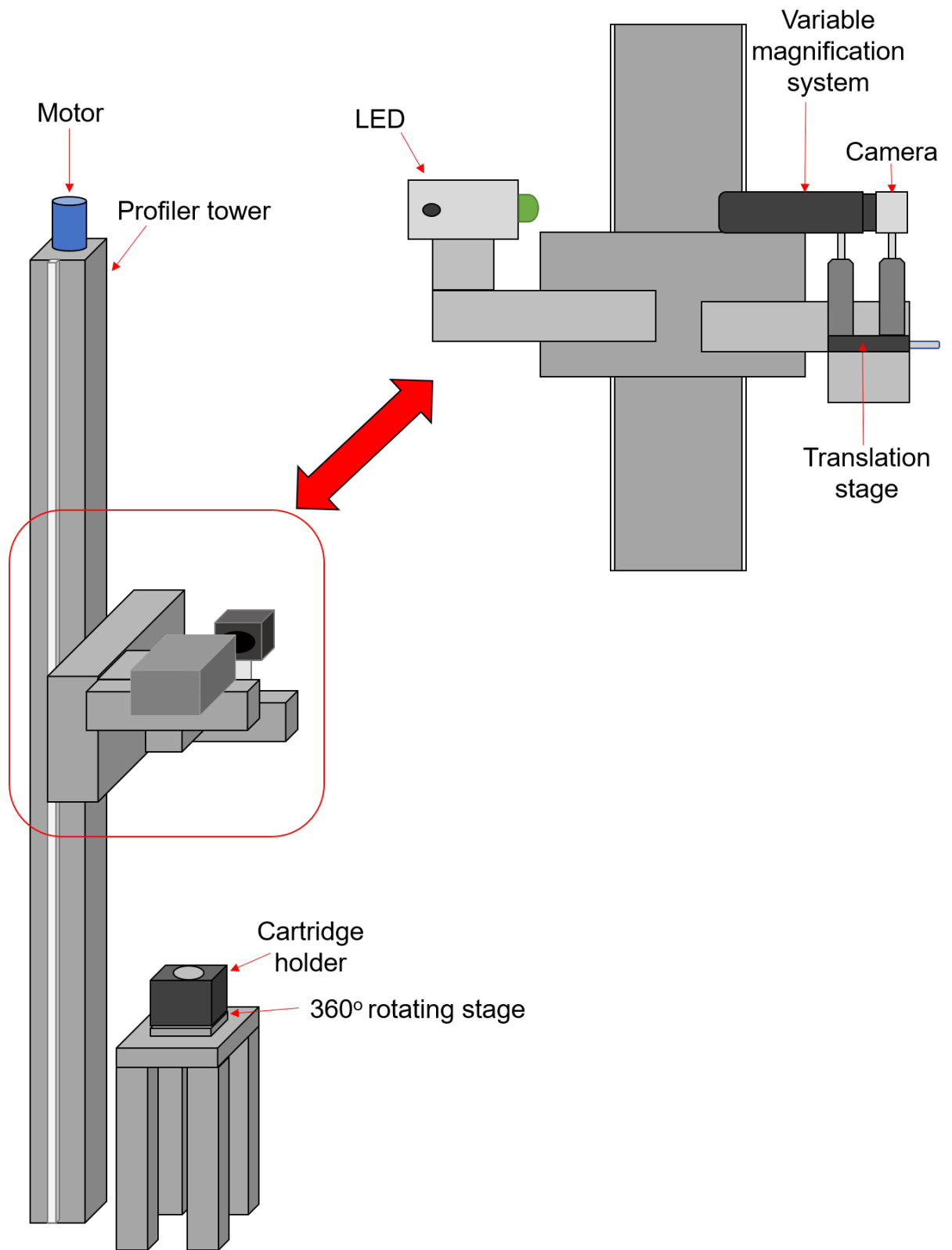
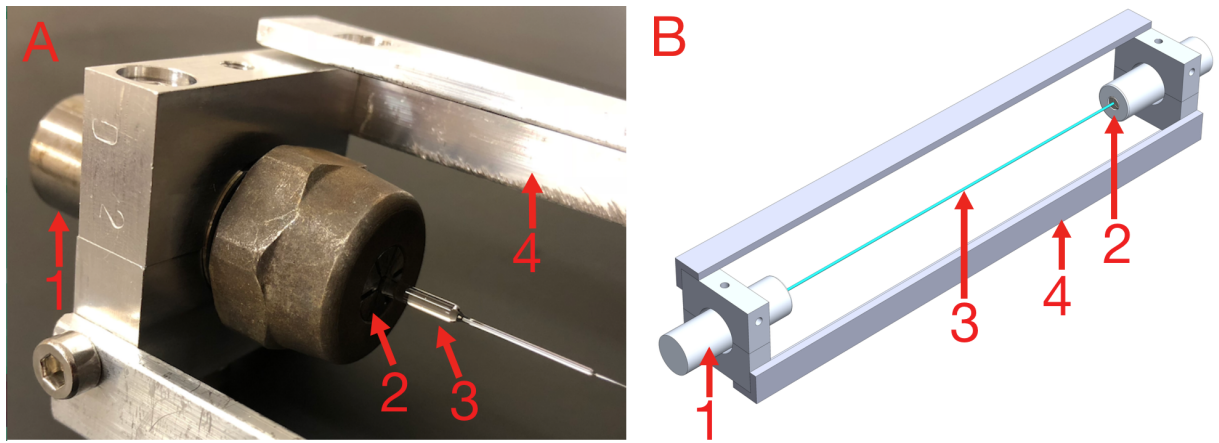
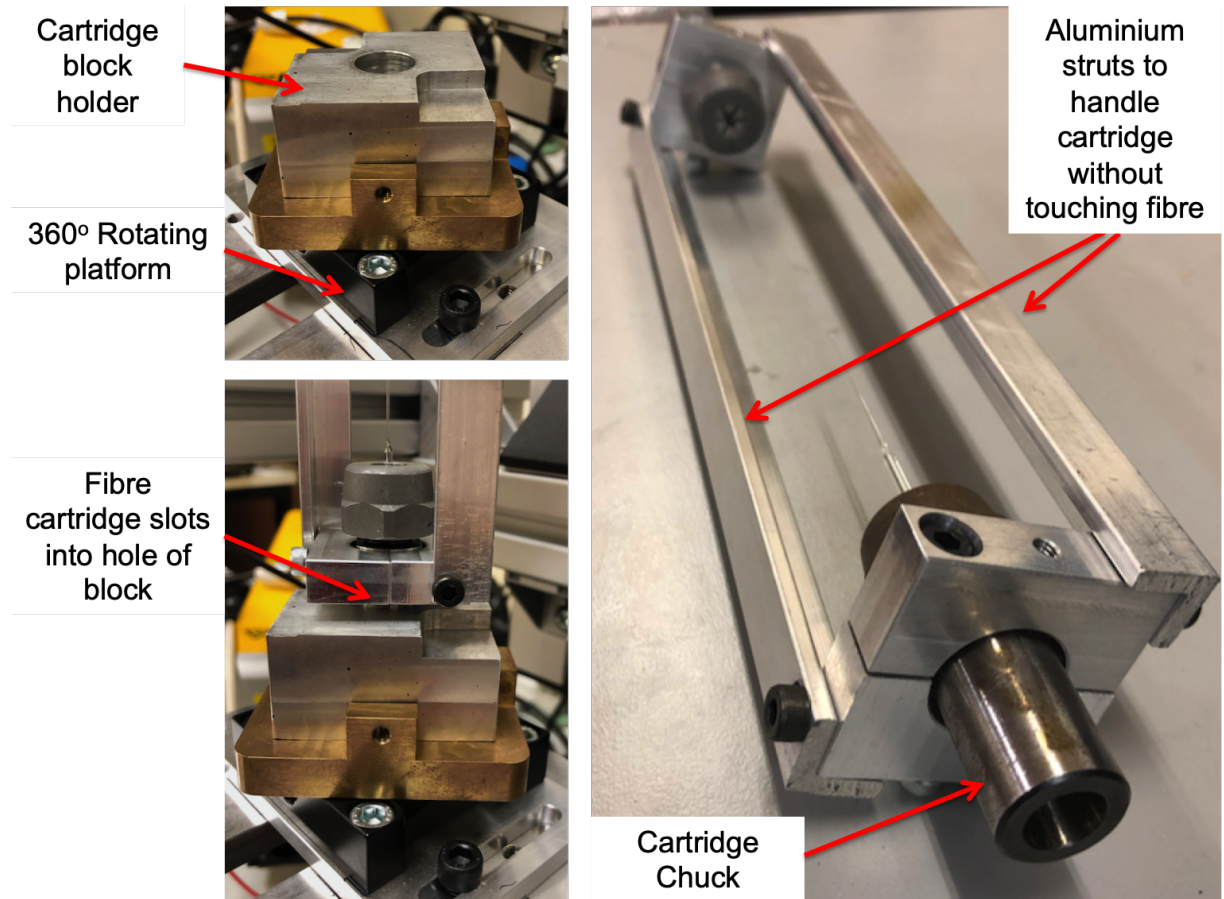


Figure 5.4: Diagram of the ultra-thin fibre profiler.



**Figure 5.5:** Image A: One end of the ultra-thin fibre cartridge, B: SolidWorks rendering of a full fibre cartridge. Labels: 1 - Cartridge chuck, 2 - cartridge nut, 3 - fused silica fibre, 4 -Cartridge strut.



**Figure 5.6:** Top left: Cartridge block holder sitting on the 360° rotation stage. Bottom left: Fibre cartridge sitting within slot of block holder. Right: Full fibre cartridge.

### 5.2.1 Improved optical set-up

The ultra-thin fibre profiler, had to meet two main criteria to lower the previously mentioned uncertainty value when measuring the diameter of the fibre:

- Greater and variable magnification system
- Greater camera resolution

The current aLIGO profiler [121] [122], shown in figure 5.7 with an ultra-thin fibre placed within the profiler, utilises two 640x480 Unibrain Fire-i digital board monochrome cameras with a fixed lens with a focal length of 12 mm. These cameras were set up such that two perpendicular views of the fibre could be simultaneously taken. This allows any misalignments of the fibre to be observed, as discussed previously in chapter 3. The lenses chosen combined with a lens tube [148] [149] in between the lens and the CCD, gives a fixed magnification that could be calculated with:

$$M = \frac{d_i}{d_o} \quad (5.1)$$

where  $M$  was the magnification,  $d_i$  was the length of the lens tube and  $d_o$  was the distance between the object and the lens. Using this equation, the magnifications of the two cameras were approximately  $\times 1.75$  and  $\times 6$ .

The number of pixels taken up by an object could be calculated by the following equation:

$$\text{Object size per pixel} = \frac{\text{width of pixel}}{\text{Magnification}} \quad (5.2)$$

where the width of a pixel was  $5.6 \mu\text{m}$  and the magnification was defined by equation 5.1. This gives  $0.93 \mu\text{m}$  per pixel for a magnification of 6.

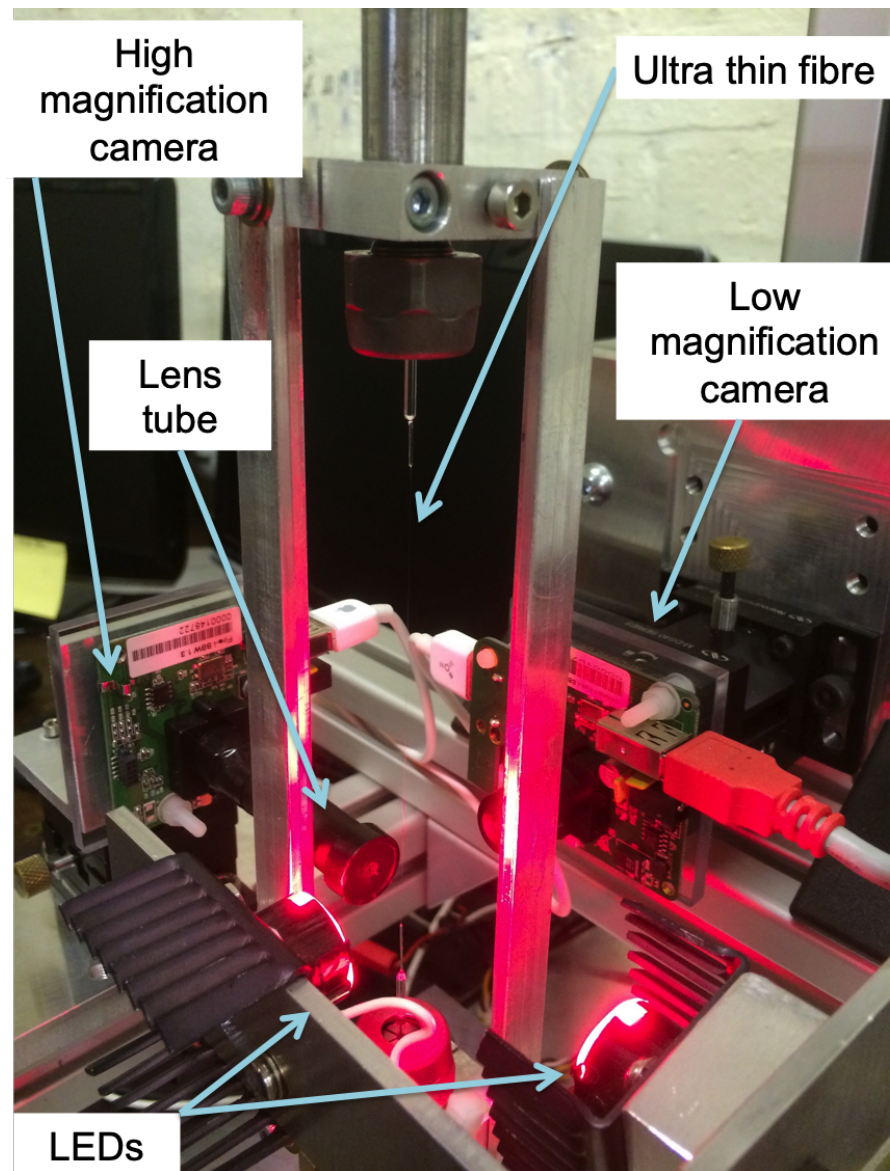


**Figure 5.7:** An ultra-thin fibre cartridge within the aLIGO profiler

Previous investigations [93] with ultra-thin fibres only utilised the  $\times 6$  magnification camera on the aLIGO profiler, with a slight modification. The fixed length lens tube, shown in figure 5.8, was increased in length to increase the magnification to approximately  $\times 8.3$ . Using equation 5.2, this gives  $0.68 \mu\text{m}$  per pixel compared to the previously mentioned  $0.93 \mu\text{m}$  per pixel for  $\times 6$ . Any attempt to increase the magnification further by increasing the length of the tube ran into difficulties. The lens required a pinhole aperture to enable focusing onto the fibre by increasing the depth of field. Due to the combination of light sources and pinholes available, it was not possible to achieve a depth of field sufficient enough to allow focusing and therefore could not increase the magnification any further, therefore reaching the limit of the profiler lens set-up.

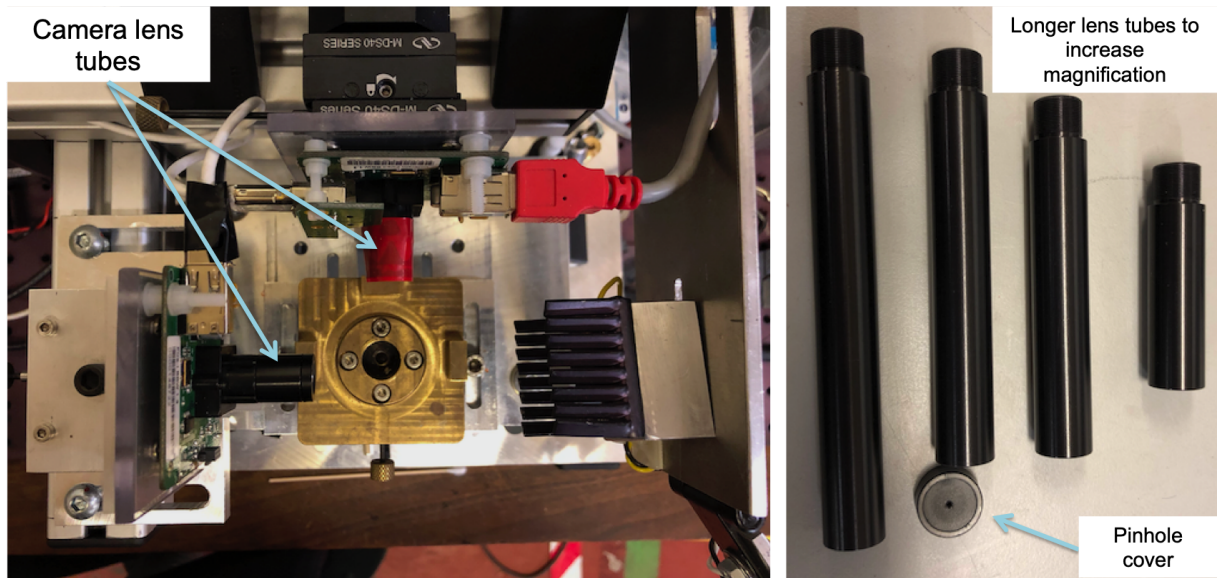


**Figure 5.8:** Left: current installed lens tubes on the aLIGO fibre profiler [149]. Right: Various lengths of lens tubes and the pinhole cover that could be installed to increase magnification.

It was decided that the ultra-thin fibre profiler would have the following camera set-up:

- Thorlabs DCC1240M CMOS  $1280 \times 1024$  camera [150]
- Thorlabs MVL12X20L  $\times 2$  magnification lens [151]
- Thorlabs MVL20A  $\times 2$  magnification lens [152]
- Thorlabs MVL12X12Z  $\times 7$  variable magnification [153]

The new optical set-up for the ultra-thin fibre profiler is shown in figure 5.9. The combination of the fixed and variable magnification lens system allows for a magnification of up to  $\times 28$ . Using equation 5.2, with the magnification set to the maximum value of  $\times 28$ , a value of  $0.19 \mu\text{m}$  per pixel could be achieved. This was approximately a factor of 3 improvement on the previous set-up that allowed for  $0.68 \mu\text{m}$  per pixel.

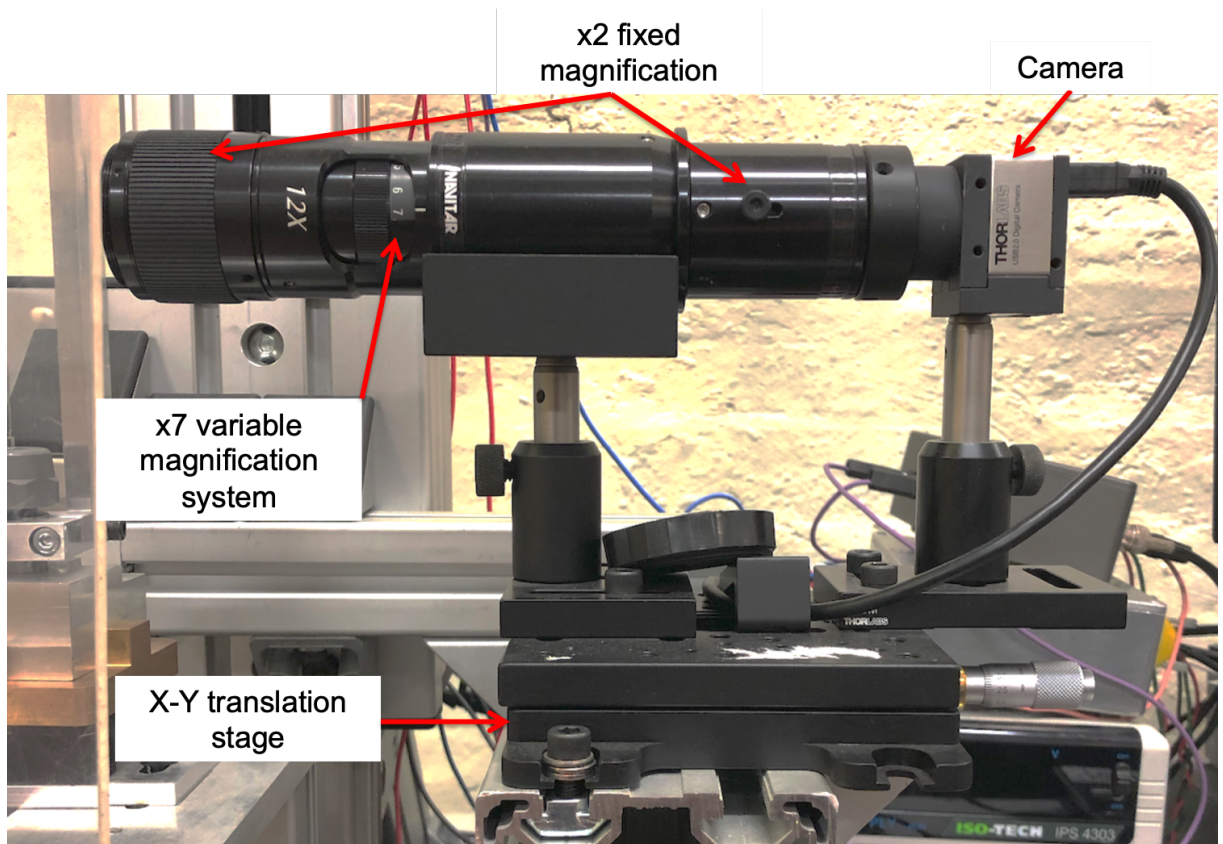


**Figure 5.9:** The current lens and camera set-up of the ultra-thin fibre profiler.

Early tests were carried out with the new camera system to determine the optimal set-up of the new camera system. Leah Perri, an IREU student who spent a summer at Glasgow assisted with this early work [154]. The camera manufacture software [150] was used to image a  $50 \pm 3 \mu\text{m}$  feeler gauge [155] at a range of magnifications. The set-up, shown in figure 5.10, consists of a  $50 \mu\text{m}$  feeler gauge held securely within a clamp with a LED positioned behind it. The feeler gauge was then placed in front of the lens system and imaged at various magnifications. A conversion between the number of pixels that were covered by the shadow of the feeler gauge on the camera sensor could then be obtained, shown in table 5.2. The feeler gauge was then replaced with a  $75 \pm 0.75 \mu\text{m}$  wire [156], shown in figure 5.11, and the same process repeated.

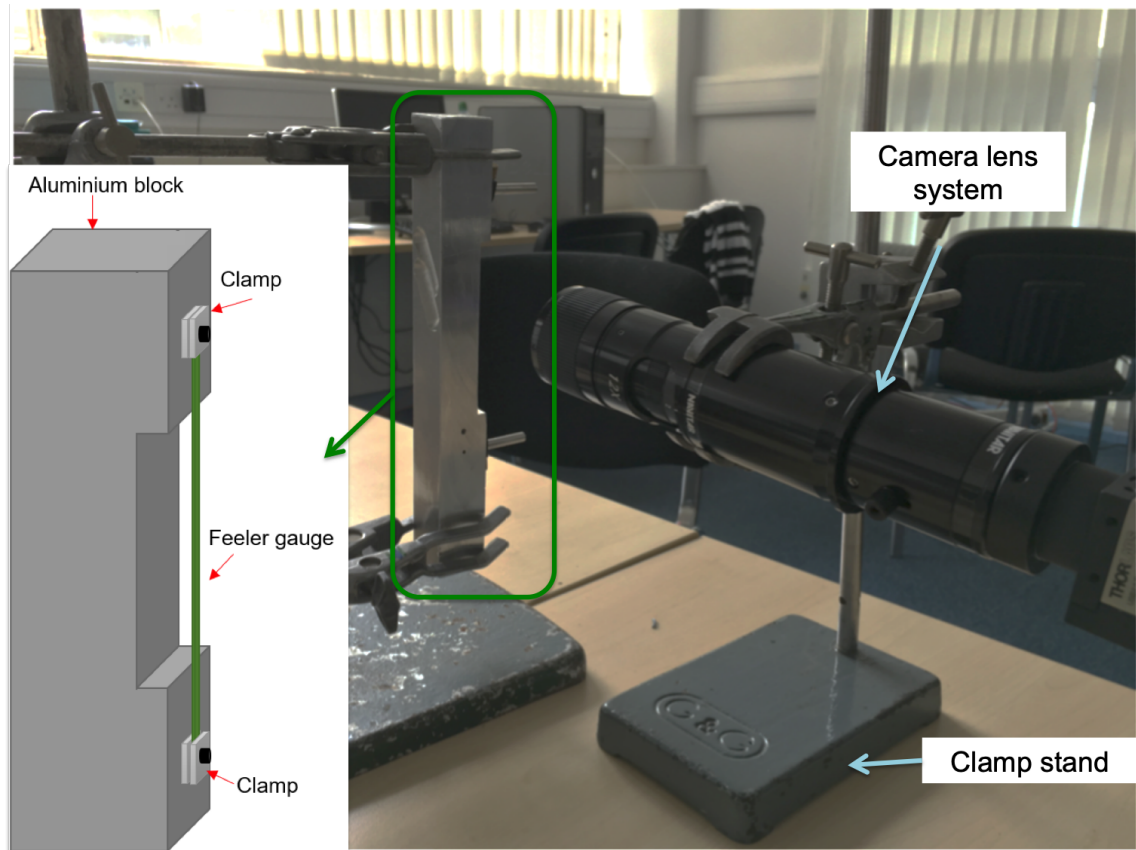


**Figure 5.10:** Experimental set-up of early tests of the new optical set-up for ultra-thin fibre profiler (LED out of shot). Original image taken from final report [154] with labels added.

**Table 5.2:** The number of pixels occupied by the feeler gauge's shadow and the resulting size of the image. Data from final report [154].

Magnification	Number of pixels
2.32	29.9
4	40.9
6	59.2
8	81.3
10	103.2
12	121.9
16	155.6
20	193.4
24	230.1
28	266.3

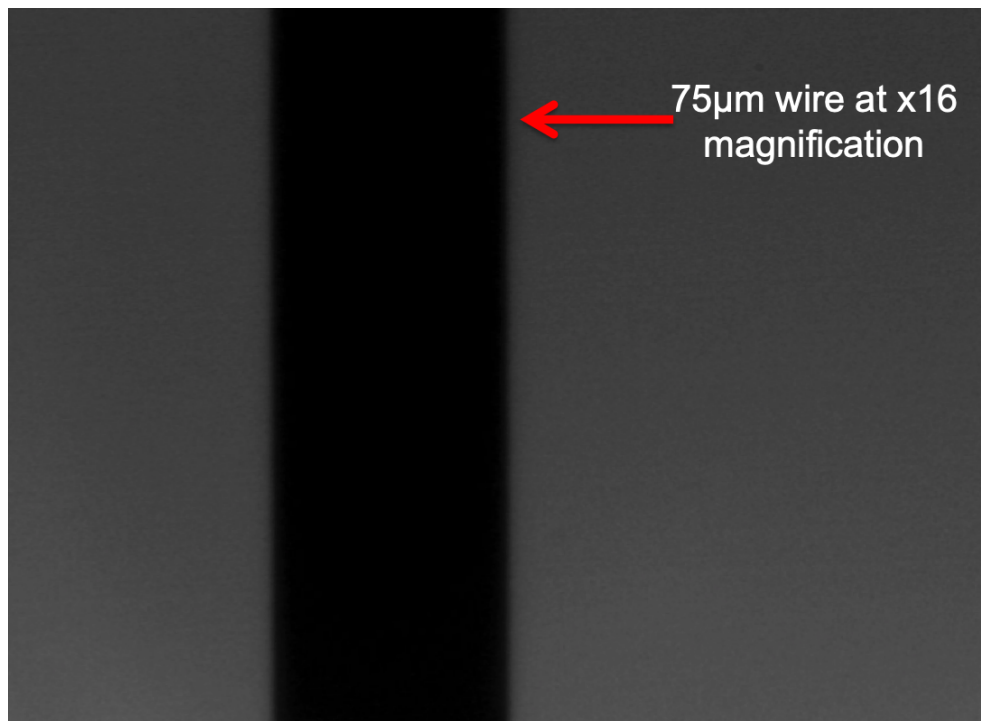


**Figure 5.11:** Screenshot of a 75  $\mu\text{m}$  wire under a magnification of  $\times 16$ . Original image from final report [154].

## 5.2.2 Hardware and design

The overall hardware design of the ultra-thin fibre profiler was conceptually similar to the aLIGO profiler. It utilises the same ball screw motor stage tower and base platform to hold the fibre that was on the aLIGO profiler. The camera and lens system sits on a Thorlabs X-Y translation stage [157] to allow the position and focus of the camera system to change. A green high intensity 4W "Lumiled" LED with variable brightness, that was previously used for a different set-up [122], was used to illuminate the fibre. Both the camera system and LED were each attached to a Bosch strut. These struts were then attached to the moving motorised stage, such that they were opposite each other.

This set-up only uses one camera to image the fibre due to practicability and cost factors at the time. The variable magnification system has a length of approximately 272 mm. This would mean that if a second system were to be installed on the same profiler, modifications to the profiler stage would have to be made to accommodate the length of a second identical system. The arms that the LED and camera system sit on would need to be lengthened by approximately 280 mm to give enough room for adjustability of the second system. This would allow another arm to be attached between the two of them for the second camera system. A smaller LED housing would have to be made to then sit opposite the second camera system. Additional tests would then need to be carried out with the motor stage to ensure it could perform to the design specifications with what would be a large and heavy cantilever attached. While not impossible,

this was a decision made at the time to not pursue, but could be considered for any future upgrades.

The motorised stage was controlled by using a circuit board utilising a L6205 DMOS dual full bridge driver [158]. A circuit diagram of the final version of the motorised stage controller is shown in figure 5.12.

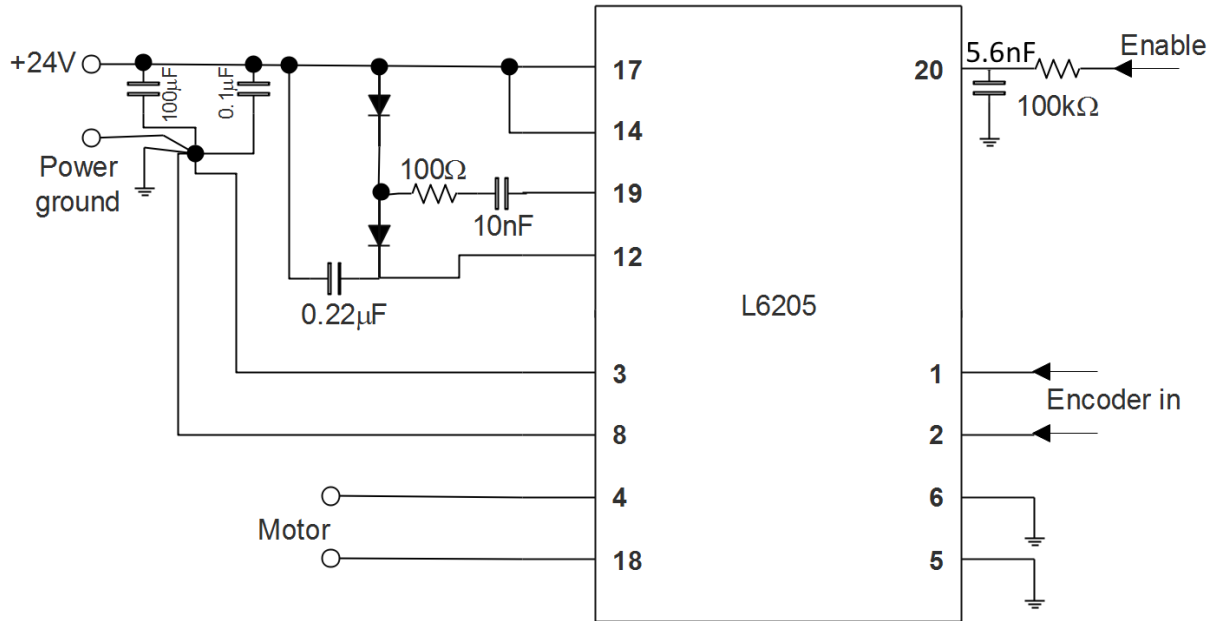


Figure 5.12: Circuit schematic for the motor controller board.

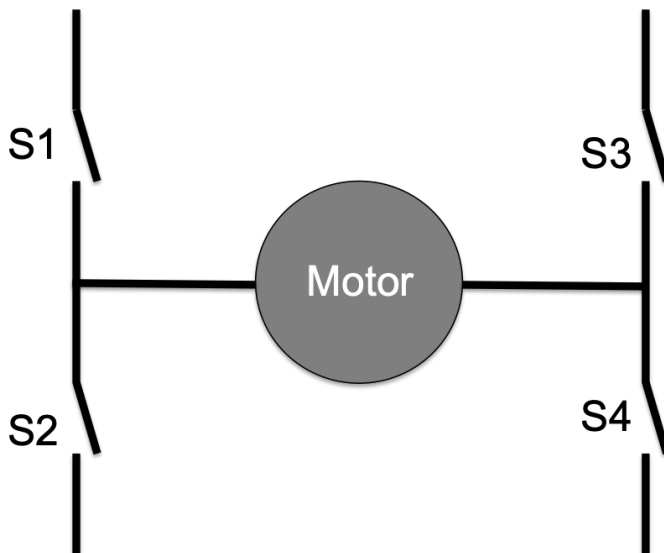


Figure 5.13: A schematic of a H-bridge concept to control the profiler motor. S# dictates the switch and its associated number.

This circuit in figure 5.12 was based on one of the recommended L6205 typical application

diagrams in the manufacture data sheet [158]. Figure 5.13 shows a schematic of the H-bridge. A H-bridge works by sending a signal to two of the input pins to dictate how the motor will move. In the example shown in figure 5.13, if switches S1 and S4 were closed and S2 and S3 remain open, the motor would move in a clockwise direction. When S2 and S3 are closed and S1 and S4 are open, it moves in an anticlockwise direction. To stop the motor, both S1 and S3 (or S2 and S4) were open or closed. A H-bridge could work with either relays, as in the above example, or through a solid-state design. The latter was the case in the L6205.

The L6205 works by sending a high/low input to the motor that controls the stage to make the stage move/stop. The L6205 provides dynamic braking to stop the motor and hold the stage in position once the signal was sent, when the signal sent to the enable and input were both high. The first iteration of this circuit was tested by connecting the enable channels into a 5 V power supply to control the motorised stage. Depending on which pin was connected to the 5V signal determined the direction of the motor stage. This allowed the stage to be tested to ensure the motor and the moving stage were in a working condition.

This board was then configured to allow control of the motorised stage through both a custom LabVIEW motor control program and the LabVIEW program that would control the ultra-thin fibre profiler (discussed later in this chapter). The input signals were sent to the circuit board via the +5 V terminals on a LabJack U12 [139]. The motor control program could then be set to send the desired combination of high/low values to the circuit board to move the stage up or down. Limit switches, as used in the aLIGO profiler and shown in figure 5.14, were fixed at the bottom and top of the tower to stop the stage from clashing with the optical board or beyond the top of the tower. At both ends, there were two sets of switches: software limit and hardware limit switches. The software limit switches were programmed to stop the motor moving within the fibre profiler LabVIEW program. The hardware limit switch cuts off all power to the motor when triggered. This could be overridden by pressing the override switch which will complete the circuit and cause the stage to move.

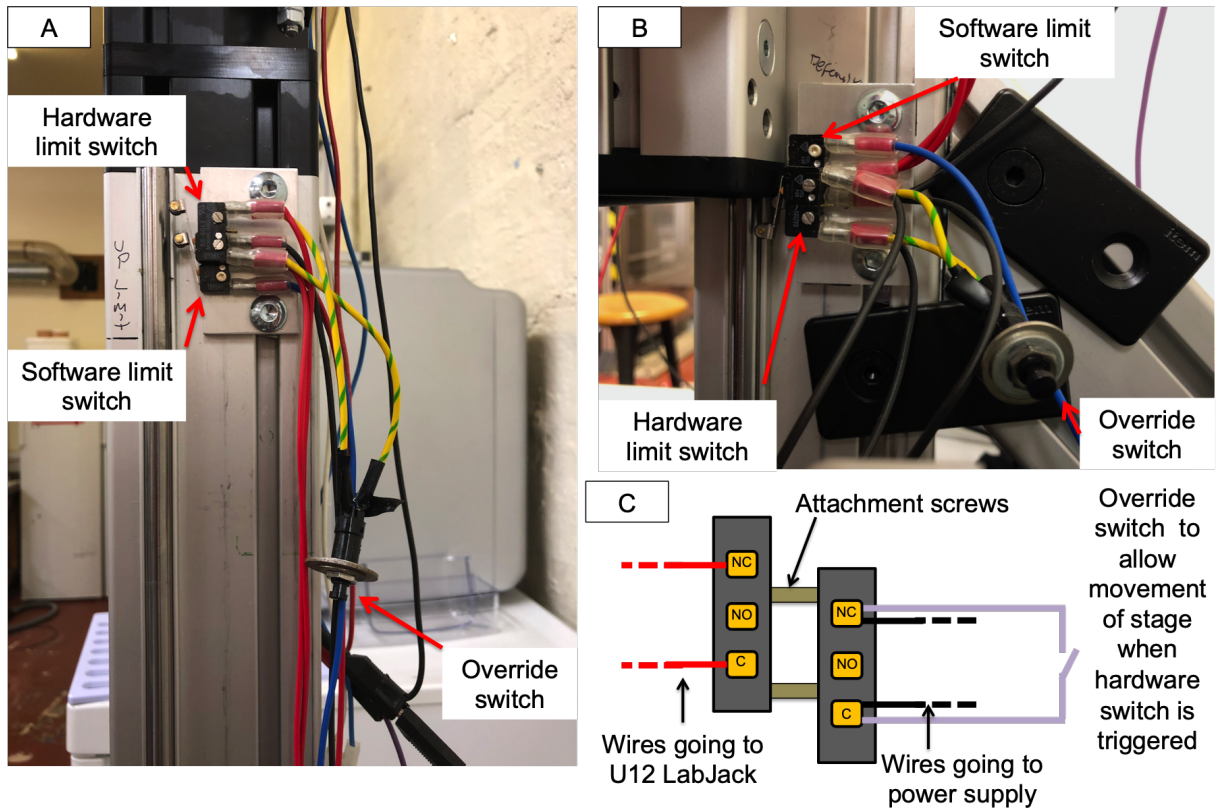


**Figure 5.14:** A: Limit switches fixed to the top of the profiler tower. B: Limit switches fixed to the bottom of the profiler tower. C: Wiring of software and hardware limit switches.

To measure the distance that the motor has moved, a SIKO MSK320 magnetic encoder [124] was attached to the side of the motor stage. A magnetic strip was attached to the side of the tower for the encoder to move over as the stage moves. The encoder works by sensing magnetic peaks within the strip. The peak registers a "high" voltage reading which could be registered as a "count", shown in figure 5.15. This was the same concept that was used for the aLIGO fibre pulling machine and profiler. The two channels for the encoder, A and B, read the strip pattern separately. As the two lines were  $90^\circ$  out of phase, when the encoder moves across figure 5.15 left to right, channel A leads channel B. If it moves right to left, channel B leads channel A. This allows for a directional distinction to be made so that it was possible to determine whether the motorised stage would be moving up or down.

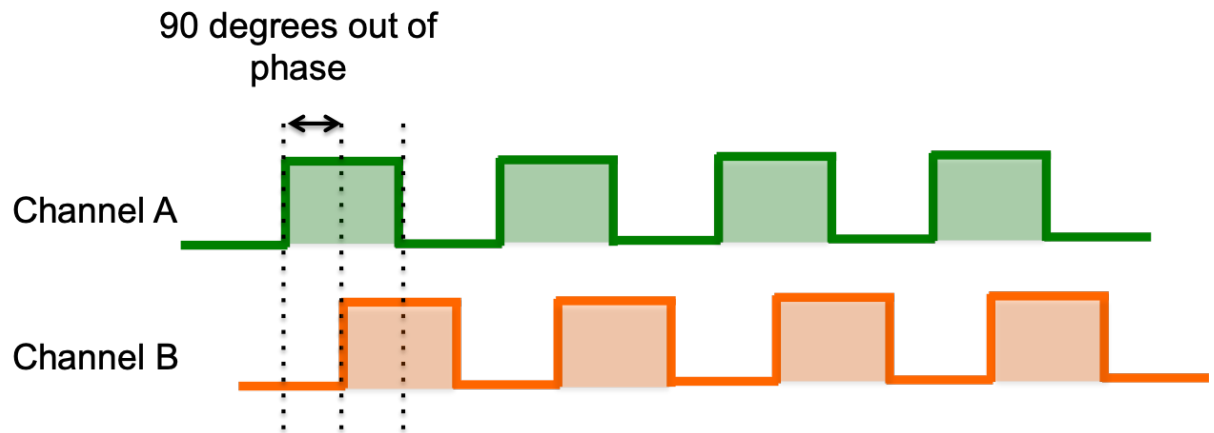


**Figure 5.15:** Example of the pattern on the magnetic encoder strip showing the high-low pattern the encoder passes over.

The data for the encoder was read into a custom made read-in circuit board [159]. This board was originally developed for the aLIGO profiler and was replicated for the ultra-thin fibre profiler. A digital schematic of the circuit board is shown in figure 5.16. This circuit works by taking in the high-low transitions from the encoder and passing this signal through a 74LS123 multivibrator [160]. When the encoder passes over a transition point, a pulse is generated from the 74LS123. As both channels are read through simultaneously, this means a pulse is generated at every transition for both channels A and B. Each pulse is then sent to the LabJack U12. Counting pulses on both channels allows for an encoder to be changed by the user. If 0.4 mm counting is required, then only one channel needs to be fed to the U12. If 0.1 mm is desired, then both channel pulses would be combined to give 0.1 mm counts. This was achieved through a switch wired into the circuit to swap between 0.1 mm and 0.4 mm count distances. This signal was then sent to the LabVIEW program where the pulses were counted and converted to a distance [121] [159]. The circuit board allows for either 0.1 mm or 0.4 mm counts to be recorded. This means that a pulse would be generated either every 0.1 mm or every 0.4 mm.

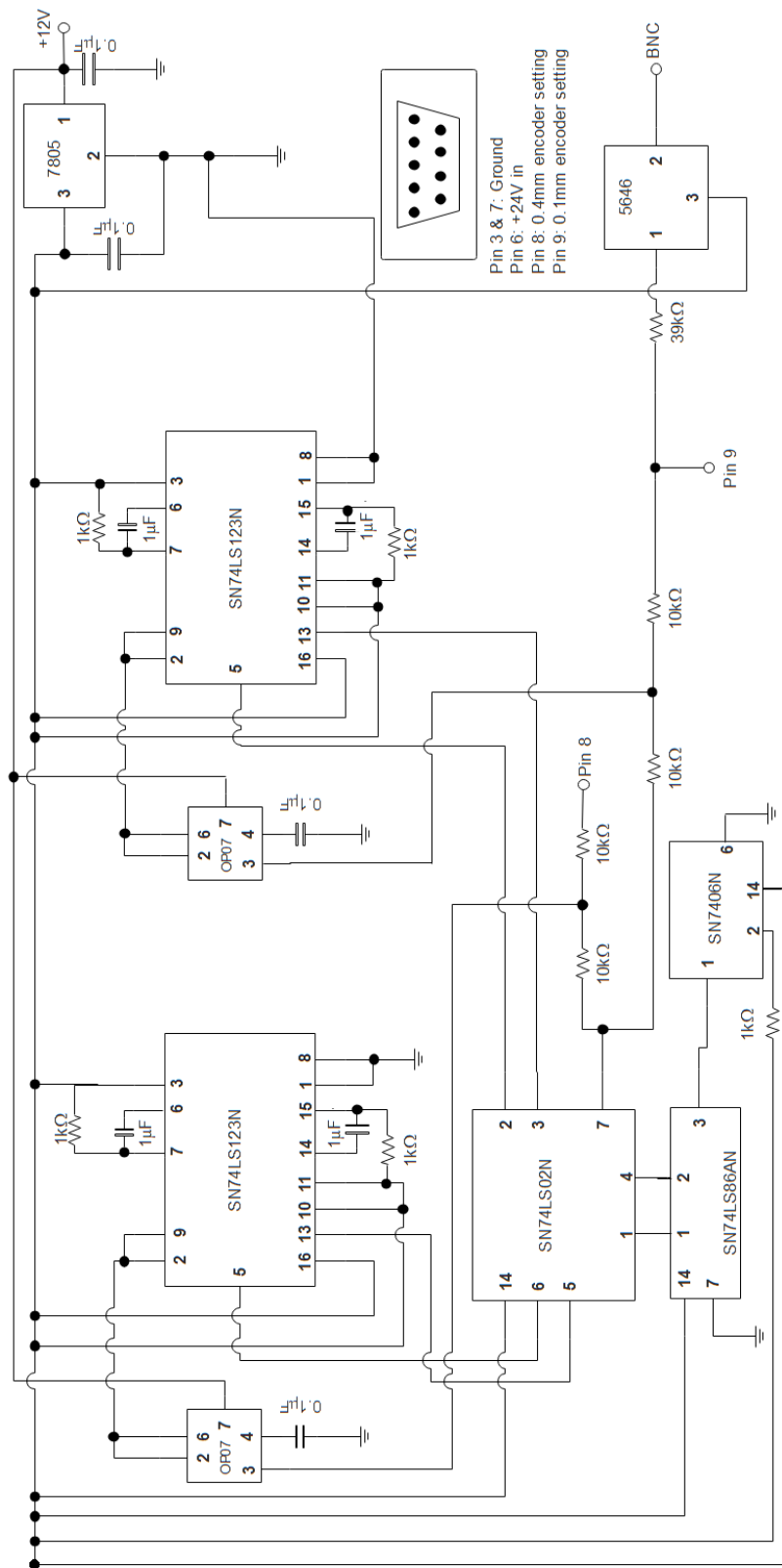


**Figure 5.16:** The circuit schematic for the encoder read-in board, initially designed for the aLIGO profiler [159].

### 5.2.3 LabVIEW

Once the hardware had been assembled, the ultra-thin fibre profiler LabVIEW program was created. The full LabVIEW block diagram can be found in appendix B. The front panel of the ultra-thin fibre profiler program is shown in figure 5.17

The program used was a modified version of the aLIGO profiler program that was previously developed in [121]. This program has a state-machine structure. This means that the program was developed such that specific actions, or states, were only performed when specific conditions were met. This could be from inputs from the user or in-state conditions being met to then move to the next state. The program works through the following states:

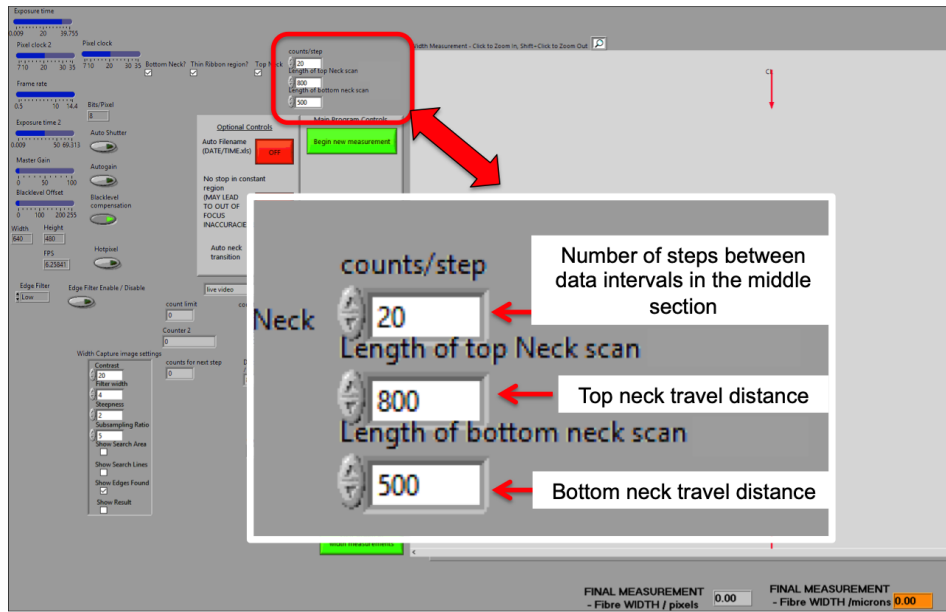
- Initialisation of the program.
  - Loads up the settings for:
    - \* The camera.
    - \* Encoder counts for measurements.
    - \* Calibration values for the camera.
- Create files.
  - A file name was given by the user.
  - 3 files were automatically generated and named with the suffix of "Bottom", "Middle" and "Top" added to the end of the name.
  - These three files were for three sections of the fibre: Bottom neck, middle thin section and the top neck.
- Start data taking for "Bottom" file.
  - This setting takes full screen scan measurements of the shadow edge measurements from top to bottom for every row of pixels.
  - Each pixel along this scan was a data point where values of the following were taken for each camera:
    - \* Fibre position - This was the encoder value of the stage at that particular point.
    - \* Fibre diameter - This was the distance between the left and right edge of the pairing of pixels. This distance was then converted to  $\mu\text{m}$  through a calibration value that was set prior to starting the program.
    - \* Left edge pixel distance - This was the distance from the left of the screen to the left data point.
    - \* Right edge pixel distance - This was the distance from the left of the screen to the right data point.

- The data from the scan was then saved to the file with the suffix, "bottom".
- The motorised stage then moves up 0.1 mm to the next data point and repeats the scan measurement. The default value that was set for the aLIGO profiler was 0.3 mm to ensure that there was an overlap between each scan region. This value could be changed by the user to their discretion. Care should be taken to ensure overlap in data so no regions were missed as the motor moves between each iteration.
- This process will repeat until the motorised stage has moved the pre-determined distance set in the initialisation process.
- Start data taking for "middle" file.
  - \* This setting takes 6 edge measurements in the centre of the screen. All 6 values were then averaged together to give one value.
  - \* This value was saved in the "middle" file, with its corresponding position measurement.
  - \* This process was repeated until the user presses the "move to top neck" button.
- Start taking data for "top" file.
  - \* This was the same process as the "bottom" file, but for the "top" file.
- Once complete, the motorised stage will travel down to its reset position. This was determined by the position of the bottom software switch.
- User could then insert a new fibre to repeat the process or exit the program and the three files were available to use.

The distance the motor moves during the "bottom" and "top" sections were determined by the user prior to starting the program. These values were set in the "length of top neck scan steps" and "length of bottom neck scan step" boxes. The values were determined from the pulling profile that was used to create the fibre as the length of the neck regions could be calculated from these pulling profiles. These boxes are shown in figure 5.18.

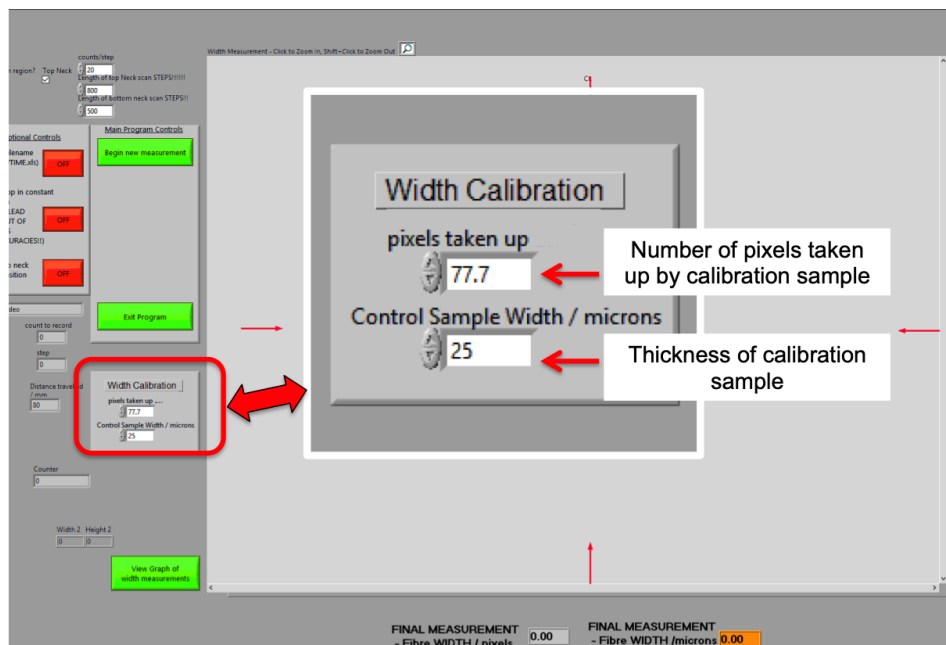


Figure 5.17: Front panel of the LabVIEW program for the ultra-thin fibre profiler.



**Figure 5.18:** Input boxes to determine interval between points during the thin section of the fibre and the length of measurements for the top and bottom necks.

The calibration values were also set prior to starting the program for a measurement. To calibrate the cameras, a  $500 \pm 0.12 \mu\text{m}$  slip gauge was placed into the profiler and a "middle" measurement was carried out 10 times. An average of the 10 pixel width values was noted down and set as the default value in the calibration box, shown in figure 5.19. The number of times this measurement was repeated was to the discretion of the user. This process was carried out for both cameras separately.



**Figure 5.19:** Calibration boxes to calibrate the profiler.

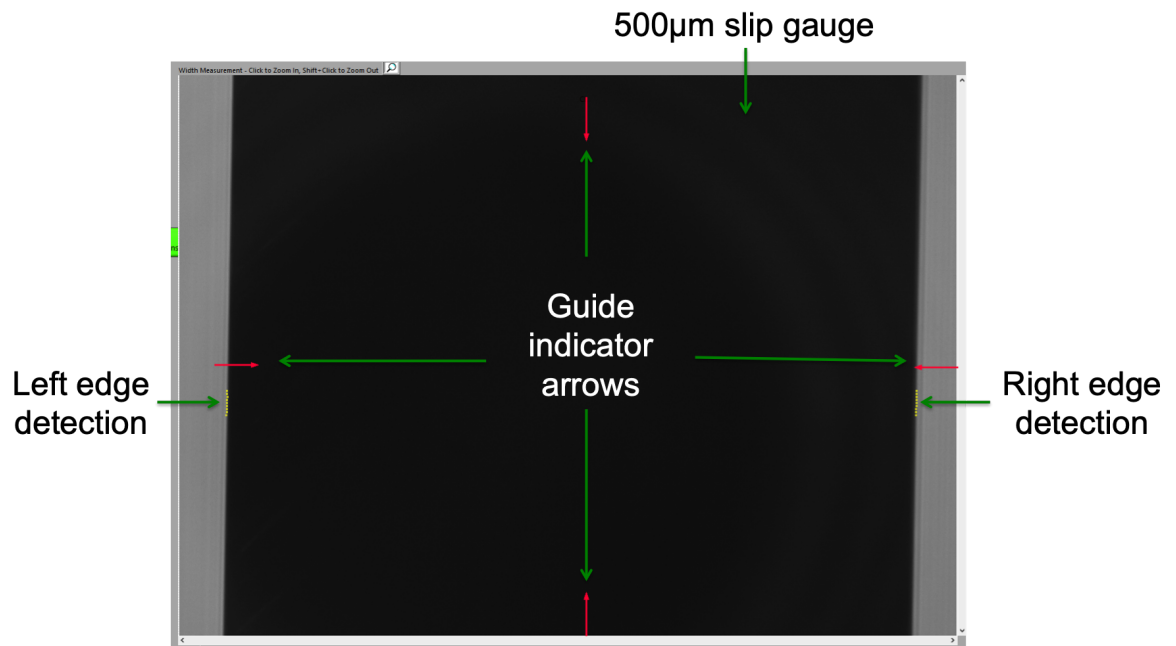


**Figure 5.20:** Screenshot of a 500  $\mu\text{m}$  slip gauge being profiled for calibration at a magnification of approximately  $\times 12$ .

The major modifications that had to be made to the existing program for the ultra-thin fibre profiler were in the following areas:

- Removal of the dual camera set-up so it works with just one camera
- Initialisation, settings and read-in of the new camera
- Control of the motor that drives the moving stage with the new circuit board
- Edge detection and data save settings of the fibre

There were multiple "virtual instruments", known as VIs, within the LabVIEW program. These VIs were pre-written subprograms that could be used to control any software or hardware components within the overall program. In this case, the majority of sub VIs used control specific aspects of the profiler, such as camera settings, initialisation of components, encoder read in, etc. The VIs that controlled the previous fire-wire cameras were removed and replaced with the VIs of the Thorlabs camera that were supplied by the manufacturer. These newly installed VIs initialise the camera and load the camera setting values for the exposure, exposure range, brightness, frame rate, pixel clock and blacklevel offset. The image capture VIs were also used to obtain the live feed footage and snapshots during profiling.

Controlling of the motor only occurs in specific program states. A case structure in LabVIEW was a specific scenario that was only triggered when the appropriate conditions were met. There were multiple case structures within this program. The motor only needs to be controlled in the following structures:

- Reset
- Motor off
- Move step (neck)
- Motor on

In the state "move step (neck)", the motor will move a distance that could be set by the user in the scan distance box until the full distance that was set by the user on the front panel "length of top/bottom neck scan steps" boxes was covered. In the state "motor on", the motor will move the desired distance set by the user in between each data point. In the structure "motor off", the motor was stationary. In the structure "reset", the motor moves back to its starting position and stops when the software limit switch was triggered. In all four cases, the high/low values for the appropriate pins have to be set to ensure the motor was moving in the correct direction when instructed, and that it stops correctly after moving the desired distance in between points.

The live image shown on the front panel was inverted. This was because the edge detection works from the top of the screen to the bottom. In order to save the data collected to have the correct position readings within the spreadsheet, this inversion was necessary.

The middle section was currently set to average over 9 points, before moving to the next point. This value was chosen to ensure a long enough uniform region could be averaged over, but not too long so that there would be a greater chance of the edge detection picking up large dust particles that could land on the fibre and skew the diameter reading.

The next step to get the profiler into working order was to characterise its capabilities over various diameters and magnifications

#### **5.2.4 Varying magnifications and repeated profiles**

Initial tests on the assembled profiler were carried out using wire. The wire used was a nickel-chromium alloy with a diameter of  $25 \pm 1.25 \mu\text{m}$  [161]. The wire was imaged at various different magnifications to observe the depth of field of the optical set-up. The camera would start out of focus and would be moved at set intervals of  $1 \mu\text{m}$  until the wire was in focus. This interval was achieved through the micrometer attached to the translation stage. A schematic of this state is shown in figure 5.21 and a screenshot of the wire both in and out of focus is shown in figure 5.22. There were ten diameter readings of the wire diameter taken at every interval. This allowed the standard deviation to be calculated for each interval. Once in focus, the camera would continue to move the same distance as before in the same direction, moving out of focus of the wire.

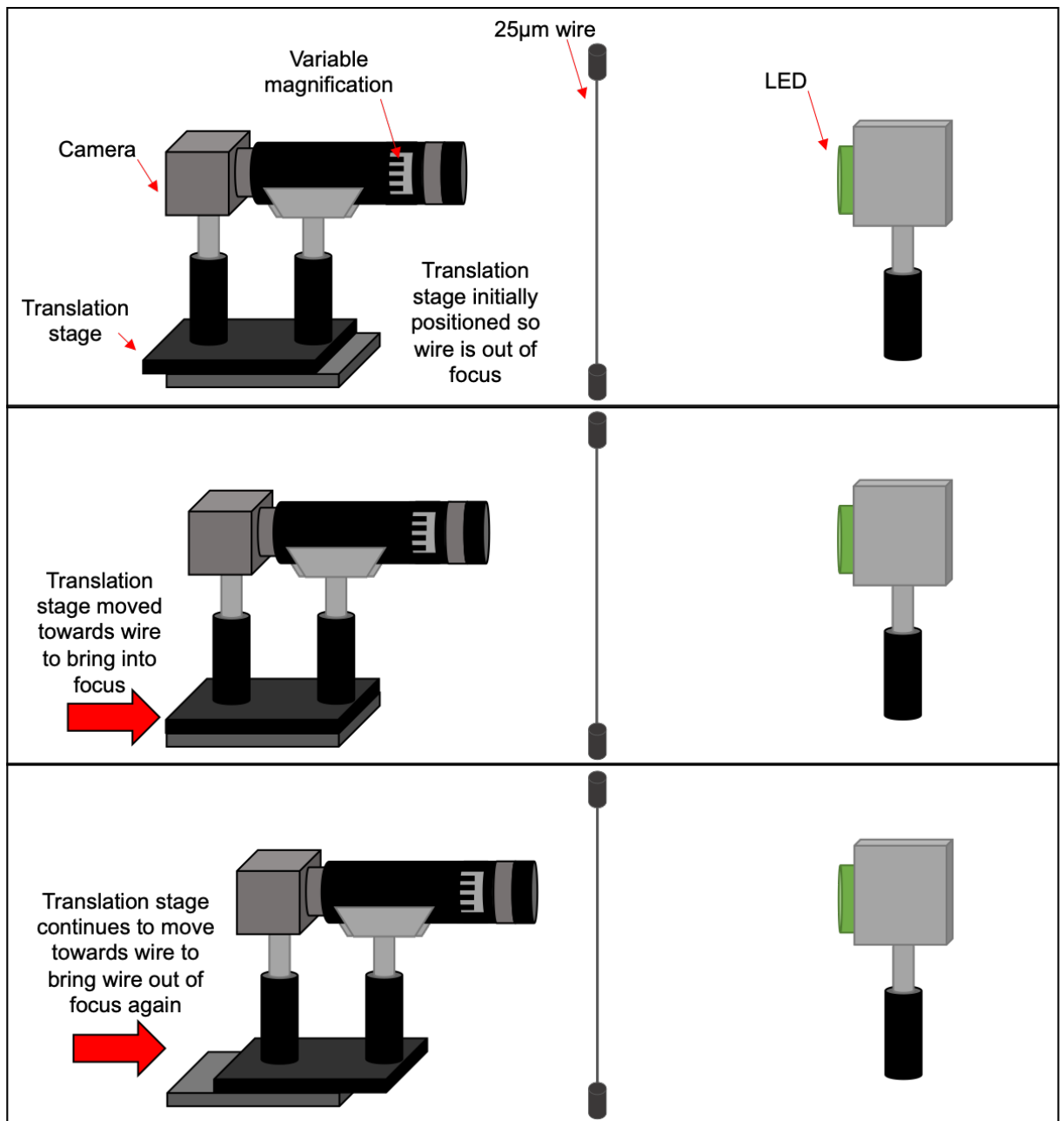


**Figure 5.21:** Illustration of the experimental set-up of the depth of field tests.

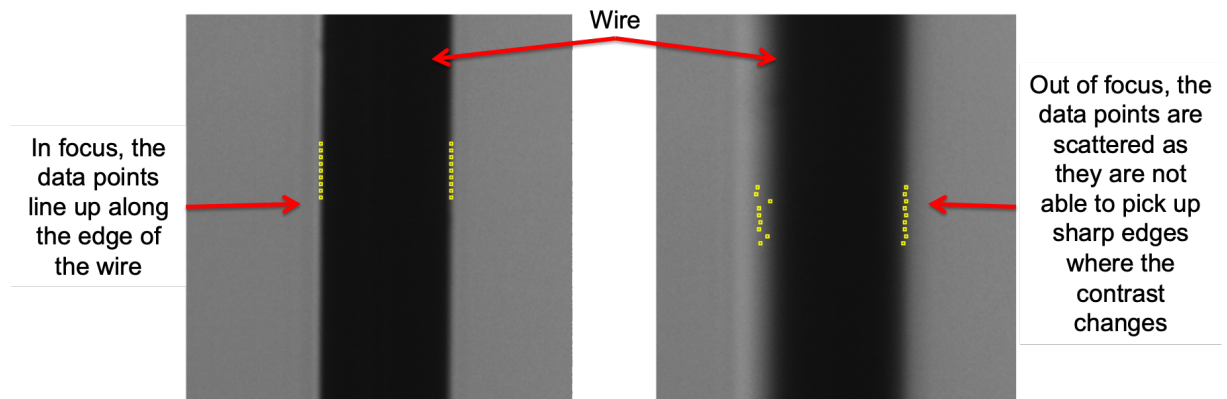


**Figure 5.22:** Two screenshots of a  $25\ \mu\text{m}$  wire under  $\times 20$  magnification. The left image was the wire in focus and the right image was the wire out of focus. The difference in camera position between these two images was approximately  $10\text{--}15\ \mu\text{m}$ .

Figure 5.23 shows the  $25\ \mu\text{m}$  wire under various magnifications during this investigation. Figures 5.24 and 5.25 show the results of this test for various magnifications. The vertical error bars are the standard deviation of the 10 measurements that were taken at every interval. The horizontal error bars represent the uncertainty associated with turning the micrometer on the translation stage,  $\pm 0.5\ \mu\text{m}$ .

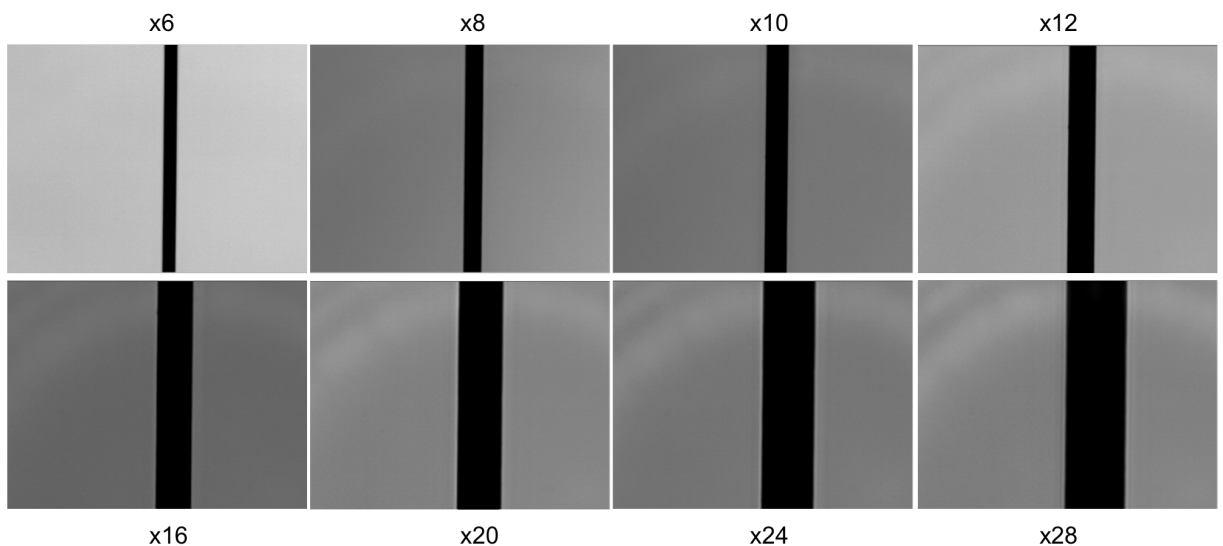


**Figure 5.23:** The  $25\ \mu\text{m}$  wire imaged with various magnifications.

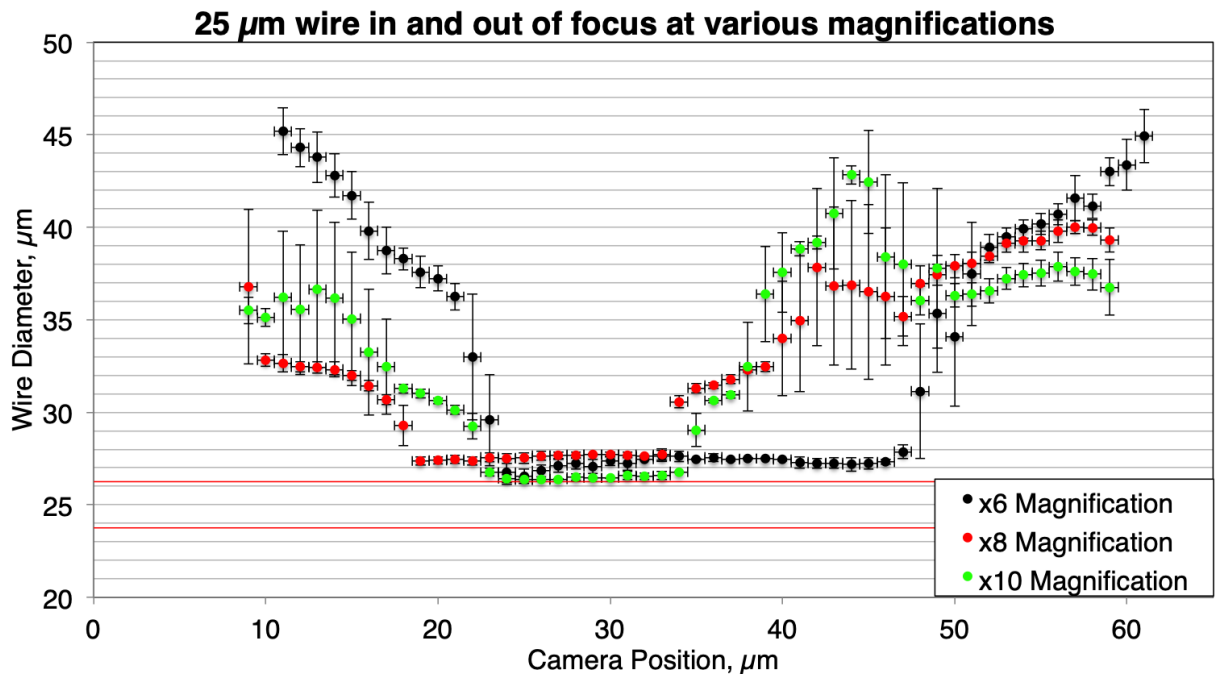


**Figure 5.24:** Diameter values obtained for magnifications  $\times 6$ ,  $\times 8$  and  $\times 10$  during the depth of field tests. The horizontal lines at diameter values  $26.25 \mu\text{m}$  and  $23.75 \mu\text{m}$  indicate the wire tolerance.

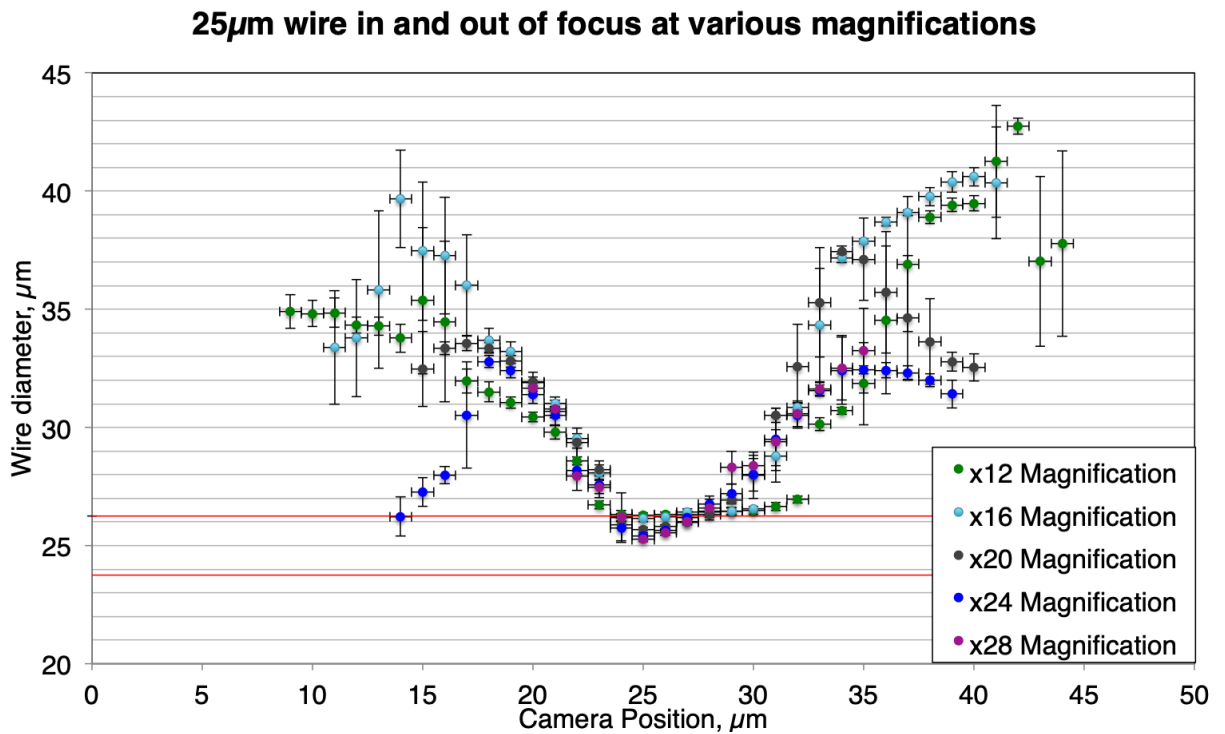


**Figure 5.25:** Diameter values obtained for magnifications  $\times 12$ ,  $\times 16$ ,  $\times 20$ ,  $\times 24$  and  $\times 28$  during the depth of field tests. The horizontal lines at diameter values  $26.25 \mu\text{m}$  and  $23.75 \mu\text{m}$  indicate the wire tolerance.

From figures 5.24 and 5.25, it can be seen that the higher the magnification, the smaller the depth of field is. This means that the higher the magnification, the more alert the user must be to ensure the fibre was in focus, as a small distance change of a couple of microns in the case of  $\times 28$  magnification could result in the wire being out of focus. In figure 5.24, it can be seen that the lower magnifications of  $\times 6$  and  $\times 8$ , the diameter of the wire falls outside the wire uncertainty tolerance. The magnification of  $\times 10$  in figure 5.24 also falls out the tolerance values when considering an average of all the data points in the focused region. There were 3 data points in this region that lie just inside the tolerance value. This could be due to the number of pixels per micron being too large, with low magnifications of  $\times 6$  and  $\times 8$ . It would suggest that magnifications of 10 or below should not be used for objects that lie below  $25\ \mu\text{m}$ . For magnifications of  $\times 12$  and above, diameter values were found to be within the wire tolerance. It would be a recommendation for any opaque object that was approximately  $25\ \mu\text{m}$  and below that magnifications of  $\times 12$  and above be used. The final choice of magnification from this range was to the discretion of the user.

In figure 5.24, there was a trend that could be seen for all three of these magnifications in that they were all above the wire tolerance. This could be due to the calibration used for each magnification where the location of the wire used to calibrate the profiler was such that it was an area close to the  $+1.25\ \mu\text{m}$  uncertainty. It was possible that taking an average reading along the length of the wire during calibration could limit the chance of calibrating the profiler with an upper limit section of the wire.

Vertical error bars in areas out of focus were large due to the large spread in diameter values that were obtained when attempting to profile the wire out of focus. As previously seen in figure 5.22, when the wire was out of focus, dark lines start appearing further from the edge of the wire's shadow. The edge detection algorithm starts to pick up these lines instead of the edge of the shadow, which could result in obtaining a mixture of larger and smaller diameter values than expected. This could be seen in figure 5.25 for the  $\times 16$  and  $\times 24$  magnification. Prior to bringing the wire into focus, the diameter gradually increases before decreasing as the fibre comes into focus, before showing the same trait when going back out of focus. When the wire was in focus, these dark lines beyond the edge of the wire do not show up, and a sharp image of the edge of the wire could be obtained.

An additional set of data was taken by profiling the  $25\ \mu\text{m}$  wire, but this time carrying out "neck scans" as well. It should be noted that no "neck" would be expected along the wire, but was just the name of the state the machine was in during profiling. This was carried out to ensure that the data points in between scans have an overlap region. If there were no overlap, there would be a visible gap in the scan data where no measurements would have been taken. Figure 5.26 shows the profile data obtained of the wire at a magnification of  $\times 24$ . During the neck scans, the encoder moves at  $0.1\ \text{mm}$  intervals in between each scan. This was the minimum distance that the current encoder allows for. During the middle section where the averaging takes place

instead of scans, the distance between each data point was set to 2 mm. There was no specific reason for this distance value apart from personal choice. Figure 5.27 was the left hand side scan region of the profile shown in figure 5.26 and figure 5.28.

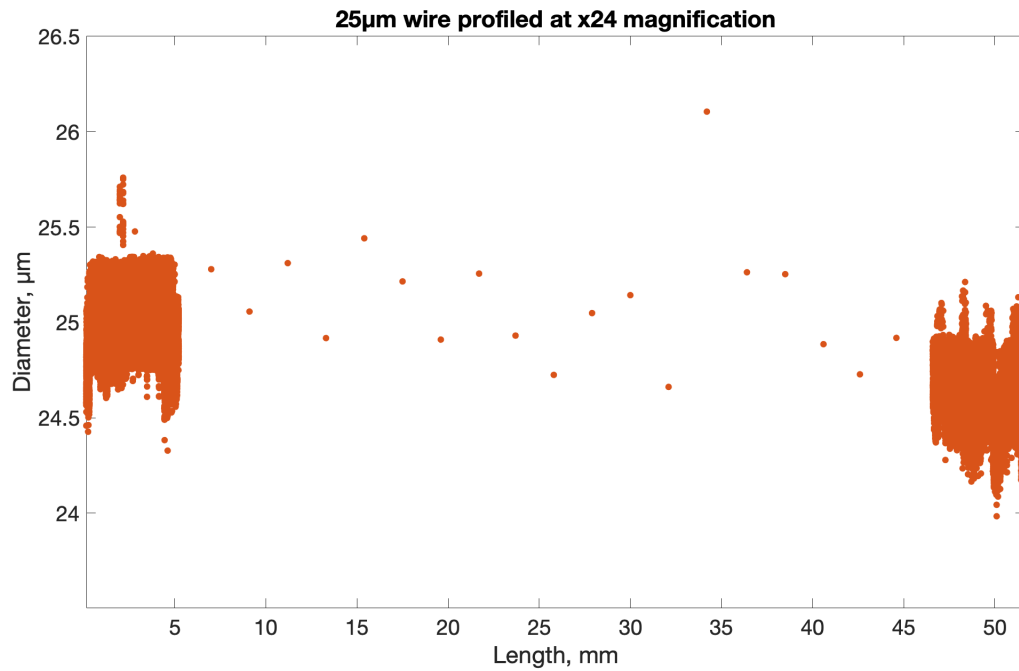


**Figure 5.26:** A full profile of a  $25 \pm 1.25 \mu\text{m}$  wire at a magnification of  $\times 24$ . The distance between each scan point was 0.1 mm and the distance in the middle region between data points was 2 mm.

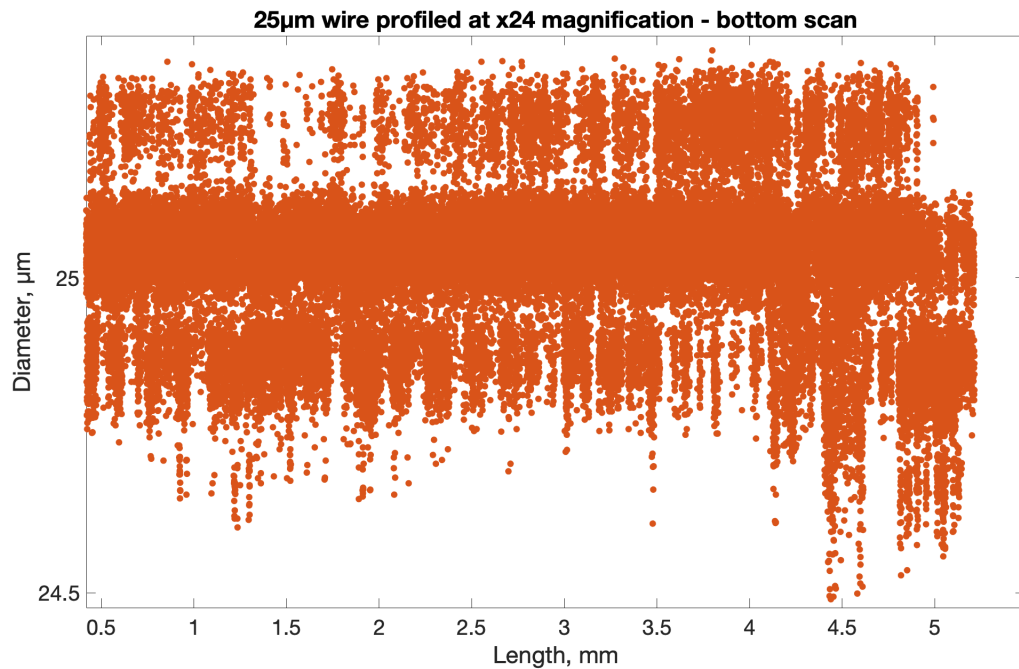


**Figure 5.27:** The zoomed in view of the bottom scan of the  $25 \pm 1.25 \mu\text{m}$  wire. Note that all data points in this region sit within the wire tolerance.

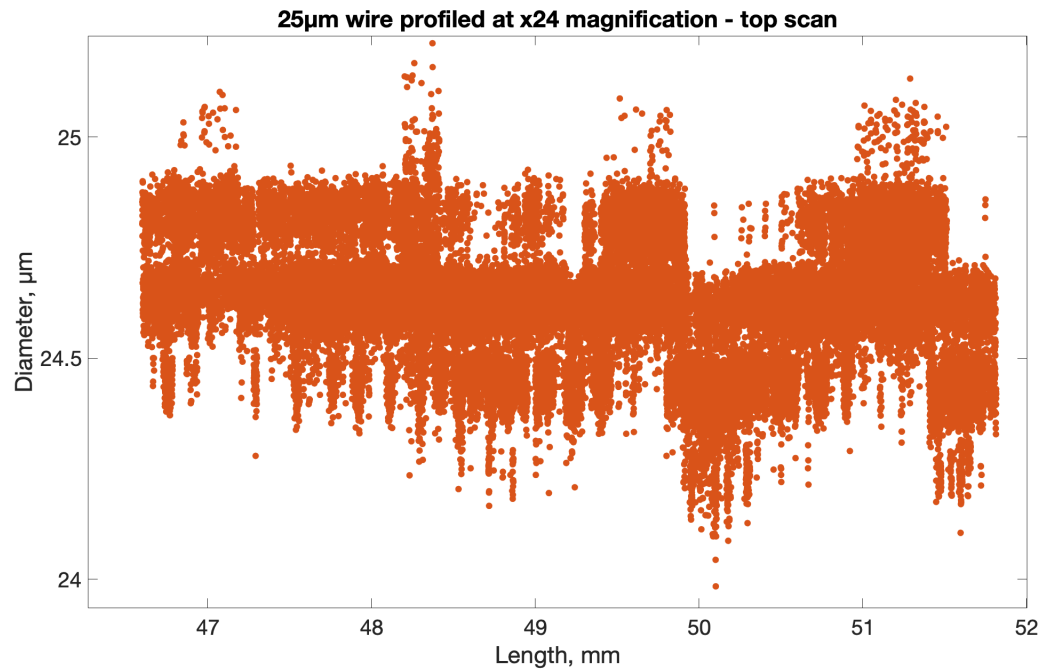


**Figure 5.28:** The zoomed in view of the bottom scan of the  $25 \pm 1.25 \mu\text{m}$  wire. Note that all data points in this region sit within the wire tolerance.

While there was an overlap region between the neck scan positions, the overlap was quite small. From the data file, the overlap was 0.11 mm. To increase the overlap, the intervals between scan measurements need to decrease. This will require changing the current encoder to one with a better resolution, such as a SIKO MSK5000-0373 [162], which will be used and discussed later in this chapter. In figures 5.27 and 5.28, a step-like feature could be seen where there was a sharp change in diameter with a change of approximately  $0.2 \mu\text{m}$ . This could be a digitisation artefact where the camera system was reaching its limitation and will be discussed in detail in 5.2.5.

Following this, the same investigations that were carried out with the wire were performed with a fused silica fibre. This fibre was pulled in the ultra-thin fibre pulling machine [93] [99]. Figure 5.29 shows a fused silica fibre under the same range of magnifications as carried out with the wire. A fused silica fibre appears different on the image compared to the wire. The transparent fibre has a bright central region where the light was focused as the fibre acts like a lens, unlike the opaque wire. This could lead to issues when trying to image the fibre when it was out of focus. The edge detection could pick up one of the inner edges next to the central bright line, which could lead to a false diameter reading. This was important for higher magnifications when the fibre could easily be out of focus by a couple of millimetres. This effect could be seen in figure 5.31. For magnifications above  $\times 20$ , once the fibre was out of focus towards the right side of the graph, the diameter starts to decrease after  $35 \mu\text{m}$  on the x-axis. The edge detection will be picking up a mixture of outer and inside edges to give these values.

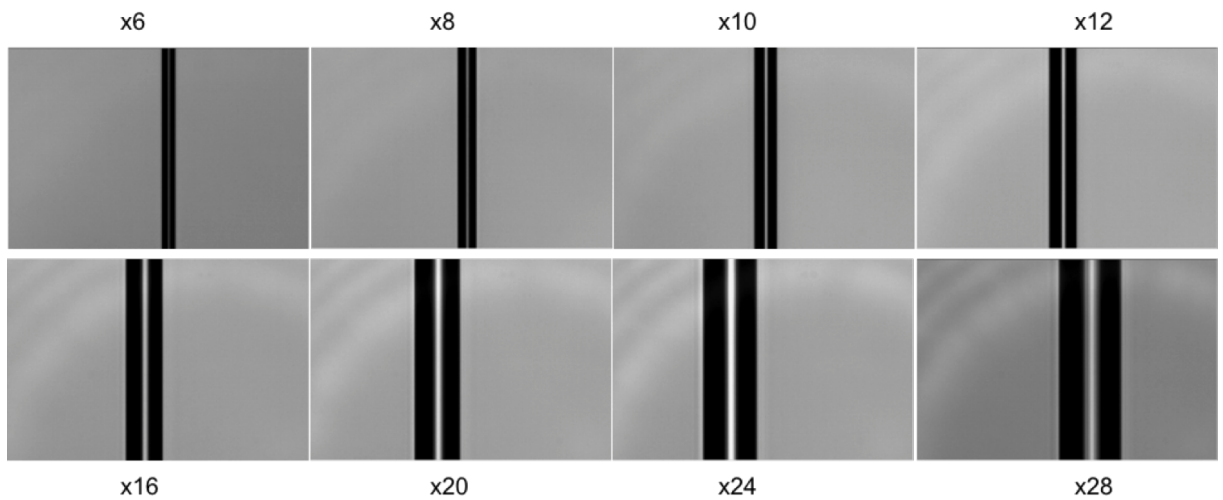


**Figure 5.29:** Fused silica fibre imaged at various magnifications. The diameter values at each magnification are shown in figures 5.30 and 5.31.

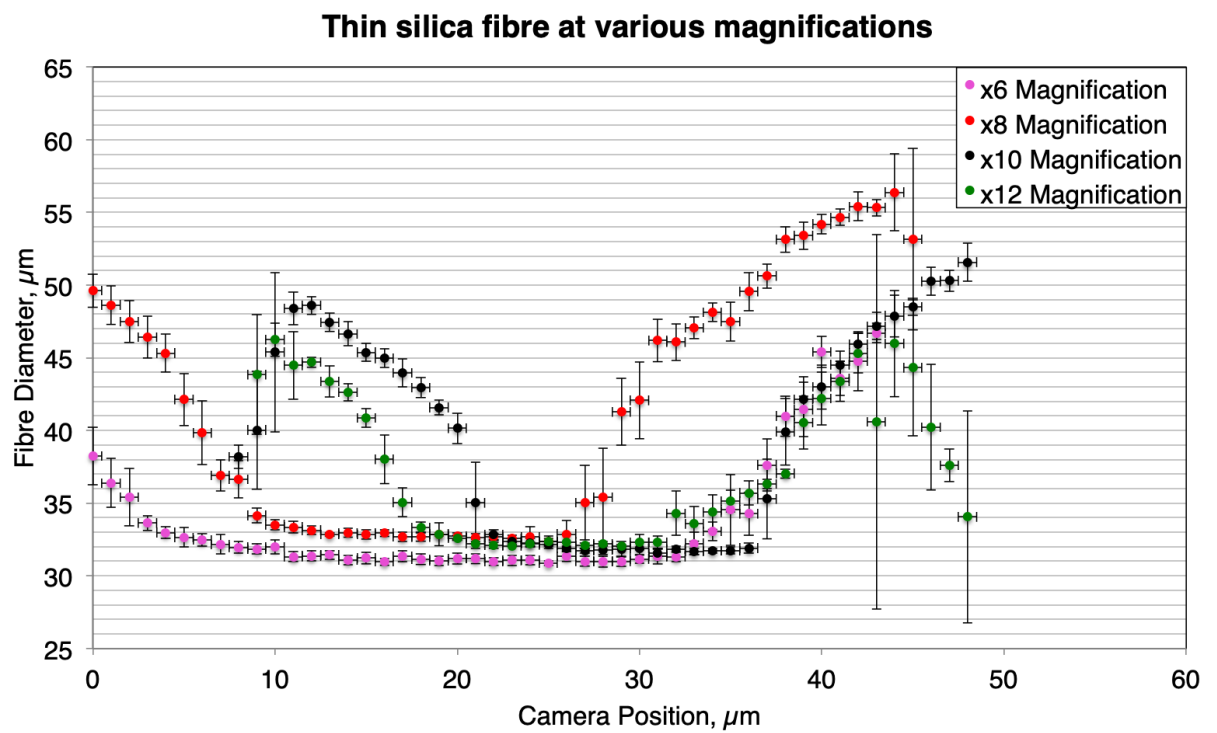


**Figure 5.30:** Fibre diameter values obtained for  $\times 6$ ,  $\times 8$ ,  $\times 10$  and  $\times 12$  magnifications during depth of field tests.

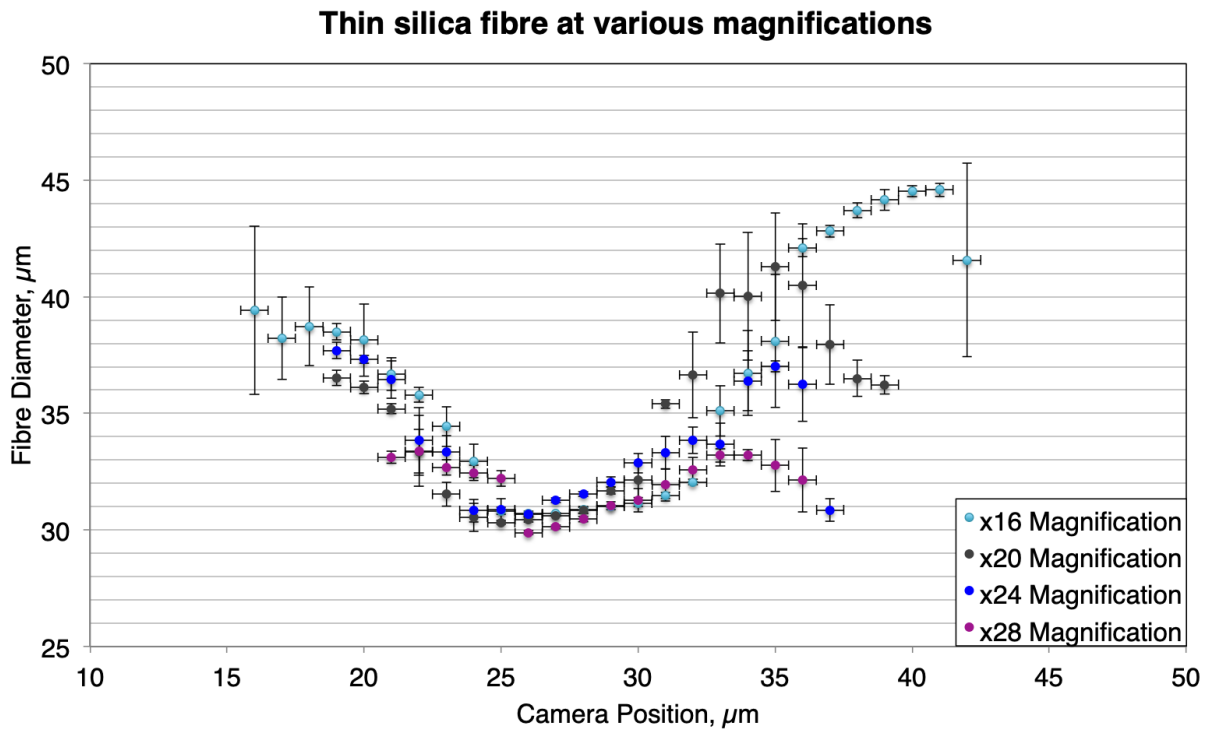


**Figure 5.31:** Fibre diameter values obtained for  $\times 16$ ,  $\times 20$ ,  $\times 24$  and  $\times 28$  magnifications during depth of field tests.

The tests carried out with the fibre agree with the wire tests as expected. The higher up in magnification, the shorter the depth of field is, which means more care must be taken when profiling a fibre with the higher magnifications to obtain accurate diameter readings. The variation in error bars is due to the same artefact as previously discussed for figures 5.24 and 5.25. It would be a recommendation that for fibres that were approximately  $30\ \mu\text{m}$ , a magnification of at least  $\times 16$  should be used. This was higher than the recommendation of the wire due to the nature of focusing onto a transparent fibre being more difficult to achieve than an opaque wire.

The next test that was carried out was taking repeated full profiles of a fused silica fibre. The aim of this test was to see how repeatable profiles could be made. This test was carried out with a fused silica fibre produced with the ultra-thin fibre pulling machine [99]. The pulling machine used is described in detail in the following chapter. Figure 5.32 shows 5 profiles of this fused silica fibre. All these profiles were taken one after another on the same day. It could be seen from figure 5.32 that all 5 profiles lie on top of each other and follow the same characteristic diameter values.

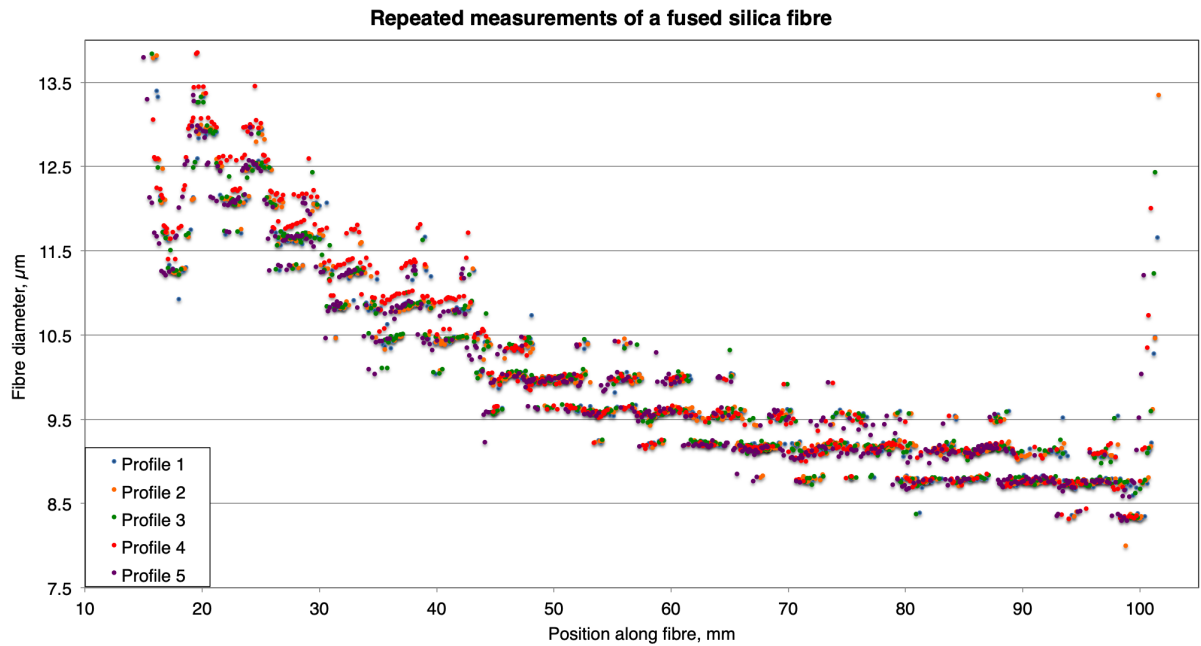


**Figure 5.32:** Five separate profiles of one fused silica fibre. A stepping artefact could be seen in the profiles, similar to that seen in figures 5.27 and 5.28.

Singular data points that were out from the main trend could be attributed to slight differences in focusing. Due to the short depth of field at higher magnifications discussed earlier, a few microns difference on the translation stage could have an effect on the level of focus at which the fibre was sitting. Table 5.3 shows the minimum diameter that was found during the repeated profiling of this fibre.

**Table 5.3:** Minimum diameter of the fibre for all five profiles.

Fibre profile	Diameter, $\mu\text{m}$
1	8.3
2	8.0
3	8.3
4	8.3
5	8.3

The uncertainty in the diameter shown was calculated by calculating the systematic uncertainty between all 5 profiles at each position along the fibre. The standard deviation of the systematic uncertainty was then attributed to the fibre diameter uncertainty. Four of the 5 profiles all have a minimum diameter within a  $0.2\ \mu\text{m}$  spread. Profile 2's minimum point was an outlier just before the 100 mm mark on figure 5.32, which could be contributing to a focusing factor due to the tightness of the spread for the four other profiles. It could be possible to average over a larger number of data points during the profiling process to eliminate the possibility of obtaining outliers. It could be seen in figure 5.32 that there was a step like artefact in the profiler diameter data. This could have an effect on the previously calculated uncertainty values

associated with the fibre diameter in table 5.3, and will be discussed in the follow subsection.

### 5.2.5 Uncertainties

The purpose of developing this dedicated ultra-thin fibre profiler was to minimise the uncertainty associated with the fibre diameter compared to that on the aLIGO profiler for these types of fibres. Previous investigations [93] found that the uncertainty associated with profiling ultra-thin fibres on the aLIGO profiler could be as high as 13%. The uncertainty associated with the fibre diameter was calculated by calculating the systematic uncertainty associated with each data point. This percentage uncertainty was obtained by firstly profiling the calibration wire over a length, and dividing the standard deviation of that length by the minimum diameter obtained. This can then be multiplied by the diameter value obtained when profiling a fibre to give the systematic uncertainty for each data point. The standard deviation of the systematic uncertainty over all points was then taken, converted to a percentage and then applied to the data points. From table 5.3, all the percentage uncertainty values for the minimum diameter were under 1%, with the greatest being 0.72% for profile 1 and 4.

It was however noticeable from figure 5.32 that there was a step-like artefact in between points as the fibre tapers down in diameter. These steps appear at approximately 0.3  $\mu\text{m}$  intervals and was only observed on fibres that have a sharp taper along it during the "middle" state of the LabVIEW program. This could be considered a limiting aspect of the fibre profiler when using high magnifications. It is possible that this arises from the capability of the sensor to resolve the image close to the edge of the fibre between pixels. The  $\mu\text{m}$  per pixel value could be calculated using the previously mentioned equation 5.2. A magnification of  $\times 17.6$  (despite the camera system being set for  $\times 16$ ) would be needed to give a value of approximately 0.3  $\mu\text{m}$  per pixel.

At the maximum magnification of  $\times 28$ , a value of 0.19  $\mu\text{m}$  per pixel value would be achieved. For the previously discussed wire scans in figures 5.27 and 5.28, the step-like artefacts occur at 0.2  $\mu\text{m}$  intervals. Carrying out similar calculations gives 0.22  $\mu\text{m}$  per pixel. This value would be consistent with the step artefacts with the lens system set to  $\times 24$ . Table 5.4 shows the calculated micrometre per pixel values for various magnification values. It was possible that a sensor with a denser number of pixels could lower this stepping artefact. This is shown in figure 5.33. Smaller sized pixels in a similar sensor area will result in a lower  $\mu\text{m}$  per pixel value for corresponding magnifications. For example, a camera with a pixel size of  $3.45 \times 3.45 \mu\text{m}$  at the maximum mentioned magnification would have a  $\mu\text{m}$  per pixel value of 0.12. At this point, this was reaching the extreme limitations of the resolution ability of this optical set-up. Along with the previously mentioned uncertainty values for individual points on the fibre, this stepping artefact needs to be considered in the diameter uncertainty value at each magnification. Combining the  $\mu\text{m}$  per pixel value with the standard deviation in quadrature changes the uncertainty to 0.31  $\mu\text{m}$ . This equates to a percentage uncertainty of 3.8-3.9%, which was still a significant improvement to the previous uncertainty of up to 13% for the aLIGO profiler set-up.

**Table 5.4:** Micrometre per pixel values for a range of magnification values. These magnifications would give the step-like artefacts with intervals of the corresponding  $\mu\text{m}$  per pixel values.

Magnification	$\mu\text{m}$ per pixel
6	0.93
8	0.68
12	0.44
16	0.33
17	0.31
18	0.29
20	0.26
24	0.22
28	0.19

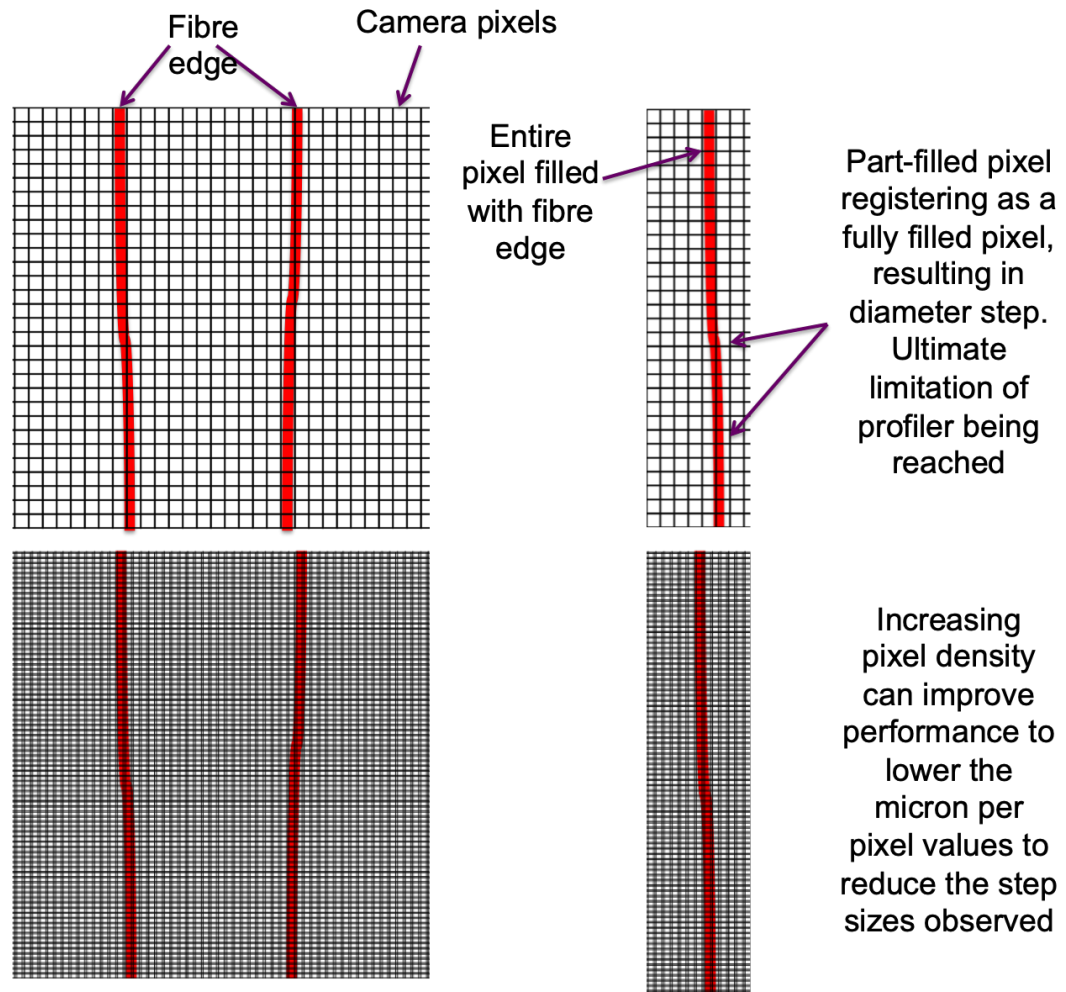


**Figure 5.33:** A schematic illustrating the possible cause of the stepping artefact that appears in figure 5.32.

In addition, as there were no small divisions on the lens system to tell exactly what mag-

nification the camera was set to, this was a possible reason for a magnification of  $\times 17.6$  being used instead of  $\times 16$ . Should an exact magnification ever be needed for an investigation, the calibration of the profiler could include calculating the magnification value that the lens system was set to, by using the previously mentioned equation 5.2.

The encoder attached to the motorised stage has a stated manufacture uncertainty of  $\pm 0.04$  mm [124]. A movement test was carried out to check the performance of the encoder in the profiler set-up. This was achieved by measuring the distance travelled over 10 cm using two independent measurement methods:

- Magnetic encoder attached to the motorised stage that will be used for profiling.
- SIOS SP 5000 NG interferometer attached to the motorised stage for this measurement [163]. This has an uncertainty of  $\pm 0.1$  pm, which was significantly smaller than the uncertainty of the encoder.

A schematic of the experimental set-up for this investigation is shown in figure 5.34. The vibrometer works by sending laser beams out of the unit to a mirror placed against a flat surface. In this case, the flat surface was the table that the profiler was sitting on. The beam was reflected off the mirror and back to the vibrometer. When the motorised stage moves, there will be a phase change of the beam which could be converted through the manufacture software [163] to read out the distance the motorised stage has travelled. This gives a completely independent measurement to the magnetic encoder that was already attached to the motorised stage. Prior to measurements being taken, the SIOS had to be aligned to ensure the beam stays within the unit when the return beam enters to reach the sensor. This was achieved through a status monitor box in the manufacture software that gives a percentage value of how well the beam was aligned. An alignment through all the measurements of 98% was achieved with the current set-up of the table on which the profiler was stationed on. It was not possible to achieve 100%.

The motorised stage was controlled via a custom LabVIEW program that reads out the counts and distance travelled. The stage was moved until the distance reading showed that the stage had travelled approximately 10 cm. The reason this was approximate was because the motor controller runs via an on-off switch that the user controls and the controller was turned off once the encoder count reaches 1000 (or close to this value). The distance travelled was then compared to the distance travelled by the vibrometer. This was repeated a total of 20 times, where the stage was measured moving 10 cm upwards 10 times, and downwards 10 times. This data is shown in table 5.5.

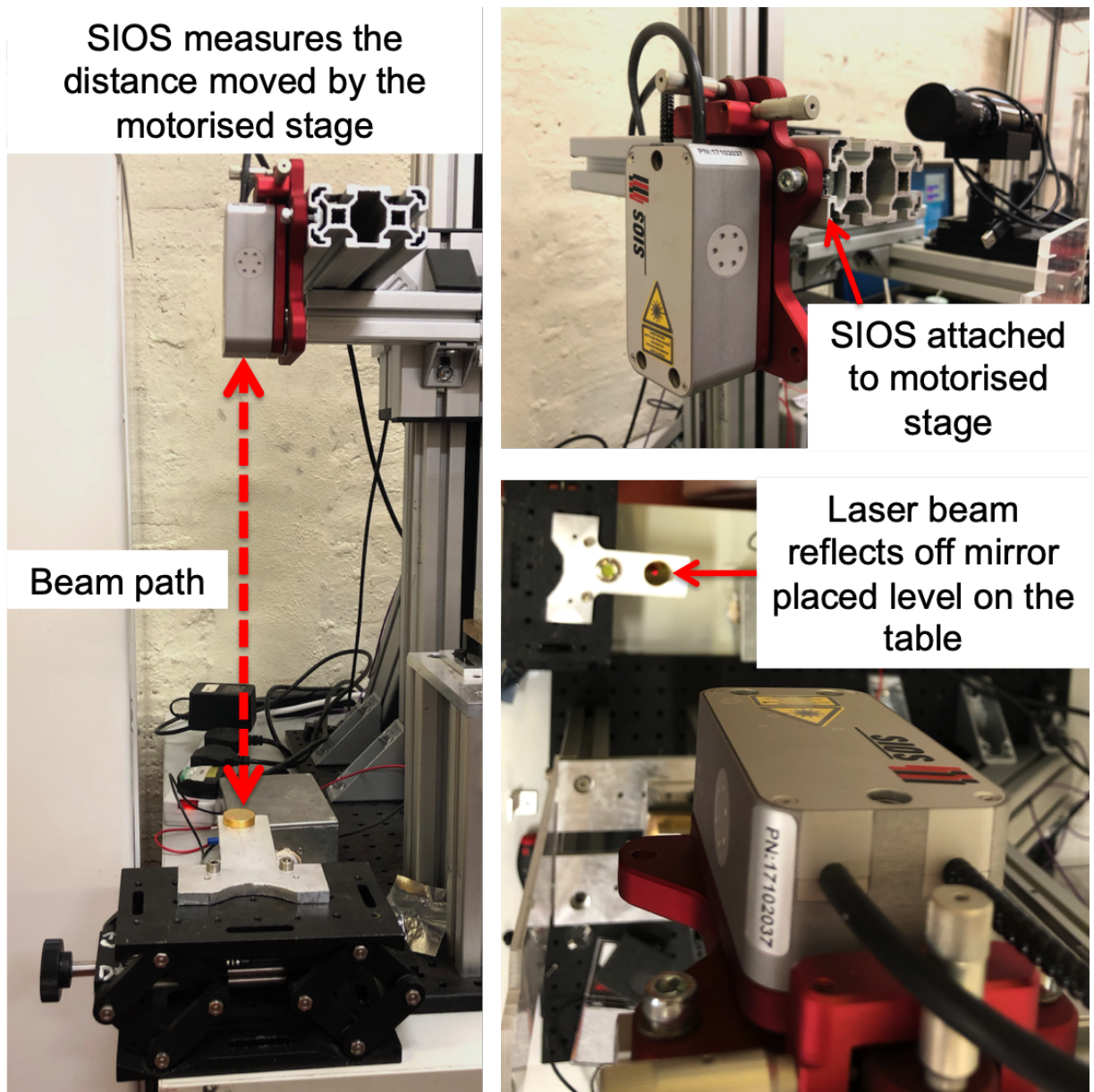


**Figure 5.34:** The set-up of the SIOS for the motorised stage position measurements investigation.

The results shown in table 5.5 show that the largest difference between the values of the encoder and the SIOS was 0.08 mm, which was 0.04 mm greater than the stated tolerance of the SIKO encoder. This could potentially be due to the alignment of the SIOS not having an alignment percentage of 100%. As the scan settings for the neck regions was set to 0.1 mm intervals, it could be a possibility that if there was a slight overrun in the motorised stage of 0.08 mm, that a 0.08 mm section was missed in the fibre profile when using the maximum magnification. For the research carried out in this thesis, this was not a critical issue that needed to be attended to, but should be taken into consideration for future upgrades where the SIKO encoder was replaced with an encoder with a smaller resolution. This is an upgrade discussed in the following

subsection.

**Table 5.5:** Distance travelled by motorised stage during repeated up and down movements.

Direction of movement	Encoder counts	Distance travelled, encoder, mm. $\pm 0.04$	Distance travelled, SIOS, mm. $\pm 0.1 \mu\text{m}$
Down	1002	100.20	100.23
Up	1000	100.00	100.05
Down	1001	100.10	100.14
Up	999	99.90	99.95
Down	1003	100.30	100.34
Up	1003	100.30	100.34
Down	1004	100.40	100.43
Up	1000	100.00	100.07
Down	999	99.90	99.98
Up	1001	100.10	100.16
Down	1004	100.40	100.42
Up	1000	100.00	100.06
Down	999	99.90	99.96
Up	1003	100.30	100.35
Down	999	99.90	99.96
Up	999	99.90	99.97
Down	1001	100.10	100.17
Up	1000	100.00	100.08
Down	1001	100.10	100.17
Up	1002	100.20	100.26

## 5.2.6 Future improvements

There was potential to make improvements to the ultra-thin fibre profiler in the future. The first suggested improvement that could be made was the addition of a second camera and lens system that was previously discussed. This would bring the ultra-thin profiler in line with the design of the aLIGO profiler and allow for dual readings at perpendicular angles to observe if there were any angular defects. Dual camera systems could also be beneficial when profiling different shaped samples. One example would be silicon ribbons. One camera could be set-up to profile the thickness of the ribbon sample while the perpendicular camera could profile the width of the samples. This would save time as two measurements would not have to be taken separately one after the other. Difficulties in this upgrade would be the practicability of having two cameras working in this set-up. The current arms would have to be lengthened to accommodate the strut that would hold the second camera set-up. Tests on the motor stage would have to be carried out to ensure that it works to the design specifications due to the set-up being a large and heavy

cantilever. Large holes in the Bosch struts could be drilled out to help reduce the weight from the arms. Changing the cameras completely to one that has a greater pixel density was another possible upgrade to the profiler. This, as previously described, would decrease the  $\mu\text{m}$  per pixel that could reduce the stepping artefact that appears in fibres with a sharp taper.

Another suggested improvement would be a measuring track guide for the variable magnification set-up. Currently, the magnification is change by turning the dial on the variable lens tube. This could move with ease by hand, but does not have a track guide on the dial to reliably revisit a previously set magnification value. Markings engraved onto the magnification tube would allow for previous magnifications to be revisited if an optimal magnification was found for specific types of samples.

An additional improvement related to the magnification would be to replace the current set-up with a "snap to" style variable magnification system. The procedure of pulling ultra-thin fibres, described in detail in the following chapter, requires a two stage pulling process. This means that from the original stock material, the first pull produces a new, approximately  $500\ \mu\text{m}$  piece of stock. The second pull produces the ultra-thin fibre from this new  $500\ \mu\text{m}$  section. Due to the need for high magnification to profile the ultra-thin fibre, this results in the  $500\ \mu\text{m}$  section being too large to profile at the same time. A "snap to" system would allow the  $500\ \mu\text{m}$  section to be profiled with lower magnification, followed by consistently "snapping to" a higher magnification value to profile the ultra-thin fibre section. This would require two calibration values to be set per camera for each magnification. A dual camera set-up could remove the need of having a "snap to" system by having each camera set to different magnifications to accommodate both the stock and the ultra-thin section. This would however sacrifice the possibility of accurately dual profiling the ultra-thin section, as the magnification of one camera would be too low. It would however allow for one camera to profile the stock material with a lower magnification, which was necessary when profiling fibres that will be used in suspensions.

An alternate design could potentially be developed that utilises an absolute measurement technique. Using a laser beam, a diffraction pattern could be obtained when directed at a fused silica fibre. The observed pattern could be calibrated to allow for diameter measurements to be observed. Early tests through an undergraduate project showed encouraging results, and this type of measurement could be pursued in the future.

As previously shown in table 5.5, there was the possibility of a slight overrun from the motorised stage. This overrun could be up to  $0.08\ \text{mm}$  which was not critical for the work carried out in this thesis, but when using the maximum magnification on the lens system, it should be kept in mind if the overlap region in the profile was critical. This could be minimised through the use of a magnetic encoder that has a smaller resolution than the current SIKO MSK320 [124] that was used, such as a SIKO MSK5000 [162]. The smaller resolution will allow for greater precision of the motorised stage.

### 5.3 Upgrades to ultra-thin fibre strength tester

The second of the major source of uncertainty that were listed at the start of this chapter was the uncertainty associated with measuring the stretch of the fibre at point of failure within the ultra-thin fibre strength tester, shown in figure 5.35. The ultra-thin fibre strength tester was previously developed by an undergraduate student [164], and was utilised in previous research [93].

In principle, it was the same as the aLIGO strength tester [117], only scaled down. A Omega S-Beam load cell [118] was attached to a top fixed stage with a clamp attachment to hold the chuck of the ultra-thin fibre cartridge. A digital readout was also attached to the load cell to read the load being applied. The digital readout would be set to the maximum load setting, which stores the maximum load that was applied until the system was reset. The bottom stage was attached to a stepper motor which drives the stage, that also holds the clamp to attach the bottom chuck. The stepper motor was controlled via a custom LabVIEW program [164]. Previously, data was taken by reading the maximum load value shown on the digital readout of the load cell at the point the fibre failed. The distance the motorised stage travelled was measured using a set of digital calipers. Best efforts were made at the time to ensure the calipers were always reading from the exact same positions on the stage against the drive rods, but would always be a source of reading uncertainty.

To reduce this uncertainty, as well as improve the set-up, it was decided that the ultra-thin fibre strength tester would undergo multiple upgrades:

- Lengthened drive rods
  - Allows for fibres longer than 10 cm to be tested within the strength tester. This is important for strength testing fibres that would be used to suspend mirrors for research activities both in and out of Glasgow.
- Installation of a magnetic encoder to read the distance traveled by the motorised stage
  - Allows for repeatable and reliable measurement of the distance travelled by the motorised stage. An accurate measurement of the extension of the fibre could then be obtained.
- Read in load cell values directly to the LabVIEW program running the strength tester
  - Allows for a real-time plot of the force applied to the fibre against the extension of the fibre through the LabVIEW front panel. This means that the exact time that the fibre was under tension and when it breaks could be accurately tracked.

The work within this section was carried out in conjunction with an IREU student, Erin Momany. Her project during her time in Glasgow was to install these desired upgrades. Data from her report will be cited and credited accordingly.

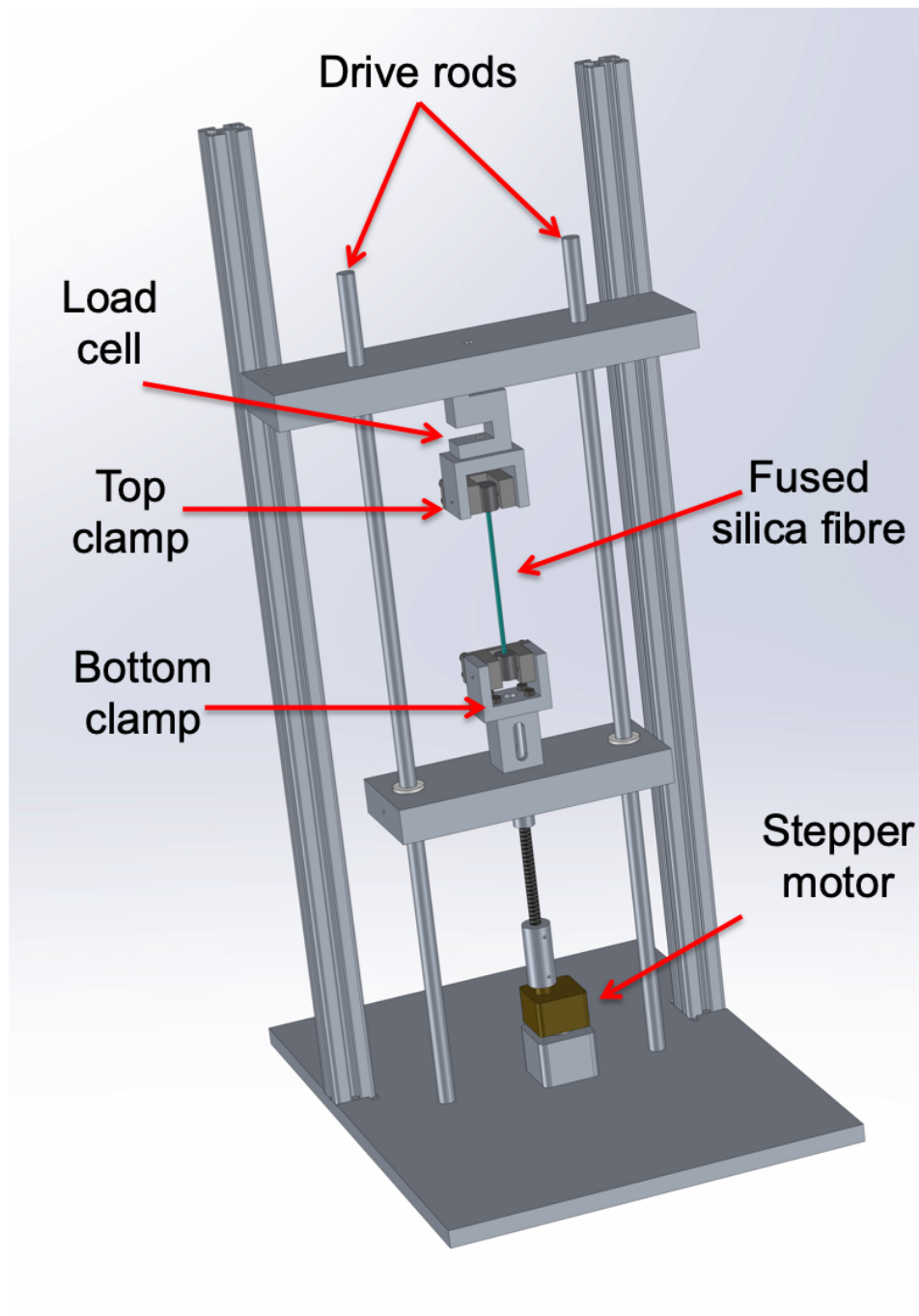


**Figure 5.35:** SolidWorks CAD rendering of the ultra-thin fibre strength tester prior to upgrades [164].

### 5.3.1 Installation of upgrades

Previous research that was carried out with the ultra-thin fibre strength tester mainly utilised fibres that had a length of approximately 10 cm. Due to the length of the original drive rods, it was not possible to test fibres that were any longer than this in the strength tester. As there were experiments that wanted to utilise fibres that were 20 cm in length, the strength tester needed to be

modified to allow for this upgrade. The drive rods were replaced with 95 cm drive rods to allow for longer fibres to be installed, shown in figure 5.36. The ultra-thin fibre pulling machine could produce fibres up to 30 cm. Including the added length of the two chucks on the fibre cartridge, the new drive rods were sufficiently long enough to accommodate the longest fibres that could be produced. The top fixed stage has adjustments available to allow the stage to slide to the required height for any length fibre sample that was required. This set-up suits all lengths of thin fibres that have been tested.

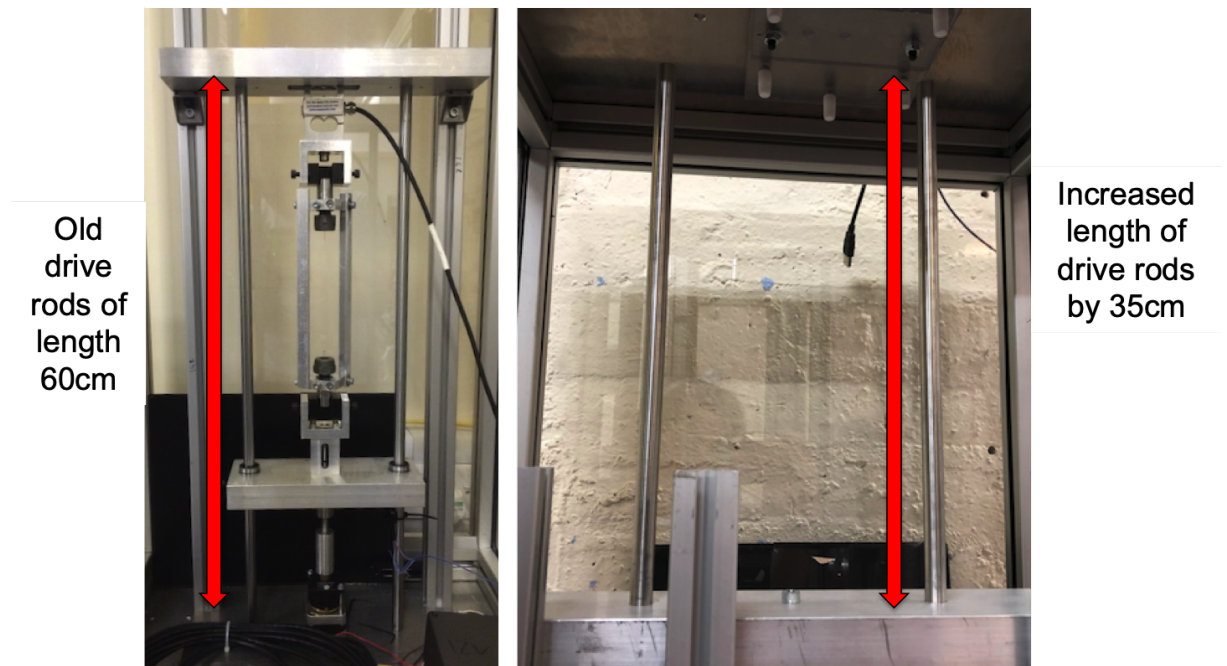


**Figure 5.36:** Left: The original drive rods. Right: The newly installed lengthened drive rods.

The second upgrade carried out was the installation of the magnetic encoder to the motorised stage. The encoder used was a SIKO MSK5000-0373 [162]. This encoder has a smaller resolution than that which was installed into the ultra-thin fibre profiler described previously. The encoder and magnetic strip, shown in figure 5.37, has a minimum resolution of 1  $\mu\text{m}$ . This would allow for greater accuracy and position resolution than the digital calipers that were previously used. To connect the encoder to the motorised stage, a right-angled bracket mount was attached to the side of the motorised stage. This positions the encoder to sit just above the magnetic strip. The encoder could then be read into the LabVIEW program to show the distance travelled in real time.

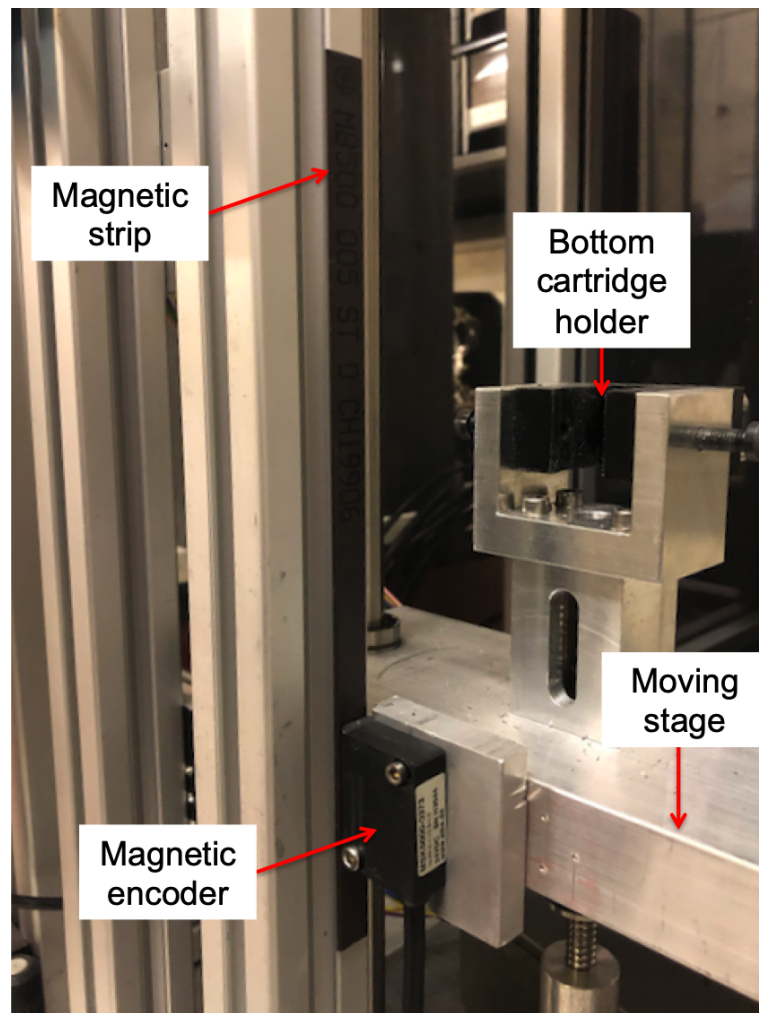


**Figure 5.37:** The MSK5000-0373 magnetic encoder installed onto the side of the motorised stage.

To test that the encoder was working properly, measurements of the distance travelled were compared between the encoder and calipers. The stepper motor was set to travel down 10000 steps, followed by a measurement reading of the distance travelled with calipers. This was then compared to the value that was displayed on the LabVIEW program from the encoder.

**Table 5.6:** Distance of motorised stage moving up from calipers and magnetic encoder. Data taken from Erin Momany's final report [165].

Number of steps travelled	Distance travelled, caliper, mm	Accumulated encoder counts	mm/counts
10000	$1.35 \pm 0.03$	1103	0.001
20000	$2.27 \pm 0.03$	2198	0.001
30000	$3.31 \pm 0.03$	3311	0.001
40000	$4.59 \pm 0.03$	4424	0.001
50000	$5.84 \pm 0.03$	5518	0.001

**Table 5.7:** Distance of motorised stage moving down from calipers and magnetic encoder. Data taken from Erin Momany's final report [165].

Number of steps travelled	Distance travelled, caliper, mm	Accumulated encoder counts	mm/counts
10000	$1.22 \pm 0.03$	1017	0.001
20000	$2.49 \pm 0.03$	2114	0.001
30000	$3.47 \pm 0.03$	3221	0.001
40000	$4.72 \pm 0.03$	4337	0.001
50000	$6.77 \pm 0.03$	5426	0.001

Tables 5.6 and 5.7 show the distance values of the motorised stage measured with both calipers and the magnetic encoder [165]. The encoder values for counts per millimetre match the resolution values given in the data sheet of  $1 \mu\text{m}$  [162]. The larger variation in the caliper values compared to the encoder values obtained could be attributed to the position the calipers were placed when measuring the distance travelled. This is the issue that the encoder is aiming to solve as it is fixed into position on the stage.

The third upgrade was changing the load cell read out. As previously mentioned, the load cell was read out onto a digital reader that could be observed. The digital reader had two main settings that were utilised during previous investigations:

- Live value
- Maximum value

The live value setting would display the load on the load cell in real time, where as the maximum value setting would display the maximum load to which the load cell was exerted until the reset button was pressed. Previously, load cell readings would be noted down after

regular distance intervals to plot the load to which the fibre was exerted. By reading in the load cell values through the LabVIEW program and recording the values, the load cell reading at every point during the strength test process could be plotted and saved for analysis. To do this, the digital read out of the load cell was connected to the desktop PC via a National Instruments 6008 USB DAQ [166]. The DAQ could then be read into the LabVIEW program to allow the load cell data to be plotted in real time, as well as saved to an excel file. Combining this upgrade with the addition of the encoder, live graphs of load against stretch of the fibre could be plotted during strength tests. The front panel of the updated LabVIEW program is shown in figure 5.38. The live plotted graph could be seen in the bottom right of the front panel.

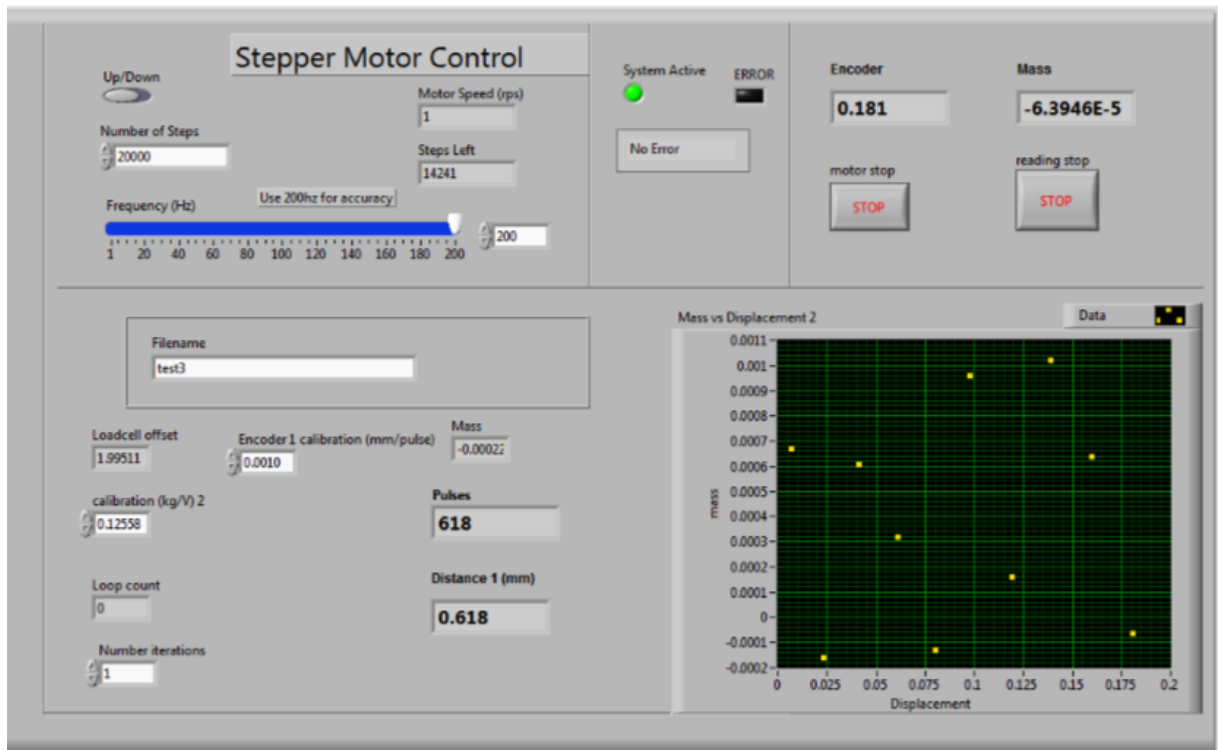


**Figure 5.38:** The updated custom LabVIEW program for the ultra-thin fibre strength tester [165].

The load cell could be calibrated through the LabVIEW program. A mass with a known load could be attached to the load cell and read through the program. The mass should be as close to the expected load that would be applied to the fibres. A load of  $529 \pm 0.5$  g was attached to the load cell and a kg/V value was inserted into the calibration box on the front panel. This converts the voltage signal that the digital readout sends to the DAQ into kg that was saved to the file and plotted on the live graph.

Having a live plot of the force on the fibre allows for the initial slack removal period to be recorded. This was the period where the fibre was slack within the strength tester and not under any tension. As the fibre was slack, then no load is applied to the load cell, hence no load is also

showing on the live graph. Once the fibre was no longer slack, a load is applied to the load cell and appears on the live graph. The corresponding stage position from the encoder on the graph could then be noted down as the point the fibre starts to stretch. All this data was also recorded in the text file that was saved.

### 5.3.2 Uncertainties

The main source of uncertainty was attributed to the measurement of the motorised stage. This was due to the uncertainty in the caliper measurements and differences in ensuring that the calipers were always reading values from the same point on the stage. The magnetic encoder has an uncertainty of  $\pm 0.01$  mm, which was better than the best case scenario uncertainty of the caliper which was  $\pm 0.03$  mm [167]. The encoder also has the benefit of reading its distance from the same position, as it was fixed to the motorised stage. To test the performance of the encoder to see if the uncertainty value was accurate, a repeated movement test was carried out. This involved moving the motorised stage down by 10000 steps and recording the distance the stage had travelled every 200 steps. The stage was then moved up by the same number of steps and the distance travelled also recorded. This was repeated 5 times. The systematic uncertainty at each 200 step interval was calculated for all 5 times the stage was moved up and down, respectively. The standard deviation of this uncertainty was then calculated. The standard deviation when the stage was moving down was found to be 0.0027 mm, and 0.0018 mm when the stage was moving up. Adding these uncertainties in quadrature gives an uncertainty of 0.003 mm associated with the position of the motorised stage. Combining this with the uncertainty of the encoder still gives a rounded uncertainty of 0.01 mm. The uncertainty associated with the load cell was unchanged during these upgrades and remains at 0.01% [118]. Combining this uncertainty with the uncertainty in the calibration mass which was 0.1%, the overall uncertainty on the load was 0.1%.

## 5.4 Conclusion

The purpose of the work carried out in this chapter was to develop and improve the apparatus associated with the ultra-thin fibre research that was carried out at Glasgow. The end goal of this was to reduce the uncertainty associated with the fibre diameter and fibre stretch during characterisation investigations. The development of the ultra-thin fibre profiler has significantly improved the capabilities of characterising fibres down to below 10  $\mu\text{m}$  in diameter. The uncertainty associated with the fibre diameter has been reduced from up to 13% to approximately 4%, depending on the thickness of the fibre and the magnification used, due to the installation of a variable high magnification lens system. Future improvements to the profiler, such as the installation of a second identical camera and lens system could be made if decided necessary. This apparatus has since been used for various different areas of research, such as fibre production

and characterisation for the Glasgow Sagnac Speedmeter experiment and the AEI 10 m prototype interferometer experiment, imaging of MEMS gravimeters [168], imaging silicon ribbon samples, and was used extensively in the following two chapters in this thesis.

The upgrades of the ultra-thin fibre strength tester has successfully decreased the associated uncertainties associated with the position of the motorised stage with the installation of a magnetic encoder to measure the distance travelled by the motorised stage. This therefore decreases the uncertainty of the stretch of the fibre from a best case scenario of  $\pm 0.03$  mm to a consistent  $\pm 0.01$  mm. The ability to record the live load feed during the strength test also decreases the uncertainty in the stretch as the slack removal period could be accurately measured to locate the moment the fibre was under tension. This apparatus was extensively used in chapter 7 to investigate the Young's modulus of fused silica with the goal of reducing the uncertainty in the previously obtained values [93].

The next step was to proceed further with the stress fatigue investigation that was carried out in chapter 4. Instead of thick fused silica fibres of approximately 200  $\mu\text{m}$  in diameter, ultra-thin fibres that match the diameters that Proctor had investigated will be used. As well as this, the experiment will be extended using fibres thinner than what was used by Proctor to see if the data still agrees, or if there was any significant change.

# Chapter 6

## Stress fatigue in 10-40 $\mu\text{m}$ diameter fibres

### 6.1 Motivation

Following the investigation that was carried out previously in chapter 4, there was a desire to expand the range of diameters for stress fatigue tests. The fibres tested in that chapter ranged between  $183.5 \pm 2.4 \mu\text{m}$  and  $208.3 \pm 2.7 \mu\text{m}$ . These were significantly thicker than those investigated by Proctor [131]. Proctor's fibres ranged between 20-40  $\mu\text{m}$  in diameter, and were seen to have superior stress fatigue performance. Therefore it was desirable to test a range of fibre diameters around the diameters Proctor used, including thinner fibres than Proctor used. The fibres tested in this investigation will be referred to as ultra-thin fibres.

This chapter will detail this continued investigation by discussing the production process of ultra-thin fused silica fibres, characterisation of these fibres with the new ultra-thin fibre profiler that was discussed in chapter 5, the experimental set-up and the results obtained.

### 6.2 Production and characterisation of ultra-thin fused silica fibres

#### 6.2.1 ultra-thin fibre pulling machine hardware overview

The production of the ultra-thin fibres was carried out using the ultra-thin fibre pulling machine [93] [99]. This pulling machine, shown in figures 6.1 and 6.2 was previously developed and characterised by the author for a MSc thesis [93]. The procedure to align this pulling machine can be found in this thesis. This pulling machine works around the same concept as the aLIGO pulling machine [62] that was used previously in chapters 2-4, though with several hardware differences. The first difference was the high velocity pulling stage, a Newport IMS400-LM [169]. This pulling stage was chosen due to its fast acceleration and maximum velocity values, which were  $26000 \text{ mms}^{-2}$  and  $500 \text{ mms}^{-1}$ , respectively. Having a high acceleration allows

the stage to accelerate to its desired speed in milliseconds, which allows for a sharp change in diameter at the initial stage of the pull. The pulling stage was also set horizontal along the pulling bench. The reason the stage was not vertical was that when there was no power applied to the pulling stage, the stage platform could move freely. If the pulling stage was therefore set to be vertical, the pulling platform would fall to the bottom of its travel.

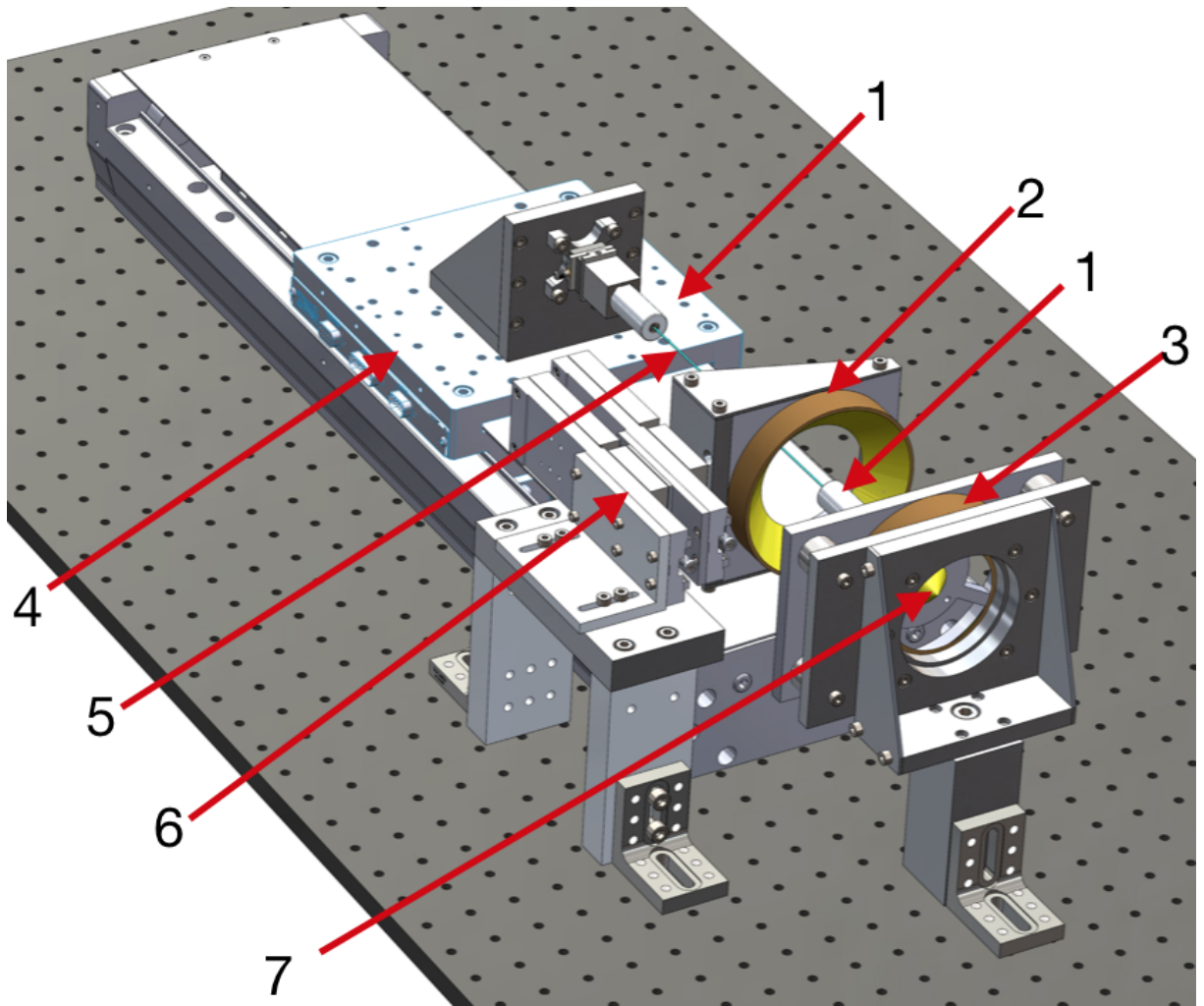


**Figure 6.1:** SolidWorks rendering of the ultra-thin fibre pulling machine that was used to produce the fibres that were investigated in this chapter. Labels: 1 - Cartridge chuck. 2 - Feed mirror. 3 - First conical mirror. 4 - Pulling stage. 5 - Fused silica stock. 6 - Feed mirror motorised stage. 7 - Axicon [99].

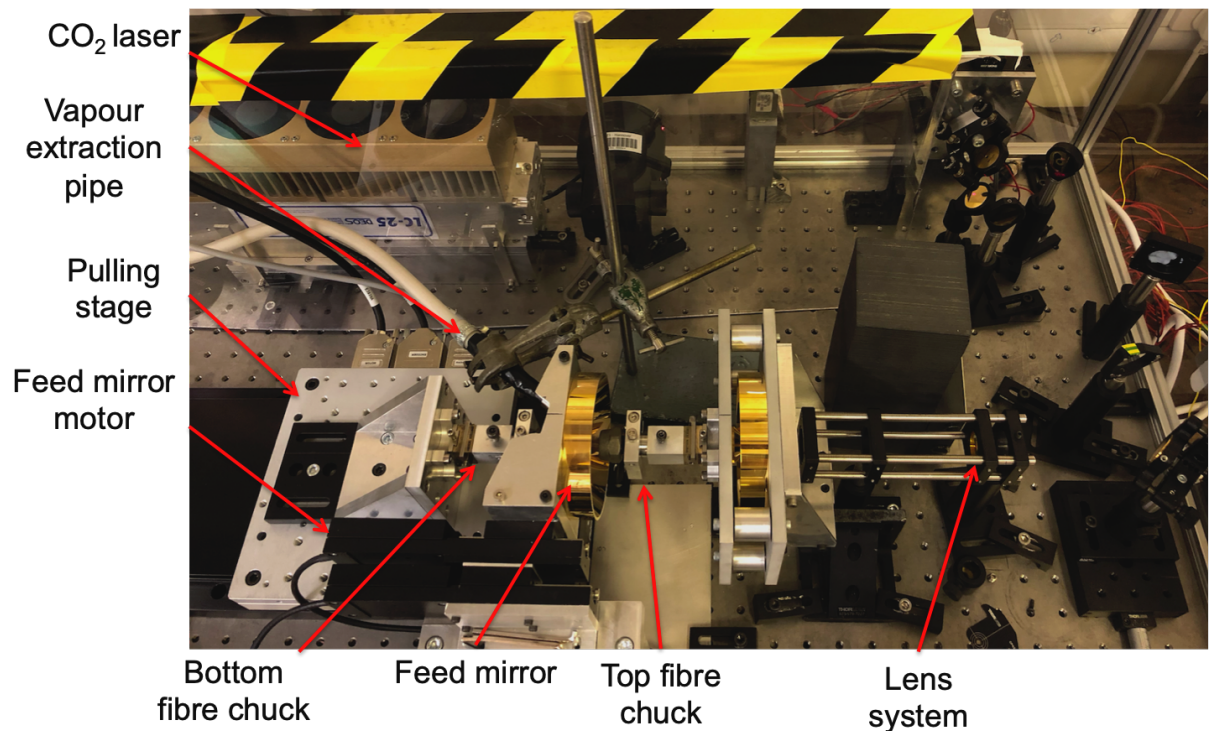


**Figure 6.2:** The ultra-thin fibre pulling machine in its current set-up as of writing this thesis.

The second major difference was the use of what was known as an "axicon" to deliver the  $\text{CO}_2$  beam to the first conical mirror instead of a rotating  $45^\circ$  mirror [170] [171]. The axicon and beam path is shown in figure 6.3. This was a fixed cone mirror that spreads the beam out to the conical mirror by reflecting the  $\text{CO}_2$  beam off the tip of the cone. The reason this delivery method was chosen was due to the desire to heat all around the stock material simultaneously, instead of through a rotating  $45^\circ$  mirror that was used in the aLIGO pulling machine. There was also a lens system installed onto the optical bench to focus the  $\text{CO}_2$  beam onto the fused silica stock. This lens system comprises of two zinc selenide (ZnSe) lenses with focal lengths of 110 mm and -100 mm to give a beam waist of approximately  $100\ \mu\text{m}$  at the focal point on the stock. This means the area of stock that was heated could be controlled better than no lenses as the beam will be concentrated over a smaller area. Should the beam be spread over a larger area, this would result in the neck length tapering down, as the fibre is greater in length and is pulled from a larger molten area, which was not desirable for these fibres.

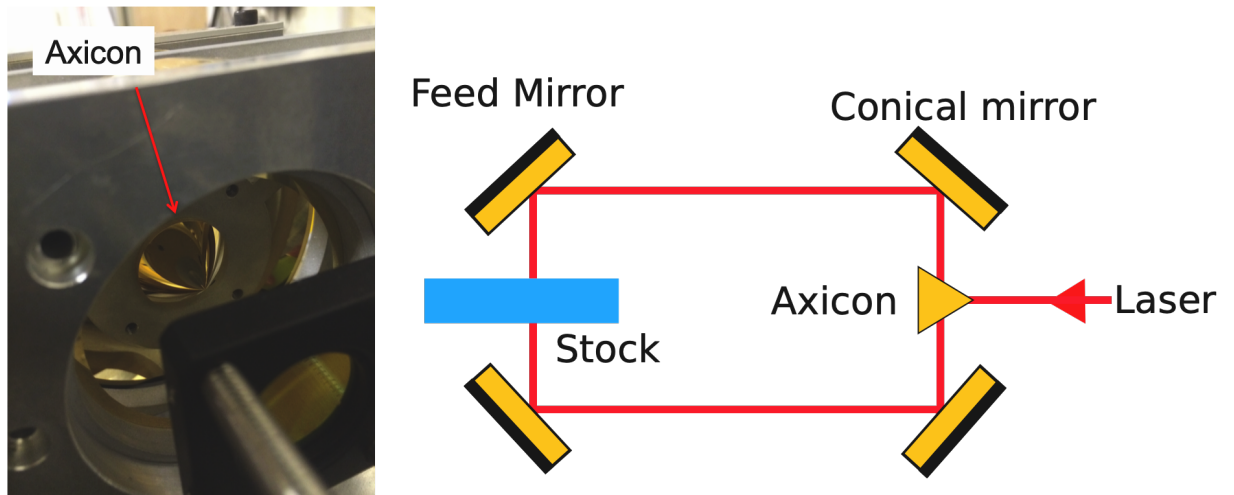


**Figure 6.3:** Left: The axicon that was used to spread the CO<sub>2</sub> beam out to the first conical mirror. Right: Cross section of the beam path of the CO<sub>2</sub> mirror after reflecting off the axicon. [99].

Two fibre cartridge chucks, previously described in chapter 5.2, were installed into their holder prior to the installation of the fused silica fibre. The fused silica stock was installed into the collets that were within the chucks and were tightened by hand. The stock material then follows the aLIGO cleaning procedure of alternately wiping with methanol and acetone [97]. The fibre could then be produced through the use of velocity profiles, described in the following subsection.

### 6.2.2 Velocity profiles and fibre production

The pulling machine was controlled via a custom LabVIEW program [172] that differs to the aLIGO puller LabVIEW program [62]. The aLIGO pulling stage was controlled by applying a voltage defined within the voltage pulling profile for each encoder count of the loop during the pulling process. The ultra-thin fibre pulling machine was controlled through the use of velocity pulling profiles, comprising a text file with three columns of values:

- Velocity
- Acceleration
- Time

The velocity of the stage was a value between 0 and 500  $\text{mm s}^{-1}$ . The acceleration column included values between 0 and 26000  $\text{mm s}^{-2}$ . The time column was a value in seconds to indicate how long the pulling stage will travel at the corresponding velocity value. Once the time has elapsed, the stage will move to the next line of the pulling profile and move to the given velocity, acceleration and time values. The final line of the pulling profile will have all

three columns at 0 to bring the stage to a stop. Failure to put a row of 0s at the end will result in the pulling stage naturally decelerating to a stop, which could include triggering the in-built kill-switches. By using the velocity, acceleration and time values, the distance travelled by the stage could be calculated for each line of the pulling profile. The velocity profile values that were chosen in this investigation were through a combination of past experience pulling fibres, as well as modifications of previously used velocity pulling profiles [93].

The stock used in this investigation was 2 mm diameter Heraeus Suprasil 3 [132]. To produce fibres of the previously mentioned desired diameter, a 2 stage pull needs to be utilised. This comprises of initially pulling the starting stock down to a thinner diameter, before pulling the final fibre from the stock material that was produced from the first stage pull. For fibre production in this chapter, the first stage pull would bring the diameter down to approximately 500  $\mu\text{m}$  over a length of 5 cm. This diameter and length was chosen as this velocity profile was developed previously by the author for fibre production related to the previously mentioned sagnac speedmeter [144] and the AEI 10 m [173] experiments. Once the first stage pull was undertaken, the feed mirror was reset to its start position and a second velocity profile was uploaded. The second velocity profile then produces the ultra-thin fibre from the central thin section of the first stage pull.

In total, 2 main pairs of velocity profiles were used. The first to produce fibres that were aimed to be approximately around 10  $\mu\text{m}$  in diameter, and the second to produce fibres that were approximately to be 20  $\mu\text{m}$  in diameter. Both of these pairs of velocity profiles were produced with various polishing conditions. The 10  $\mu\text{m}$  fibres were produced firstly with no polishing to the initial stock material, and then produced with polishing of the initial stock material. This was to see if the polishing process would have any difference when the second stage pull was produced from newly made stock material. The 20  $\mu\text{m}$  fibres were produced with no polishing, one full polish and two full polishes. The reason that two polishes were not carried out with the 10  $\mu\text{m}$  fibres was the issue of vaporising too much material off during polishing that fibre production became difficult when attempting to produce fibres of this diameter.

Polishing the initial stock was carried out with a laser duty cycle set to 80% laser power over a length of 7 mm. This equates to approximately 28-30 W of power. This polish length was chosen as it would cover more than the entire length of stock that would be used during the whole pulling process. The laser duty cycle of 80% was chosen as the stock would start to vaporise too much material during polishing and therefore potentially cause issues with the ability to actually produce a fibre. The feed mirror would move at a velocity of 0.0275  $\text{mm s}^{-1}$  which was the equivalent velocity of the feed mirror for the aLIGO fibre polishing procedure [97]. There was currently no laser stabilisation system set-up on the ultra-thin fibre pulling machine unlike the Glasgow aLIGO fibre pulling machine. This was a potential feature that could be installed in the future which would allow for greater control of the laser power during polishing and pulling. The laser duty cycle was controlled manually by using a Synrad UC-2000 laser controller [174].

There were visual indicators, such as the operating light on the feed stage control box, on the optical bench that indicates when the pulling process has started and finished. The laser was turned off when this light switches off.

Tables 6.1 and 6.2 show the first and second stage velocity profiles used to produce the fibres that were aimed to be around 10  $\mu\text{m}$  in diameter. The first stage was carried out with the feed mirror velocity at  $0.7 \text{ mm s}^{-1}$  and the laser duty cycle set to the maximum value of 95%. The second stage was carried out with the feed mirror velocity set to  $0.05 \text{ mm s}^{-1}$  and the laser duty cycle set to approximately 25-30%. Beyond 30%, the stock could vaporise very quickly which could compromise the chances of producing a fibre from that stock.

**Table 6.1:** The first stage velocity pulling profile for the 10  $\mu\text{m}$  diameter fibres.

Velocity ( $\text{mm s}^{-1}$ )	Acceleration ( $\text{mm s}^{-2}$ )	Time (ms)	Distance (mm)
0.1	20000	200	0.02
1	20000	1500	1.52
2	20000	200	1.92
3	20000	200	2.52
4	20000	1000	6.52
7	20000	1000	13.52
13	20000	1832	37.37
0	0	0	

**Table 6.2:** The second stage velocity pulling profile for the 10  $\mu\text{m}$  diameter fibres.

Velocity ( $\text{mm s}^{-1}$ )	Acceleration ( $\text{mm s}^{-2}$ )	Time (ms)	Distance (mm)
0.1	20000	140	0.014
10	20000	100	1.014
20	20000	100	3.014
30	20000	200	9.014
200	20000	433	95.614
10	20000	100	96.614
5	20000	200	97.614
0	0	0	

Tables 6.3 and 6.4 show the first and second stage velocity profiles used to produce the fibres that were aimed to be around 20  $\mu\text{m}$  in diameter. The first stage was carried out with the feed mirror velocity at  $0.7 \text{ mm s}^{-1}$  and the laser duty cycle set to the maximum value of 95%. The second stage was carried out with the feed mirror velocity set to  $0.5 \text{ mm s}^{-1}$  and the laser duty cycle set to approximately 25-30%. Note that these fibres were longer in length for both the first stage and second stage. This was due to the fact that these velocity profiles were developed

by the author for the previously mentioned experiments associated with the Sagnac speedmeter and the AEI 10 m prototype experiments. Research has shown that the fibre length should not have an impact on the strength performance [128]. These profiles were also used to minimise the need to develop additional hardware for cartridge components.

**Table 6.3:** The first stage velocity pulling profile for the 20  $\mu$ m diameter fibres.

Velocity ( $\text{mm s}^{-1}$ )	Acceleration ( $\text{mm s}^{-2}$ )	Time (ms)	Distance (mm)
0.1	20000	200	0.02
1	20000	1500	1.52
2	20000	200	1.92
3	20000	200	2.52
4	20000	1000	6.52
7	20000	1000	13.52
13	20000	2750	49.27
0	0	0	

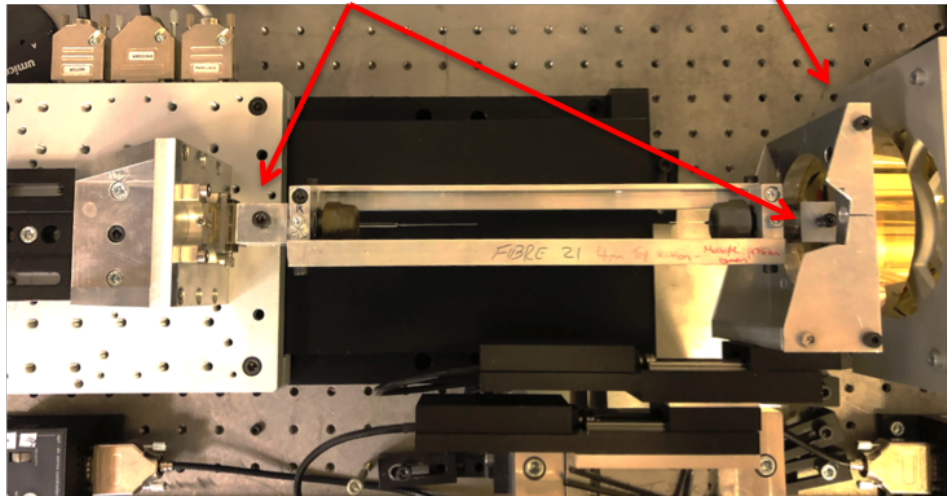
**Table 6.4:** The second stage velocity pulling profile for the 20  $\mu$ m diameter fibres.

Velocity ( $\text{mm s}^{-1}$ )	Acceleration ( $\text{mm s}^{-2}$ )	Time (ms)	Distance (mm)
0.1	20000	140	0.014
10	20000	100	1.014
20	20000	100	3.014
50	20000	200	13.014
190	20000	962	195.794
10	20000	100	196.794
5	20000	200	197.794
0	0	0	

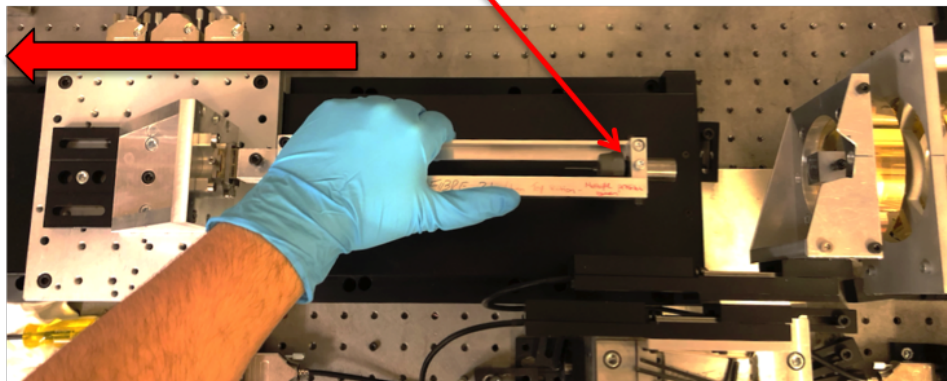
The fibres were extracted from the pulling machine by running the feed mirror past the cartridge chuck holder. This is shown in figure 6.4 This allows for enough space to install the cartridge struts to each chuck. The grub screws that hold the chucks in place in their holders were then loosened and the LabVIEW program was stopped. As previously mentioned, when there was no power going to the pulling stage, it is free to move. This allows for easy extraction of the cartridge as the pulling stage could be slid to the far end of its path and the cartridge could slide out of the holders. The end that was designated as the top end of the cartridge was assigned to the end of the fibre that was produced last. This orientation was kept constant through the remainder of the chapter. The fibres were then stored in a modified non-powered freezer, shown in figure 6.5. This was used as it was a sealed room temperature storage container that could be modified inside to house shelves that the cartridges could sit in. The bottom tray was filled with desiccant to minimise humidity in the container.

Feed mirror moved all the way to the face of the conical mirror holder to allow removal of cartridge

Grub screws loosened to release cartridge



Pulling stage moved to the left to pull the right side of the cartridge out the holder



Cartridge can then be pulled out of pulling stage holder

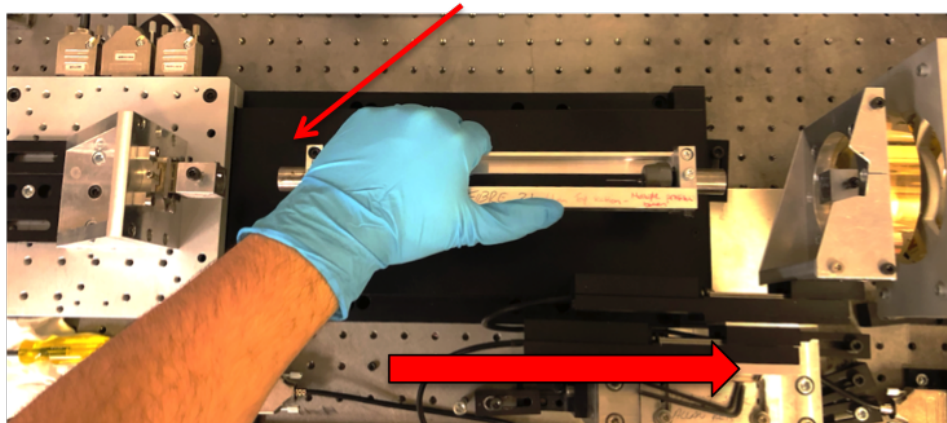


**Figure 6.4:** The extraction process of a fibre cartridge from the pulling machine.

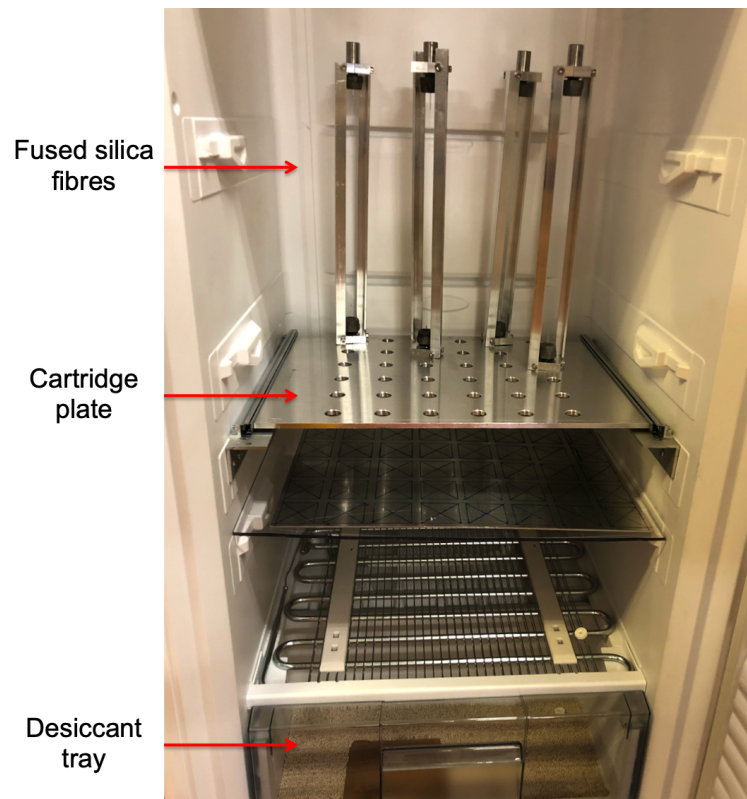


**Figure 6.5:** Fibre storage that was used for the fibres investigated in this chapter. The bottom tray was filled with desiccant to reduce the humidity within.

### 6.3 Experimental set-up

The experimental set-up for this investigation was based on the configurations that were used in chapter 4 and in the research carried out in parallel by Dr Lee [92]. An illustration of the set-up is shown in figure 6.6. A fibre was housed in an enclosure, shown in figures 6.7 and 6.8, with a mass attached to one end and the other end fixed to the roof of the enclosure. This enclosure helps minimise any chance of dust touching the fibre while it was under tension during the investigation. A universal joint was attached to the end of a M10 screw that has been shaved on two opposite sides, as shown in figure 6.7. This screw sits in a slot that has been milled out of the top plate, which was attached to one half of the enclosure. The height of the screw could therefore be adjusted by turning the nuts on either side of the plate without the screw physically turning. This was set prior to the fibre being installed by taking into consideration the length of the cartridge and how much room was needed for the mass installation jig, which will be described later in this subsection. The top end of the fibre cartridge was then slotted into the universal joint. The universal joint was used to ensure that the fibre chuck, and therefore the fibre, will be sitting perpendicular to local gravity. The chuck was then held in place with a grub screw on the side of the universal joint.

Two micro-switches connected in parallel sit at the bottom of the enclosure with a platform connecting the two levers on the switch, as shown in figure 6.6. The platform was attached to

the two levers with superglue to ensure it stays attached when the mass falls. These switches were attached to a right angle bracket which was attached to the same half of the enclosure as the top plate. When the fibre fails, the mass will fall and hit the platform that was connected to the levers on the switch. This then sends a signal to a program on a Raspberry Pi [175]. This program was a modified version of one that was used in Dr Lee's investigation [92] to allow for more switches to be controlled for multiple enclosures. The two halves of the enclosure were attached to each other through two metal attachment plates on each side of the enclosure. These four plates were then held in place with M4 screws that screw into tapped holes on the enclosure halves. A small cut out was made at the bottom of the enclosure to allow exit of the timer switch wires that go to the Raspberry Pi.

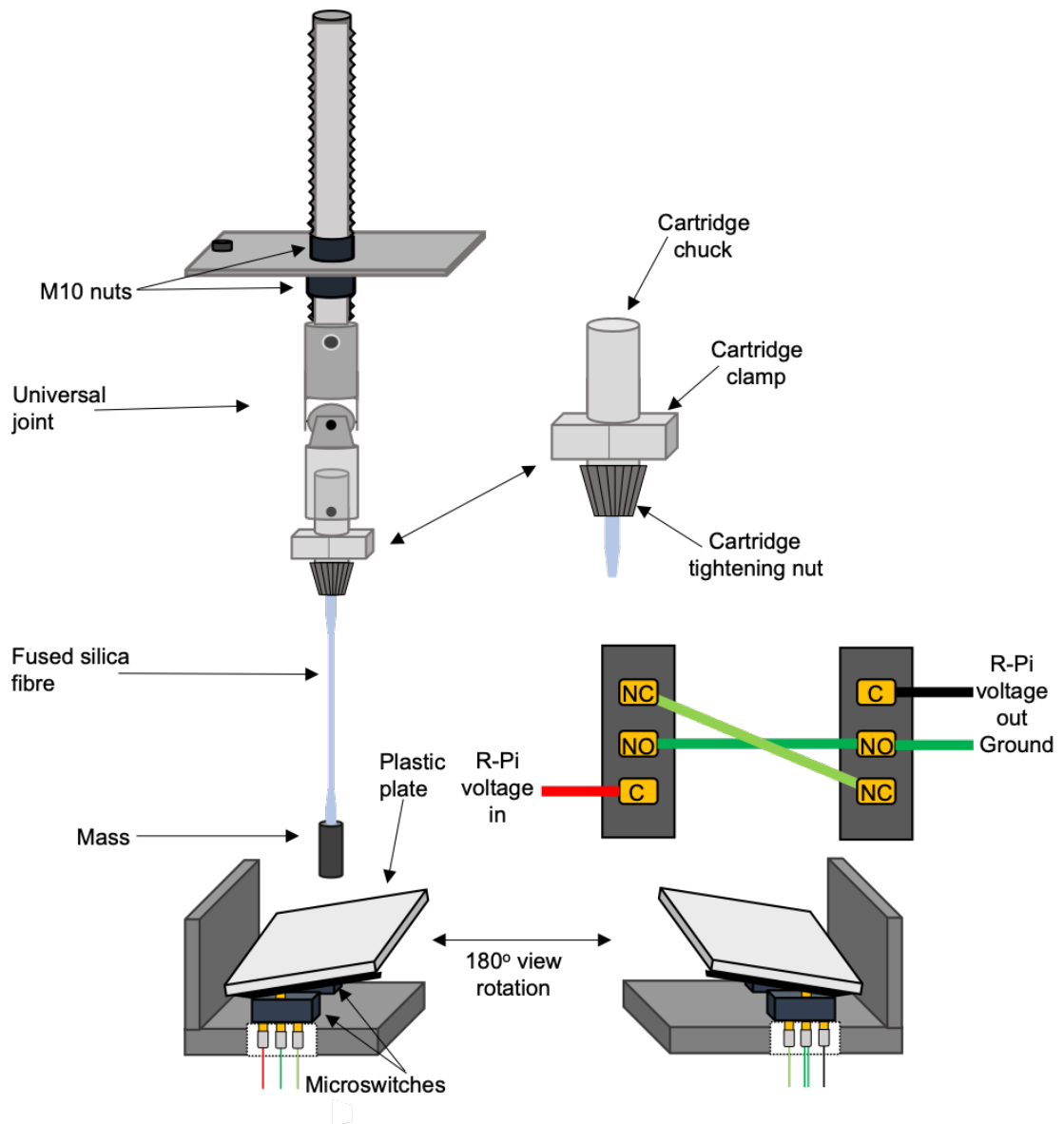


**Figure 6.6:** The experimental set-up that was used to carry out the stress fatigue investigation in this chapter. The two switches that were connected to the Raspberry Pi were connected together in parallel so that the timer recording was triggered when either switch was pressed.

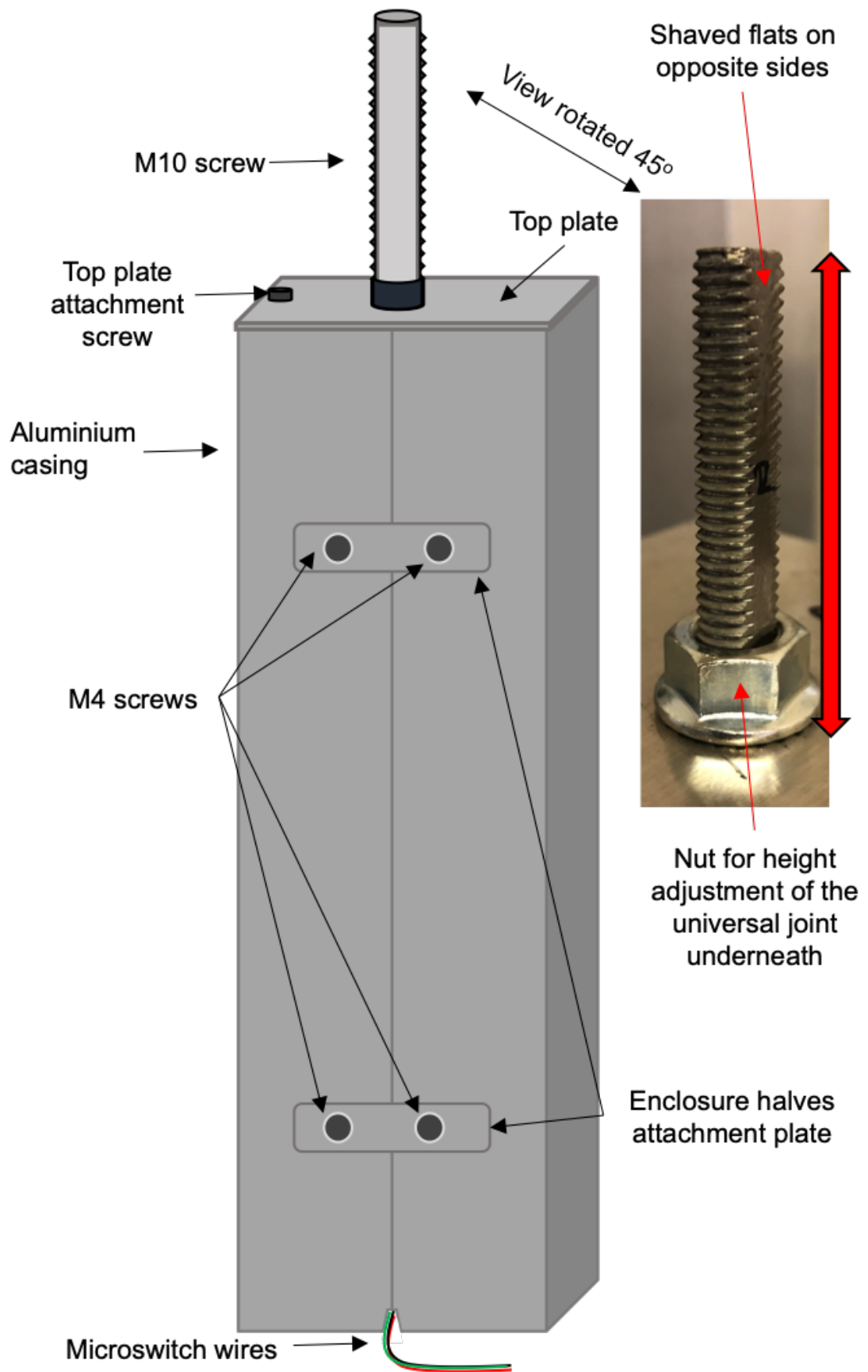


**Figure 6.7:** The closed enclosure used in this investigation. Photo inset: Shaved screw used to adjust the height of the universal joint within the enclosure.

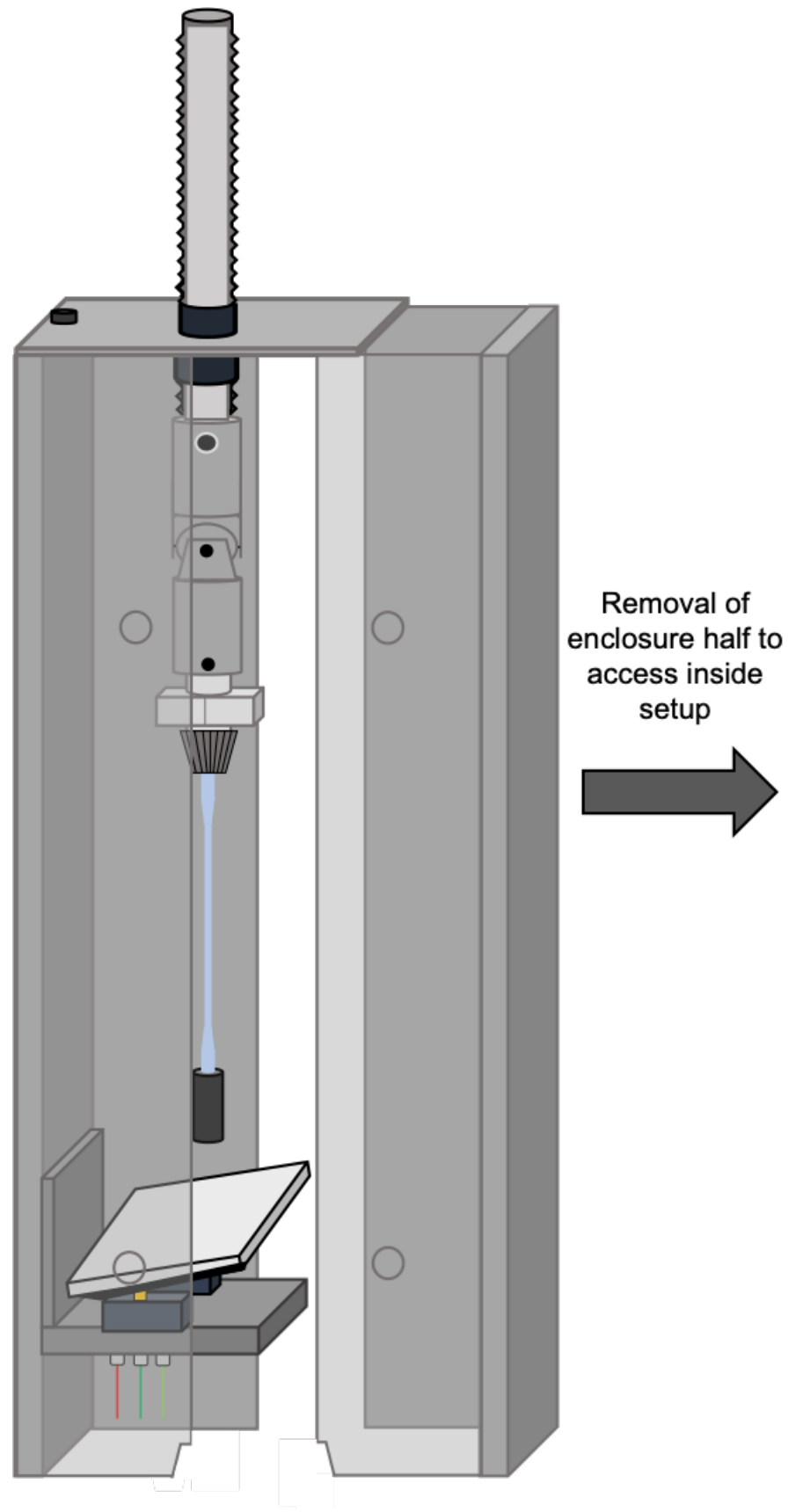


**Figure 6.8:** An open view of the enclosure showing the internal layout, and indicating how one half of the enclosure comes apart from the other half.

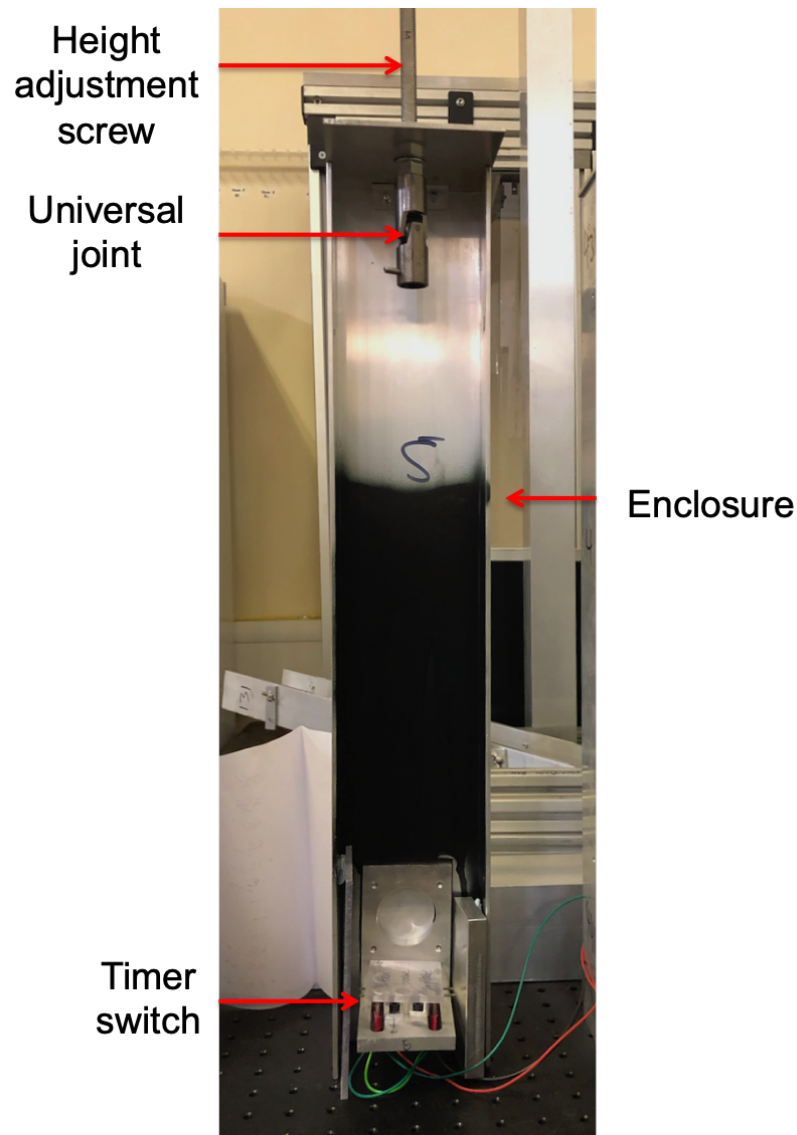


**Figure 6.9:** The inside of the enclosure that was used to enclose the fibres in this investigation. Note that the black paint allowed for the fibre to be easily seen as the reflective metal background cause difficulty.

As the fibres used in this investigation required extreme care and caution to firstly free the bottom of the fibre from the bottom chuck, and to secondly attach the mass, without damaging the fibre in the process, a mass installation jig had to be developed. This jig had to securely hold the bottom stock of the fibre in place so that the removal of the bottom chuck could be carried out. It then also had to be able to securely hold the mass that would be attached to the fibre for installation. Finally, it needed the ability to lower the mass and for the jig to be removed from the enclosure space in a controlled manner. The final design of the mass installation jig is shown in figure 6.10. It comprises of a vertical Bosch strut attached to a 5 cm adjustable horizontal translation stage. Figure 6.11 shows a walk-through of how the masses were installed to the fibres.

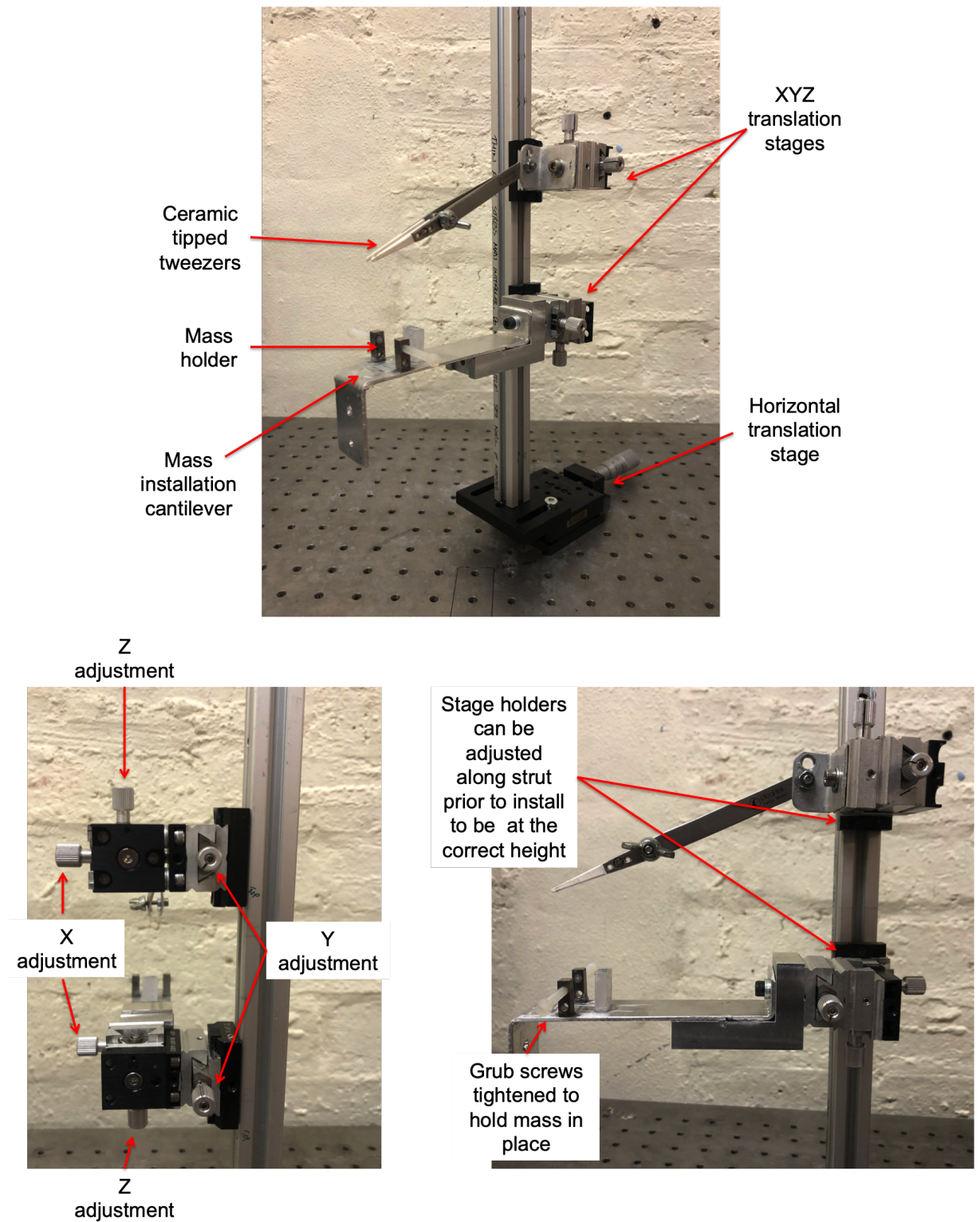


**Figure 6.10:** Top: The mass installation jig used to remove the bottom chuck and to install the mass to the bottom stock of the fibre. Back (bottom left) and side (bottom right) view of the mass installation jig showing the XYZ adjustments that were available. The position of the holder for both stages could be set prior to installation and moved along the strut they were attached to.

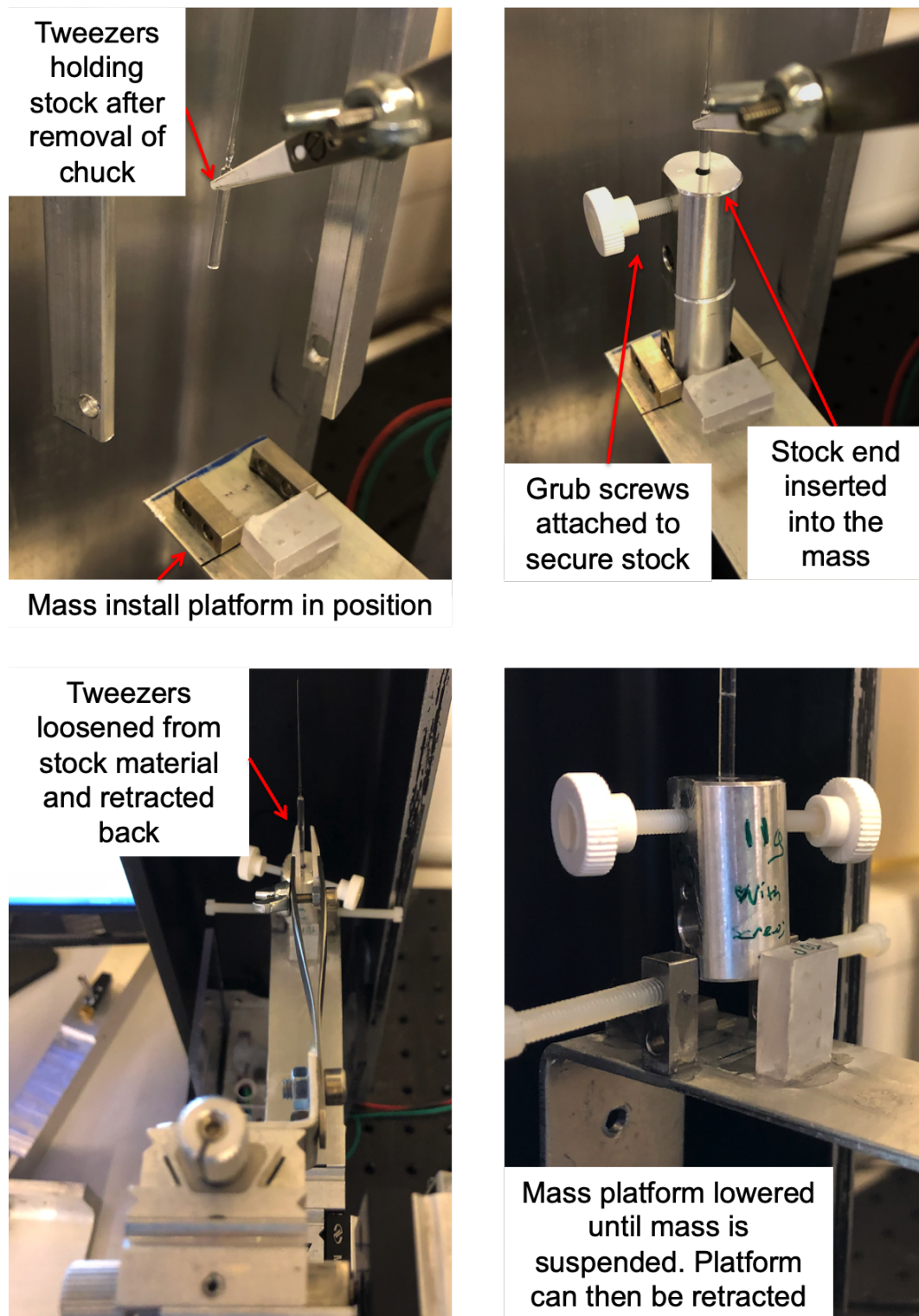


**Figure 6.11:** Top left: Tweezers moved into position and tightened to secure the bottom stock as the chuck was removed from the stock. Top right: Mass installed by inserting stock into hole in mass. Stock secured in place by inserting and tightening grub screws on opposite sides. Bottom left: Tweezers loosened and retracted once mass was secured to the stock. Bottom right: Mass platform lowered until mass was suspended. The platform could then be retracted.

Two XYZ translation stages were attached to the vertical strut. The top XYZ translation stage has ceramic tipped tweezers attached to it [176]. The ceramic tips have a 2 mm groove carved into them. These grooves allow the tweezer to grab the fused silica stock and to securely hold it in place by tightening the nut on the tweezers. The bottom XYZ translation stage has a removable cantilever that could securely hold the mass to be installed securely in place. The reason this cantilever was removable was because it would be in the way of the bottom chuck during removal. Once the tweezers were in place and attached to the stock, the nut on the bottom chuck was loosened with care to ensure no movement of the chuck during this process. Once loosened, the screws attaching the cartridge struts were removed from the bottom clamp. This process was carried out by hand where one hand was holding the bottom chuck while the other hand loosens and removes the screws. Once the bottom chuck was free of the cartridge struts, the stock could slowly be removed from the chuck by gently bringing the chuck down. The stock should not move as it was held securely by the tweezers, but care should be taken to ensure no movement of the stock was occurring during this process. Once the chuck was removed, the cartridge struts could then be fully removed by removing the top screws. The cantilever could then be installed onto the bottom XYZ translation stage.

The cantilever has a block attached to it with grooves that align with the holder on the XYZ translation stage, allowing for easy removal and attachment. At the end of the cantilever was a holder for the masses that were attached to the fibre. The holder consists of two metal blocks with a M4 tapped hole in each. These holes house grub screws that could be tightened by hand to secure and release the mass.

The horizontal translation stage sits on top of a vertical jack to allow for additional vertical adjustments. When the mass was attached to the fibre, the tweezers could be released from the stock and retracted away from the stock through the XYZ translation stage. The XYZ translation stage holding the mass could then be lowered until the mass was suspended by the fibre. If this adjustment isn't enough, then the vertical jack could be lowered until the mass was suspended. Once suspended, the horizontal translation stage could be retracted all the way and the vertical jack holding the installation jig could be removed. The front half of the enclosure was then slid into position, and attached to the other enclosure half. A viewport in the front half of the enclosure allows for inspection of the fibre within the enclosure.

For the fibres that were approximately 10 $\mu\text{m}$  in diameter, the masses that were attached were modified aLIGO fuse ends. A 2 mm hole was drilled into the bottom of the fuse end, with two M3 tapped holes in the side for grub screws to feed into. For the fibres that were 20 $\mu\text{m}$  in diameter, they were sufficiently thick at the bottom cartridge chuck could be used as a mass. In this case, the mass holder at the end of the cantilever was not necessary and was instead used as a platform to hold the chuck in place. In both cases, as there was a stress range of 3-5 GPa that was to be investigated, several different masses were used to fill in different stress values. These masses ranged between 11.5 g to 209.0 g. Each mass though was based on either using the fuse

end or the bottom chuck as its core. Figure 6.12 shows two modified masses. On the left was a modified fuse end with washers used to add weight. On the right, a plastic ring that could slot over the bottom chuck with additional washers was used to add weight. All masses used were weighed prior to installation and after fibre failure. The first weighing was to give an estimate of the stress that the fibre was under during the test. The second weighing was to give a final value of the weight that was attached to the fibre to include the fused silica stock that was still intact. The fuse end masses were weighed using a RS 10 g calibrated scale [177], and the chuck masses were weighed using a Beetle B218D-6 scale. These scales have uncertainties of 0.001 g and 0.5 g, respectively.

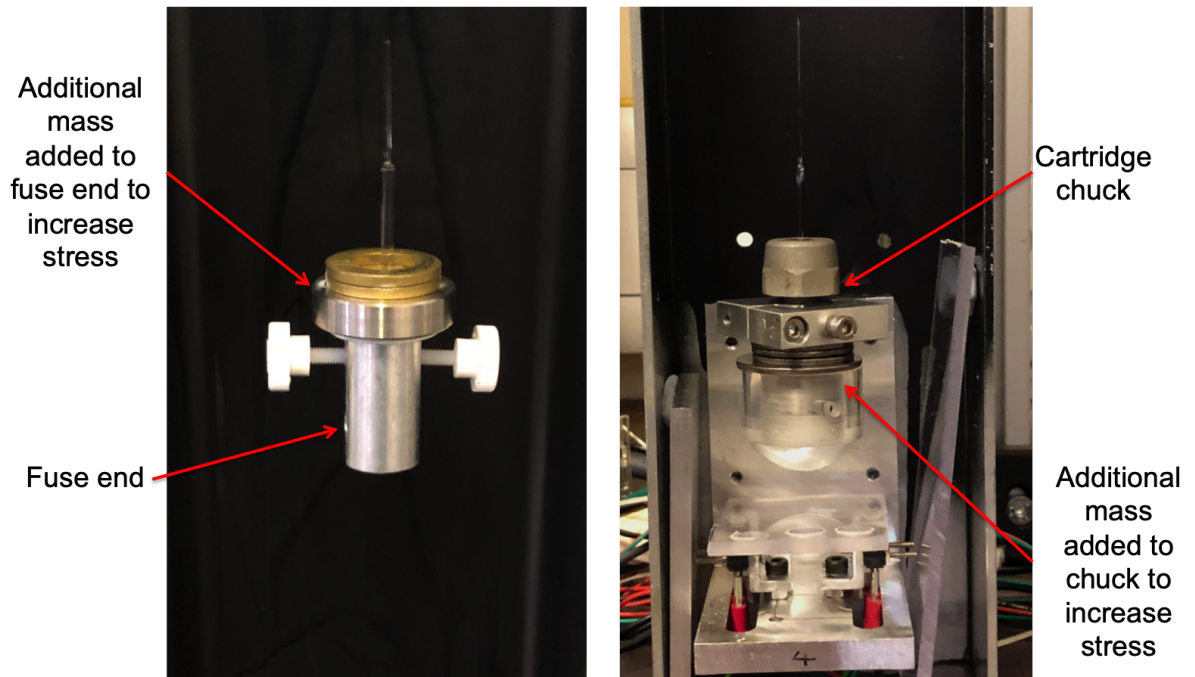


**Figure 6.12:** The two types of masses that were used during this investigation. Additional modifications were made to change the mass.

## 6.4 Results

### 6.4.1 First stage pull down

Figure 6.13 shows the profile of the first stage pull down for the 10  $\mu\text{m}$  velocity profiles that was used in this investigation. Figure 6.14 shows the result of the fibre pulled from the first stage pull down. This first stage creates the stock material that will be used for the second stage pull down to create the final fibre. The second stage pull down was pulled from the highlighted region in figure 6.13, which has an approximate diameter in that region between 480-520  $\mu\text{m}$ . The laser controller during the first stage was set to the maximum 95% duty cycle. It can be seen in figure 6.13 that the first stage pull down has a similar bump artefact that occurred previously in fibres that were investigated in chapters 3 and 4. As the second stage pull occurs at the opposite end of this region, this was not an issue that had to be taken into consideration.

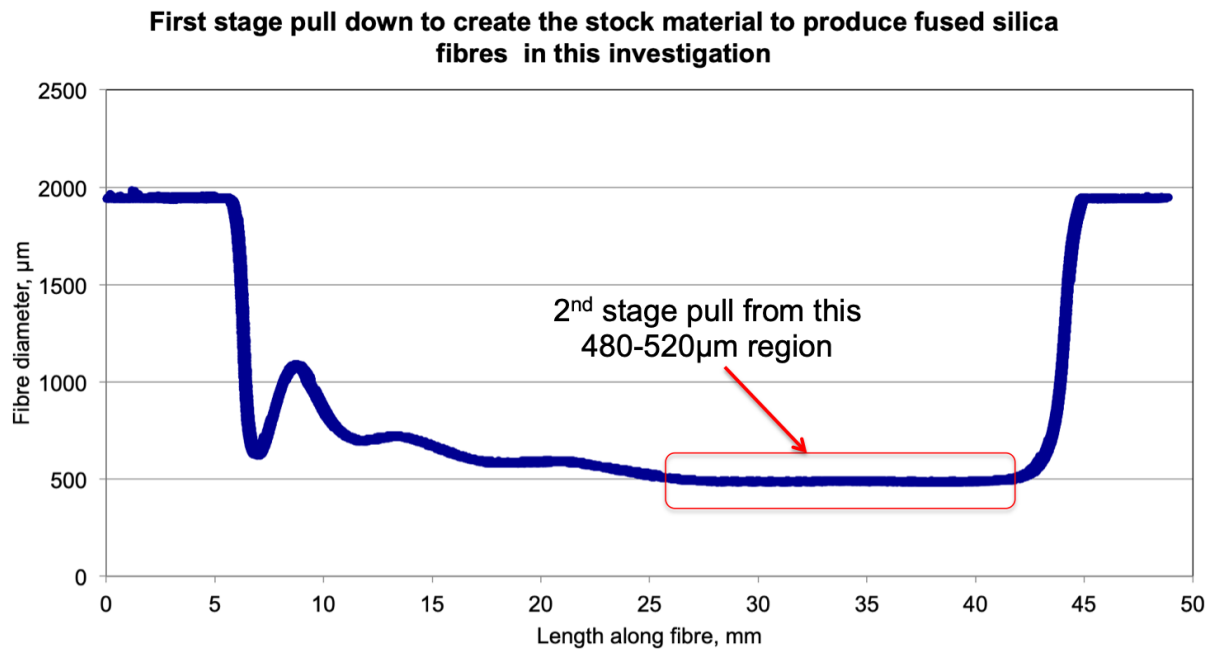


**Figure 6.13:** Profile of the first stage pulldown for the 10  $\mu\text{m}$  velocity profile. The first stage pulldown for the 20  $\mu\text{m}$  was the same, except that the final length was longer.

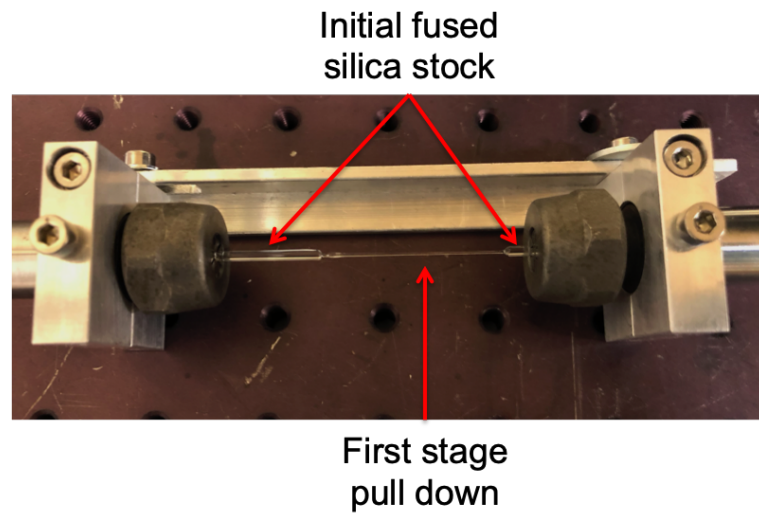


**Figure 6.14:** The first stage pull down from which the final fibre was pulled, held in a fibre cartridge.

#### 6.4.2 10 $\mu\text{m}$ velocity profile fibre batch

As mentioned previously, the velocity profiles shown in tables 6.1 and 6.2 were designed to produce fibres that had a diameter of approximately 10  $\mu\text{m}$ . Figure 6.15 shows an example of a profile of a fused silica fibre that was taken with magnification set to  $\times 24$ . This magnification was chosen as it was sufficiently high to image the thin section of the fibre. This however results in the rest of the fibre (stock and taper region of both necks) being too thick to profile. This was not problematic as the diameter difference was too large to have any major contribution. Figure 6.16 shows the minimum diameter values of all the fibres that were tested that were produced using the 10  $\mu\text{m}$  velocity profile.

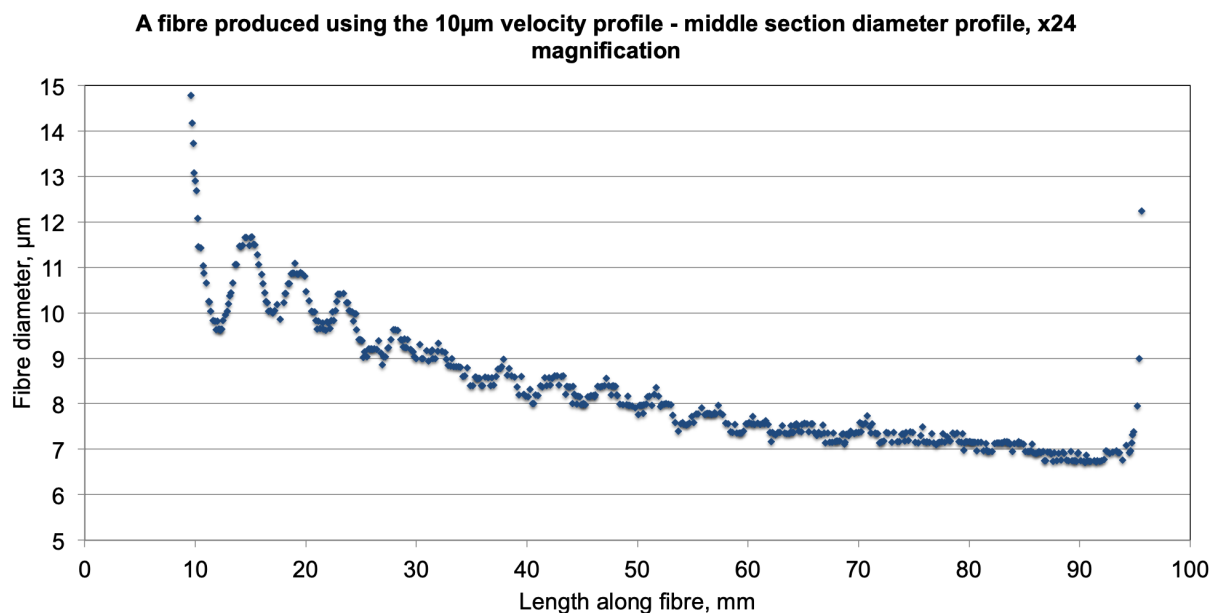


**Figure 6.15:** A fibre profile of a fibre that was produced with the 10  $\mu\text{m}$  velocity profile. Note that only the thin middle section was shown due to the high magnification that was used.

It can be seen in figure 6.15 that the fibre diameter seems to follow an oscillating ring down in the fibre diameter. This could potentially be due to the stability of the viscous molten fused silica during the start of the pull where a large amount of force was being applied to the stock. This will be discussed in section 6.5.

### Fibre diameters using the 10 $\mu\text{m}$ velocity profile

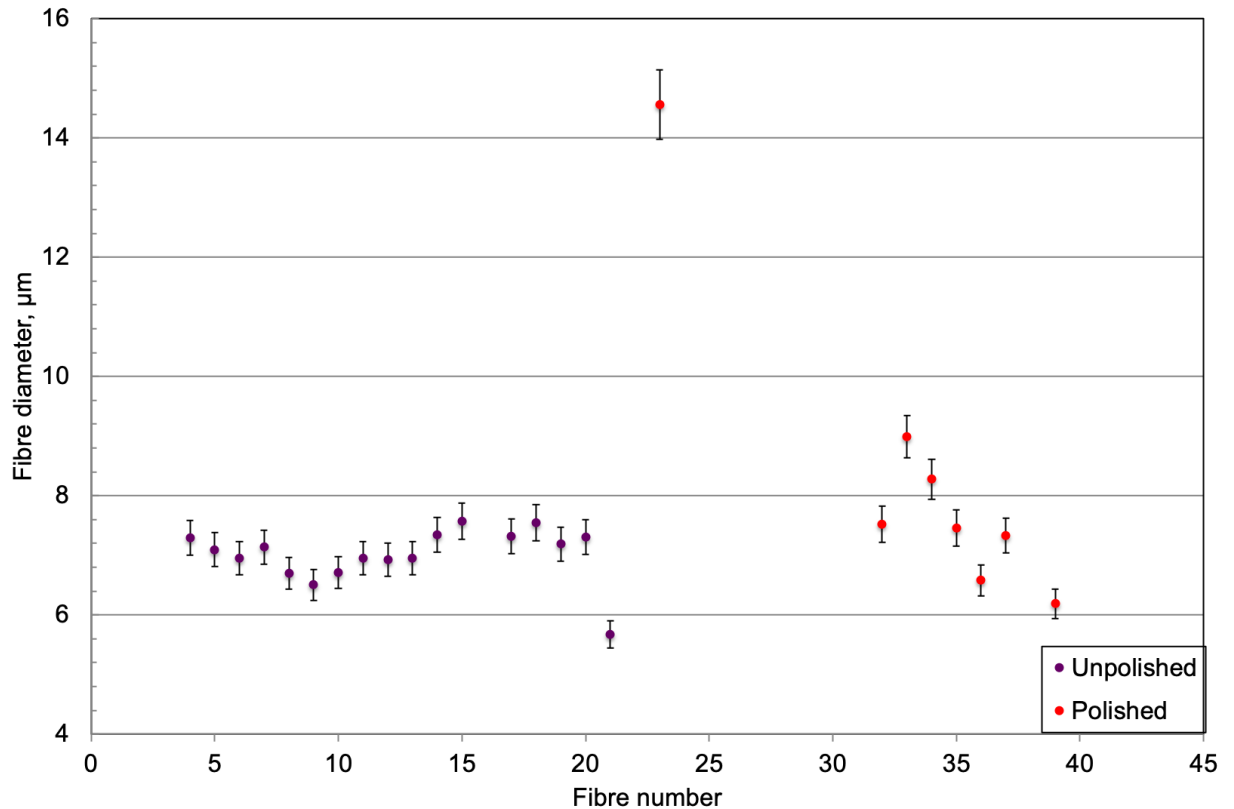


**Figure 6.16:** All minimum diameter values from the non-polished and polished fibres that were produced with the 10 $\mu\text{m}$  velocity profile. Blank spaces in fibre numbers were fibres that were not successfully suspended.

In total, 25 fibres were produced in this investigation. The velocity profile shown in tables 6.1 and 6.2 were designed to produce fibres that had a minimum diameter of approximately 10 $\mu\text{m}$ . Figure 6.16 show that all except 1 fibre that was produced were below 10 $\mu\text{m}$  in diameter. The vertical error bars come from the 3.9% uncertainty that was discussed previously in chapter 5.2.5. The thinnest fibre produced was fibre 21 which had a minimum diameter of  $(5.7 \pm 0.2) \mu\text{m}$ . Due to the minimum diameter being so small, this fibre could not be tested as no mass was available that was sufficiently small enough. The minimum diameter would be located towards the end of the top end of the fibre. This was the end of the fibre that was produced last during the production process. Fibre 23 was the only fibre that did not have a minimum diameter under 10 $\mu\text{m}$ , with a diameter of  $(14.6 \pm 0.6) \mu\text{m}$ . This was due to the fact that the wrong feed mirror velocity was set during the second stage pull. It should be noted that all the fibres produced

above were thinner than the fibres that were tested by Proctor [131].

16 of the 25 fibres were not polished. The remaining 8 fibres that were polished were polished according to the process in section 6.2.2. The limited number of polished fibres that were produced was due to the polishing process vapourising initial stock material. There were many attempts to produce polished fibres with the velocity profile in this section, but reliable production could not be achieved. It was possible that the addition of a laser stabilisation system, similar to that installed on the aLIGO pulling machine [92] could improve the reliability of producing polished fibres with the above velocity profile.

The experimental set-up for fibres in this subsection is shown in figure 6.17. Figure 6.18 shows the stress values that were tested within this section. The data from Proctor [131] is also shown in this figure. The stress range investigated for non-polished fibres was  $(2.5 \pm 0.1) \rightarrow (3.4 \pm 0.1)$  GPa. The stress range investigated for polished fibres was  $(2.7 \pm 0.1) \rightarrow (4.4 \pm 0.2)$  GPa. The uncertainty value for the calculated stress was a combination of the profiler uncertainty when calculating the area cross section at the minimum diameter and the uncertainty in the weighing scales mentioned in section 6.3. The uncertainty in the time was taken as the average human reaction time of 0.2 seconds [141]. This was because all the micro-switches of the enclosures were connected to the Raspberry Pi and controlled through the same timer program, and not through individual programs. A timer on a separate computer screen was set up next to the enclosure to note the time the mass was suspended. The time that was noted down was the start time for that enclosure. The time between the separate computer and the Raspberry Pi was synchronised.

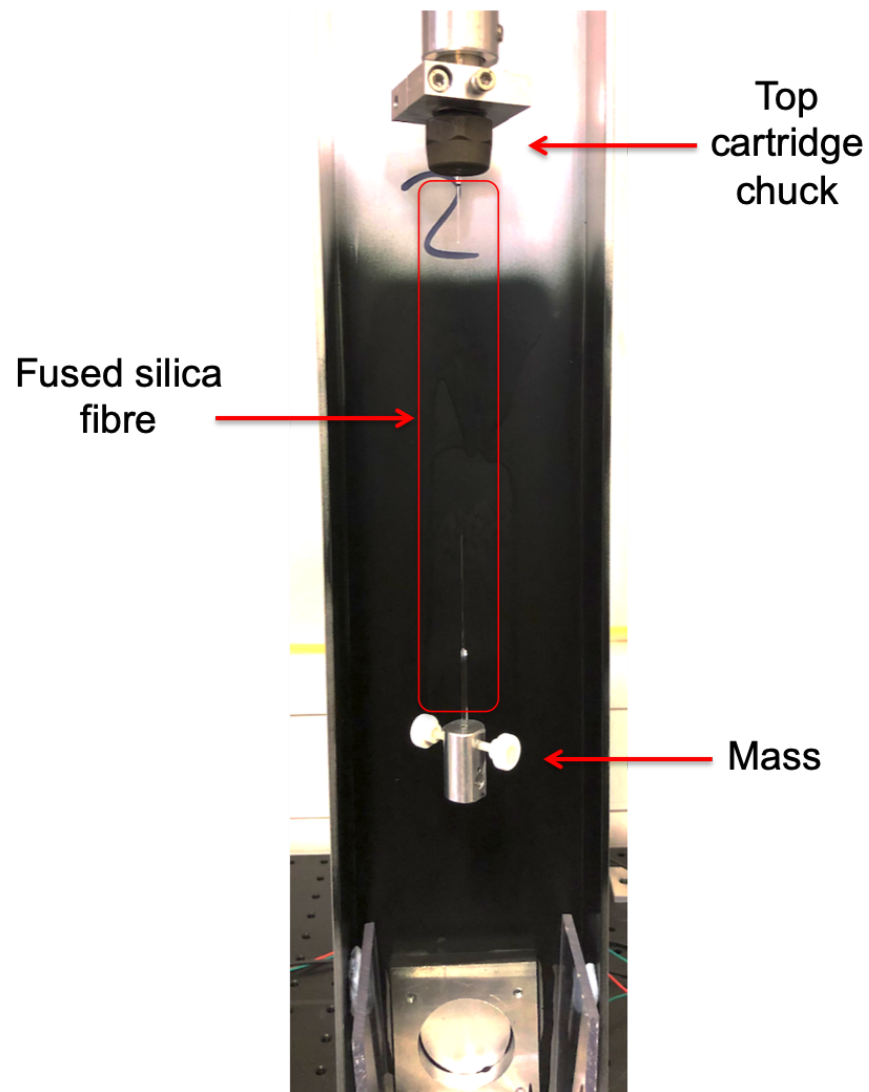


**Figure 6.17:** A fuse end mass suspended on a fused silica fibre. The front of the enclosure was then attached to ensure the fibre was protected from the surrounding environment.

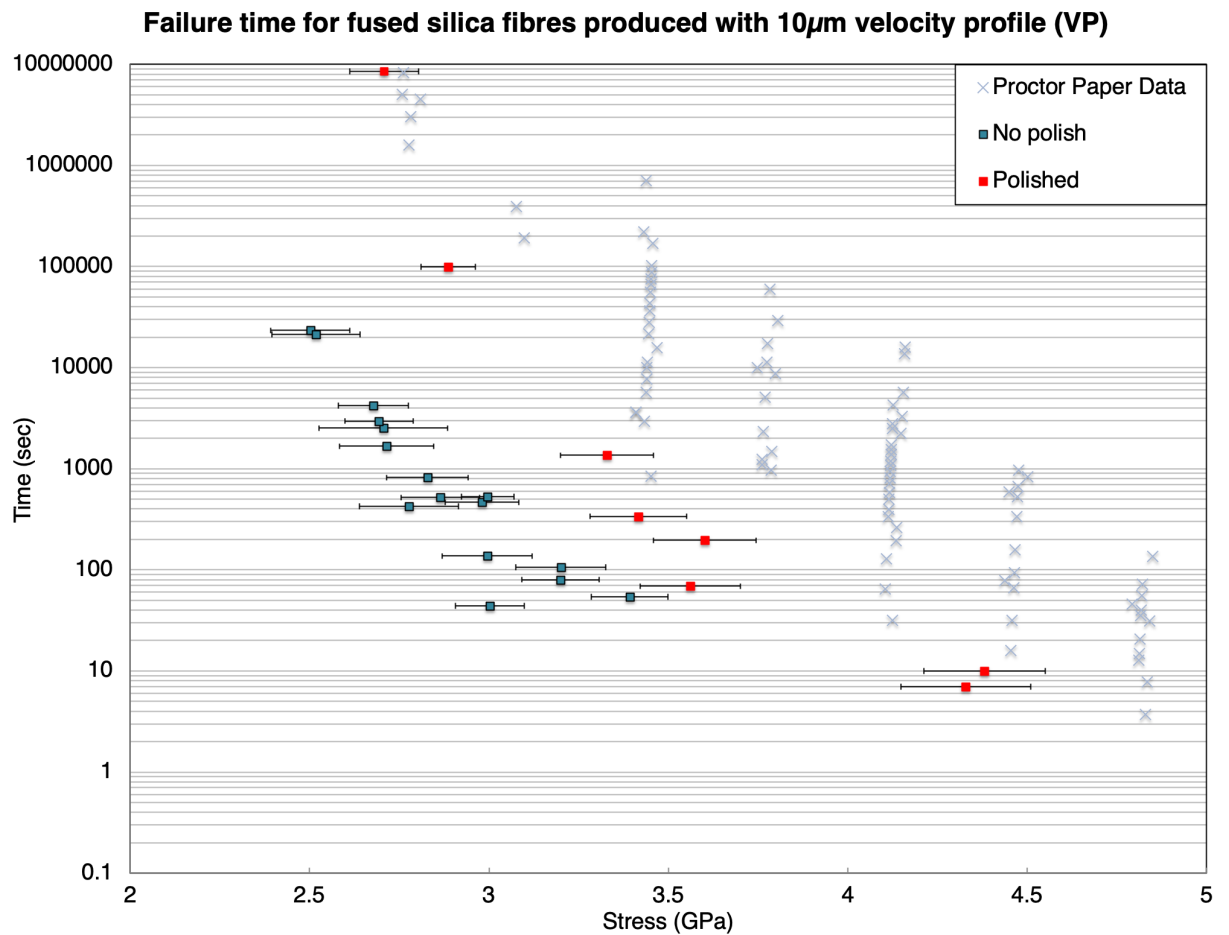


**Figure 6.18:** The failure time of the fibres that were produced using the 10 $\mu$ m velocity profile under a range of stresses.

### 6.4.3 20 $\mu$ m velocity profile fibre batch

The previously mentioned velocity profiles in tables 6.3 and 6.4 were used to produce fibres that had a diameter of approximately 20 $\mu$ m. Figure 6.19 shows the diameter profile from a fibre that was produced using this velocity profile. It can be seen that there is a dip artefact at approximately 15 mm along the length of the profile that appeared in the LHO fibres in chapter 4. This region was where the minimum diameter of the fibre would be for the fibres in this section. This was in contrast to the fibres discussed in section 6.4.2 that had the minimum diameter occur towards the top end of the fibre. Figure 6.20 shows the minimum diameter values of all fibres that were produced using the 20 $\mu$ m velocity profile.

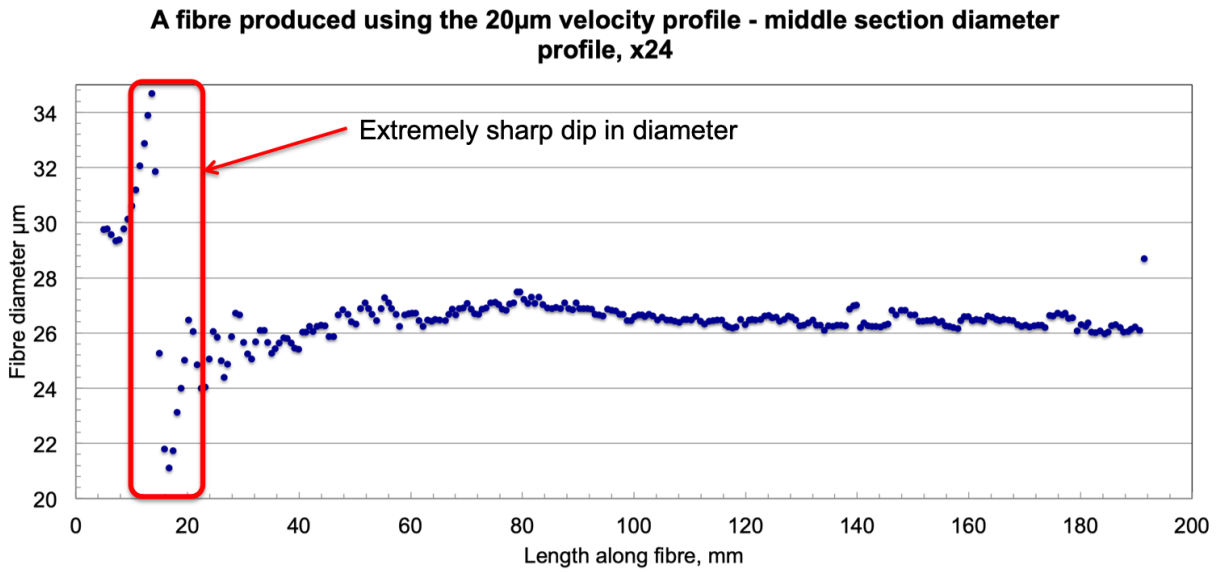


**Figure 6.19:** A fibre profile of a fibre that was produced with the 20µm velocity profile. Note that only the thin middle section was shown due to the high magnification that was used.

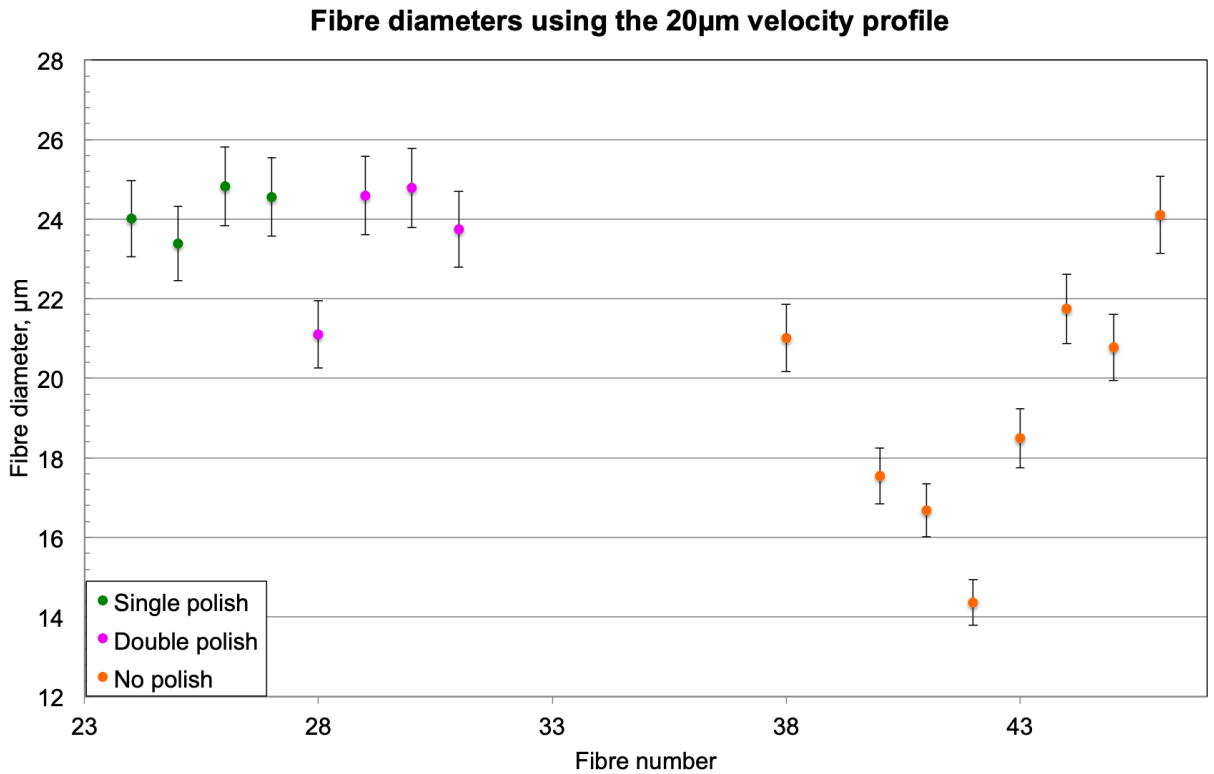


**Figure 6.20:** All minimum diameter values from the non-polished and polished fibres that were produced with the 20µm velocity profile. Blank spaces in fibre numbers were fibres that were not successfully suspended.

In total 16 fibres were tested in this section, including 4 polished and 4 double polished.

The experimental set-up is shown in figure 6.21. The polishing conditions were the same as the fibres in section 6.4.1. In the case of the double polish, the process was carried out twice. The vertical error bars were also the same as that described in section 6.4.2. When considering the three production conditions, the range of minimum diameters that were produced with the 20 $\mu\text{m}$  velocity profile were greater than that produced by the 10 $\mu\text{m}$ , excluding fibre 23 that was previously described. The spread in diameters from the 10 $\mu\text{m}$  velocity profile was 3.3 $\mu\text{m}$ , where as here it was 10.4 $\mu\text{m}$ . The minimum diameter of the fibres ranged from  $(14.4\pm 0.6)\mu\text{m}$   $\rightarrow$   $(24.8\pm 1.0)\mu\text{m}$ . 12 of the 16 fibres were in the same diameter range as that tested by Proctor, which was 20-40 $\mu\text{m}$  in diameter [131]. Figure 6.22 shows the range of stress values that were tested in this section. The error bars shown were the same as calculated in 6.4.2. The stress range that was investigated for these fibres was  $(3.2\pm 0.3)$   $\rightarrow$   $(4.8\pm 0.2)$  GPa.

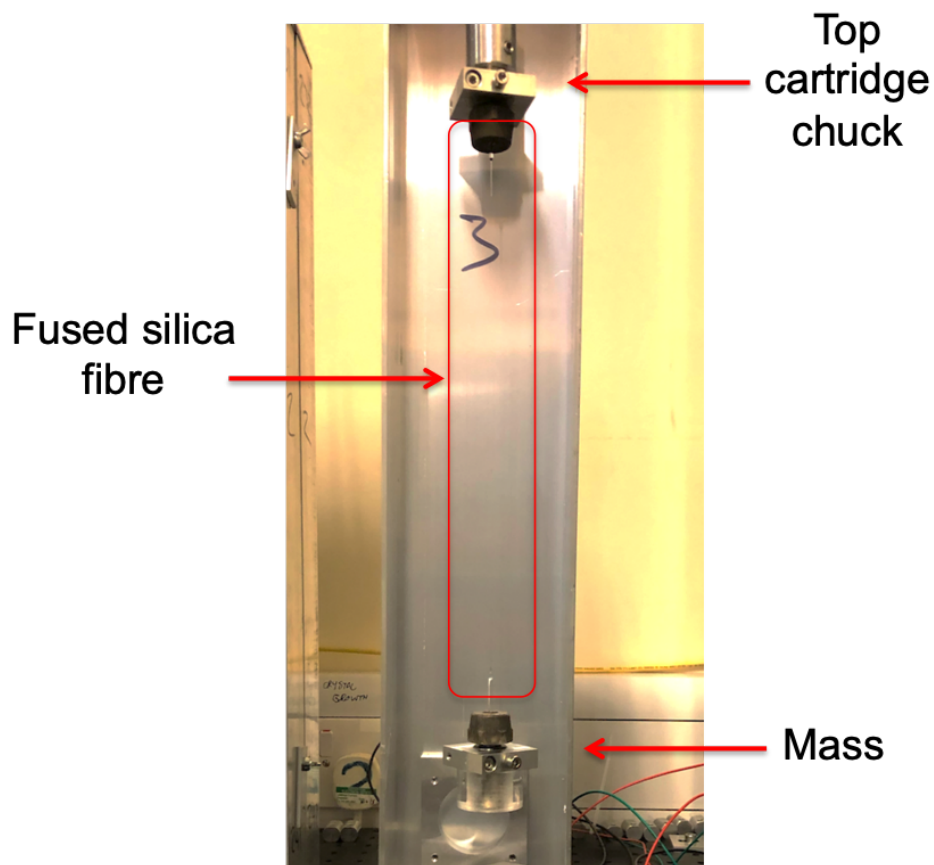


**Figure 6.21:** The experimental set-up for the fibres that were tested in this subsection. Note that the chuck masses were used in this set-up. This was also carried out prior to spray painting the enclosures black, making it difficult to see the fibre in this set-up.

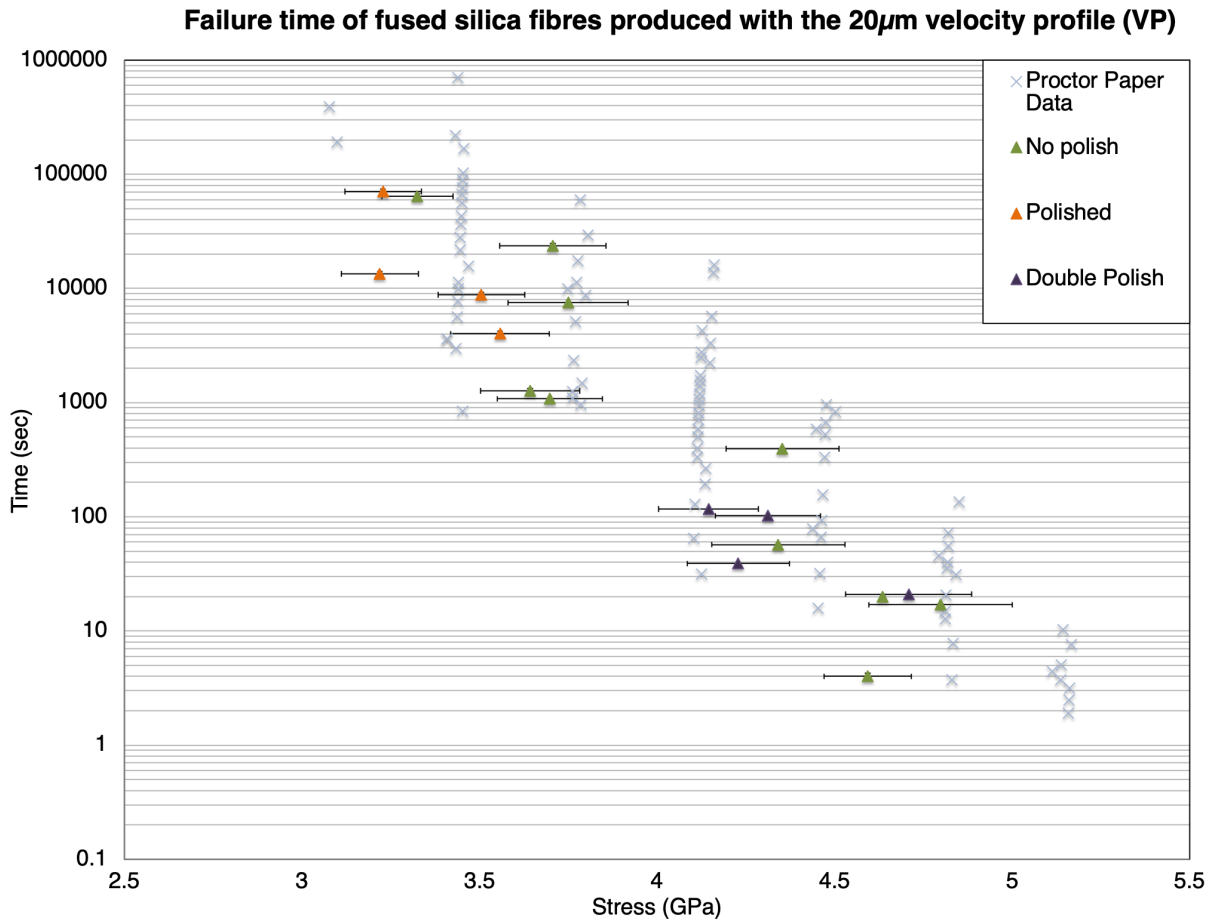


**Figure 6.22:** The failure time of the fibres that were produced using the 20 $\mu\text{m}$  velocity profile under a range of stresses.

## 6.5 Discussion

All fibres produced in this chapter followed the cleaning procedure that was applied to the preparation of fused silica stock material set out for aLIGO production [97]. This means that at no point does the final produced fibre get exposed to additional heat or coating of any material. All polishing that was carried out was only applied to the initial stock material. The location of the minimum diameter point between the two velocity profiles was at opposite ends of the fibre. This could be down to the nature of the velocity profile. In the case of the 10 $\mu\text{m}$  velocity profile, the characteristic fibre shape would be a taper from the start of the pull all the way to the end of the pull, as shown in figure 6.15. For the 20 $\mu\text{m}$  velocity profile, the fibre shape would have a large bump and dip at the start of the pull, before levelling out for the rest of the pull. This resulted in the minimum diameter region being located in this dip region, as shown previously in figure 6.19. As well as a taper, all the fibres from the 10 $\mu\text{m}$  velocity profile also show an oscillation in the fibre diameter along the length of the fibre. This could be seen again in figure 6.15. This oscillation would appear to ring down in amplitude over the length of the fibre. The

cause of this could be from the stability of the viscous molten fused silica during the start of the pull. As the pulling stage was accelerating at a rate of  $20000 \text{ mm s}^{-2}$ , a huge amount of force was pulling on the fused silica stock. As the actual weight of the moving stage was not mentioned in the data sheet [169], an estimated weight of 5 kg would give a force of 100 N being applied to the fused silica stock at the start of the pull. This could potentially cause a shockwave to travel through the stock material. This ring down over the length of the fibre was not shown in figure 6.19, but the same mechanism could be the cause of the large bump and dip artefact previously described. The different velocities used in the velocity profiles, as well as the temperature of the stock material, could also have an impact on the characteristics of the ring down. Changes in the heat distribution around the fused silica could also be a potential source of the oscillation feature of the fibre. There was no aLIGO style laser stabilisation system [92] on the ultra-thin fibre pulling machine, meaning that there could be slight variations in the laser power. This could contribute to the range of minimum diameters that was achieved as it was possible stock material could have been vapoured off at various points during the production process, such as during polishing and during the two stage pulls.

The results shown in figure 6.18 display some notable features. All fibres but one had a minimum diameter under  $10 \mu\text{m}$  in diameter, and all fibres were below the diameters that were investigated by Proctor, but of the same order of magnitude. Non-polished fibres had the biggest differential of failure times compared to Proctor that had been tested so far, sitting 2-3 orders of magnitude lower. There was a noticeable increase in performance when the initial stock material was polished, of up to just under 2 orders of magnitude, but this still resulted in fibres sitting in the low end of the spread obtained by Proctor. Fibre 23 that was previously mentioned to being the thickest fibre in this batch as  $(14.6 \pm 0.6) \mu\text{m}$  was the only fibre that does not follow the trend and sits in the middle of the range of Proctor values.

This suggests that there was potentially a change in material properties for fibres that have a minimum diameter under  $10 \mu\text{m}$ . It has been suggested that there was a surface layer of fused silica with a thickness of  $1 \mu\text{m}$  [178] [179]. It was therefore possible that this indicates the mechanical structure of the surface layer, which in the case for the thinnest fibre tested makes up a significant 35% of the diameter at its thinnest point, has influence on the failure time of the fibre. The polishing procedure is designed such that it removes surface impurities which could potentially be more critical when testing fibres with a diameter under  $10 \mu\text{m}$ . Polishing does not seem to affect the performance of  $10\text{-}20 \mu\text{m}$  diameter fibres, suggesting that the first stage pull down effectively acts as a polishing procedure by producing new stock material. This is an area that could be investigated in the future by trying to locate the diameter at which the transition occurs where the surface layer becomes a more dominant feature in terms of performance and the need for a greater attention to detail when polishing. Further discussions on the breaking stress of these fibres will be presented in the following chapter.

Due to the configuration of the fibre profiler, it was not possible to image the fibre as it tapers

sharply down from the 500  $\mu\text{m}$  stock to the thin middle diameter. It was therefore not possible to determine whether or not there were additional artefacts such as alignment that could potentially have a greater effect at sub-10  $\mu\text{m}$  diameters than at thicker aLIGO diameters. Upgrading the profiler with the suggested improvements from chapter 5.3 could help identify if this could be a contributing factor to the performance of these fibres. The previous upgrade suggestion of a laser stabilisation system on the ultra-thin fibre pulling machine could also increase the probability of producing sub-10  $\mu\text{m}$  diameter fibres with double polishing. Double polishing was not possible with the current set-up as too much material would be vapourised away during the process. A new second stage velocity profile could be developed to compensate for this by running at lower velocities, but this was not pursued due to time constraints. This could be a future area to be investigated.

As there was a small level of improvement in the failure time of the polished fibres previously discussed in figure 6.18, it was interesting to see that polished fibres did not show an improvement in performance in figure 6.22. The polishing process was carried out as previously described with the laser duty cycle set to 80%. Both single and double polished fibres lay among the spread of values obtained for the non-polished fibres. This was in contradiction to previous findings that polished fibres will show an improvement in strength [62] [92] [110]. It was possible that the first stage pull down where new stock material was created from the initial molten region was sufficient enough to replicate the polishing process. Future tests could look into producing these fibres through more than two stage pulls to see if there was any effect. For example, a three stage pull could consist of 2 mm stock material initially pulled down to 1 mm, followed by the 1 mm region being pulled down to 500  $\mu\text{m}$ . The final stage pull to produce the fibre could then be produced from the 500  $\mu\text{m}$  stock. Creating new stock material at each pull down could potentially remove further imperfections that could be within the centre of the stock. Fibres pulled with this velocity profile showed a level of performance that was consistent to that obtained by Proctor, with values obtained filling out a wide range of the spread that was obtained. These fibres also included fibres that sat within the diameter range that was investigated by Proctor (20-40  $\mu\text{m}$ ), as well as going below this down to  $(14.4 \pm 0.6) \mu\text{m}$ . It was encouraging that fibres produced in this investigation that sat in comparable diameter ranges showed performance similar to Proctor when produced with different techniques. This consistency leads to more support suggesting that there was a mechanism that needs to be further investigated that was related to the fibres that were produced with the 10  $\mu\text{m}$  velocity profile to fully understand the difference in performance for fibres with minimum diameters under 10  $\mu\text{m}$ .

A comparison of all of the above data to the values that were found previously in chapter 4 is shown in figure 6.23. From figure 6.23, it can be seen that all the fibres that were not polished and produced from the 10  $\mu\text{m}$  velocity profile fall significantly off the trend of the rest of the results by up to 2 order of magnitudes. The vast majority of data points lie either below, or in the lower region of the spread that was obtained by Proctor [131]. The vast majority of fibres that

were produced with the 20  $\mu$ m velocity profile show a clear increase in performance compared to the LHO results that were obtained. The same brand fused silica, Heraeus, was used, though the LHO fibres had a 3 mm starting diameter instead of 2 mm in this chapter [132]. Proctor's results were obtained with 1 mm fused silica stock from a brand previously known as Thermal Syndicate Limited, namely their product called Vitreosil [180]. It is unknown what iteration of Vitreosil was used during Proctor's tests.

Further investigations could be carried out in vacuum to see how the vacuum performance would compare with that obtained in previously described research [131]. Research carried out at Glasgow has already seen an increase in performance in vacuum compared to in air, following the trend seen by Proctor [92].

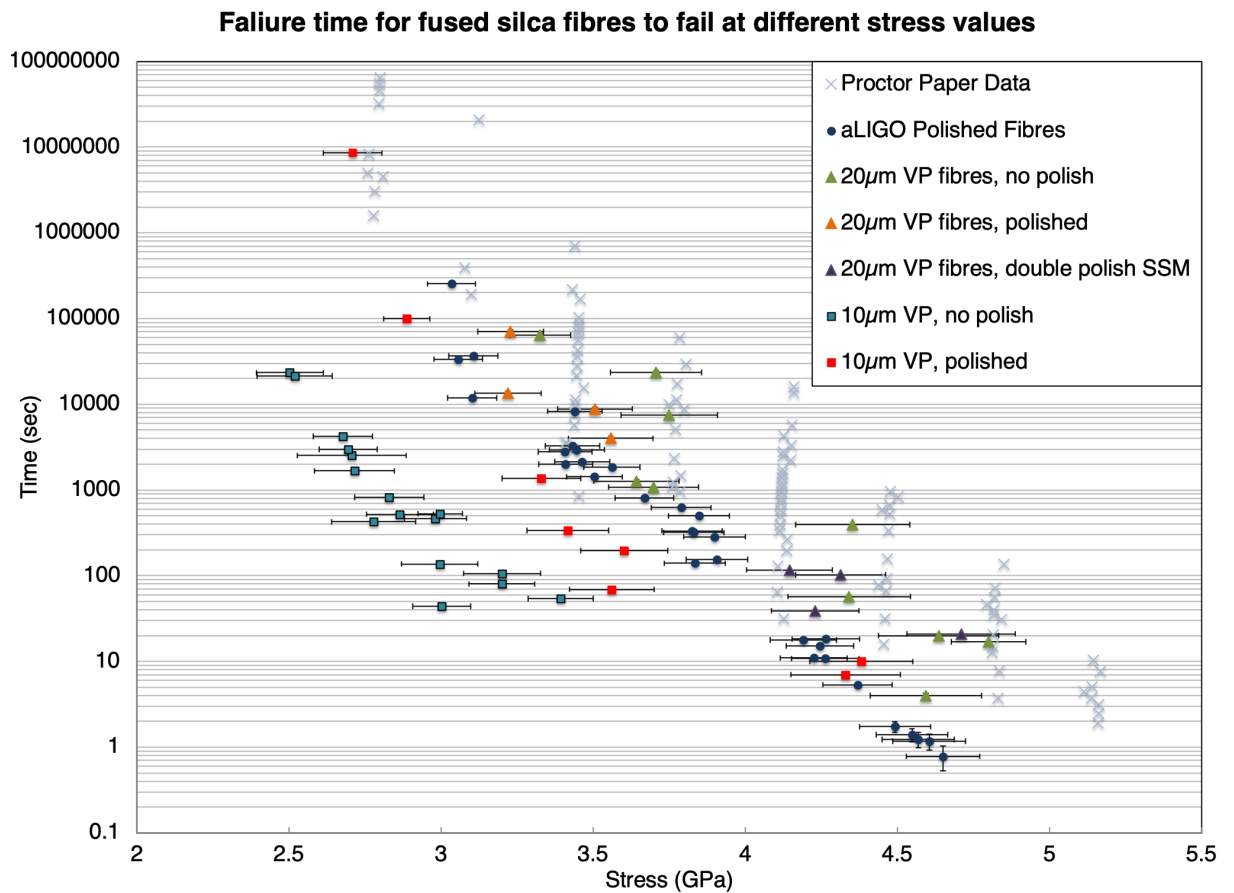


**Figure 6.23:** All stress fatigue data obtained from chapters 4 and 6 compared to the data obtained by Proctor [131]. Shown here were the values obtained from the investigation carried out at LHO, and the fibres that were produced using the 10  $\mu$ m and 20  $\mu$ m velocity profiles (VP) under various polish/non-polish conditions.

## 6.6 Conclusion

The aim of the investigation carried out in this chapter was to expand on the previous research that was carried out on stress fatigue from chapter 4 at LHO and research that was carried out in parallel [92]. The fibres tested in chapter 4 had a diameter range between  $(183.5 \pm 2.4)$   $\mu$ m and

(208.3 $\pm$ 2.7) $\mu\text{m}$ . These fibres, as well as the investigation that was carried out in parallel [92], that were tested had a failure time that was lower than expected when comparing to data obtained by Proctor [131]. It was therefore determined that the next step would be to carry out a similar investigation, but with fibres that lay in the range investigated by Proctor of 20-40 $\mu\text{m}$ . As well as this, fibre diameters below this range was aimed to be investigated as well.

The ultra-thin fibre pulling machine that was previously developed [93] [99] was used to produce a range of fibres to suit the above range conditions. An experimental set-up was then fabricated based on the concept of the previously mentioned research where a mass was attached to a fused silica fibre and suspended. The total hang time was recorded when the mass falls at the point of fibre failure to trigger a timer switch.

Fibres were produced in two main batches through the use of two velocity profiles. The first velocity profile, named "10 $\mu\text{m}$  velocity profile", was created with the aim to produce fibres that had a diameter that was approximately 10 $\mu\text{m}$  in diameter. This velocity profile produced a range between (5.7 $\pm$ 0.2) $\mu\text{m}$  and (14.6 $\pm$ 0.6) $\mu\text{m}$ . These fibres were separated into two sub-batches of polished and non-polished fibres. The second velocity profile, named "20 $\mu\text{m}$  velocity profile" was created with the aim to produce fibres that had a diameter that was approximately 20 $\mu\text{m}$  in diameter. The range of fibres that were produced with this velocity profile had a diameter range between (14.4 $\pm$ 0.6) $\mu\text{m}$  and (24.8 $\pm$ 1.0) $\mu\text{m}$ . These fibres were separated into three sub-batches of non-polished, single polished and double polished fibres.

Of all the fibres tested, the non-polished fibres from the 10 $\mu\text{m}$  velocity profile had the biggest differential to Proctor's data, performing significantly lower than expected. A difference of up to two orders of magnitude was observed for these fibres compared to Proctor's data. Polishing the stock material prior to fibre production did increase the performance of these fibres, but only enough to lay in the bottom range of the spread when comparing the data. Interestingly, there was no improvement in performance observed for single and double polishing for fibres that were produced using the 20 $\mu\text{m}$  velocity profile. All fibres from this batch performed best of all the fibres that had been tested, including from chapter 4, covering a wide range of the spread that was obtained by Proctor. This consistency between the two sets of data show that there must be a mechanism causing the fibres from the 10 $\mu\text{m}$  velocity profile batch to underperform.

Further investigation was decided to be carried out looking to see if this difference between the two main batches of fibres continues for other characteristics associated with the fused silica. The previous chapter described an upgrade that was carried out to the ultra-thin fibre strength tester. Previous research has shown that the Young's modulus could potentially change for fibres under 20 $\mu\text{m}$  in diameter [93]. It is possible this characteristic could be linked to the results obtained in this chapter. With the development of the thin fibre profiler and strength tester described in chapter 4, it was decided that this research should be revisited to decrease the associated uncertainty with the results and to see if there is any significant change in results with the improved characterisation apparatus.

# Chapter 7

## Measuring Young's modulus of sub-20 $\mu\text{m}$ fibres

The results discussed in this chapter were journal peer-reviewed for publication in Classical and Quantum Gravity, volume 35, number 165004, 2018 [99].

### 7.1 Motivation

Previous research carried out by the author [93], and previously described in chapter 5.1, had shown that the Young's modulus of fibres could reach up to  $(106.0 \pm 6.8)$  GPa. This was an increase in the accepted Young's modulus value of fused silica which is 72 GPa [181]. This research was however carried out prior to the development of the thin fibre profiler and upgrades to the thin fibre strength tester from chapter 5. This meant the Young's modulus uncertainties were as high as 16%. The upgrades described in chapter 5 should lower these uncertainties and also provide more consistency with how some measurements, such as profiling and extension of the fibre, were measured.

The Young's modulus is the stress to strain ratio where the stress can be calculated by:

$$\sigma = \frac{F}{A_{xs}} \quad (7.1)$$

where  $\sigma$  is the stress on the fibre at a segment with cross sectional area,  $A_{xs}$ , when a force,  $F$ , is exerted onto it. The strain of the fibre can be calculated by:

$$\varepsilon = \frac{\Delta L}{L} \quad (7.2)$$

where  $\varepsilon$  is the strain on the fibre with length,  $L$ , when it is stretched by length,  $\Delta L$ . The Young's modulus is therefore:

$$Y = \frac{FL}{A_{xs}\Delta L} \quad (7.3)$$

where  $Y$  is the Young's modulus.

The goal of the investigation in this chapter was to compare results previously obtained through the old experimental set-up with those obtained through the newly developed set-up to minimise the uncertainty values obtained. Due to the difference in failure time of the fibres that were under 10 $\mu\text{m}$  in diameter that were tested in the previous chapter, it was decided that it would be interesting to investigate if fibres under 10 $\mu\text{m}$  in diameter would show a difference in performance to those greater than 10 $\mu\text{m}$  in diameter.

## 7.2 Experimental set-up

To investigate the Young's modulus of fibres, an experimental set-up that could record the stress applied to the fibre, as well as the stretch of the fibre was needed. All fibres produced in this chapter were produced using the ultra-thin fibre pulling machine, as used in chapter 6 [99]. The upgrades to the strength tester previously described in chapter 5 were carried out specifically with this investigation in mind. Previous research into the Young's modulus of sub-100 $\mu\text{m}$  fibres were carried out prior to the installation of these upgrades [93] [164]. These investigations would measure the stretch of the fibre through measuring the position change of the motorised stage using a digital caliper. The use of digital calipers to measure the extension resulted in an additional human uncertainty that would have to be considered when it came to the position of the calipers. This would be in combination to the  $\pm 0.3$  mm uncertainty that is already associated with the calipers. The calipers would have to be positioned in exactly the same place and held perfectly parallel to the drive rods on the strength to measure the extension of the fibre accurately. The addition of a magnetic encoder to the set-up ensures that the position of the motorised stage would be read from exactly the same position throughout the entire pulling process. Position readings could also be taken continuously through each fibre test instead of periodically, which was the case in the previous research [93].

The addition of reading the load cell digital readout through the LabVIEW program helps to locate the exact point of the motorised stage where the fibre is no longer slack, and begins to take up the tension. This is necessary, as the fibre is installed into the clamps while slack to minimise any accidental stretching within the clamps prior to the LabVIEW program starting. Previously, the digital readout was read from the front of the control unit. The program would then have to be stopped to measure the position of the stage. As both the encoder and the load cell were read into the new LabVIEW program, the load cell data could be plotted against the position data to locate the point at which the fibre begins to stretch.

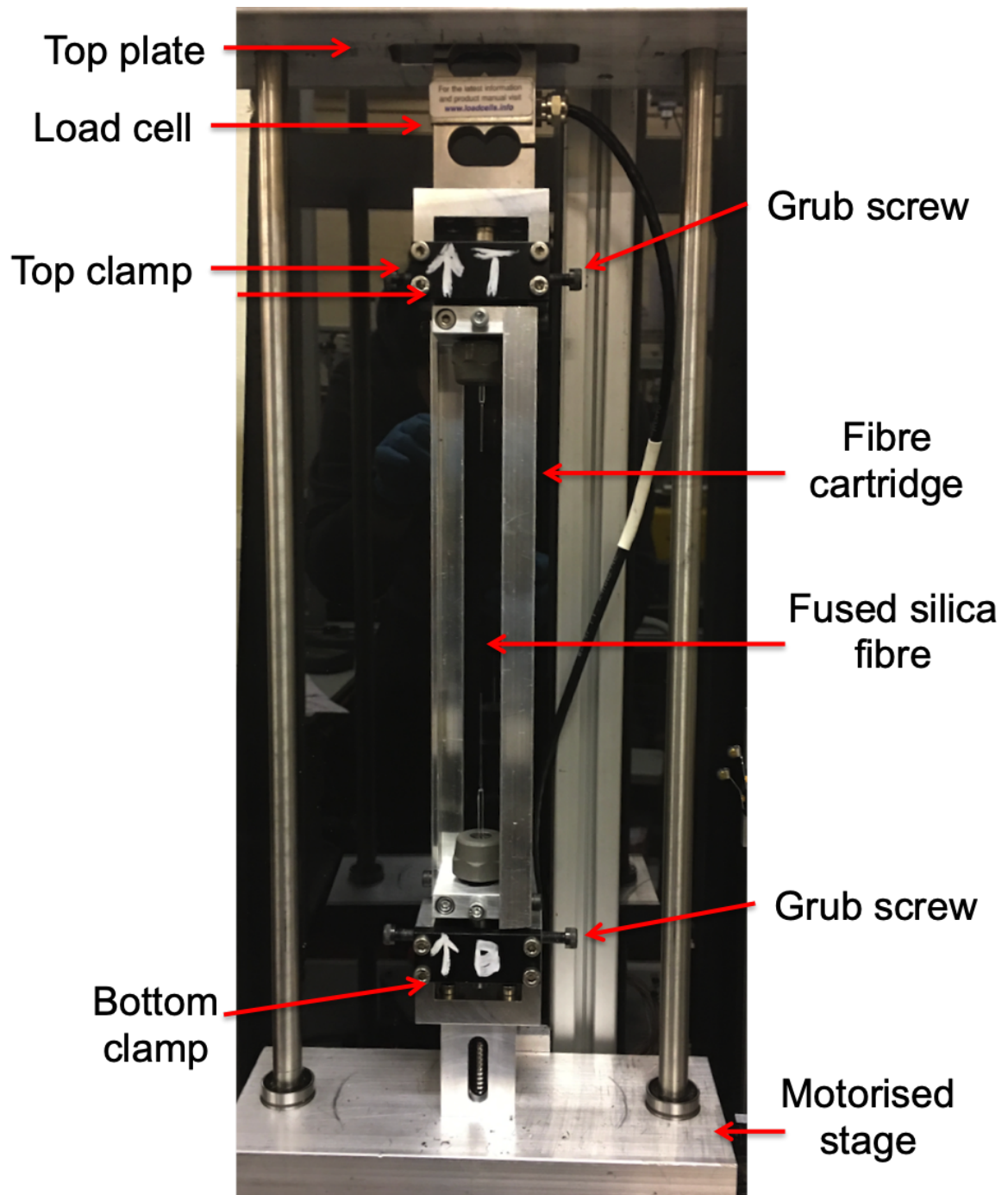


**Figure 7.1:** The experimental set-up used in this Young's modulus investigation with key components of the strength tester labelled.

Figure 7.1 shows the experimental set-up. A fibre cartridge housing a fused silica fibre was installed into the bottom clamp. This clamp was the end that was attached to the motorised stage. Two grub screws were tightened once the bottom cartridge chuck is in its holder to hold the chuck in place. The top plate, which has the top clamp attached to the load cell, is then moved down the drive rods and the holder slid onto the top chuck. The grub screws for the top plate was then tightened to ensure that the plate does not move during the tests. The grub

screws for the top clamp was then tightened to ensure the chuck does not move during the tests. The forces that were being applied to the fibre were small enough so that slippage of the top plate or any of the chucks is not a factor that needs to be considered. This was determined by applying forces to these components by hand where no visible slippage was observed to any of these components. The load cell was calibrated through the same method that was described previously in chapter 5.3.

### 7.3 Fibre production

This investigation consisted of producing fibres in four separate batches. Though four batches were produced, only two velocity profiles were used. The first three batches were produced using the velocity profile that was developed by the author for use in the Sagnac speedmeter (SSM) investigation that was being carried out at Glasgow at the time to suspend 1 g masses. The decision to use these velocity profiles was to firstly minimise the time needed to develop additional velocity profiles at the time, but also to strength-test fibres that would be used for these experiments to ensure that they were sufficiently strong to cover the safety factor that would be required. This safety factor is similar to that of the aLIGO suspensions in that the fibres must be able to take at least 3 times the load it would take installed into the suspension [62] [56]. The difference between the fibres that were produced during the first three batches were the feed velocity values.

Table 7.1 shows the first stage that was used for both velocity profiles in this chapter. This produces a slightly longer fibre, equivalent to the first stage pull down that was shown previously in chapter 6.4.1. The first stage was pulled with a corresponding feed velocity of  $0.8 \text{ mm s}^{-1}$ . The second stage of the velocity profile is shown in table 7.2. The corresponding feed velocity values for batches 1, 2 and 3 were  $0.05 \text{ mm s}^{-1}$ ,  $0.7 \text{ mm s}^{-1}$  and  $1 \text{ mm s}^{-1}$ , respectively. The fourth batch had a slightly modified second stage. This second stage is shown in table 7.3.

The first stage pull required the  $\text{CO}_2$  laser to be set to the maximum value of 95%. The second stage pulls used for all four batches were pulled with the laser controller set to approximately 25-35%. No fibres in this chapter were laser polished which is consistent to the production of fibres for SSM suspensions. All fused silica stock was wiped down with methanol once installed into the cartridge clamps.

**Table 7.1:** The first stage velocity pulling profile for both velocity profiles used in this investigation. This first stage is used with a corresponding feed velocity of  $0.8 \text{ mm s}^{-1}$ .

Velocity ( $\text{mm s}^{-1}$ )	Acceleration ( $\text{mm s}^{-2}$ )	Time (ms)
0.1	20000	140
1	20000	200
2	20000	200
3	20000	200
4	20000	200
7	20000	1000
11	20000	3000
0	0	0

**Table 7.2:** The second stage velocity pulling profile used to produce fibres for batches 1-3. This second stage is used with a corresponding feed velocity of  $0.05 \text{ mm s}^{-1}$ ,  $0.7 \text{ mm s}^{-1}$  and  $1 \text{ mm s}^{-1}$  for batches 1, 2 and 3, respectively.

Velocity ( $\text{mm s}^{-1}$ )	Acceleration ( $\text{mm s}^{-2}$ )	Time (ms)
0.1	20000	140
10	20000	100
20	20000	100
30	20000	100
200	20000	448
10	20000	100
5	20000	200
0	0	0

**Table 7.3:** The second stage velocity pulling profile used to produce batch 4 fibres. This second stage is used with a corresponding feed velocity of  $0.5 \text{ mm s}^{-1}$ .

Velocity ( $\text{mm s}^{-1}$ )	Acceleration ( $\text{mm s}^{-2}$ )	Time (ms)
0.1	20000	140
10	20000	100
20	20000	100
50	20000	200
190	20000	385
10	20000	100
5	20000	200
0	0	0

All fibres in this investigation were profiled using the ultra-thin fibre profiler that was previously described in chapter 5, with a magnification of  $\times 28$  [99]. The fibre profiler was calibrated

using a  $(25.00 \pm 1.25) \mu\text{m}$  nickel-chromium wire [161]. Figure 7.2 shows profiles of selected fibres from batch 1 [99]. All fibres were profiled in the same manner as those profiled previously in chapter 6. This means that the magnification is set too high to profile the thicker stock and taper down regions in order to be able to profile the thinner middle section of the fibre. Table 7.4 shows the range of minimum diameter values that were obtained in this investigation for all 4 fibre batches.

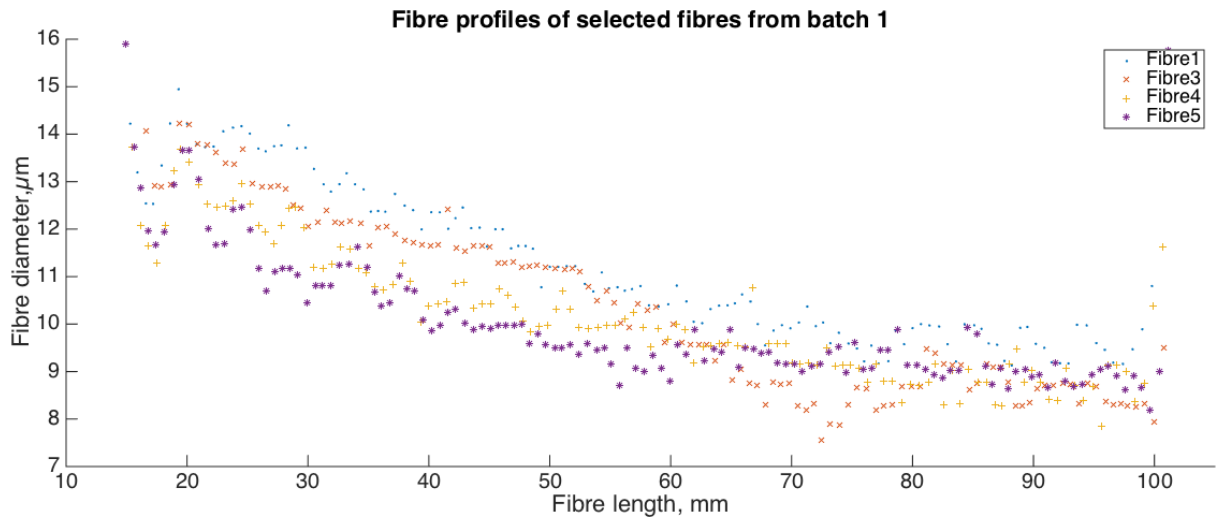


**Figure 7.2:** Selected profiles from batch 1 [99]. Note that "fibre 2" does not appear on this graph as it is part of batch 2.

**Table 7.4:** The range of minimum diameter values that were obtained for all 4 batches of fibres that were produced.

Batch	Range of minimum diameter values( $\mu\text{m}$ )
1	$7.6 \pm 0.2 \rightarrow 9.3 \pm 0.2$
2	$12.2 \pm 0.2 \rightarrow 15.6 \pm 0.2$
3	$10.9 \pm 0.2 \rightarrow 14.7 \pm 0.2$
4	$16.2 \pm 0.3 \rightarrow 18.8 \pm 0.5$

It can be seen from figure 7.2 that the bump artefact that has been discussed in several of the previous chapters still appears on the left side of the graph. This was consistent with all other fibres in that it appears at the start of the pulling process.

## 7.4 Results

In total, 28 fibres were tested to failure in this investigation. This consisted of 13 fibres produced from batch 1, and 5 fibres for each batch between batches 2-4. Figure 7.3 shows an example of

the data that was obtained through the thin fibre strength tester LabVIEW program. The slack removal period, which can also be seen in the inset of figure 7.3, can be seen at the start of the run. The length of the slack removal period depends on the installation of the fibre cartridge into the clamps and the position of the motorised stage prior to the test starting.

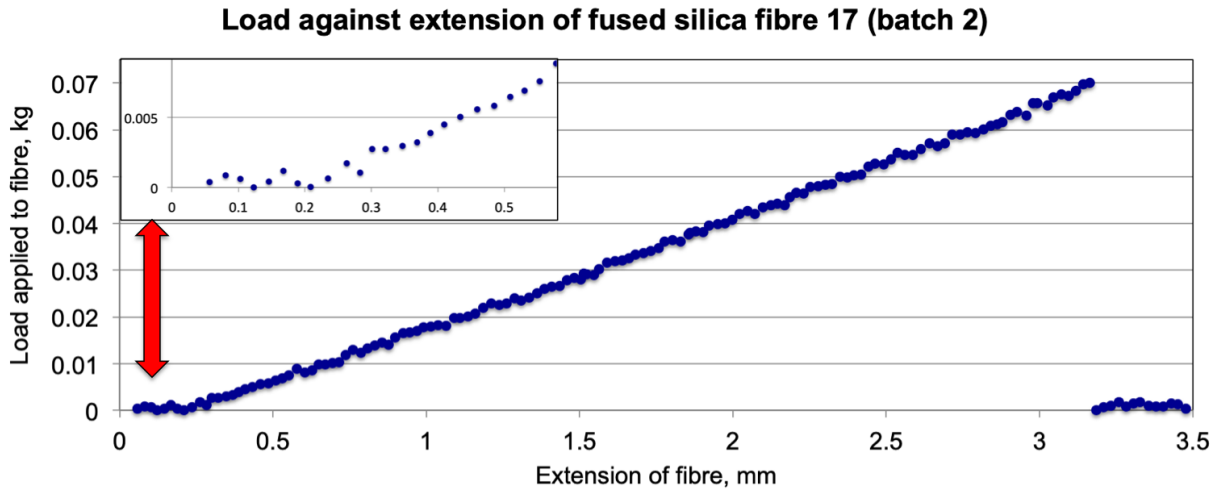


**Figure 7.3:** Graph of the load applied to the fused silica fibre against the extension of the fibre for fibre 17. This fibre was chosen to show the clear slack removal period that could occur prior to the fibre going under stress. Inset: Zoom in view of the slack removal period.

The breaking stress range for all fibres tested is shown in table 7.5. As there was no high speed camera available to use during this investigation, the assumption that the fibre breaks at the minimum diameter was made. Resulting Young's modulus values obtained for all fibres mentioned above are shown in figure 7.4 [99]. The process of how these values were obtained will be discussed in the following section.

**Table 7.5:** The range of breaking stress values for the 4 batches of tested fibres.

Batch	Range of breaking Stress(GPa)
1	$2.0 \pm 0.1 \rightarrow 3.0 \pm 0.1$
2	$3.3 \pm 0.1 \rightarrow 4.0 \pm 0.1$
3	$3.4 \pm 0.1 \rightarrow 4.1 \pm 0.1$
4	$3.7 \pm 0.2 \rightarrow 4.1 \pm 0.2$

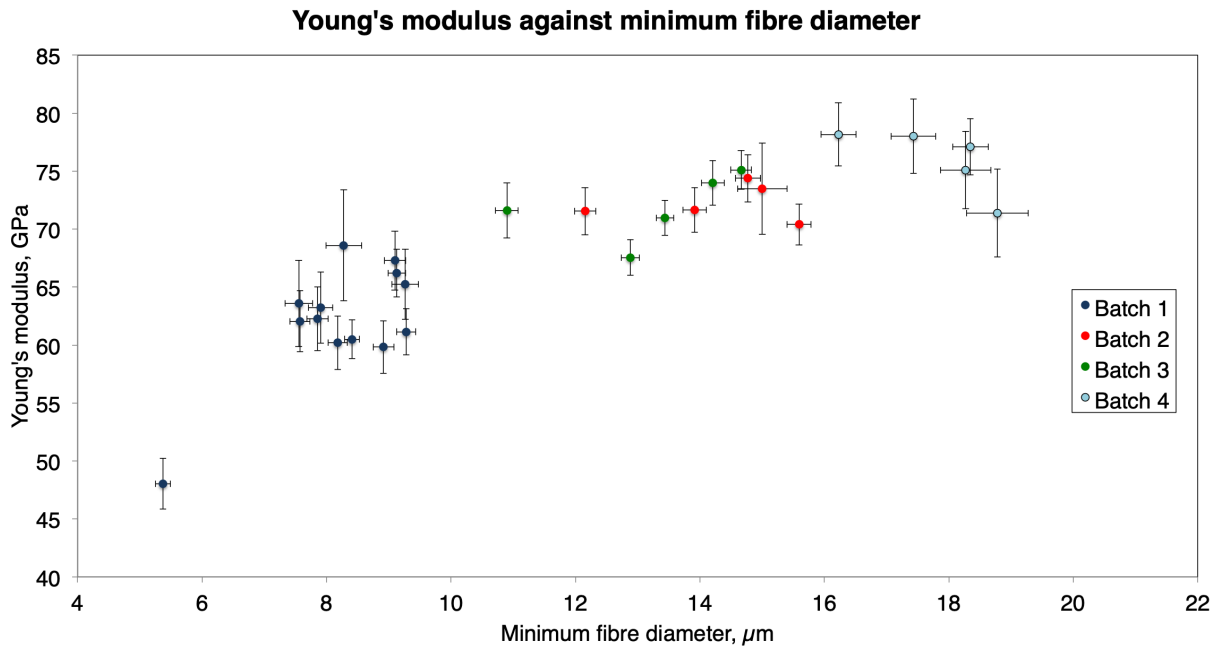


**Figure 7.4:** Young's modulus values obtained for all fibres from batches 1-4 [99].

## 7.5 Discussion

### 7.5.1 Young's modulus values and uncertainty calculations

The breaking stress was calculated by:

$$\sigma_{break} = \frac{F_{max}}{A_{min}} \quad (7.4)$$

where  $\sigma_{break}$  is the maximum breaking stress applied to the fibre,  $F_{max}$  is the force that was applied to the fibre to cause failure, and  $A_{min}$  is the minimum cross section area of the fibre. This assumes that the fibre breaks at the minimum diameter on the fibre. Locating the exact breaking point of the fibre was not possible due to no high speed camera available at the time this investigation was carried out. The uncertainty associated with the strain,  $\delta\epsilon$ , described previously in equation 7.2, could be calculated by:

$$\frac{\delta\epsilon}{\epsilon} = \sqrt{\left(\frac{\delta\Delta L}{\Delta L}\right)^2 + \left(\frac{\delta L}{L}\right)^2}. \quad (7.5)$$

The uncertainty associated with the Young's modulus,  $\delta Y$ , could then be defined by:

$$\frac{\delta Y}{Y} = \sqrt{\left(\frac{\delta\sigma}{\sigma}\right)^2 + \left(\frac{\delta\epsilon}{\epsilon}\right)^2}. \quad (7.6)$$

This however only applies should the diameter of the fibre be uniform all along the length of the middle thin section. As figure 7.2 shows, the fibres produced were not perfectly uniform along the whole length of the fibre. The Young's modulus needs to therefore be calculated by modelling the fibre as individual segments of constant diameter. As the fibre profiler takes data at set intervals, this gives an accurate way to calculate the cross section area of the fibre at separate segments. This means the extension of each segment at the breaking force could be calculated by:

$$\Delta L_n = \frac{L_n F}{Y A_n} \quad (7.7)$$

where  $\Delta L_n$  is the extension of the  $n^{\text{th}}$  segment,  $L_n$  is the length of the  $n^{\text{th}}$  segment and  $A_n$  is the cross section area of the  $n^{\text{th}}$  segment. The theoretical total extension of the fibre could therefore be calculated via:

$$\Delta L = \sum_{i=1}^n \Delta L_n = \sum_{i=1}^n \frac{L_n F}{Y A_n}. \quad (7.8)$$

To obtain the Young's modulus from equation 7.8, the theoretically calculated extension of the fibre was made equal to the experimental extension of the fibre obtained from the LabVIEW file. This could be achieved by calculating the Young's modulus so that the theoretical extension matches the experimental extension. Uncertainty values for the stress were calculated in the same way as calculated previously in chapter 6.4.2, and the strain value uncertainty calculated as described in chapter 5.3.2. These uncertainties were then combined to give the overall uncertainty in the Young's modulus.

The range of Young's modulus values, shown previously in figure 7.4, is shown in table 7.6. There was one fibre from batch one, shown in figure 7.4, that was not included in table 7.6 that has a Young's modulus value of  $(48.0 \pm 2.2)$  GPa. This was due to a sudden dip that occurs at the very end of the fibre that brings the fibre diameter down to  $(5.3 \pm 0.2)$   $\mu\text{m}$ , which can be seen in figure 7.5. This could have been due to a sudden increase in laser power caused from the power variation that could occur and was therefore treated as an outlier. There has been research showing that sudden dips in diameter in the fibre could have a negative effect on the overall strength of the fibre due to the additional thermal stress in the region [92]. Further investigation would need to be carried out by testing fibres with this artefact to determine how significant of an impact this dip artefact could have on the overall strength of the fibres with diameters similar to that which was tested here. This would require installing a camera monitoring system to measure the intensity of the laser on the fibre during the pull. Should this value be included in the average Young's modulus value of batch 1, it would lower it by approximately 2% from  $(63.3 \pm 2.7)$  GPa to  $(62.2 \pm 2.7)$  GPa.

**Table 7.6:** The range of Young's modulus values for the 4 batches of tested fibres. Note that 1A includes the average value without fibre 12 with a Young's modulus of 48.0 GPa, and 1B shows the average value with fibre 12.

Batch	Young's modulus (GPa)	Average Young's modulus, GPa
1A	$(59.8 \pm 2.3) \rightarrow (68.6 \pm 4.8)$	$(63.3 \pm 2.7)$
1B	$(59.8 \pm 2.3) \rightarrow (68.6 \pm 4.8)$	$(62.2 \pm 2.7)$
2	$(70.4 \pm 1.8) \rightarrow (74.4 \pm 2.0)$	$(72.3 \pm 2.3)$
3	$(67.5 \pm 1.5) \rightarrow (75.1 \pm 1.7)$	$(71.8 \pm 1.8)$
4	$(71.4 \pm 3.8) \rightarrow (78.2 \pm 2.7)$	$(75.9 \pm 3.0)$

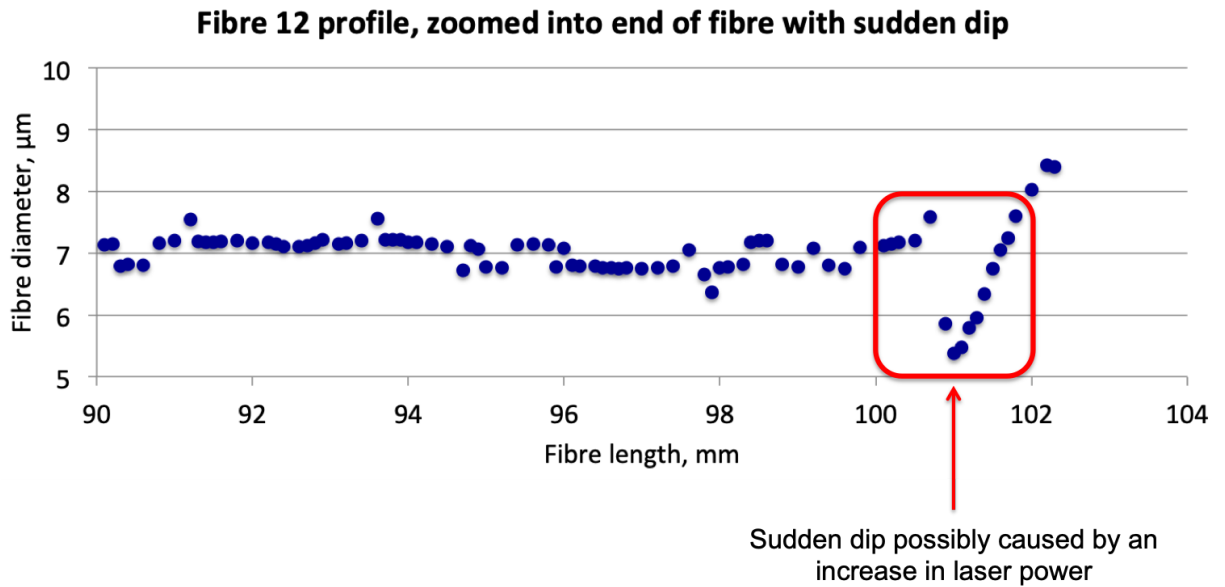


**Figure 7.5:** Zoomed in view of the sudden dip artefact that appeared in fibre 12 of batch 1 that was being treated as an outlier.

It can be seen from table 7.6 that fibres that were tested from batches 2-4 have an average value that falls around the expected Young's modulus of fused silica of 72 GPa [181]. Calculating the weighted average of batches 2-4 gives a value of  $72.1 \pm 1.3$  GPa, again agreeing with the expected Young's modulus value. The batch 1 average however falls below this value. It should be noted that batch 1 was the only batch that had fibres under 10  $\mu\text{m}$  in diameter and had no fibres larger than 10  $\mu\text{m}$ . It was decided that one extra fibre would be produced and tested non-destructively. This was carried out by stretching a fibre to a stress of 1 GPa by driving the motorised stage down, followed by bringing the motorised stage back up to approximately its starting position. The reason this was approximate was to ensure that the fibre was slack and not under tension. This could be observed either through the live plot on the LabVIEW front panel, or by visually observing the fibre moving freely within the enclosure. The distance the fibre stretched was determined by observing the position of the motorised stage when the fibre takes

up the tension, as shown previously in figure 7.3. This test was repeated a total of 5 times, with the resulting Young's modulus values shown in figure 7.6. The values obtained were consistent with that obtained previously from batch 1, with an average value of  $(62.9 \pm 2.8)$  GPa.

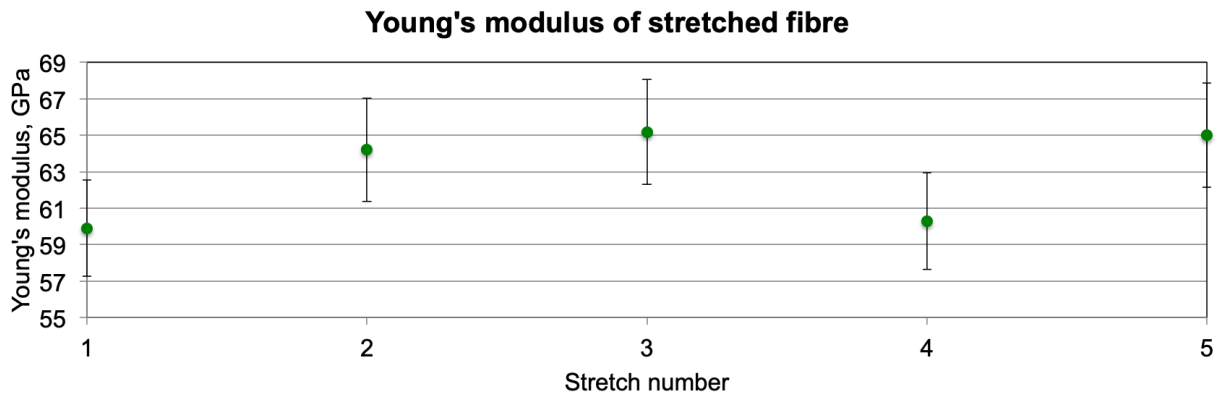


**Figure 7.6:** Non-destructive Young's modulus results from a fibre that was pulled under the same conditions as batch 1.

## 7.5.2 Comparison to other investigations

This investigation was consistent with the findings that were obtained in chapter 6 in that fibres under  $10\mu\text{m}$  would not agree with the trend that was set from fibres above  $10\mu\text{m}$  in diameter. This suggests that there is an additional mechanism at play, however what exact mechanism this is will require further extensive research to determine what factor affects the ratio between the stress and the strain the most. The results shown in chapter 6 showed that polishing the stock material before production shows an increase in breaking stress for fibres under  $10\mu\text{m}$  in diameter of up to approximately 2 orders of magnitude. It is possible that polishing the stock before production could potentially give different Young's modulus values, however it was not possible to pursue this due to time constraints. As mentioned previously, there are suggestions that there is a  $1\mu\text{m}$  thick surface layer for fused silica [128] [95]. For fibres under  $10\mu\text{m}$  in diameter, this surface layer makes up a significant percentage of the cross sectional area of the fibre.

Figure 7.7 shows the Young's modulus values obtained in this investigation, as well as fibres that were obtained previously when this investigation was carried out with the old experimental set-up [93]. The largest uncertainty in the Young's modulus in this investigation was 7%, where as during the previous research, the maximum uncertainty was up to 16.4%. It is interesting to see that fibres between  $10\text{-}16\mu\text{m}$  in diameter from this investigation and the previous investigation do seem to follow a trend when taking the error bars for the MSc investigation into consideration. It is clear from figure 7.7 that the spread between the two investigations has decreased. This will be down to the dedicated ultra-thin fibre profiler and strength tester upgrades that were described in chapter 5. No fibres exceeded 100 GPa like the one stand alone fibre did

during the MSc investigation.

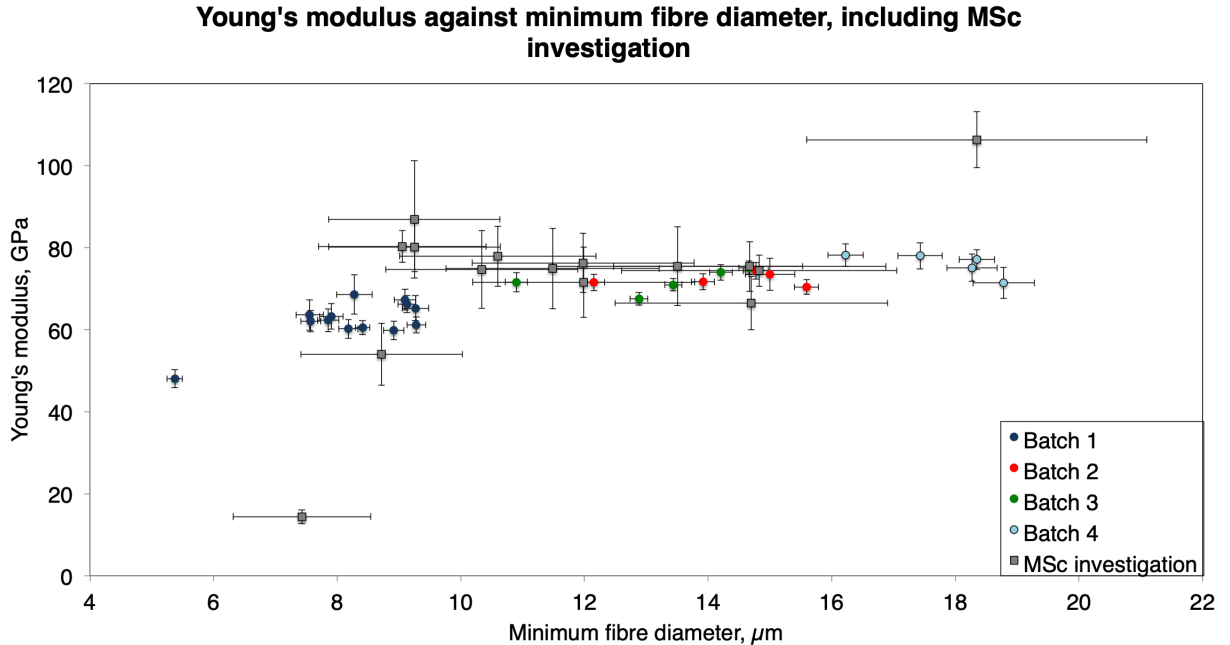


**Figure 7.7:** Data from all four fibre batches that were tested in this investigation compared to the data that was previously obtained during the MSc investigation [93].

There has been research looking at fibres with diameters between 50-300 nm in diameter that have been shown to have breaking stress values between 10-25 GPa, resulting in a Young's modulus in excess of 100 GPa [182]. This was significantly higher than all fibres that have been investigated in this chapter. These fibres were produced using a flame brushing technique instead of a  $\text{CO}_2$  laser to produce 6 mm long "nanowires". However, a flame polishing technique was applied to the actual fibre itself. This was not possible to carry out with the  $\text{CO}_2$  laser as all fibres were produced according to the aLIGO fibre pulling procedure where nothing, including excess laser beam exposure, should be applied to the fibre itself to minimise any damage or artefacts introduced to the fibre structure that could compromise the performance.

Investigations on fibres with diameters between 1-3  $\mu\text{m}$  have also shown breaking stress values of up to 16 GPa [128] [183], but these fibres were treated through additional heating of the fibre in vacuum or through the use of chemical reagents to treat the surface of the fibre. Chemical treatments also show an increase in breaking stresses for fibres of 100  $\mu\text{m}$  in diameter [184]. The goal of these treatments aims at further removing any surface impurities, such as cracks or surface moisture, as previously discussed research has shown that these could be critical in terms of longevity of a fibre. Due to these treatments were added in post-production once the fibre is made, none of these were an option for any of the fibres that were produced in this thesis and were therefore not carried out. This could be an option that could be explored in the future, however it will take a significant amount of research.

The lower Young's modulus value for sub-10  $\mu\text{m}$  fibres that were obtained in this investigation means that any calculations regarding modelling of suspensions utilising these fibres should

take into account this change in value from the accepted value of 72 GPa. Failure to do so could result in differences between simulation and real experimental scenarios. Characteristics such as the fibres not stretching to their predicted value and affecting the values of the violin and bounce modes [185] could be a resulting effect which could lead to sub-optimal alignment and noise performance that differs more than expected from the models used.

## 7.6 Conclusion

The aim of the investigation carried out in this chapter was to repeat previous measurements of Young's modulus of fused silica fibres, but with improved characterisation and testing apparatus to minimise the uncertainty values. This also allows for the comparison of both data sets to observe if there were any consistencies or differences between the two. Four batches of fibres were tested in this investigation, with three of them having minimum diameters greater than 10  $\mu\text{m}$  and one batch with fibres under 10  $\mu\text{m}$  in diameter. It was found that for fibres that had a minimum diameter above 10  $\mu\text{m}$ , the Young's modulus value agrees with the accepted value of 72 GPa [181]. The average value of these three batches were found to be  $(72.3 \pm 2.3)$  GPa,  $(71.8 \pm 1.8)$  GPa and  $(75.9 \pm 3.0)$  GPa. For the batch that contained fibres with a minimum diameter under 10  $\mu\text{m}$ , there was a noticeable difference between the obtained values and the accepted value. The average value obtained was  $(63.3 \pm 2.7)$  GPa and was consistent with non-destructive tests that were carried out with a value of  $(62.9 \pm 2.8)$  GPa. There was one fibre in batch 1 that did have a significantly lower Young's modulus value of  $(48.0 \pm 2.2)$  GPa

Comparing this data to the previously obtained results shows an agreement for values where the fibre minimum diameter was between 10-16  $\mu\text{m}$  in diameter. For fibres under 10  $\mu\text{m}$  in diameter, there was a wider spread in data from the MSc investigation that the fibres from this investigation sit in between. The spread of values from this investigation was a lot tighter with a spread of  $(59.8 \pm 2.3)$  GPa  $\rightarrow$   $(68.6 \pm 4.8)$  GPa, compared to  $(54.0 \pm 7.5)$  GPa  $\rightarrow$   $(87.0 \pm 14.3)$  GPa. Overall, the goal of improving the uncertainties of the Young's modulus values were achieved by decreasing the uncertainties from the previous maximum of 16% down to a maximum of 7%. Further extensive investigations need to be carried out in the future to fully understand the reasons why fibres under 10  $\mu\text{m}$  in diameter behave differently. This could involve investigating possible alignment defects that were not detectable through single-camera profiling, as well as investigating other properties such as shear modulus which has a greater dependency on the radius of the fibres. Shear modulus is proportional to  $r^4$ , unlike Young's modulus which is proportional to  $r^2$ . An investigation into the shear modulus could be carried out by creating a torsion pendulum on a fibre and measuring the period. Comparisons of obtained shear modulus values at different diameters could potentially lead to a greater understanding of the surface layer of fused silica and its influence on fibres under 10  $\mu\text{m}$  in diameter.

# Chapter 8

## Conclusion

This thesis presented various areas of research related to the use of fused silica fibres for gravitational wave research. A procedure was documented to standardise the alignment process of the aLIGO fibre pulling machine. Previously, this alignment process was subjective to the user as there were no documented set of instructions, which increased the probability of manufacturing defects to be introduced into the fibre production. This procedure also highlighted common issues that were related to the misalignment of the pulling machine and how these misalignments could be corrected. This work will be written up in the future as a LIGO DCC document that can be referred to and updated for all future fibre production work on the fibre pulling machines.

One of the manufacturing defects that could be introduced into the fibres were angular misalignments in the thermoelastic nulling region. This became a prominent issue during the commissioning break between O2 and O3 where there were several instances of suspension fibres failing where these misalignments were observed. Though it was not concluded that these were the cause of the failures, an investigation was carried out to determine how great of an effect these angular misalignments have on the ultimate strength of the fibres. This investigation confirmed that these angular misalignments could be introduced into the fibre due to beam distribution misalignment around the stock material during the pulling process. These angular misalignments however did not show any adverse effect on the ultimate strength of the fibre. These tests were carried out through destructive strength testing to observe whether or not the fibres were breaking at the angular misalignment region. It was determined that the fibres were not breaking at the region where the angle occurred, but in the thin section of the fibre. Further research looking at long term stress tests rather than destructive short term tests would determine conclusively whether these angular misalignments are a safety factor that needs to be re-evaluated in the suspension fibre selection process.

During this PhD, the opportunity to work at LHO arose for a four-month period on a long term attachment (LTA). During this LTA, an investigation into the stress fatigue of fused silica fibres was carried out in the fibre production lab at LHO. The aim of this investigation was to investigate the hang time of fused silica fibres under high stress compared to what aLIGO sus-

pension fibres were currently subjected to. This investigation involved looking at a stress range between 3-5 GPa, as this range would yield fibres that would break in a time scale of less than a day to maximise the number of data points that could be obtained during this LTA. All tests at LHO were carried out in air in parallel to tests that were being carried out in Glasgow at a similar stress range, but both in air and in vacuum. The results of these investigations were then compared to an investigation by Proctor in the 1960s to see if there were any differences observed. It was found that data from both LHO and Glasgow did not align with the data that Proctor had obtained in his investigation, but did align with each other, showing that investigations carried out at LHO or Glasgow can be considered to be consistent with each other. Due to the data not aligning with Proctor's results, a follow-on investigation looking at fibres with comparable diameters were investigated.

To do this, a dedicated fibre profiler had to be developed first that was designed specifically to profile fibres within this diameter range. This included being able to profile fibres that were under 10  $\mu\text{m}$  in diameter. A new fibre profiler was developed based on the design of the current aLIGO fibre profiler, but with a variable magnification system installed. This allows for a wide range of fibres to be profiled on this machine. The thin fibre strength tester was also upgraded to add a magnetic encoder to measure the distance travelled by the motorised stage. This was relevant to a future investigation that was carried out in this thesis.

An investigation into the stress fatigue of sub-40  $\mu\text{m}$  diameter fibres was then carried out to compare results with the previous investigation with aLIGO fibres. It was found that fibres that were above 10  $\mu\text{m}$  in diameter showed strong performances similar to that of Proctor, regardless of the initial stock material being polished, double polished, or no polish. Fibres under 10  $\mu\text{m}$  however did not show this strong performance and were weaker performing. Polishing the initial stock material did show an increase in suspension time, however these were still weaker than the >10  $\mu\text{m}$  diameter fibres. To see if this behaviour was consistent with other fibre characteristics, an investigation into the Young's modulus of the ultra-thin fibres was investigated.

A previous investigation into the Young's modulus of ultra-thin fibres was carried out by the author, however there were several factors in the equipment used at the time that lead to large uncertainties being associated with the Young's modulus values obtained. With the new upgraded strength tester and dedicated fibre profiler, this investigation was revisited to see if results obtained were consistent or different to that previously found. The uncertainties associated with the Young's modulus were successfully decreased from 16%, down to 7%. For fibres that had a minimum diameter greater than 10  $\mu\text{m}$ , the Young's modulus value tended to agree with the accepted value of 72 GPa. The average value of three batches that were tested with diameters greater than 10  $\mu\text{m}$  were found to be  $(72.3 \pm 2.3)$  GPa,  $(71.8 \pm 1.8)$  GPa and  $(75.9 \pm 3.0)$  GPa. This gives a weighted average of  $(72.7 \pm 1.3)$  GPa. For the batch that had fibres under 10  $\mu\text{m}$  in diameter, the average Young's modulus value was  $(63.3 \pm 2.7)$  GPa and a weighted average of  $(62.8 \pm 1.9)$  GPa. Non-destructive tests on these fibres showed an average value of  $(62.9 \pm 2.8)$ .

This is consistent with the stress fatigue tests where fibres under  $10\ \mu\text{m}$  showed different characteristics. Further extensive investigations need to be carried out in the future to fully understand the reasonings that fibres under  $10\ \mu\text{m}$  in diameter behave differently. This could involve investigating possible alignment defects that were not detectable through single-camera profiling, as well as investigating other properties such as shear modulus which has a greater dependency on the radius of the fibres.

# Appendix A

## Fused silica fibre angle python script

This appendix references the Python 3 code, written by the author, that was used to produce the results obtained in chapter 3. It is set such that all the conditions, values and outputs are shown for fibre 20 that was investigated as an example of the script working.

The python script has been uploaded to the LIGO Document Control Centre, with DCC number LIGO-T2000329.

## Appendix B

# Ultra-thin fibre profiler LabVIEW block diagram

This appendix contains the LabVIEW block diagram for the ultra-thin fibre profiler. This code is a modified version of the aLIGO fibre profiler LabVIEW code that had previously been developed [122] [159].

The python script has been uploaded to the LIGO Document Control Centre, with DCC number LIGO-T2000330.

# Bibliography

- [1] A. Einstein, “Naherungsweise integration der feldgleichungen der gravitation,” *Sitzungsberichte der Koniglich Preussischen Akademie der Wissenschaften Berlin*, pp. 688–696, 1916.
- [2] “Massive bodies warp space-time.” <https://www.ligo.caltech.edu/image/ligo20160211e>, Last accessed: October 2019.
- [3] M. Pitkin, S. Reid, S. Rowan, and J. Hough, “Gravitational wave detection by interferometry (ground and space),” *Living Reviews in Relativity*, vol. 14, no. 5, pp. 8–23, 2011.
- [4] P. R. Saulson, *Fundamentals of interferometric gravitational wave detectors*. World Scientific Publishing, 1993.
- [5] G. M. Harry, “Advanced LIGO: the next generation of gravitational wave detectors,” *Classical and Quantum Gravity*, vol. 27, p. 084006, 2010.
- [6] J. Aasi *et al.*, “Advanced LIGO,” *Classical and Quantum Gravity*, vol. 32, no. 074001, 2015.
- [7] B. F. Schutz, “Determining the Hubble constant from gravitational wave observations,” *Nature*, vol. 323, pp. 310–311, 1986.
- [8] C. D. Ott *et al.*, “Core-collapse supernovae, neutrinos and gravitational waves,” *Nuclear Physics B - Proceedings Supplement*, vol. 235-236, pp. 381–387, 2012.
- [9] B. S. Sathyaprakash and B. F. Schutz, “Physics, astrophysics and cosmology with gravitational waves,” *Living Reviews in Relativity*, vol. 12, no. 2, pp. 18–19, 2009.
- [10] J. H. Taylor, L. A. Fowler, and P. M. McCulloch, “Measurements of general relativistic effects in the binary pulsar PSR1913+16,” *Nature*, vol. 277, pp. 437–440, February 1979.
- [11] R. A. Hulse and J. H. Taylor, “Discovery of a pulsar in a binary system,” *The Astrophysical Journal*, vol. 195, pp. L51–L53, January 1975.
- [12] J. M. Weisberg and J. H. Taylor, “Relativistic Binary Pulsar B1913+16: Thirty years of observations and analysis,” *ASP Conference Series*, vol. 328, p. 4, 2005.

- [13] E. W. Kolb and R. Peccei, eds., *Proceedings of the Snowmass 95 Summer Study on Particle and Nuclear Astrophysics and cosmology*, World Scientific Singapore, 1995.
- [14] B. F. Schutz, “Networks of gravitational wave detectors and three figures of merit,” *Classical and Quantum Gravity*, vol. 28, no. 12, p. 125023, 2011.
- [15] The LIGO Scientific Collaboration and the Virgo Collaboration, “Upper Limits on the Stochastic Gravitational-Wave Background from Advanced LIGO’s First Observing Run,” *Phys. Rev. Lett.*, vol. 118, p. 121101, 2017.
- [16] The LIGO Scientific Collaboration and the Virgo Collaboration, “GW170817: Implications for the Stochastic Gravitational-Wave Background from Compact Binary Coalescences,” *Phys. Rev. Lett.*, vol. 120, p. 091101, 2018.
- [17] J. Weber, “Detection and generation of gravitational waves,” *Physical Review*, vol. 117, no. 1, p. 309, 1960.
- [18] J. Weber, “Gravitational wave detector events,” *Physical Review Letters*, vol. 20, no. 23, pp. 1307–1308, 1968.
- [19] J. Weber, “Evidence for discovery of gravitational radiation,” *Physical Review Letters*, vol. 22, no. 24, pp. 1320–1324, 1969.
- [20] J. A. Tyson and R. P. Giffard, “Gravitational wave astronomy,” *Annual review of Astronomy and Astrophysics*, vol. 16, pp. 521–554, 1978.
- [21] A. Abramovici *et al.*, “LIGO: The Laser Interferometer Gravitational-Wave Observatory,” *Science*, vol. 256, pp. 325–333, 1992.
- [22] T. Accadia, F. Acernese, M. Alshourbagy, *et al.*, “Virgo: a laser interferometer to detect gravitational waves,” *Journal of Instrumentation*, vol. 7, no. 3, p. 03012, 2012.
- [23] F. Acernese *et al.*, “Advanced Virgo: a 2nd generation interferometric gravitational wave detector,” *Classical and Quantum Gravity*, vol. 32, p. 024001, 2015.
- [24] T. Accadia *et al.*, “The seismic Superattenuators of the Virgo gravitational waves interferometer,” *Journal of Low Frequency Noise Vibration and Active Control*, vol. 30, pp. 63–79, 2011.
- [25] B. Willke *et al.*, “The GEO 600 gravitational wave detector,” *Classical and Quantum Gravity*, vol. 19, pp. 1377–1387, 2002.
- [26] A. Khalaidovski, H. Vahlbruch, N. Lastzka, *et al.*, “Status of the GEO 600 squeezed-light laser,” *Journal of Physics: Conference Series*, vol. 363, p. 012013, 2011.

- [27] B. Willke *et al.*, “The GEO-HF project,” *Classical and Quantum Gravity*, vol. 23, no. 8, p. S207, 2006.
- [28] T. Akutsu *et al.*, “KAGRA: 2.5 generation interferometric gravitational wave detector,” *Nature Astronomy*, vol. 3, pp. 35–40, 2019.
- [29] R. Kumar *et al.*, “Status of the cryogenic payload system for the KAGRA detector,” *Journal of Physics: Conference Series*, vol. 716, p. 012017, 2017.
- [30] M. A. Arain and G. Mueller, “Design of the Advanced LIGO recycling cavities,” *Optics Express*, 2008.
- [31] R. Weiss, “Electromagnetically coupled broadband gravitational antenna,” *Quarterly Progress Report, Research Laboratory of Electronics (MIT)*, no. 105, p. 54, 1972.
- [32] H. Billing *et al.*, “An argon laser interferometer for the detection of gravitational radiation,” *Journal of Physics E: Scientific Instruments*, vol. 12, p. 1043, 1979.
- [33] R. Schilling *et al.*, “A method to blot out scattered light effects and its application to a gravitational wave detector,” *Journal of Physics E: Scientific Instruments*, vol. 14, p. 65, 1981.
- [34] B. J. Meers, “Recycling in laser-interferometric gravitational-wave detectors,” *Physical Review D*, vol. 38, no. 8, p. 2317, 1988.
- [35] K. A. Strain and B. J. Meers, “Experimental demonstration of dual recycling for interferometric gravitational-wave detectors,” *Physical Review Letters*, vol. 66, no. 11, p. 1391, 1991.
- [36] M. Punturo, M. Abernathy, F. Acernese, *et al.*, “The Einstein Telescope: a third generation gravitational wave observatory,” *Classical and Quantum Gravity*, vol. 27, p. 194002, 2010.
- [37] Einstein Telescope Science Team, “Einstein gravitational wave telescope conceptual design study,” Tech. Rep. ET-0106C-10, Einstein Telescope Science Team, 2011.
- [38] A. V. Cumming *et al.*, “Silicon mirror suspensions for gravitational wave detectors,” *Classical and Quantum Gravity*, vol. 31, no. 205017, 2013.
- [39] P. Amaro-Seoane, S. Aoudia, S. Babak, *et al.*, “Low-frequency gravitational-wave science with eLISA/NGO,” *Classical and Quantum Gravity*, vol. 29, p. 124016, 2012.
- [40] O. Jennrich, “LISA technology and instrumentation,” *Classical and Quantum Gravity*, vol. 26, no. 15, p. 153001, 2009.

- [41] M. Armano *et al.*, “Beyond the required LISA free-fall performance: New LISA Pathfinder results down to 20  $\mu\text{Hz}$ ,” *Physical Review Letters*, vol. 120, no. 061101, 2018.
- [42] B. P. Abbott *et al.*, “Observation of gravitational waves from a binary black hole merger,” *Physical Review Letters*, vol. 116, no. 6, p. 061102, 2016.
- [43] B. P. Abbott *et al.*, “GW151226: Observation of Gravitational waves from a 22 solar mass binary black hole coalescence,” *Physical Review Letters*, vol. 116, p. 241103, 2016.
- [44] B. P. Abbott *et al.*, “GW170104: Observation of a 50-Solar-Mass Binary Black Hole Coalescence at Redshift 0.2,” *Physical Review Letters*, vol. 118, p. 221101, 2017.
- [45] B. P. Abbott *et al.*, “GW170608: Observation of a 19 solar mass binary black hole coalescence,” *The Astrophysical Journal Letters*, vol. 851, no. 2, p. L35, 2017.
- [46] B. P. Abbott *et al.*, “GW170814: A Three-Detector Observation of Gravitational Waves from a Binary Black Hole Coalescence,” *Physical Review Letters*, vol. 119, p. 141101, 2017.
- [47] B. P. Abbott *et al.*, “GWTC-1: A Gravitational-Wave Transient Catalog of Compact Binary Mergers Observed by LIGO and Virgo during the First and Second Observing Runs,” *Phys. Rev. X*, vol. 9, no. 031040, 2018.
- [48] B. P. Abbott *et al.*, “Binary Black Hole Mergers in the First Advanced LIGO Observing Run,” *Phys. Rev. X*, vol. 6, p. 041015, October 2016.
- [49] B. P. Abbott *et al.*, “GW170817: Observation of Gravitational Waves from a Binary Neutron Star Inspiral,” *Physical Review Letters*, vol. 119, p. 161101, 2017.
- [50] “LIGO/VIRGO binary black hole orrery.”  
<https://www.ligo.caltech.edu/image/ligo20181203b>, Last accessed: October 2019.
- [51] The LIGO Scientific Collaboration and the Virgo Collaboration, “Properties of the binary neutron star merger GW170817,” *Phys. Rev. X*, vol. 9, p. 011001, 2019.
- [52] B. P. Abbott *et al.*, “Multi-messenger observations of a binary neutron star merger,” *Astrophysical Journal Letters*, vol. 848, no. 12, 2017.
- [53] B. P. Abbott *et al.*, “Gravitational waves and gamma rays from a binary neutron star merger: GW170817 and GRB 170817A,” *Astrophysical Journal Letters*, vol. 848, no. 13, p. 27, 2017.
- [54] “Waveforms and chirps.” <https://www.eso.org/public/videos/eso1733j/>, 2017.

- [55] “GraceDB - Gravitational-wave candidate event database public alert page.” <https://gracedb.ligo.org/latest/>.
- [56] A. V. Cumming *et al.*, “Design and development of the advanced LIGO monolithic fused silica suspension,” *Classical and Quantum Gravity*, vol. 29, no. 3, p. 035003, 2012.
- [57] S. M. Aston *et al.*, “Update on quadruple suspension design for Advanced LIGO,” *Classical and Quantum Gravity*, vol. 29, no. 23, p. 235004, 2012.
- [58] G. D. Hammond *et al.*, “Reducing the suspension thermal noise of advanced gravitational wave detectors,” *Classical and Quantum Gravity*, vol. 29, p. 124009, 2012.
- [59] J. Odell *et al.*, “Advanced LIGO Quadruple Suspension Assembly,” tech. rep., DCC Number D0901346, 2018.
- [60] M. V. Plissi *et al.*, “Aspects of the suspension system for GEO600,” *Review of Scientific Instruments*, vol. 69, p. 3055, 1998.
- [61] S. Reid and I. Martin, “Development of mirror coatings for gravitational wave detectors,” *Coatings*, vol. 6, no. 4, p. 61, 2016.
- [62] A. Heptonstall *et al.*, “Invited Article: CO<sub>2</sub> laser production of fused silica fibers for use in interferometric gravitational wave detector mirror suspensions,” *Review of Scientific Instruments*, vol. 82, no. 1, p. 011301, 2011.
- [63] M. van Veggel *et al.*, “Final design document ETM/ITM ears,” tech. rep., DCC Number T0900447, 2009.
- [64] S. Rowan *et al.*, “Mechanical losses associated with the technique of hydroxide-catalysis bonding of fused silica,” *Physics Letters A*, vol. 246, no. 6, pp. 471–478, 1998.
- [65] E. J. Elliffe *et al.*, “Hydroxide-catalysis bonding for stable optical systems for space,” *Classical and Quantum Gravity*, vol. 22, no. 10, p. S257, 2005.
- [66] L. Cunningham *et al.*, “Re-evaluation of the mechanical loss factor of hydroxide-catalysis bonds and its significance for the next generation of gravitational wave detectors,” *Physics Letters A*, vol. 374, no. 39, pp. 3993–3998, 2010.
- [67] D. Davis *et al.*, “Improving the sensitivity of Advanced LIGO using noise subtraction,” *Classical and Quantum Gravity*, vol. 36, p. 055011, 2019.
- [68] G. Hammond, S. Hild, and M. Pitkin, “Advanced technologies for future ground-based, laser-interferometric gravitational wave detectors,” *Journal of Modern Optics*, vol. 61, no. S1, pp. S10–S45, 2014.

- [69] “LHO Summary page.” <https://ldas-jobs.ligo-wa.caltech.edu/detchar/summary/>.
- [70] S. Hild, *Advanced Interferometers and the Search for Gravitational Waves - Lectures from the First VESF School on Advanced Detectors for Gravitational Waves - A basic introduction to quantum noise and quantum non demolition techniques*, vol. 404. Springer International Publishing, 2014.
- [71] C. M. Caves, “Quantum-mechanical noise in an interferometer,” *Physical Review D*, vol. 23, no. 8, pp. 1693–1708, 1981.
- [72] J. Miller *et al.*, “Prospects for doubling the range of Advanced LIGO,” *Physical Review D*, vol. 91, no. 6, p. 062005, 2015.
- [73] C. Affeldt *et al.*, “Advanced techniques in GEO 600,” *Classical and Quantum Gravity*, vol. 31, no. 22, 2014.
- [74] J. Aasi *et al.*, “Enhanced sensitivity of the LIGO gravitational wave detector by using squeezed states of light,” *Nature Photonics*, vol. 7, pp. 613–619, 2013.
- [75] J. Driggers, J. Harms, and R. X. Adhikari, “Subtraction of newtonian noise using optimized sensor arrays,” *Physical Review D*, vol. 86, pp. 102001–1, 2012.
- [76] M. Coughlin *et al.*, “Towards a first design of a Newtonian-noise cancellation system for Advanced LIGO,” *Classical and Quantum Gravity*, vol. 33, no. 24, p. 244001, 2016.
- [77] G. Cella, “Underground reduction of gravity gradient noise.” LIGO Document G060331, 2006.
- [78] A. Effler *et al.*, “Environmental influences on the LIGO gravitational wave detectors during the 6th science run,” *Classical and Quantum Gravity*, vol. 32, no. 3, 2015.
- [79] “Low frequency sensitivity still problematic after the Montana EQ.” aLIGO LHO Logbook entry 37590, July 2017.
- [80] J. Travasso *et al.*, “Status of the Monolithic Suspensions for Advanced Virgo,” *Journal of Physics: Conference Series*, vol. 857, no. 012012, 2018.
- [81] F. Matichard *et al.*, “Seismic isolation of Advanced LIGO gravitational waves detector: review of strategy, instrumentation and performance,” *Classical and Quantum Gravity*, vol. 32, p. 185003, 2015.
- [82] R. Brown, “A brief account of microscopical observations on the particles contained in the pollen of plants; and on the general existence of active molecules in organic and inorganic bodies,” *Edinburgh new philosophical journal*, vol. 5, pp. 358–371, 1828.

- [83] A. Einstein, “Über die von der molekularkinetischen theorie der wärme geforderte bewegung von in ruhenden flüssigkeiten suspendierten teilchen,” *Annalen de Physik*, vol. 322, pp. 549–560, 1905.
- [84] H. B. Callen and T. A. Welton, “Irreversibility and generalized noise,” *Physical Review*, vol. 83, no. 1, pp. 34–40, 1951.
- [85] R. F. Greene and H. B. Callen, “On the formalism of thermodynamic fluctuation theory,” *Physical Review*, vol. 83, no. 6, pp. 1231–1235, 1951.
- [86] A. S. Nowick and B. S. Berry, *Anelastic relaxation in crystalline solids*. 111 Fifth Avenue, New York, New York 10003: Academic Press, New York, 1972.
- [87] C. J. Bell *et al.*, “Experimental results for nulling the effective thermal expansion coefficient of fused silica fibres under a static stress,” *Classical and Quantum Gravity*, vol. 31, no. 6, p. 065010, 2014.
- [88] P. R. Saulson, “Thermal noise in mechanical experiments,” *Physical Review D*, vol. 42, no. 8, pp. 2437–2445, 1990.
- [89] N. A. Robertson *et al.*, “Design of a tuned mass damper for high quality factor suspension modes in advanced LIGO,” *Review of Scientific Instruments*, vol. 88, no. 035117, 2017.
- [90] LIGO Scientific Collaboration, “Instrument science white paper,” tech. rep., DCC Number T1900409, 2019.
- [91] A. V. Dmitriev, S. D. Mescherlakov, K. V. Tokmakov, and V. P. Mitrofanov, “Controllable damping of high-Q violin modes in fused silica suspension fibers,” *Classical and Quantum Gravity*, vol. 27, p. 025009, 2010.
- [92] K. H. Lee, *Suspension upgrades for future gravitational wave detectors*. PhD thesis, University of Glasgow, 2019.
- [93] K. Toland, “Development and characterisation of a pulling machine to produce small diameter silica fibres for use in prototype advanced gravitational wave detectors,” Master’s thesis, University of Glasgow, December 2015.
- [94] R. Jones, “aLIGO SUS CO2 Laser Machine - Overall Assembly,” tech. rep., DCC Number D070560, 2010.
- [95] A. Heptonstall *et al.*, “Enhanced characteristics of fused silica fibers using laser polishing,” *Classical and Quantum Gravity*, vol. 31, no. 10, p. 105006, 2014.
- [96] <https://www.contecinc.com/products/anticon-gold-sorb/>, “Anticon Gold Wipes,” July 2019.

- [97] G. D. Hammond, M. van Veggel, A. Cumming, *et al.*, “QUAD Monolithic Fibre pulling/welding procedure,” tech. rep., DCC Number E1000366, 2010.
- [98] “Thorlabs PTL802.” <https://www.thorlabs.com/thorproduct.cfm?partnumber=PTL802>, Last accessed: July 2019.
- [99] K. Toland, A. Conway, L. Cunningham, *et al.*, “Development of a pulling machine to produce micron diameter fused silica fibres for use in prototype advanced gravitational wave detectors,” *Class. Quantum Grav.*, vol. 35, no. 165004, 2018.
- [100] R. Jones and A. Cumming, “CO2 Laser Pulling Machine Alignment Plate 2,” tech. rep., DCC Number D1800134, 2018.
- [101] R. Jones and A. Cumming, “CO2 Laser Pulling Machine Alignment Plate 1,” tech. rep., DCC Number D1800133, 2018.
- [102] D. Cook, “Pulling machine conical mirror alignment target,” tech. rep., DCC Number D110055, 2011.
- [103] R. Jones and A. Cumming, “CO2 Laser Pulling Machine 3mm stock alignment plate,” tech. rep., DCC Number D1800247, 2018.
- [104] “Data sheet for Synrad Firestar F100 laser.” <http://www.synrad.com/fseries/f100.htm>, Last accessed: July 2019.
- [105] “Data sheet for Synrad Firestar i401 laser.” [https://www.synrad.com/sites/default/files/2017-06/OperatorsLast accessed: July 2019.](https://www.synrad.com/sites/default/files/2017-06/OperatorsLast%20accessed%3A%20July%202019.pdf)
- [106] “Thorlabs VRC6S.” <https://www.thorlabs.com/thorproduct.cfm?partnumber=VRC6S>, Last accessed: July 2019.
- [107] “NB1-L01 gold coated mirror.” [https://www.thorlabs.com/newgrouppage9.cfm?objectgroup\\_id=7040](https://www.thorlabs.com/newgrouppage9.cfm?objectgroup_id=7040), Last accessed: August 2019.
- [108] “Threaded precision kinematic mirror mount.” <https://www.thorlabs.com/thorproduct.cfm?partnumber=KS1T>, Last accessed: August 2019.
- [109] “Thorlabs LMR1AP.” <https://www.thorlabs.com/thorproduct.cfm?partnumber=LMR1AP>, Last accessed: July 2019.
- [110] K. H. Lee *et al.*, “Improved fused silica fibres for the advanced LIGO monolithic suspensions,” *Class. Quantum Grav.*, vol. 36, no. 18, p. 185018, 2019.

- [111] A. V. Cumming, “Private communications,” 2019.
- [112] N. A. Robertson, “Report on fiber breaks during monolithic assemblies between O2 and O3,” tech. rep., DCC Number T1800363, 2018.
- [113] A. Bell and N. A. Robertson, “Fiber break root cause analysis,” tech. rep., DCC Number T1800317, 2018.
- [114] A. Cumming, B. Sorazu, and A. Bell, “Weld pictures from 2017, 2018 installs, and analysis,” tech. rep., DCC Number T1800166, 2018.
- [115] A. Bell and A. Heptonstall, “Data set (text files) for polishing and pulling silica fibres,” tech. rep., DCC Number T1000367, 2013.
- [116] “Araldite 2011, 50 ml Yellow Dual Cartridge Epoxy Adhesive for Polyamide.” <https://uk.rs-online.com/web/p/epoxy-resins-epoxy-adhesives/3888926/>, Last accessed: August 2019.
- [117] R. Jones, “The Design of the IGR MKII Strength Testing Machine,” tech. rep., DCC Number T1000345, 2010.
- [118] “Omega s-beam load cell.” [www.omega.co.uk/pptst/LC101.html](http://www.omega.co.uk/pptst/LC101.html), Last accessed: August 2019.
- [119] “Phantom VEO high speed camera.” <https://www.phantomhighspeed.com/products/cameras/veo>, Last accessed: October 2019.
- [120] “Phantom PCC software.” <https://www.phantomhighspeed.com/resourcesandsupport/phantomresources/pccsoftware>, Last accessed: October 2019.
- [121] A. V. Cumming *et al.*, “Apparatus for dimensional characterization of fused silica fibers for the suspensions of advanced gravitational wave detectors,” *Review of Scientific Instruments*, vol. 82, p. 044502, 2011.
- [122] A. V. Cumming, *Aspects of mirrors and suspensions for advanced gravitational wave detectors*. PhD thesis, University of Glasgow, 2008.
- [123] “UniBrain Fire-i board camera.” <https://www.unibrain.com/products/fire-i-board-camera/>, Last accessed: October 2019.
- [124] “SIKO MSK320 Magnetic Sensor.” <https://www.siko-global.com/en-gb/products/magline-magnetic-linear-and-angular-measurement/magnetic-sensors/msk320>, Last accessed: July 2019.

- [125] “Python 3.” <https://www.python.org/download/releases/3.0/>, Last accessed: July 2019.
- [126] “Jupyter notebooks.” <https://jupyter.org/>, Last accessed: July 2019.
- [127] “Scipy linregress function.”  
<https://docs.scipy.org/doc/scipy/reference/generated/scipy.stats.linregress.html>, Last accessed: September 2019.
- [128] K. V. Tokmakov, A. Cumming, J. Hough, *et al.*, “A study of the fracture mechanisms in pristine silica fibres utilising high speed imagine techniques,” *Journal of non-crystalline solids*, vol. 358, pp. 1669–1709, 2012.
- [129] S. Appert, C. Torrie, and N. A. Robertson, “FEA of a fused silica fiber in ANSYS: Angular offsets to model irregularities in fiber welding or fiber pulling,” tech. rep., DCC Number T1800169, 2018.
- [130] “ANSYS - Finite element analysis tool.” <https://www.ansys.com/en-gb>, Last accessed: October 2019.
- [131] B. A. Proctor *et al.*, “The strength of fused silica,” *Proceedings of the Royal Society of London A: Mathematical, Physical and Engineering Sciences*, vol. 297, no. 1451, pp. 534–557, 1967.
- [132] “Heraeus, pure silica rods for specialty fiber applications.”  
[https://www.heraeus.com/media/media/hca/doc\\_hca/products\\_and\\_solutions\\_8/optical\\_fiber/Pure\\_Silica\\_Rods\\_EN.pdf](https://www.heraeus.com/media/media/hca/doc_hca/products_and_solutions_8/optical_fiber/Pure_Silica_Rods_EN.pdf), Last accessed: August 2019.
- [133] R. Jones, A. Bell, A. Cumming, *et al.*, “aLIGO SUS ETM ITM Monolithic Assembly - Pulled Fibre with Fuse Ends Assembly,” tech. rep., DCC Number: D1101052, 2011.
- [134] R. Jones, “aLIGO CO2 Laser Pulling Machine - Monolithic Assembly Tooling - Fuse Assembly,” tech. rep., DCC Number D080404, 2010.
- [135] L. Cunningham, “Fibre fuse end jig,” tech. rep., DCC Number D1001532, 2013.
- [136] R. Jones and E. Sanchez, “aLIGO SUS ETM ITM Monolithic Assembly - fibre cartridge assembly,” tech. rep., DCC Number D1001504, 2010.
- [137] R. Jones and A. Cumming, “aLIGO SUS Monolithic Assembly Fibre Profiler Overall Assembly,” tech. rep., DCC Number D070519, 2010.
- [138] “McDry MCU-340A storage cabinet.” <http://www.mcdry.us/seihin/mcu.html>, Last accessed: August 2019.
- [139] “LabJack U12.” <https://labjack.com/products/u12>, Last accessed: July 2019.

- [140] Arizona-Software, “GraphClick data extraction software.” <https://graphclick.en.softonic.com/mac>, Last accessed: October 2018.
- [141] A. Jain *et al.*, “A comparative study of visual and auditory reaction times on the basis of gender and physical activity levels of medical first year students,” *International Journal of Applied and Basic Medical Research*, vol. 5, pp. 124–127, May 2015.
- [142] T. A. Michalske and S. W. Freiman, “A molecular mechanism for stress corrosion in Vitreous Silica,” *Journal of the American Ceramic Society*, vol. 66, no. 4, pp. 284–288, 1983.
- [143] W. J. Duncan *et al.*, “The effect of environment on the strength of optical fiber,” *Plenum Press, New York*, pp. 309–326, 1985.
- [144] C. Gräf *et al.*, “Design of a speed meter interferometer proof-of-principle experiment,” *Classical and Quantum Gravity*, vol. 31, p. 215009, 2014.
- [145] J.-S. Hennig, *Mirror suspensions for the Glasgow Sagnac speed meter*. PhD thesis, University of Glasgow, 2018.
- [146] T. Westphal, G. Bergmann, A. Bertolini, *et al.*, “Design of the 10 m AEI prototype facility for interferometry studies. A brief overview,” *Applied Physics B: Lasers and Optics*, vol. 106, no. 3, pp. 551–557, 2012.
- [147] K. Toland *et al.*, “Development of a thin silica fibre pulling machine,” in *LIGO Virgo Collaboration Meeting - Budapest*, 2015.
- [148] R. Jones and A. Cumming, “aLIGO SUS Monolithic Assembly Fibre Profiler\_Camera Assembly\_Adjuster A\_Lens Tube\_Lrg,” tech. rep., DCC Number D1001564, 2010.
- [149] R. Jones and A. Cumming, “aLIGO SUS Monolithic Assembly Fibre Profiler\_Camera Assembly\_Adjuster B\_Lens Tube sml,” tech. rep., DCC Number D1001570, 2010.
- [150] “Thorlabs DCC1240M.” <https://www.thorlabs.com/thorproduct.cfm?partnumber=DCC1240M>, Last accessed: July 2019.
- [151] “Thorlabs MVL12X20L.” <https://www.thorlabs.com/thorproduct.cfm?partnumber=MVL12X20L>, Last accessed: July 2019.
- [152] “Thorlabs MVL20A.” <https://www.thorlabs.com/thorproduct.cfm?partnumber=MVL20A>, Last accessed: July 2019.

- [153] “Thorlabs MVL12X12Z.”  
<https://www.thorlabs.com/thorproduct.cfm?partnumber=MVL12X12Z>, Last accessed: July 2019.
- [154] L. Perri, “The construction of an upgraded fiber profiler involving the installation of a high resolution USB CCD camera with a 12x zoom lens,” tech. rep., University of Glasgow, 2016.
- [155] “Feeler gauge blade tolerances - DIN 2275.” Email communications
- [156] “0.075mm tungsten wire.” <https://www.advent-rm.com/catalogue/tungsten/wire/W5588/>, Last accessed: August 2019.
- [157] “Thorlabs XYT1/M.” <https://www.thorlabs.com/thorproduct.cfm?partnumber=XYT1/M>, Last accessed: July 2019.
- [158] “L6205 - DMOS dual full bridge driver.”  
<https://www.st.com/resource/en/datasheet/l6205.pdf>, Last accessed: July 2019.
- [159] A. V. Cumming, “Dimensional characterisation equipment for advanced LIGO fused silica suspension fibres,” tech. rep., DCC Number T1000024, 2010.
- [160] “74LS123 Data sheet.” <https://www.ti.com/lit/ds/symlink/sn54123.pdf>, Last accessed: October 2019.
- [161] “0.025mm nickel chromium wire.” <https://www.advent-rm.com/catalogue/nickel-chromium/wire/>.
- [162] “SIKO MSK5000 Magnetic Sensor.” <https://www.siko-global.com/en-gb/products/magline-magnetic-linear-and-angular-measurement/magnetic-sensors/msk5000>, Last accessed: July 2019.
- [163] “SIOS Vibrometer.” <https://sios-de.com/products/laser-vibrometer/>, Last accessed: October 2019.
- [164] G. Taylor, “Design of the MKIII IGR Strength Testing Unit,” tech. rep., University of Glasgow, 2013.
- [165] E. Momany, “Upgrading the small strength tester to test thin silica fibres material properties and calculate the young’s modulus,” tech. rep., University of Glasgow, 2017.
- [166] “National Instruments USB-6008.” <https://www.ni.com/en-gb/support/model.usb-6008.html>, Last accessed: September 2019.

- [167] “RS PRO 159mm digital caliper.” <https://uk.rs-online.com/web/p/calipers/1243515/>, Last accessed: August 2019.
- [168] S. Bramsiepe, *The development of a field-portable MEMS gravimeter*. PhD thesis, University of Glasgow, 2019.
- [169] “Newport IMS400-LM motorised Linear stage, linear motor, 400mm travel.” <https://www.newport.com/p/M-IMS400LM-S>, Last accessed: September 2019.
- [170] V. M. Weerasinghe, J. Gabzdyl, and R. D. Hibberd, “Properties of a laser beam generated from an axicon resonator,” *Optics and Laser Technology*, vol. 21, no. 6, pp. 389–391, 1989.
- [171] S. R. Mishra *et al.*, “Generation of hollow conic beams using a metal axicon mirror,” *Optical Engineering*, vol. 46, no. 8, p. 084002, 2007.
- [172] A. Conway, “Preliminary design and control program for CO<sub>2</sub> laser based fused silica “micro” fiber pulling machine,” Master’s thesis, Lake Forest College, August 2014.
- [173] S. Großler *et al.*, “The AEI 10 m prototype interferometer,” *Classical and Quantum Gravity*, vol. 27, p. 084023, 2010.
- [174] “Synrad UC-2000 laser controller.” <https://www.synrad.com/sites/default/files/2019-05/Operators%20Manual%20UC2000.pdf>, Last accessed: September 2019.
- [175] “Raspberry Pi.” <https://www.raspberrypi.org>.
- [176] L. Cunningham, “Fibre bow tweezers,” tech. rep., DCC Number D1001786, 2010.
- [177] “RS PRO Bench Scales, 10g Weight Capacity, With RS Calibration.” <https://uk.rs-online.com/web/p/weighing-scales/1113679/>, Last accessed: September 2019.
- [178] A. M. Gretarsson and G. M. Harry, “Dissipation of mechanical energy in fused silica fibers,” *Review of Scientific Instruments*, vol. 70, p. 4081, 1999.
- [179] A. Heptonstall *et al.*, “Characterisation of mechanical loss in synthetic fused silica ribbons,” *Physics Letters A*, vol. 354, pp. 353–359, 2006.
- [180] “Saint-Gobain Vitreosil.” <http://www.matweb.com/search/datasheettext.aspx?matguid=f4e946aaecef4558a888d421e2b2cce2>, Last accessed: May 2020.
- [181] Heraeus, “Properties of fused silica.” [https://www.heraeus.com/en/hqs/fused\\_silica\\_quartz\\_knowledge\\_base/properties/properties.aspx](https://www.heraeus.com/en/hqs/fused_silica_quartz_knowledge_base/properties/properties.aspx).

- [182] G. Brambilla and D. N. Payne, “The ultimate strength of glass silica nanowires,” *Nano letters*, vol. 9, no. 2, pp. 831–835, 2009.
- [183] S. Zhurkov *Sov. Phys. -JETP*, vol. 1, pp. 189–193, 1933.
- [184] V. P. Pukh *et al.*, “Atomic structure and strength of inorganic glasses,” *Physics of the solid state*, vol. 47, no. 5, pp. 876–881, 2005.
- [185] B. Sorazu, “aLIGO monolithic suspensions violin modes data compilation,” tech. rep., DCC Number T1800327, 2018.